The Interaction of Fluid Transients with Pipeline Anomalies

Author:

Jane ALEXANDER

Supervisors:

Professor Pedro LEE

Professor Mark DAVIDSON

Dr. Zhao LI

A thesis submitted in partial fulfilment of the requirements

for the degree of Doctor of Philosophy in Civil Engineering

Department of Civil and Natural Resources Engineering

University of Canterbury

Christchurch, New Zealand

June 28, 2021

Abstract

A functional and secure water supply is essential for supporting social and economic development. However, although pipelines account for the majority of water infrastructure assets and require a significant amount of capital and operational expenditure, knowledge of network condition is generally poor. As networks age, the gap between asset renewal and depreciation is widening. The formation of long-term renewal plans is hampered by lack of access and of a consistent testing methodology. A pro-active and non-intrusive approach is required to enable effective prioritisation of repairs and renewal.

Fluid transients may be used as a tool for diagnosing anomalies which compromise the operation of water supply pipe networks. Controlled transients can be generated in pipe networks and the resulting pressure disturbances measured at receivers. Any anomalies in the system's physical properties create wave reflections which may be interpreted to assess the type, location, and severity of the anomaly. While the method has promise, the effects of possible system features and faults must be well understood so that meaningful conclusions can be drawn from the transient signals.

This thesis explores the effects of two key anomaly types on the transient response: air pockets and deteriorated sections. The work includes experimental investigations using the University of Canterbury laboratory facilities and evaluation of numerical modelling approaches in the time and frequency domain. The primary aim is to identify key characteristics of the transient interaction with each fault type and identify modelling methods which are able to accurately reproduce these characteristics. The findings inform the further development of transient-based diagnostic techniques.

A comprehensive set of experimental data is collected to investigate the effect of air pockets on the transient response, spanning a range of pocket volumes, initial hydrostatic pressures, and air pocket configurations. A short duration pulse is used to obtain specific information regarding the transient transmission and reflection. Air pockets are characterised in the time domain by their reflectivity, which is calculated based on impedance theory. The lack of dependence on flow rate allows air to be differentiated from solid blockages. The presence of air is also observed to increase the transient damping rate. However, the most identifiable effects of air are observed in the frequency domain. The frequency-dependent reflectivity of in-line and off-line air pockets is due to the resonant properties of air, and is primarily determined by the pocket geometry. This frequency-dependent behaviour is unique to air among common pipeline faults, so is a potentially useful tool when developing diagnostic frameworks.

It is also important to investigate how the air-transient interaction may be incorporated into transient modelling approaches. The method of characteristics time domain model is combined with a variable wave speed consideration to more accurately describe the timing of the transient response due to an in-line air pocket. When modelling an off-line air pocket, inertia in the connecting water column should also be considered. A frequency response model based on plane wave theory is developed to improve upon previous modelling approaches which have treated the connecting water column as an incompressible unit.

The final section of this thesis assesses an accelerated corrosion methodology for testing a range of deterioration scenarios in the laboratory. A series of small-scale and large-scale mild steel pipe specimens are subjected to internal, external, or internal and external corrosion, and the transient wave speed is measured at regular intervals to track the reduction in wave speed with wall thickness loss. The findings show that reductions in the wave speed observed in the field are likely to correspond to either severe corrosion or erroneous pipe material records. The key consideration associated with the accelerated corrosion method is managing precipitate build-up, particulary on the internal surface of the pipe.

Deputy Vice-Chancellor's Office
Postgraduate Research Office

UNIVERSITY OF CANTERBURY
Te Whare Wānanga o Waitaha
CHRISTCHURCH NEW ZEALAND

Co-Authorship Form

This form is to accompany the submission of any thesis that contains research reported in co-authored work that has been published, accepted for publication, or submitted for publication. A copy of this form should be included for each co-authored work that is included in the thesis. Completed forms should be included at the front (after the thesis abstract) of each copy of the thesis submitted for examination and library deposit.

Please indicate the chapter/section/pages of this thesis that are extracted from co-authored work and provide details of the publication or submission the extract comes from:

Chapter 3 is extracted from the publication: Alexander, J., Lee, P.J., Davidson, M., Li, Z, Murch, R., Duan, H.F., Meniconi, S., Brunone, B. (2020). Experimental investigation of the interaction of fluid transients with an in-line air pocket. Journal of Hydraulic Engineering, 146(3). Sections of the methods described in Chapter 2 are also reproduced from this publication.

Please detail the nature and extent (%) of contribution by the candidate:

The candidate was the primary author of the publication (95%), with supervision and guidance provided by co-authors.

Certification by Co-authors:

If there is more than one co-author then a single co-author can sign on behalf of all
The undersigned certifies that:

- The above statement correctly reflects the nature and extent of the Doctoral candidate's contribution to this co-authored work
- In cases where the candidate was the lead author of the co-authored work he or she wrote the text

Name: Pedro Lee Signature:

Date: *19th Nov, 2020*

Deputy Vice-Chancellor's Office
Postgraduate Research Office

UNIVERSITY OF CANTERBURY
Te Whare Wānanga o Waitaha
CHRISTCHURCH NEW ZEALAND

Co-Authorship Form

This form is to accompany the submission of any thesis that contains research reported in co-authored work that has been published, accepted for publication, or submitted for publication. A copy of this form should be included for each co-authored work that is included in the thesis. Completed forms should be included at the front (after the thesis abstract) of each copy of the thesis submitted for examination and library deposit.

Please indicate the chapter/section/pages of this thesis that are extracted from co-authored work and provide details of the publication or submission the extract comes from:

Chapter 4 is extracted from the publication: Alexander, J., Lee, P.J., Davidson, M., Duan, H.F., Li, Z., Murch, R., Meniconi, S. and Brunone, B. (2019). Experimental validation of existing numerical models for the interaction of fluid transients with in-line air pockets. Journal of Fluids Engineering, 141(12). Sections of the methods described in Chapter 2 are also reproduced from this publication.

Please detail the nature and extent (%) of contribution by the candidate:

The candidate was the primary author of the publication (95%), with supervision and guidance provided by co-authors.

Certification by Co-authors:

If there is more than one co-author then a single co-author can sign on behalf of all

The undersigned certifies that:

- The above statement correctly reflects the nature and extent of the Doctoral candidate's contribution to this co-authored work
- In cases where the candidate was the lead author of the co-authored work he or she wrote the text

Name: Pedro Lee Signature:

Date: *19th Nov, 2020*

Deputy Vice-Chancellor's Office
Postgraduate Research Office

UNIVERSITY OF CANTERBURY
Te Whare Wānanga o Waitaha
CHRISTCHURCH NEW ZEALAND

Co-Authorship Form

This form is to accompany the submission of any thesis that contains research reported in co-authored work that has been published, accepted for publication, or submitted for publication. A copy of this form should be included for each co-authored work that is included in the thesis. Completed forms should be included at the front (after the thesis abstract) of each copy of the thesis submitted for examination and library deposit.

Please indicate the chapter/section/pages of this thesis that are extracted from co-authored work and provide details of the publication or submission the extract comes from:

Chapter 5 is extracted from the publication: Alexander, J., Li, Z., Lee, P.J., Davidson, M., Duan, H.F. (2020). Experimental investigation of the effects of air pocket configuration on fluid transients in a pipeline. Journal of Hydraulic Engineering, 146(12). Sections of the methods described in Chapter 2 are also reproduced from this publication.

Please detail the nature and extent (%) of contribution by the candidate:

The candidate was the primary author of the publication (95%), with supervision and guidance provided by co-authors.

Certification by Co-authors:

If there is more than one co-author then a single co-author can sign on behalf of all

The undersigned certifies that:

- The above statement correctly reflects the nature and extent of the Doctoral candidate's contribution to this co-authored work
- In cases where the candidate was the lead author of the co-authored work he or she wrote the text

Name: Pedro Lee Signature:

Date: *19th Nov, 2020*

Deputy Vice-Chancellor's Office
Postgraduate Research Office

UNIVERSITY OF CANTERBURY
Te Whare Wānanga o Waitaha
CHRISTCHURCH NEW ZEALAND

Co-Authorship Form

This form is to accompany the submission of any thesis that contains research reported in co-authored work that has been published, accepted for publication, or submitted for publication. A copy of this form should be included for each co-authored work that is included in the thesis. Completed forms should be included at the front (after the thesis abstract) of each copy of the thesis submitted for examination and library deposit.

Please indicate the chapter/section/pages of this thesis that are extracted from co-authored work and provide details of the publication or submission the extract comes from:

Chapter 6 is extracted from the publication: Alexander, J., Li, Z., Lee, P.J., Davidson, M., Duan, H.F. Comparison of numerical models for the interaction of a fluid transient with an off-line air pocket. Accepted for publication by Journal of Hydraulic Engineering, 2020. Sections of the methods described in Chapter 2 are also reproduced from this publication.

Please detail the nature and extent (%) of contribution by the candidate:

The candidate was the primary author of the publication (95%), with supervision and guidance provided by co-authors.

Certification by Co-authors:

If there is more than one co-author then a single co-author can sign on behalf of all

The undersigned certifies that:

- The above statement correctly reflects the nature and extent of the Doctoral candidate's contribution to this co-authored work
- In cases where the candidate was the lead author of the co-authored work he or she wrote the text

Name: Pedro Lee Signature:

Date: *19th Nov, 2020*

Deputy Vice-Chancellor's Office
Postgraduate Research Office

UNIVERSITY OF CANTERBURY
Te Whare Wānanga o Waitaha
CHRISTCHURCH NEW ZEALAND

Co-Authorship Form

This form is to accompany the submission of any thesis that contains research reported in co-authored work that has been published, accepted for publication, or submitted for publication. A copy of this form should be included for each co-authored work that is included in the thesis. Completed forms should be included at the front (after the thesis abstract) of each copy of the thesis submitted for examination and library deposit.

Please indicate the chapter/section/pages of this thesis that are extracted from co-authored work and provide details of the publication or submission the extract comes from:

Chapter 7 is extracted from the publication: Alexander, J., Lee, P.J., Li, Z. (2020). Investigation of the Effects of Base Flow on the Interaction of Off-line Air Pockets with Fluid Transients. 22nd Australasian Fluid Mechanics Conference, Brisbane, Australia. Sections of the methods described in Chapter 2 are also reproduced from this publication.

Please detail the nature and extent (%) of contribution by the candidate:

The candidate was the primary author of the publication (95%), with supervision and guidance provided by co-authors.

Certification by Co-authors:

If there is more than one co-author then a single co-author can sign on behalf of all
The undersigned certifies that:

- The above statement correctly reflects the nature and extent of the Doctoral candidate's contribution to this co-authored work
- In cases where the candidate was the lead author of the co-authored work he or she wrote the text

Name: Pedro Lee Signature:

Date: *19th Nov, 2020*

Acknowledgements

Firstly, I would like to acknowledge my supervisory team, Professor Pedro Lee, Professor Mark Davidson, and Dr. Derek Li. Your wealth of enthusiasm and experience has been invaluable in the completion of this work. The breadth of research interests and viewpoints you brought to the group taught me that there's always more to learn. Thank you for investing your time in providing feedback, advice, and support, and for sparking my interest in fluid mechanics and research in the first place. I've also appreciated your support in the wide range of non-research activities I've had the chance to participate in while at UC!

In addition, I would like to thank laboratory technicians Patrick Branje, Michael Weavers, and Nick McLaughlin. The experimental work would not have been possible without your infinite patience, flexibility, and creativity. Thank you for taking the time to answer my endless questions and for always tackling my even more endless lab problems with a smile on your face.

Special thanks go to my fellow and former colleagues from the Fluids in Canterbury Cluster, Elizabeth North, Alex Meredith, Rondo Law, and Craig McConnochie. Sometimes I think I might have completed this thesis more efficiently without you all, but then I realise that if it weren't for the continual laughs, distractions, long lunches, and occasional fluid mechanics discussions, it's more likely I wouldn't have completed it at all. The same goes for the rest of the UC community, within the CNRE department and beyond - thank you for making the last three years so unexpectedly enjoyable. It's been a privilege to be part of this little family.

Last, but certainly not least, I must acknowledge my friends and family. Thank you for taking the time to understand my work, even if the specifics were sometimes a little baffling. Thank you for

sharing both the successes and the minor breakdowns with me, not just during this work, but over all the years leading up to it. Especially to Aaron - this short paragraph is not enough to encapsulate the value of the love, encouragement, and occasional tech support you provided, not to mention the tolerance of all those weekends of lab work!

Contents

List of Figures

List of Tables

List of Symbols

a	=	wave speed
A	=	area
c	=	constraint condition constant
C_A	=	polytropic constant
D	=	diameter
e	=	pipe wall thickness
E	=	Young's modulus
f	=	friction factor
F	=	Faraday's constant
g	=	gravitational acceleration
h	=	DFT amplitude
h_f	=	friction loss
H	=	piezometric head
i	=	spatial index
I	=	impressed current
j	=	temporal index
k	=	damping rate
K	=	bulk modulus
L_P	=	air pocket length
L	=	length
m	=	mass loss
M	=	molar mass
n	=	polytropic exponent
P	=	pressure
Q	=	flow rate

r	=	damping rate
RC	=	reflection coefficient
t	=	time
T	=	pipeline period
TC	=	transmission coefficient
U	=	velocity
V	=	volume
W	=	Zielke's weighting function
x	=	distance
z	=	elevation
Z	=	impedance
ϵ	=	error
ε	=	void ratio
ν	=	kinematic viscosity
ρ	=	density
ω	=	frequency
$\forall_p$	=	air pocket volume

Preamble

Chapters 3 - 7 of this thesis are composed of 4 published or accepted journal articles and 1 conference paper. The thesis author was the primary author of the papers presented. Supervision, guidance, and editing was provided by the co-authors. Minor changes have been made from the published versions for inclusion in this thesis, and some introductory sections have been removed to avoid repetition. A review of general background literature regarding the research area is covered in Chapter 1. The general experimental and numerical methods for the work in Chapters 3 - 7 have been synthesised in Chapter 2. The noted articles are as follows:

Chapter 3: Alexander, J., Lee, P.J., Davidson, M., Li, Z, Murch, R., Duan, H.F., Meniconi, S., Brunone, B. (2020). Experimental investigation of the interaction of fluid transients with an in-line air pocket. Journal of Hydraulic Engineering, 146(3). Re-used in this thesis with permission from ASCE (Appendix A).

Chapter 4: Alexander, J., Lee, P.J., Davidson, M., Duan, H.F., Li, Z., Murch, R., Meniconi, S. and Brunone, B. (2019). Experimental validation of existing numerical models for the interaction of fluid transients with in-line air pockets. Journal of Fluids Engineering, 141(12). Re-used in this thesis with permission from ASME (Appendix A).

Chapter 5: Alexander, J., Li, Z., Lee, P.J., Davidson, M., Duan, H.F. (2020). Experimental investigation of the effects of air pocket configuration on fluid transients in a pipeline. Journal of Hydraulic Engineering, 146(12). Re-used in this thesis with permission from ASCE (Appendix A).

Chapter 6: Alexander, J., Li, Z., Lee, P.J., Davidson, M., Duan, H.F.. Comparison of numerical models for the interaction of a fluid transient with an off-line air pocket. Accepted for publication by Journal of Hydraulic Engineering, 2020 (DOI 10.1061/(ASCE)HY.1943-7900.0001878). Re-used in this thesis with permission from ASCE (Appendix A).

Chapter 7: Alexander, J, Lee, P.J., Li, Z. (2020). Investigation of the effects of base flow on the interaction of off-line air pockets with fluid transients. 22nd Australasian Fluid Mechanics Conference, Brisbane, Australia., 2020. Permitted to be re-used in this thesis in accordance with the AFMC Copyright Agreement.

1 Introduction and review

1.1 Background

1.1.1 Pipeline condition assessment

A safe and reliable water supply is essential to supporting the health and sanitation of cities and communities all over the world, as well as generating significant economic benefits. Functional water supply has become an expected service in developed nations, with significant investments required to install and maintain the associated infrastructure. During the 2018-2019 period, New Zealand's operational expenditure for supplying public drinking water was estimated at NZ$275 million, with a capital expenditure of NZ$347 million (Water New Zealand, 2019). Although pipeline networks account for approximately 80% of water supply infrastructure assets, they are commonly operated with a lack of basic information. Knowledge of aging networks is poor; in New Zealand approximately 18% of drinking water is lost through leaks in buried pipes, and planned and unplanned service interruptions occur regularly due to leaks, blockages, and contamination (Water New Zealand, 2019). Most countries fall into a range of 20-30% water loss due to leakage, and the energy costs created by poor pipe condition are an international problem (Lai, 1991; Colombo and Karney, 2002). A recent audit has shown a NZ$7 billion gap between asset renewal expenditure and depreciation, creating a critical risk for New Zealand infrastructure (Auditor-General, 2014). To overcome this disparity, councils will need to invest NZ$41 billion into the water sector over the next decade, including NZ$20 billion on pipe renewal (Titchall, 2016). Despite the required level of investment, authorities experience significant struggles forming long-term renewal plans for below-ground assets such as pipes due to the lack of reliable condition data, particularly for

older installations, and instead tend to funnel investment into above-ground assets which can be more easily characterised. However, a significant renewal cycle is expected in the 2040-2060 period as many pipeline assets reach end-of-life and begin to fail (Auditor-General, 2014).

Unlike other lifelines, the monitoring of water supply networks is hampered by the inaccessibility and expanse of the buried network. The lack of comprehensive knowledge regarding pipeline condition has been one of the main factors limiting investment, with only 16% of participants in the 2018-19 Water New Zealand National Performance Review considering their pipe condition data reliable (Water New Zealand, 2019). This is particularly true for older pipes, which are also more prone to developing faults. Furthermore, there is no consistent testing or grading methodology, making it difficult to draw meaningful comparisons across data sets. A condition assessment technology is required which can improve confidence in condition data and enable effective investment in water supply assets.

The primary aim of condition assessment is to identify anomalies in the pipe's characteristics that are either reducing the efficiency of the system or are likely to reduce efficiency in the future. This may include deterioration of the pipe walls or the formation of leaks and blockages. Wall weakening or thinning is likely to result in bursts or leaks if not addressed (AWWSC, 2002), while blockages can reduce the supply pressure and increase pumping costs. The costs of water loss and energy usage associated with leaks are also well known (Colombo et al., 2009). Network operators commonly take a reactive approach, only locating and addressing faults when there are observed reductions in system performance. However, a proactive approach, where preemptive checking is used to identify faults before system operation is compromised, represents a more effective management strategy. An effective and efficient method for characterising the condition of pipe networks without excavation represents a significant cost saving for network operators, with regard to operation and maintenance expenses and sanitation. The ideal method will provide information about the pipe wall condition, as well as the ability to pinpoint and characterise discrete anomalies such as leaks and blockages, enabling a targeted repair or removal plan. The method should have sufficient sensitivity to identify minor anomalies, enabling proactive repairs or replacement.

Non-invasive methods are preferred as this will minimise both cost and disruption to the system.

A variety of existing tools and techniques can be used to assess the condition of a pipeline, with a corresponding variety of cost, inconvenience, and inaccuracy associated with each method. In some cases, pipeline condition may only be inferred from desktop investigations which consider soil conditions, user feedback, and historic failure rates (Liu et al., 2012). Although relatively low cost, this method does not provide any true information on the pipe condition. The most common industry approach for pipe condition assessment involves the excavation and physical inspection of the pipe, and in some cases a section of material may be removed from the pipe wall for material testing (Water New Zealand, 2006). This is intrusive, time-consuming, and only yields information at discrete points. It is also fundamentally error-prone as the condition of the test location may not be representative of the rest of the pipe. A range of non-destructive signal-based methods exist which can provide information about a greater length of pipe, such as electromagnetic and ultrasonic testing (Liu and Kleiner, 2012). However, these methods generally require access to the pipe wall, and the signals are subject to significant attenuation.

An alternative option is to make use of the hydraulic behaviour of pipeline systems. Propagating pressure waves, known as fluid transients, are an ideal method for communicating pipeline properties to an above-ground operator (Jönsson, 1994). Transient waves occur in pipeline systems as a result of a sudden changes in flow conditions, such as a valve closure. As the flow transitions between the two steady states pressure oscillations are created, and these oscillations propagate along the pipeline (Wylie et al., 1993). Controlled transients can be generated artificially in pipe networks to carry information through the network in the same way as an electrical signal through a wire, with wave generation and pressure measurements undertaken at existing service connections. Any changes to the physical properties of the pipeline system that alter the system's pressure and flow response, such as leaks, blockages, or changes in the pipe wall thickness, create reflections of the transient signal as shown in Fig. 1.1 (Colombo et al., 2009). Pipe deterioration may also reduce the speed of the transient wave, which depends on the pipe wall thickness, diameter, and elasticity (Gong et al., 2013a). The range of the transient signals are largely adjustable, and the maximum

possible transient range is unmatched by other signal-based methods. For example, field testing by Ebacher et al. (2011) showed that pressure disturbances created by short pump interruptions in an active water distribution system consisting of 1,590 km of pipe could be measured by sensors at the extremes of the network. If the impact of specific anomalies on the reflection and transmission of the pulse is understood, measuring the evolution of pressure in the pipe after the controlled generation of a transient wave can allow the pipe condition to be characterised (Bergant et al., 2008). This approach may be used to enable real-time, continuous monitoring of pipe networks, providing information on pipeline condition and water usage patterns. Continuous transient monitoring would enable network operators to implement a more proactive condition assessment regime, facilitating improved network management and targeted pipe renewal projects based on accurate, comprehensive condition data without the need for costly excavations. The wealth of data provided can give local government greater confidence in future infrastructure investments. Introduction of accurate condition assessment methods may also enable a standardised testing protocol and improved data comparison on national and international scales.

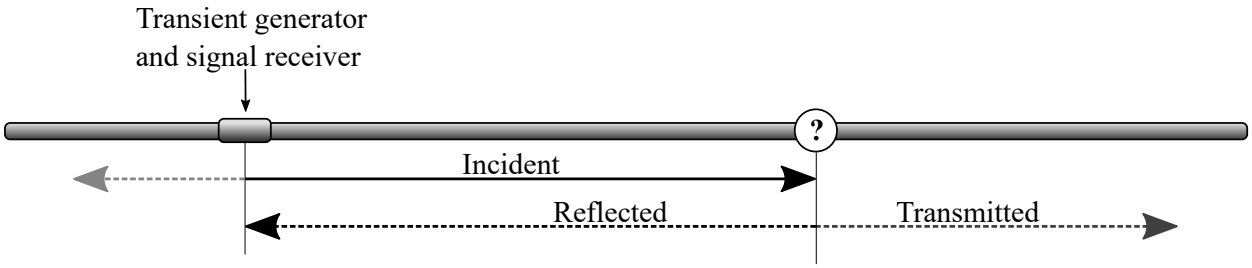

FIGURE 1.1: Transient signal wave path

While a transient-based condition assessment method has promise, for it to contribute meaningfully to asset management it is critical that the effects of possible system features are well understood, so that transient signals can be accurately interpreted (Colombo et al., 2009). This includes inherent network attributes such as junctions, valves, and fluid-structure interaction, as well as anomalies such as leaks, solid blockages, entrapped air, and pipe wall deterioration. A range of methods exist for interpreting observed transient data which are summarised in the following sections.

Transient condition assessment may be considered as an inverse problem, as first explored by Pudar and Liggett (1992) for the leak case. This approach is known as inverse transient analysis (ITA), and is used when the flow and pressure in the system are known or measured, while parameters such as anomalies, the pipe wall condition, or flow demands remain unknown. The transient trace is recorded and a numerical simulator is used to test possible system scenarios until the system response is adequately matched. The objective function for optimisation is generally the sum of the squared differences between the observed and modelled pressure traces (Pudar and Liggett, 1992). The selection mechanism is often a compromise between convergence and speed, with the two most common approaches being the more rapid derivative-based Levenberg-Marquardt (Liggett and Chen, 1994; Nash and Karney, 1999) or a sampling procedure such as a genetic algorithm (Vítkovskỳ and Simpson, 1997; Tang et al., 2001) which is more likely to converge correctly. A range of studies have focused on whether a hybrid scheme can be developed which combines the advantages of the two approaches (Vítkovskỳ et al., 2002; Kapelan et al., 2002, 2003b). When conducting ITA it is also critical to consider the number and placement of sensors to ensure that the analysis is productive and efficient, with many studies devoted to optimising sampling design (Liggett and Chen, 1994; Kapelan et al., 2003a). The approach has been evaluated in the laboratory and in the field for a range of fault types, including wall deterioration, air pockets, blockages, and leaks (Vitkovsky et al., 2001; Stephens et al., 2004a; Stephens, 2008; Covas and Ramos, 2010; Soares et al., 2011; Hachem and Schleiss, 2012; Stephens et al., 2013; Tuck and Lee, 2013). It has generally been found that while ITA is effective in a highly controlled laboratory setting, field applications may be limited by the difficulties in representing other features that affect the system response, such as flexible joints, soil interactions, restraint conditions, and pipe vibration. The ITA approach is increasingly facilitated by advances in high-speed measurement, computing power, and data storage, and a continuous sampling regime would provide a wealth of training and test data. However, Covas et al. (2001) noted that one of the key factors for the success of ITA is the accuracy of the transient simulation. This means it is critical to understand and effectively model the range of possible transient interactions that may occur in complex field systems.

Time domain reflectometry methods offer an alternative to ITA. One of the key requirements for ITA is a comprehensive system model, which may be difficult to achieve due to the many complexities which can occur, as well as lack of knowledge regarding system attributes. Instead, the observed transient trace may be examined in the time domain and its attributes used to locate system anomalies without a fully modelled trace. Time domain reflectometry (TDR) is a method that utilises the transient reflections created by anomalies. If the wave speed of the system is known to a reasonable degree of accuracy, the arrival time of the reflected transient may be used to locate faults without the need for computationally expensive optimisation algorithms (Jönsson and Larson, 1992; Brunone, 1999; Meniconi et al., 2011; Gong et al., 2013a), although the method's effectiveness can be compromised in field scenarios where reflections are masked by background transients and vibrations. A range of approaches exist for processing signals to obtain the transient reflection, including determination of the second derivative of the cross-correlated signal (Beck et al., 2005), determination of the impulse response function (IRF) (Vítkovskỳ et al., 2003b; Gong et al., 2012), and the discrete wavelet transform (Ferrante and Brunone, 2003; Meniconi et al., 2013). Ideally, a complex input signal should be selected such that reflections are easily identifiable amongst background transients. In addition to TDR, the attenuation of the transient signal observed in the time domain may also be used to diagnose pipeline anomalies. It is possible to identify faults such as leaks through the damping rate of each harmonic frequency within the transient signal (Wang et al., 2002). Similar to other time domain approaches, further research is required before this approach can be applied to field systems with many features which may affect the damping behaviour (Nixon and Ghidaoui, 2007).

Frequency domain techniques may also be used to characterise the pipe condition. The frequency response diagram may be obtained either via Fourier transform of the time domain trace for a signal containing a range of frequencies, or by collecting responses for a set of single-frequency signals. The frequency response diagram can then be compared to the expected or previously observed frequency response for the system. Singularities such as leaks and blockages may be identified and located by the changes they impose on the amplitude and location of the resonant

frequencies of the response. For instance, leaks have been observed to impose a sinusoidal pattern on the resonant peak amplitudes (Lee et al., 2005). The frequency response may be used for diagnostics via either an inverse fitting process, or using resonance peak-sequencing (Lee et al., 2005). Frequency domain analysis has been explored for leaks, discrete blockages, and extended blockages (Jönsson and Larson, 1992; Lee et al., 2006; Mohapatra et al., 2006; Duan et al., 2012; Rubio Scola et al., 2017). For cases where a single transient signal is used, it is critical to ensure the input signal contains a bandwidth wide enough to capture a suitable number of system modes (Lee et al., 2006).

As discussed, it is important to understand how the range of anomalies that may occur in a distribution network affect the transient signal in terms of its reflection, transmission, and wave speed. This research focuses on two key anomaly types: entrapped air pockets and deterioration of the pipe wall material. The following sections and sub-sections review the current understanding of these fault types in more detail in terms of their effects on network operation and their interaction with transient signals.

1.1.2 Entrapped air pockets

Dissolved air exists naturally in water, with the amount of dissolution dependent on temperature and pressure. Under normal conditions water used in civil engineering applications contains approximately 2% air (Lauchlan et al., 2005), but this can vary in non-uniform systems such as water supply pipes. Low pressure regions created by pump action or local turbulence can cause air to come out of solution, creating tiny bubbles which may coalesce to form accumulated pockets. Martin and Wiggert (1986) noted that cooling systems, such as those in power stations, are prone to developing bubbles, slugs, or large masses of entrapped air, due to entry of air at the intake, through leaking seals, or as a result of gas release due to fluctuations in pressure or temperature. Air can also enter a pipeline through a range of other mechanisms. Air transport can be slow during the filling of pipelines, resulting in collections of air remaining trapped in the filled pipe (Lee, 1991). Air can also be released as a byproduct of biological activity within the pipe, particularly in

poorly designed, constructed, and maintained systems (USA National Research Council, 1982). At sections where there is a suction pressure within the pipe, air can enter through joints, fittings, and leaks in the pipe walls if the pipe is above the water table (Spellman, 2003). Furthermore, many pipelines contain air chambers as a form of surge control, and vortex action at their entrances can result in the transfer of air from the chamber to the pipeline.

When air is trapped in the pipeline, its form depends on the pipeline conditions. Numerous two-phase horizontal flow pattern maps have been developed to characterise the behaviour of the air under different steady state flow conditions. Mandhane et al. (1974) concluded that the fluid velocity and air velocity (the velocity at which entrapped air is moving along the pipe) represented a reasonable set of discrimination criteria, as opposed to the complex axis properties developed for previous maps. The resultant map (Fig. 1.2) is based on an extensive set of experimental data, including that used to develop previous schemes, and the layout of the map is substantiated by the theoretical results presented by Barnea (1987) for two-phase horizontal flow. The flow definitions in Fig. 1.2 correspond with those presented in Govier and Aziz (1972).

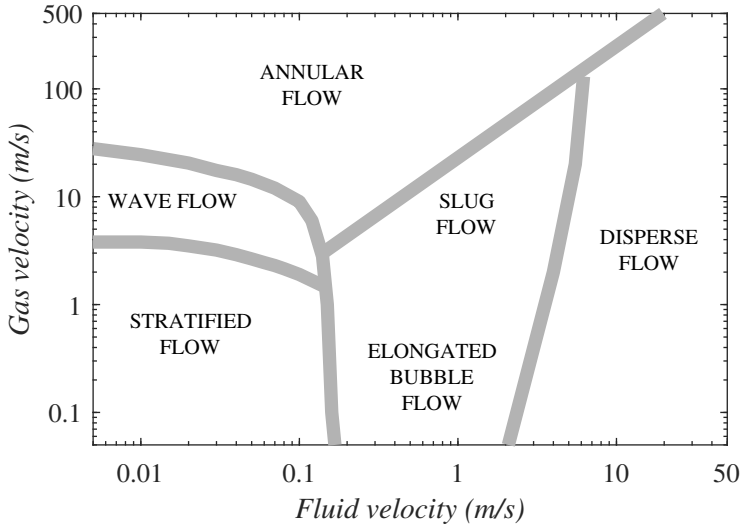

FIGURE 1.2: Flow pattern map for two-phase horizontal flow reproduced from Mandhane et al. (1974)

In water reticulation design codes, the maximum flow velocity is limited to approximately 2.5 m/s (Watercare, 2014) and entrapped air tends to gravitate to pipe crests or local high points, where it

becomes fixed, i.e., the air velocity is zero (Burrows and Qiu, 1995). Based on these conditions and the flow map developed by Mandhane et al. (1974), air collected at high points in the main flow will exist as elongated bubbles (Fig. 1.3a), where the air forms a pocket at the top of the pipe whilst liquid flows past below. This form of air pocket will be referred to as in-line air. Alternatively, the air may collect in a cavity outside the main flow path, such as beneath a valve or a hydrant. In this scenario, air does not block the main flow, and will be referred to as off-line air (Fig. 1.3b).

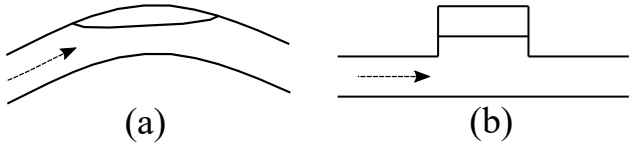

FIGURE 1.3: Entrapped air pockets: (a) in-line configuration, (b) off-line configuration.

Entrapped air in a pipeline can pose a range of problems for network operators. Similar to a blockage, accumulated in-line air reduces the pipe cross-section, causing a flow restriction and resulting in increased head loss, energy consumption, and ultimately pumping cost. Pozos et al. (2010) found that pumping accounts for around 75% of the operating costs of a distribution network, and entrapped air can reduce the overall efficiency by 30%. Off-line pockets do not create a blockage and are therefore less likely to compromise the hydraulic operation of the system. From this perspective, it is useful to be able to differentiate between these two air pocket configurations when carrying out condition assessment. In addition, the collapse of an entrapped pocket or rapid expulsion through a valve can create large transient events and vibrations in the pipe (Wylie et al., 1993), posing a risk to the network integrity. Lauchlan et al. (2005) lists a comprehensive summary of other network issues resulting from the presence of air including false readings on measuring apparatus and increased corrosion in ferrous pipes.

Air pockets also have the potential to interfere with transient diagnostic techniques. Even small air pockets which do not pose a risk to the system operation have been observed to create substantial transient reflections and affect the shape and timing of the transient wave (Whiteman and Pearsall, 1959, 1962; Kim, 2008b; Stephens, 2008). Early investigations showed the compressibility of air

also has a significant effect on wave speed (Pearsall, 1965; Falconer et al., 1983). When in a distributed form, as little as one part air in 10,000 parts water by volume causes a 50% reduction in the wave speed (Pearsall, 1965), which may also lead to significant dispersion of the pressure wave. A similar level of sensitivity was observed by Lee (1991). These considerations mean the effects of air pockets should be considered as part of a robust transient detection program. It is critical to accurately model in-line and off-line air pockets, so they can be incorporated into numerical network models to provide reliable approximations of likely transient responses.

If left unchecked, the gradual growth of the pocket could cripple the operation of the system, particularly for undulating networks. Air valves are placed at system high points to manually or automatically bleed off air (Wylie et al., 1993), but it is possible that air will gather at a point not equipped with a valve or the valve may malfunction, making air pockets difficult to locate and remove. As an alternative, Wisner et al. (1975) proposed the use of a sweeping velocity to force air downstream. This approach is less disruptive than excavation, meaning it is useful to be able to differentiate air blockages from solid blockages which are more likely to require excavation. The velocities required to expel isolated pockets depend on the pipe diameter and slope, and while air can be swept from the system by flow velocities of less than 1.5 m/s, the time of clearance is long and may not always be practically or economically viable. When the air cannot be easily swept downstream or bled through a valve, expensive and intrusive methods such as pipeline excavation or drilling vents at pipe high points may be required. This means it is desirable to pinpoint air pocket locations before treatment in order to minimise the cost and disruption associated with removal.

1.1.3 Pipe material deterioration

Water supply pipes can become deteriorated through internal or external corrosion. Corrosion on either surface may be classified as aqueous corrosion, as although water pipes are buried underground, the water contained in soil means it can often be considered an aqueous electrolyte (Schaschl and Marsh, 1963). The heaviest corrosion generally occurs in metallic ferrous pipes such as those made from ductile iron or mild steel (Cole and Marney, 2012). In Australia, over 70% of

the pipes used by water utilities are made of ferrous metal (Cole and Marney, 2012), while in New Zealand, the majority of water supply pipes installed before 1990 were made from ferrous materials such as steel, cast iron, or galvanised iron (Cubrinovski et al., 2014). As a result, the ferrous pipes that are still in use will be affected by corrosion to some extent. Deterioration of ferrous pipes generally occurs through electrochemical corrosion. Electrochemical corrosion involves the dissolution of metal via an oxidation reaction, while the cathodic reaction is generally water or oxygen reduction (Rodhe and Herrera, 1988). This results in loss of pipe mass to soluble iron or iron-bearing scale which collects on the pipe surface. As the material is gradually eroded, the pipe walls become thinner. The mechanism, influencing factors, and consequences of corrosion primarily depend on the pipe material, as well as the surrounding environment. Damage to pipe walls is often intermittent; for instance, around 10 metres of significant damage was observed for each 1000 metres of pipe tested during a condition assessment in South Australia (Stephens et al., 2008).

Deterioration of ferrous pipes poses a range of risks to the network. Firstly, one of the primary physical effects of corrosion is a reduction in the pipe wall thickness, leading to leaks or large-scale bursts (Cole and Marney, 2012). In particular, corrosion pits can act as focal points for subsequent stresses imposed on the pipe, accelerating the corrosion process and increasing the probability of leak formation (Mohebbi and Li, 2011). As discussed previously, the losses in network efficiency and water resources due to leaks are well known, and it is desirable to identify susceptible sections proactively, so that repair or replacement may be carried out before leaks develop. Increases in the pipe wall roughness and by-product accumulation due to corrosion will also compromise hydraulic efficiency (Tran et al., 2010) and can lead to aesthetic and health issues due to either ingress of contaminants in the case of a leak, or directly from the corrosion by-products (Millette et al., 1980; Volk et al., 2000; Vreeburg and Boxall, 2007). Similar to an air pocket, the changes to the pipe wave speed and flow area created by corrosion have the potential to interfere with transient testing for other fault types (Gong et al., 2012). Corrosion is often non-uniform, meaning a number of discontinuities in the pipe properties may occur along its length, and transient reflections at

each discontinuity create significant distortions in the pressure trace. As a result, it is critical to understand the effects of deteriorated sections when testing in field pipes.

Current methods of deterioration assessment in the field are typically destructive, expensive, or provide limited information. The condition of both ferrous and cement pipes can be assessed using CCTV inspection, but this method requires pipes to be shut down and de-watered, which can be costly and disruptive, and its accuracy is subject to operator experience (Costello et al., 2007). The likelihood of deterioration can also be inferred through soil and water quality testing (Hu et al., 2010), although this method is indirect and cannot yield specific information about the pipe. Soils are complicated systems and the rate and type of corrosion are influenced by factors such as the acidity, moisture content, grain size distribution, aeration, redox potential, electrical conductivity, chloride concentration, presence of sulfur and nitrogen compounds, and microbiological activity (Denison, 1931; Rodhe and Herrera, 1988; Rajani and Kleiner, 2001). As a result, predicting the actual degree of corrosion that will occur can be difficult, or requires such extensive data on the local ground and water supply conditions that it becomes prohibitive. In many cases, destructive testing is required to yield conclusive information about the pipe wall condition, with short sections of pipe material removed to carry out mechanical testing (Gong et al., 2016). As discussed previously, these methods are generally expensive and provide only localised information regarding the pipe condition, meaning probabilistic algorithms are needed to interpolate the pipe condition between samples. Additional non-invasive methods include georadar-based and acoustic-based wall thickness measurement (Smolders et al., 2009; Bracken et al., 2010). The georadar technique can achieve high resolution for pipe diameters greater than 200 mm, but the method is expensive and requires access to the exterior of the pipe.

1.2 Previous transient-based studies

1.2.1 Entrapped air pockets

The majority of the investigations into the air-transient interaction have focused on air pockets trapped at the end of a dead-end pipe, acted upon by a compression wave. These investigations were primarily aimed at understanding how the pocket volume, and other system conditions such as base flow, affected the peak transient pressures generated following a sudden valve opening (Lee and Martin, 1999; Zhou, 2000; Lee, 2005; Zhou et al., 2011). Smaller air pockets were observed to lead to increased transient pressures due to acceleration, and large air pockets resulted in lower peak transient pressures than those observed for the no-air case due to the additional energy absorption provided (Jönsson, 1985; Vasconcelos and Leite, 2012). This field of study has mainly focused on the system response to sudden start-up or shut-down, with the peak pressures from low frequency transient signals generated using valve movements in the time-frame of 1-2 seconds. This meant the detailed interaction of the signal with the air pocket, such as its reflection and transmission characteristics, could not be quantified due to interference from the subsequent end reflections. These detailed features may be used to evaluate the accuracy of theoretical equations for use in network models, and to identify key diagnostic features of the air pocket response.

The case of a stationary in-line air pocket in the middle of the pipe has not been investigated as thoroughly. This is a more challenging field for experimental research as high points are required in experimental systems to reliably anchor in-line air pockets, and systems with base flow may not be practicable due to the potential for pocket movement. Pozos (2007) successfully utilised a linear equation to identify high points where air would gather in experimental systems. Later, Pozos-Estrada (2017) carried out laboratory experiments to verify the open channel flow model for large in-line pockets followed by a hydraulic jump, finding that the presence of the pocket reduces the amplitude of transmitted pressure oscillations. Wan et al. (2017) carried out an experimental investigation into the geometry of in-line air pockets under steady-state conditions. Chapter 3 provides more detail on previous laboratory- and field-based investigations into the

transient interaction with in-line air is provided.

Similarly, little research has been completed on the specific case of unwanted air trapped inside an off-line cavity. The most comparable case to an off-line air pocket is an air chamber. These are closed vertical tanks connected to the pipeline, designed to relieve water hammer pressures or act as an energy storage device (Besharat et al., 2016). The chambers generally have a throttled outlet to assist with reducing water velocities through turbulent dissipation (Fig. 1.4a) but can exist as a pure cushioning vessel (Fig. 1.4b).

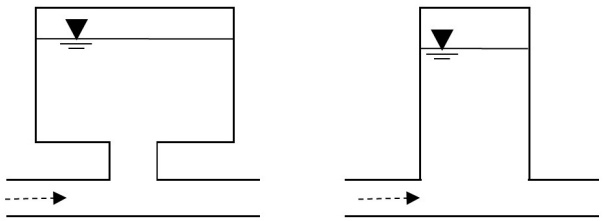

FIGURE 1.4: Example air chamber schematics: (a) Throttled, (b) Open

Early experimental investigations for the off-line scenario have shown that peak transient pressures decrease with increasing volume of air, due to the additional energy absorption provided by the compression of the air pocket (Wood, 1970). The peak pressures are also influenced by the initial hydrostatic pressure, the base flow within the system, and the properties of the cavity and connecting sections (Kim et al., 2014a; Besharat et al., 2016). Similar to the in-line case, the majority of the experiments carried out into the air-transient interaction for the off-line configuration involved low frequency transient waves and focused on the peak pressures generated as opposed to the specific shape and amplitude properties of the air pocket reflection and transmission. Outside the field of surge protection, Kim (2008b) carried out a set of experiments for off-line air pockets trapped in a brass block attachment using a high speed valve movement in the order of milliseconds to generate the transient. In this scenario the air pocket was confined to an open cavity (similar to Fig. 1.4b) and the air entirely filled the cavity. The air pocket was found to result in major changes to the shape and magnitude of the transient response, which were highly dependent on the pocket volume and initial hydrostatic pressure.

1.2.2 Pipe material deterioration

Deteriorated sections are best diagnosed by identifying irregularities in the transient wave speed. The transient wave speed is related to the pipe properties and may be used to assess pipe wall condition. The theoretical transient wave speed is given by

$$\frac{1}{a^2} = \frac{d\rho}{dP} + \frac{\rho}{A}\frac{dA}{dP} \tag{1.1}$$

where a = wave speed; P = pressure; ρ = fluid density; and A = cross-sectional area of the pipe (Wylie et al., 1993). Korteweg (1878) related the terms in Eqn. 1.1 to the properties of the fluid and the pipe, assuming that the pipe is secured with expansion joints along its length such that axial stresses and the inertia of the pipe are negligible:

$$a^2 = \frac{K_f}{\rho}\frac{1}{1 + c\frac{K_f D}{eE}} \tag{1.2}$$

where K_f = bulk modulus of elasticity of the fluid; D = pipe diameter; e = pipe wall thickness; E = Young's modulus of elasticity for the pipe material; and c = constraint condition. In general, pipeline deterioration reduces the pipe wall thickness or elastic modulus, resulting in a reduction in the wave speed. In the case of corrosion on the internal surface, the pipe diameter may also be affected. The elastic modulus is expected to remain constant for metallic pipes (Stephens et al., 2008). Experimental investigations into the suitability of the wave speed equation have led to modifications for two-phase flow, viscoelastic pipes, and systems affected by fluid structure interaction (Watters, 1971; Pearsall, 1965; Bergant et al., 2008). The wave speed is also influenced by the water temperature and pressure (Pearsall, 1965). The numerous factors affecting the wave speed and assumptions made in the theoretical equation mean that wave speed is best determined through direct measurement.

Numerous experimental studies have been completed to better understand how transient waves interact with weaker or thinner sections. Many TDR-based investigations have focused on using impedance theory to characterise pipe condition from the reflection amplitude. The impedance, Z,

of a pipe is given by $Z = \rho A/a$, where ρ = fluid density; A = pipe cross-sectional area; and a = pipe wave speed. Gong et al. (2013b) showed that the head perturbation of a step wave reflected by the deteriorated section relative to the incident wave is directly related to its hydraulic impedance. This impedance can therefore be used to estimate the wave speed and thus the wall thickness of the section. The method was tested experimentally using a section of pipe with a thinner wall to represent the deteriorated section, and its accuracy was found to be highly dependent on the sharpness of the input transient (Gong et al., 2013b). Gong et al. (2012) used the impulse response function (IRF) to improve the accuracy of estimates of the length and location of the representative deteriorated reach. Extending the approach to multiple deteriorated reaches, Gong et al. (2014) developed an inverse approach based on reconstructing the impedance distribution of the pipe using a backward method of characteristics, using the first half period of transient data measured experimentally. The method is much less computationally costly than ITA, but requires the assumption that the pipe diameter is constant throughout, i.e., the loss in internal wall thickness due to deterioration is not significant compared to the diameter. The method could identify the point of low impedance, with a 3% error between the wave speed predicted by the model and that obtained from the theoretical equation, though the value was not confirmed experimentally. In the ITA field, Tuck and Lee (2013) used a genetic algorithm to locate regions within the experimental system with a larger internal diameter. In another wave speed application, Hachem and Schleiss (2012) used aluminium and PVC sections to represent deterioration within a steel system, for the more complex deterioration case where the pipe stiffness is also affected. Across the range of experimental investigations carried out to test either ITA or TDR approaches, the corroded section is invariably represented using an intact pipe with a smaller wall thickness or a different material. This approach therefore does not consider the inherent variability and roughness which will occur in a real corroded sample. Further investigations are needed to understand the effects of actual corrosion on the transient wave speed within a controlled laboratory environment.

A range of field studies have also been carried out to diagnose deterioration using the transient wave speed. Some of the earliest work on detecting areas of pipe deterioration using transients was

completed by Stephens (2008), comparing measured pressure traces generated in an abandoned pipeline to the results of a numerical model based on its original condition. In another field study, Stephens et al. (2008) used ITA to predict the degree of wall thinning in sections of a 26 km pipeline in South Australia, achieving errors in the predicted wall thickness of up to, but generally less than, 25%. In this approach the wave speeds along the pipeline were estimated by trial and error or a genetic algorithm. Similar investigations based on ITA were carried out by Stephens et al. (2013). The impedance method was also applied to lined pipes in the field by Gong et al. (2015), who derived a set of equations for determining the wave speed based on whether the deterioration has reduced the wall thickness internally or externally, and whether the steel, mortar lining, or both are affected. However, the relative changes in wall thickness predicted did not always agree with those measured, particularly for the more complex case of internal deterioration. This was thought to be due to inaccuracies in the estimated pressure head perturbation and damping of the transient. Field-based ITA studies show the promise of using the wave speed as a diagnostic tool. However, it can be difficult to inspect and fully characterise pipelines in the field as they are often buried. The significant variation in wall thickness with distance means that the characteristics of the corroded pipe cannot be comprehensively characterised without time-consuming and destructive testing.

To summarise, previous research into the effects of pipe deterioration on transient transmission falls into two key areas: controlled experimental studies, where corroded sections are represented using intact lengths of pipe with different wall characteristics, and field studies, where tests are carried out on real corroded sections, but a definite comparison with theoretical predictions is not possible as the detailed pipe wall characteristics remain unknown. Controlled corrosion and transient testing of pipe samples in the laboratory is a research area which may advance understanding of transient behaviour and diagnosis techniques for this scenario. This will require an accelerated electrochemical corrosion program, where levels of corrosion can be achieved in the laboratory which may occur over years or decades in the field. Such approaches have been previously used to understand corrosion of small-scale pipe sections (Yang et al., 2020), culverts (Regier, 2015) and steel reinforced concrete (El Maaddawy and Soudki, 2003; Caré and Raharinaivo, 2007; Kivell

et al., 2011), and the general theory may also be applied to replicate large-scale pipeline corrosion. Chapter 8 explains the theory surrounding the accelerated corrosion process in detail.

1.3 Numerical modelling of transient signals

A range of methods exist for predicting transient behaviour using numerical models. The transient response can be modelled either in the time domain or in the frequency domain. The behaviour of unsteady pipelines is governed by the 1D momentum and continuity equations (Wylie et al., 1993).

$$\frac{\partial U}{\partial t} + g\frac{\partial H}{\partial x} + gh_f = 0 \,, \tag{1.3}$$

$$\frac{\partial H}{\partial t} + \frac{a^2}{g}\frac{\partial U}{\partial x} = 0 \,, \tag{1.4}$$

where H = pressure head; U = fluid velocity; a = pipeline wave speed; x = distance along the pipe; t = time; g = acceleration due to gravity; and h_f = friction loss per unit length. Though a closed-form solution to these equations is not available, a range of graphical and analytical approaches have been developed to solve them (Chaudhry, 1987). Pipeline anomalies are incorporated as boundary conditions, or by adjusting the pipeline properties in specific reaches. Solution methods may be either 1D or 2D. Numerous researchers have investigated 2D models for predicting transient behaviour (Vardy and Hwang, 1991; Pezzinga, 1999; Gao et al., 2018; Zhao and Ghidaoui, 2006; Cannizzaro and Pezzinga, 2005). In general, 2D models are better able to predict the shape of the pressure function and provide detailed information regarding the pressure and flow fields across the pipe cross-section as well as along the pipe. This is particularly useful when considering localised regions surrounding flow anomalies. However, 2D models inevitably incur greater computational expense (Naser et al., 2004; Jang et al., 2017). The wavelength of signals used in this work is approximately 8 metres, two to three orders of magnitude greater than the pipe diameters used. Other condition assessment applications are likely to operate with similar parameters. In addition, the primary purpose of transient-based condition assessment models is to replicate transmission and reflections from anomalies, generally at sensors located some distance away. Although 2D

models and quasi-2D models are able to provide a better estimation of the frictional resistances created by the velocity gradients at the pipe wall, the additional discretisation needed creates a significant computational burden which makes 2D modelling unrealistic for large field networks.

Alternatively, a range of 1D modelling approaches exist for predicting head and flow perturbations created by transients at different locations along the pipe. Given the complexity of water distribution networks, it is also advantageous to minimise computational cost. As such, most researchers have continued to use 1D modelling approaches, which are deemed to provide the information of interest with sufficient accuracy. In addition, a review of the literature (Chapters 4 and 6) shows that little work has been devoted to experimentally validating the equations for incorporating air pockets into 1D models. It is logical to evaluate the accuracy of the proposed equations in one dimension before extending the application to two dimensions. The method of characteristics (MOC) is a time domain method which is widely used in the field of 1D transient analysis, with its advantages including accurate simulation of steep wave fronts, computational efficiency, simplicity to program, and its useful illustration of wave propagation (Wylie et al., 1993; Streeter and Lai, 1962; Abbott, 1966). It is also well suited to systems with complex boundary conditions, and is commonly used in ITA (Liggett and Chen, 1994; Stephens et al., 2008; Gong et al., 2014). The key limitation of the approach is that the time step selected must satisfy the Courant stability condition, $a\Delta t/\Delta x \leq 1$, where Δt = time step and Δx = spatial step. The positioning of sensors and boundaries is therefore limited to the node locations in the spatial grid. Given its efficiency, and ubiquity in the transient condition assessment field, the MOC will be used for exploratory modelling in this research.

Transient events can also be modelled as 1D events in the frequency domain. This approach linearises the frequency domain equivalents of the momentum and continuity equations and assembles them into matrices. Individual matrices are used to represent each pipe element and can be concatenated to represent the whole system, meaning anomalies can be easily incorporated into the model (Lee et al., 2013; Duan and Lee, 2016). The system frequency response (SFR) can be used to obtain the response of the system to a given input disturbance at any location. As discussed previously, the frequency response may be used to characterise and locate pipeline anomalies. The

method offers greater flexibility over the MOC in that anomalies, generators, and receivers may be placed at any location with no limits due to discretisation of the domain.

In-line and off-line air pockets are incorporated into the 1D MOC or SFR model as boundary conditions, while deteriorated sections are represented as a region of reduced wave speed and, in the case of internal corrosion, increased diameter. Specific equations for the MOC and the modelling of in-line and off-line pockets can be found in Chapter 2. Background literature review concerning the modelling of in-line and off-line air pockets can be found in Chapters 4 and 6 respectively.

1.4 Research pathways identified

The preceding literature review explores the current state of the art with regard to transient-based fault detection. It was found that pipeline faults such as leaks and blockages have received a great deal of attention in the laboratory and the field, as well as being a focus of numerical modelling efforts. At present, less is known about the influence of air pockets and deteriorated sections on the propagation of transient waves, partially due to the difficulties associated with representing and quantifying these features in the laboratory and in the field. Based on the advances made by previous publications, the following areas were identified as avenues for future investigation.

Air pockets

- Previous experimental studies into the air-transient interaction have utilised low-frequency waves which do not enable identification of specific air-induced features in the transient response. In particular, the use of low frequency signals (signals with a wave length that is significantly longer than the dimension of the air pocket) means that distinct reflection and transmission characteristics of the air pocket cannot be observed. The difficulties associated with trapping in-line air pockets also means that they are under-represented in the existing literature. Experimental investigations using a high frequency (short wave length) signal

within a pipe system of length sufficient to enable extraction of individual waves reflected and transmitted by the air pocket would advance the body of knowledge in this area.

- A comprehensive set of experimental data meeting the above conditions for a range of air pocket volumes would enable identification of specific features in the reflected and transmitted pulses which may be used to differentiate between in-line and off-line air pockets, and also between air pockets and other common pipeline faults.

- Due to the lack of experimental data for the conditions mentioned, experimental validation is required for the existing theoretical equations for incorporating in-line and off-line air pockets into the 1D MOC scheme. Possible improvements to the existing equations could also be investigated.

Deteriorated sections

- Previous studies on pipe deterioration have involved testing of buried corroded pipe in the field, or simulated deterioration using pipes with thin-walled sections in the laboratory. In the case of buried pipes, it can be difficult to accurately characterise the pipe properties, while laboratory simulations do not account for the natural variability and material effects which occur as a result of corrosion. An experimental investigation of the effects of real pipe wall corrosion on transient propagation speeds on pipes would represent a useful complement to the studies discussed.

- Accelerated laboratory corrosion has not previously been carried out for full-size pipe sections and the experimental methodology, including the practicality considerations for the corrosion process, data collection on the pipe characteristics, and the wave speed testing will need to be established.

1.5 Research objectives

The primary aim of this research is to investigate the interaction between injected transient signals and pipeline anomalies, specifically entrapped air pockets and deteriorated sections. Previous work on transient-based condition assessment has shown that the ability to understand and model the transient interaction with the range of anomalies that may occur within a network is critical. Though leaks and blockages have received a great deal of attention in numerical, experimental, and field investigations, air pockets and pipe deterioration require further inquiry to better understand their effects on the transient response. The conclusions can be used to assist in the development of pipeline diagnosis and condition assessment technologies. The research can be divided into two main components:

1. Investigate the interaction of transient signals with entrapped air pockets, both in the main flow path (in-line) and outside the main flow path (off-line). This will be achieved by:
    - Conducting laboratory experiments in a small-scale system for a range of initial hydrostatic pressures and air pocket volumes in in-line and off-line configurations.
    - Comparing the experimental results in the time and frequency domains for each configuration with each other, and with similar fault types such as solid blockages, and using the results to identify key diagnostic features.
    - Assessing the performance of existing models for the air-transient interaction for each configuration and identifying key failings and improvements.
2. Investigate the propagation of transient signals through experimentally corroded ferrous pipe sections, with a focus on the effects of deterioration on the transient wave speed. This will be achieved by:
    - Conducting laboratory experiments consisting of accelerated corrosion of mild steel pipe sections with transient wave testing at regular intervals.

- Using the experimental observations to explore methods of quantifying pipe condition using the measured wave speed.

1.6 Thesis outline

This thesis presents laboratory experiments and numerical modelling that aim to explore the interaction of high-frequency fluid transients with entrapped air pockets and deteriorated pipe sections. It is hoped that the conclusions will improve the understanding of transient-anomaly interactions, and aid in the development of condition assessment and system diagnosis techniques for water supply networks.

Chapter 2 describes the methods used to generate experimental and modelled data for the transient interaction with an air pocket, which are used in Chapters 3 to 7.

Chapter 3 (Alexander et al., 2020a) presents the results of experiments focused on an in-line air pocket scenario. Key observations are made of the air-transient interaction, and compared to a solid blockage. These anomalies can have similar effects under steady-state conditions, but air pockets may be considerably easier to remove, meaning it is important to be able to differentiate between them.

Chapter 4 (Alexander et al., 2019) compares the experimental results for the in-line air pocket to existing numerical models, and assesses their accuracy with regards to the transient pulse timing and amplitude. The standard method of characteristics (MOC) model with a polytropic boundary condition for the air pocket is extended to account for the local wave speed changes created by the air pocket.

Chapter 5 (Alexander et al., 2020d) presents the results of experiments focused on an off-line air pocket scenario, with comparison to the in-line pocket scenario covered in Chapter 3. These two pocket configurations have different implications for network operators, meaning it is important to differentiate between their effects. The analysis identifies key features of the transient response specific to the off-line configuration.

Chapter 6 (Alexander et al., 2020c) tests the applicability of the lumped inertia assumption for modelling the off-line air pocket in the time and frequency domains. The results of lumped inertia models are compared to those generated using a plane wave model in the frequency domain derived without lumped inertia assumptions.

Chapter 7 (Alexander et al., 2020b) compares the transient response of an off-line pocket for a range of flow and boundary conditions. Ideally, transient testing could be carried out in operational pipes, meaning it is important to understand the effects of flow on the transient response. Experimental data and numerical modelling are used to identify the effects of flow and boundary conditions on the transient reflection and transmission.

Chapter 8 explores a method for carrying out accelerated corrosion of ferrous pipes in the laboratory. The findings are used to identify the effects of wall thickness loss on the wave transmission speed in ferrous pipes.

Chapter 9 explores the practical implications of the findings and the considerations and limitations for transient testing in real systems.

Finally, Chapter 10 provides a summary and discusses important directions for future research.

2 Air pocket: Experimental and numerical methods

This section describes the experimental and numerical methods employed to collect and interpret the data presented in Chapters 3 - 7, for the investigation of the transient interaction with an entrapped air pocket. The content in this chapter is synthesised from descriptions in Alexander et al. (2020a), Alexander et al. (2019), Alexander et al. (2020d), Alexander et al. (2020c), and Alexander et al. (2020b), with permission from the publishers. Subsequent chapters include details of additional investigation-specific numerical modelling and experiments.

2.1 Experimental methods

2.1.1 Experimental system

The experiments were completed at the University of Canterbury Fluids Laboratory, using the experimental apparatus shown in Fig. 2.1. It consisted of a valve-pipe-reservoir system. The 41.6 m straight stainless steel pipe had an internal diameter of 22.25 mm and a wall thickness of 1.6 mm. The pipe was set at a constant angle of 3.5°, resulting in a height difference of 2.51 m between the two ends of the pipe. The relatively small pipe diameter was selected to ensure the transient pulse generated and subsequent reflections would be clearly visible in the measured data. The reservoir at the downstream end of the pipe was used to pressurise the system. The upstream boundary of the system was a closed in-line valve. The air pocket test section was located 14.50 m downstream of the in-line valve. Note that the nomination of the upstream and

downstream boundary are in relation to the origin point of the transient. The transient pressure disturbances were measured at four locations using PCB Piezotronics Model 102A07 dynamic pressure transducers with a sampling frequency of 10,000 Hz. The transducers have a 345 kPa measuring range, a natural frequency of over 250 kHz, and an uncertainty of 3.45 kPa. Pressure Transducer 1 (PT1) was located at the upstream end, next to the solenoid valve. PT2 was located 8.29 m downstream of the transient generation point, 6.21 m upstream of the air pocket. PT3 was located 6.30 m downstream of the air pocket. PT4 was located at the air pocket. The pressure response was recorded by the transducers for five seconds following the generation of the transient, enough time for the system to return to steady-state. The experimental wave speed (1348.5 m/s) was estimated by cross-correlating the transient traces measured at PT1 and PT2 for the no-air case. The time lag at which the cross-correlation of the two signals was maximised represents the pulse travel time between the two sensors.

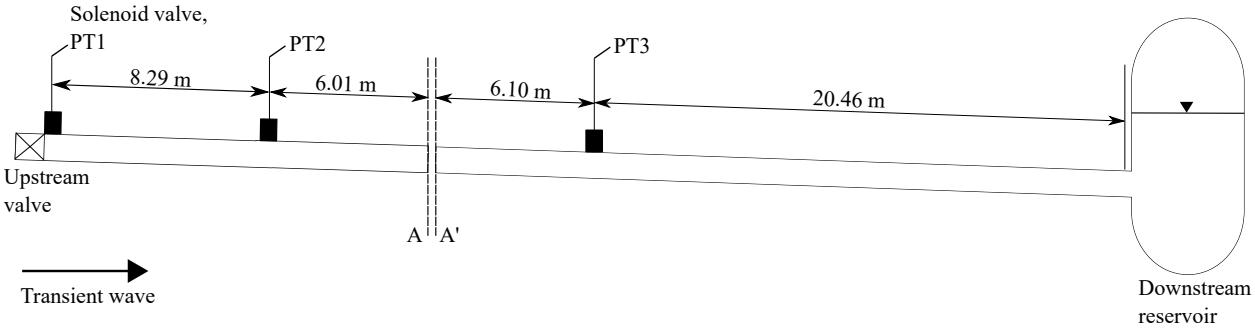

FIGURE 2.1: Diagram of experimental set-up for air pocket experiments. Section A-A' is shown in Fig. 2.2.

2.1.2 Air pocket insertion

Insertion methodology

To prevent air in the main flow path being pushed from the system, moved to another location, or sheared by the flow, the tests were carried out with no base flow. Initially, the system was tested without an air pocket to establish a base-line response. Experiments were then completed for two different air pocket configurations: in-line and off-line. Figure 2.2 shows the test sections used for

the in-line and off-line configurations. A stainless steel crest section was fitted in the main pipe to create an artificial high point to prevent air moving elsewhere in the pipe.

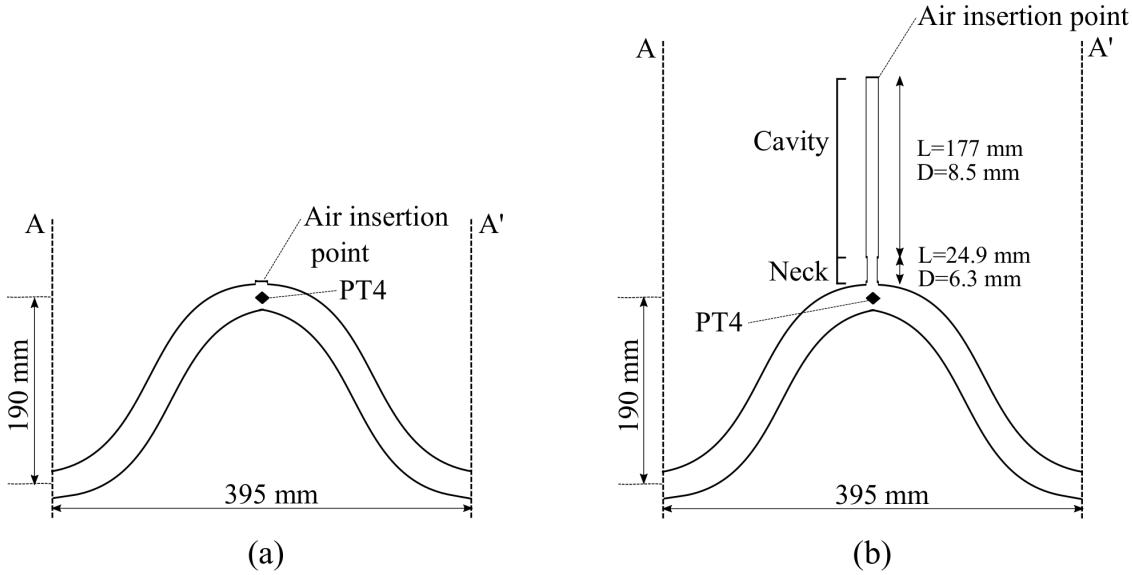

FIGURE 2.2: Section A-A': Diagram of air pocket configurations (a) in-line, (b) offline

Note that the pressure responses obtained for the no-air case were comparable for the system configurations with and without the off-line attachment. A minor reflection from the crest section of less than 5% of the incident pulse amplitude was observed for both the in-line and off-line configurations without air, as shown in Fig. 2.3. This indicates that, in this experimental scenario, the cavity alone does not create a significant transient reflection, meaning the observed responses for the air pocket cases may be assumed to be relate predominantly to the presence of the air. The air was inserted into the test section at room temperature using a measuring syringe, which enabled the volume of air (V_p) to be measured at atmospheric pressure. Once the test was complete, the system was depressurised and the air was removed using the syringe and its volume measured again to check, to the level of accuracy of the syringe (0.1 ml), that the air had not moved outside the cavity.

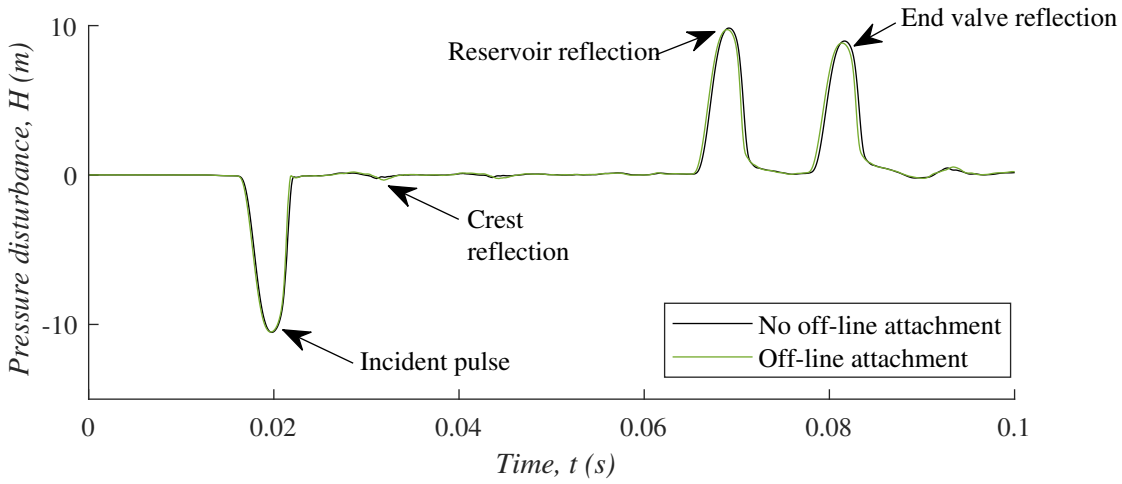

FIGURE 2.3: Example transient traces measured at PT2 (8.29 m downstream of transient generation point and 6.21 m upstream of the air pocket section), demonstrating the amplitude of the crest reflection relative to the incident signal, for the case when the off-line air pocket section is attached and when it has been unscrewed and the crest capped. No air has been inserted into the pipe in this scenario.

In-line pocket

For the in-line case, air was inserted directly into the main pipe via a bleed valve at the top of the crest section. Fourteen in-line air pocket volumes were tested, ranging from 2.9 ml to 40 ml at atmospheric pressure (V_p = {2.9; 3.5; 7.1; 7.8; 9.9; 11.3; 15.5; 16.0; 16.5; 21.6; 26.5; 33.9; 34.6; 40.0} ml). Once pressurised, the in-line air pocket volumes ranged between approximately 0.9 ml and 28.6 ml, representing scenarios between a minor flow obstruction and a collection of air which almost entirely blocks the flow. This is representative of the range of scenarios which could occur in a real system. Figure 2.4 shows the approximate dimensions of pocket volumes within the pipe, assuming the pocket was concentrated at the top of the crest and had a flat base. The maximum pocket height at the center of the crest was normalized by the pipe diameter ($h_p^* = \frac{h_p}{D}$).

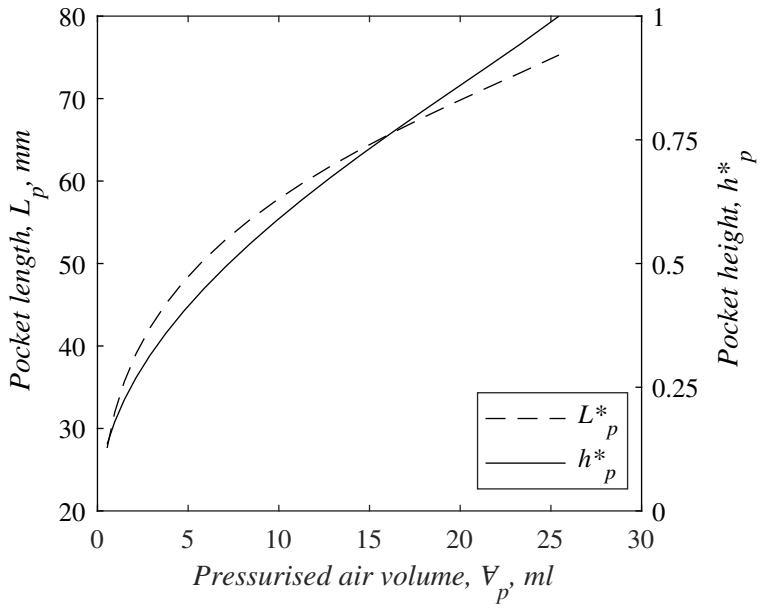

FIGURE 2.4: Approximate air pocket dimensions within the pipe. The pocket length is the estimated horizontal length of the pocket base along the pipe's long axis, and the pocket height is the estimated distance from the centre of the base of the pocket to the top of the crest section.

Off-line pocket

For the off-line pocket scenario, the bleed valve at the top of the crest was removed and a steel cavity 177 mm long (L_{cavity}) with an internal diameter of 8.5 mm (D_{cavity}) was screwed into the fitting. At the base of the cavity was a short neck section of length 24.9 mm (L_{neck}) and diameter 6.3 mm (D_{neck}). Air was inserted at the top of the cavity via a bleed valve. Nine off-line air pocket volumes were tested, ranging from 1.3 ml to 29.4 ml at atmospheric pressure ($\forall_p$ = {1.3; 5.0; 8.9; 12.8; 17.1; 21.0; 23.8; 25.7; 29.4} ml). Only the pressurised air volumes which were fully contained by the off-line cavity were considered in subsequent investigations, as the largest pocket volumes tested have shown that once the off-line pocket volume exceeds the size of the cavity its behaviour tends to that of a similarly sized in-line pocket.

Initial hydrostatic pressures

Transient tests were run for each air pocket volume at initial hydrostatic pressures ranging between 0.5 bar and 3.0 bar in 0.5 bar increments. According to Henry's Law (Sander, 2015), the increase in

pressure will result in some dissolution of the air in the crest section. However, this dissolution was calculated to be in the order of 0.01 ml, and is minor compared to the total volume of air inserted, ranging from approximately 0.03% to 2.5% of the total pocket volume, with the average expected dissolution being approximately 0.3% across the range of pocket volumes tested. The full volume of air inserted at the beginning of the test was retrieved from the crest section at the end of the test, confirming that no air had dissolved or moved elsewhere in the pipe. This also confirmed that the air was concentrated in a pocket at the top of the crest or in the off-line cavity, as the full volume of air re-entered the measuring syringe before any water during removal.

2.1.3 Transient generation

A Baccara GEM-SOL Direct Operated side discharge solenoid valve (2.4 mm orifice, 1/4-inch port) adjacent to the in-line end valve was used to generate the transient pulse, by rapidly opening and closing over a period of 6 ms. The control system for the valve was designed and made at the University of Canterbury. Computer control of the solenoid valve and transducers was programmed using National Instruments LabView software. The electronic trigger for the solenoid valve was abrupt, but the mechanical response of the valve resulted in a smooth disturbance without tripping. The 6 ms cycle time was based on the computer clock, meaning the difference from the wall-clock time was within several tens of nanoseconds, and therefore negligible relative to the transient pulse length. Figure 2.5 shows the typical transient pulse generated by the solenoid movement. The pressure disturbance H measured by the transducer is normalised by the initial hydrostatic pressure. The solenoid pulse has an amplitude of approximately 0.4 relative to the initial hydrostatic pressure of the system, and a frequency range of approximately 0-1.5 kHz. Based on the experimental wave speed determined from the system (1348.5 m/s), the valve movement time of 6 ms corresponded to a pulse length of approximately 8.1 m, or 20% of the total pipe length ($0.2L$). The pulse length provides an indication of the level of interference that may be expected in the pressure trace. As the pulse was shorter than the pipe length between the air pocket and the system boundaries, the reflections from the air pocket and system boundaries did not immediately blend together, allowing

the extraction and analysis of pulses.

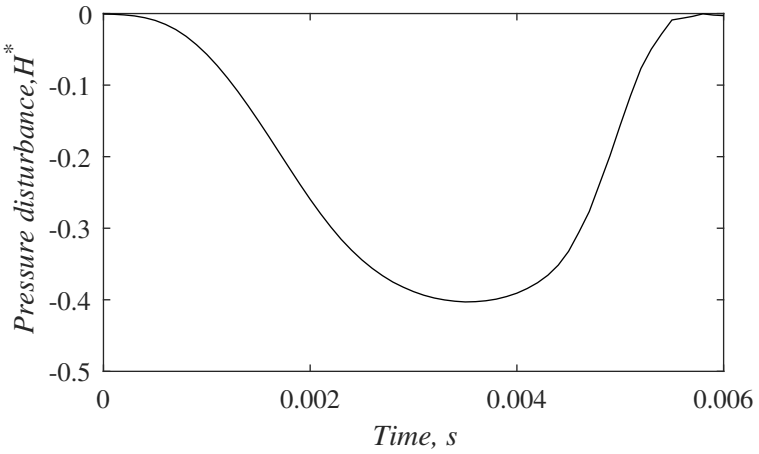

FIGURE 2.5: Typical solenoid pulse generated experimentally, measured at the transient generation point (PT1). The pressure disturbance relative to the initial system pressure H^* has been scaled by the initial hydrostatic pressure.

2.1.4 Experimental applicability and error assessment

The range of scenarios investigated here could realistically occur in a pipeline and provide a comprehensive study of the effect of an air pocket on the transient response. The air pocket volumes tested were less than 2% of the total pipe volume and so could have occurred as a result of air vaporisation (Burrows and Qiu, 1995). Noise in the system was observed to be minor. Before the generation of the transient, the average pressure disturbance measured at the pressure transducers was 0.03% of the full measuring range (345 kPa), with the maximum deviation from zero approximately 0.19% of the range. This is lower than the uncertainty associated with the instrumentation (3.45 kPa or 1%). In comparison, the initial solenoid pulse amplitude ranges from 5% to 35% of the transducer operating range. In light of this, no artificial noise was incorporated into the numerical models. To assess experimental error, testing was repeated ten times for each set of experimental conditions. The intervening period between tests was approximately one minute, to ensure the transient disturbances had damped entirely before starting the next test. A standard error was calculated for each time step in each experimental scenario. Over the time period of interest, including the incident pulse and the first reflected and transmitted pulses measured at the transducers, the average standard error was less than 0.10% of the transducers' measuring

range. To ensure no air became trapped elsewhere in the system, the pipe was bled at several side discharge valves along its length after each pressure increase, and a period of sustained base flow with the upstream valve open was applied between each air pocket test. When filling the system, the water was left standing for 24 hours without pressurisation to allow air to leave solution before commencing testing. As an additional precaution, before each air pocket test a transient test was carried out with no added air to ascertain whether any air was present in the system, identified by any additional reflections or reductions in the expected system wave speed.

2.2 Numerical modelling

2.2.1 Method of characteristics: Governing equations

A one-dimensional numerical model was implemented as part of the in-line and off-line pocket investigations. The air pocket volumes tested were small enough that the elastic water model was applicable, and the movement of the air–water interface did not need to be considered (Chaiko and Brinckman, 2002). As discussed previously, a 1D model was used in this work due to its ability to provide the information of interest regarding the transient reflections and transmissions at different locations along the pipe with sufficient accuracy while minimising computation time. Given its ubiquity in the field of 1D transient analysis, the method of characteristics (MOC) scheme was used to solve the mass and momentum conservation equations, which govern one-dimensional unsteady pipe flow (Wylie et al., 1993)

$$\frac{\partial U}{\partial t} + g\frac{\partial H}{\partial x} + g h_f = 0 \,, \tag{2.1}$$

$$\frac{\partial H}{\partial t} + \frac{a^2}{g}\frac{\partial U}{\partial x} = 0 \,, \tag{2.2}$$

where H = piezometric head; U = fluid mean velocity; a = pipeline wave speed; x = distance along the pipe; t = time; g = acceleration due to gravity; and h_f = friction loss per unit length. If the initial and boundary conditions of the system are known, these equations and the MOC can be used to calculate the evolution of head and flow with time. The MOC scheme reduces Eqn. 2.1 and

Eqn. 2.2 to the following

$$U_{i,j} = U_{i-1,j-1} - \frac{g}{a_{i-1,j-1}}(H_{i,j} - H_{i-1,j-1}) - \Delta t g h_{f,(i-1,j-1)} \ , \tag{2.3}$$

$$U_{i,j} = U_{i+1,j-1} + \frac{g}{a_{i+1,j-1}}(H_{i,j} - H_{i+1,j-1}) + \Delta t g h_{f,(i+1,j-1)} \ , \tag{2.4}$$

$$\frac{a\Delta t}{\Delta x} <= 1 \ , \tag{2.5}$$

where i = index in the spatial grid; j = index in the temporal grid; Δx = spatial step; and Δt = time step (selected to satisfy Eqn. 2.5 to ensure stability). Eqn. 2.3 and Eqn. 2.4 are referred to as the positive and negative characteristic equations, and can be solved simultaneously for the unknowns $H_{i,j}$ and $U_{i,j}$, thus stepping the solution forward from one time step to the next.

For high-speed transients, inaccuracies can arise in model predictions of energy loss and phase shift as a result of the changing velocity profile, turbulence, and laminar-turbulent transitions. The inclusion of unsteady friction in the model accounted for this effect. The methodology developed by Zielke (1968) was used for calculating friction terms

$$h_{f,(i,j)} = \frac{32\nu}{gD^2}U_{i,j} + \frac{16\nu}{gD^2}\sum_{k=1,3,..}^{j-1}(U_{i,j-k+1} - U_{i,j-k-1})W(j\Delta t) \ , \tag{2.6}$$

where h_f = total friction loss including both unsteady and steady friction; D = pipe diameter; ν = kinematic viscosity of the fluid; and W = weighting function based on the dimensionless time. The method accounts for the velocity history of the given node as well as the current flow velocity. Zielke's method is applicable for laminar flow cases. The lack of base flow in the experimental system meant that the flow velocities generated were small, and satisfied this requirement.

Air pockets can be incorporated into the MOC scheme as boundary conditions. They are assumed to behave according the polytropic relationship:

$$H_A V_p^n = C_A \tag{2.7}$$

where H_A = absolute head at the pocket; V_p = pocket volume; n = polytropic exponent; and C_A = polytropic constant which can be calculated using the initial conditions. The polytropic exponent may range between 1.0 and 1.4, but an average value of 1.2 has been commonly used in previous research on air-water interactions (Martin, 1976; Wylie et al., 1993; Izquierdo et al., 1999; Carlos et al., 2011) and was used in this study. The specific equations governing in-line and off-line pockets are defined in Section 2.2.2 and 2.2.3 respectively.

2.2.2 In-line air pocket

The accumulator model incorporates an in-line air pocket of a selected volume at a given nodal point. It is assumed that there is no column separation, i.e., the air does not occupy the full cross-section of the pipe. This assumption was used by Burrows and Qiu (1995) in a previous numerical study, and the air volumes tested were expected satisfy this. The pressure within the air pocket at any instant is assumed to be the same throughout the air pocket volume, and the compressibility of the liquid in the computational reach containing the air pocket is considered to be negligible compared to the compressibility of the air (Wylie et al., 1993). Equation 2.7 applies at any instant, and as such can be written at the end of the time interval Δt as

$$(H_P + \bar{H} - z)(\forall_p + \Delta\forall_p)^n = C_A \ , \tag{2.8}$$

where H_P = gauge pressure at the pocket; $\bar{H}$ = atmospheric pressure; z = elevation of the pipe above the datum; $\forall_p$ = pocket volume at the beginning of the time interval; and $\Delta\forall_p$ = volume change across the time interval. Applying continuity principles, the volume change can be expressed as

$$\Delta\forall_p = \frac{2\Delta t}{\pi D^2}[(U_{DS,j-1} - U_{US,j-1}) + (U_{DS,j} - U_{US,j})] \ , \tag{2.9}$$

where U_{DS} and U_{US} = flow velocities calculated immediately downstream and upstream of the pocket respectively. Combining the characteristic equations with Eqs. 2.8 and 2.9 yields a nonlinear equation with H_P as the only unknown, which can be solved using a root-finding algorithm. This

method assumes that the transient wave speed is constant along the length of the pipe.

2.2.3 Off-line air pocket

The accumulator model also applies for the off-line air pocket. However, for off-line pockets separated from the main pipe by a short water column, friction and inertia in the water column may also be considered based on a lumped inertia assumption (Wylie et al., 1993). This will be referred to as the lumped inertia model. The process is outlined in detail by Karney and McInnis (1992) and Kim (2008a). Based on a discrete linearized momentum equation applied to the cavity at neck, at a given time index j the head at the pocket interface is linked to the head at the junction with the main pipe according to the following:

$$H_j^J - H_j^S = C_{c1} + C_{c2} Q_j^{ext} \tag{2.10}$$

$$C_{c1} = H_{j-1}^S - H_{j-1}^J - \left(\frac{8L_c}{g\pi D_c^2 \Delta t} + \frac{8L_n}{g\pi D_n^2 \Delta t}\right) Q_{j-1}^{ext} \tag{2.11}$$

$$C_{c2} = \left(\frac{8L_c}{g\pi D_c^2 \Delta t} + \frac{8L_n}{g\pi D_n^2 \Delta t}\right) + \left(\frac{16 f_n L_n}{g\pi^2 D_c^5} + \frac{16 f_n L_n}{g\pi^2 D_n^5}\right) |Q_{j-1}^{ext}| \tag{2.12}$$

where H^J = head at the junction; H^S = head at the water surface; Q^{ext} = flow into the off-line section; L_c and L_n = length of the cavity and neck sections; D_c and D_n = diameter of the cavity and neck sections; and f_c and f_n = Darcy-Weisbach friction factors for the flow in the cavity and neck sections, using the formulation for laminar flow based on the flow velocity in the connection at the previous time step. The key dimensions are shown in Fig. 2.6.

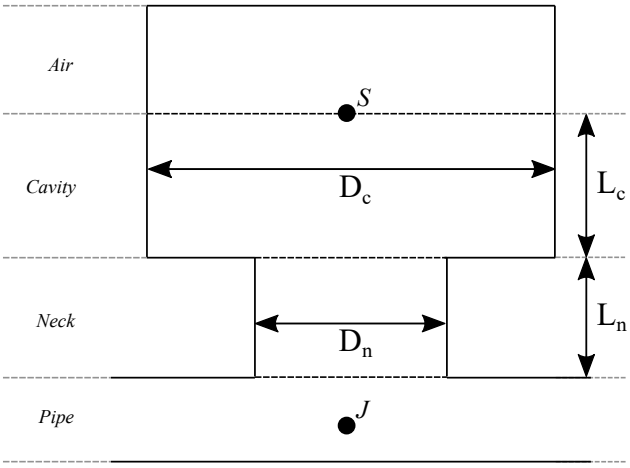

FIGURE 2.6: Schematic for off-line cavity showing key variables used in the governing MOC equations

Sensitivity testing was carried out to compare possible formulations for friction in the connecting sections. Three cases were tested for the flow regime in the cavity and neck: laminar for all time, turbulent for all time, and turbulent or laminar based on the velocity in the previous time step. The average variation between the three cases was approximately 0.08% during the first three periods. The flow was assumed to be laminar for all time for consistency with the SFR-LI model introduced in Chapter 6, as only one regime can be set for this case. The inclusion of laminar or turbulent unsteady friction in the connector was also tested using the SFR-LI (Vítkovskỳ et al., 2003a), with the average variation approximately 0.17% in the first three periods compared to steady friction alone. Unsteady friction in the connector was therefore not considered in the MOC, which is also in accordance with the equations presented in the literature (Karney and McInnis, 1992; Kim, 2008a).

Merging Eqn. 2.10 with Eqn. 2.7 and the characteristic equations, a relationship can be obtained which contains Q_j^{ext} as the only unknown:

$$\left(C_c - B_c Q_j^{ext} + \bar{H} - \left(z_{j-1} + \frac{0.5\Delta t}{A}(Q_j^{ext} + Q_{j-1}^{ext})\right) - C_{c1} - C_{c2} Q_j^{ext}\right) * \left(V_{p,j-1} - 0.5\Delta t(Q_j^{ext} + Q_{j-1}^{ext})\right)^n = C_A \tag{2.13}$$

In the above equation, $\bar{H}$ = atmospheric pressure; A = cross-sectional area of the cavity; and Δt

= time step of the MOC. The terms C_c and B_c are the MOC constants for the junction calculated using the positive and negative characteristic coefficients (Karney and McInnis, 1992).

2.2.4 Heat transfer

Zhou et al. (2013b) and Zhou et al. (2018) have noted in previous studies that heat transfer effects may be important when modelling the transient energy dissipation for air pocket scenarios, with 3D computational fluid dynamics (CFD) modelling used to describe dissipation in their simulation. Zhou et al. (2013b) states that the temperature change is related to the volume change of the pocket, with pocket compression leading to increased temperatures within the air. Zhou et al. (2013b) and Zhou et al. (2018) observed that their experimental system became noticeably hot to the touch, and although lag associated with the temperature transducer meant that the actual temperature changes could not be accurately recorded, 3D modelling with heat transfer considerations was able to more accurately predict the long-term pressure response. It is expected that heat exchange effects will be less influential for this application, given the relatively small size of the transient pulses generated ($\Delta H \approx 0.2 - 1.2$m) compared to Zhou et al. (2013b) and Zhou et al. (2018) ($\Delta H \approx 20 - 35$ m). Furthermore, the primary focus of this thesis is the first few periods of the transient response. Zhou et al. (2018) showed that even though the 3D model predicted significant temperature increases within the air, the outputs only began to diverge from 1D models for later reflections as discrepancies in the predicted energy losses began to accumulate. For these reasons, temperature variations and heat transfer between the air and adjacent water during the transient process were not considered as part of the MOC, or in the SFR modelling described in Chapter 6.

3 Experimental investigation of the interaction of fluid transients with an in-line air pocket

3.1 Introduction

The effect of a stationary air pocket part of the way along the pipe which occupies the main flow path and acts as a blockage without causing a hydraulic jump or column separation has not previously been studied experimentally. This chapter presents experimental results for a transient pulse interacting with an in-line air pocket for a range of pocket sizes and system pressures. The primary aim is to identify key features of the transient response which distinguish the in-line air pocket from other common fault types, particularly solid blockages, which can have similar effects under steady-state conditions but may be more difficult to remove.

The majority of the existing experimental investigations into the air-transient interaction focus on air pockets trapped at the end of a dead-end pipe, acted upon by a compression wave. Ocasio (1976) found that entrapped dead-end air could lead to extreme surges following an instantaneous valve opening. In the field, Jönsson (1985) observed that, for an air pocket trapped next to a valve, smaller equilibrium air volumes led to faster oscillations and larger transient peaks. Experiments by Lee and Martin (1999) and Lee (2005) for dead-end pockets ranging between 3% and 44.8% of the total pipe volume agreed with this observation. However, for the largest pocket volumes tested, the peak pressures were smaller than those obtained for the no air case, although physical

reasoning was not provided for this observation. Vasconcelos and Leite (2012) reached a similar conclusion for the case of a dead-end air pocket with base flow, while Lai et al. (2000) found that the peak pressures experienced are also influenced by the percentages of non-condensable air and vapour in the void. Zhou (2000) and Zhou et al. (2002) presented additional experimental and observational studies showing that as the air volume was reduced, the maximum pressure of the air pocket increased, confirming the conclusions of previous studies. However, Zhou et al. (2011) found that for dead-end air volumes below approximately 0.05% of the total pipe volume, the peak pressure of the air pocket begins to decrease again. The above observations for the dead-end case are explained by Zhou et al. (2011) as follows: for the upper range of air pocket volumes, peak pressures increase with decreasing volume due to the decrease of cushioning effects; however, when the air pocket reaches a certain small value, peak pressures begin to decrease with pocket volume as reduced space for water column movement decreases the water impact force.

The case of a stationary air pocket in the middle of the pipe has not been investigated to the same extent. Cabrera et al. (1992), Izquierdo et al. (1999), and Fuertes et al. (1999) carried out numerical investigations, using the rigid column model, into the case of system start-up when long columns of air are trapped in an undulating pipeline, entirely blocking the pipe cross-section. Pozos (2007) successfully utilised a linear equation to identify locations where air would gather in experimental systems. Pozos-Estrada (2017) carried out laboratory experiments to verify the open channel flow model for large in-line pockets followed by a hydraulic jump, finding that the presence of the pocket reduces the amplitude of transmitted pressure oscillations. To investigate the scenario of smaller pocket volumes that do not create a hydraulic jump, Kim (2008b) carried out a set of experiments and numerical investigations for a range of air pocket volumes located at the pipe midpoint for a range of initial hydrostatic pressures and base flow velocities. The air pocket was isolated inside a brass block adjacent to the flow, meaning that the air was outside the main flow path (off-line) rather than in-line with flow. The air pocket was found to result in major changes to the shape and magnitude of the incident compression wave compared to the no-air case, with the air pocket creating out-of-phase reflections due to the sudden drop in fluid density. These changes were

strongly dependent on the pocket volume and pressure condition. The advantage of the brass block approach is that the air is isolated outside the main flow path, so the effects of base flow can be investigated without risk of the air being swept elsewhere by the flow.

This chapter summarises experimental investigations into the reflection and transmission of a rapid transient through an in-line air pocket for a range of air volumes and initial hydrostatic pressures. The experimental results will be used to identify the effects of the in-line air pocket on a transient pulse. The experimental results will be used to identify the effects of the in-line air pocket on a transient pulse. This complements other studies by Kim (2008b) and Pozos-Estrada (2017) for discrete air pockets located part of the way along the pipe for the cases where the air pocket was off-line or large enough to cause a hydraulic jump. A greater knowledge of the observable effects of this form of air on an incident transient wave would assist in the development of a fault detection framework, as this is a common scenario compromising the efficiency of supply networks (Lauchlan et al., 2005). Some of the effects of air pockets at steady-state, such as a reduced flow rate or increased pumping cost, are shared with other flow-constricting faults, such as solid blockages and partially closed valves, but air pockets may be significantly cheaper to remove once identified. This means it is particularly useful to identify effects on the transient which are unique to air pockets.

3.2 Experimental procedure

The experimental methods for collecting the data used in this chapter are outlined in Chapter 2. The data collected for the in-line air pocket scenario are used in this chapter. Fourteen in-line air pocket volumes were tested, ranging from 2.9 ml to 40 ml at atmospheric pressure (V_p = {2.9; 3.5; 7.1; 7.8; 9.9; 11.3; 15.5; 16.0; 16.5; 21.6; 26.5; 33.9; 34.6; 40.0} ml). Each air pocket was subjected to transient tests at initial hydrostatic pressures ranging from 0.5 bar to 3.0 bar in increments of 0.5 bar. Note that the nomination of the upstream and downstream boundary referenced in this chapter are in relation to the origin point of the transient.

3.3 Numerical modelling

Numerical modelling of the experimental system, using the equations presented in Chapter 2 for the MOC and in-line pocket boundary equation, are used to supplement the experimental findings. The results of the numerical model provided a fair match to the overall shape of the experimental data, with example predictions for the pressure traces measured upstream and downstream of the pocket shown in Fig. 3.1. The specific features of the transient trace are discussed in further detail in the following section. The accuracy of the accumulator equations are explored in Chapter 4. There were noticeable discrepancies in the wave amplitudes and arrival times, with the model tending to over-predict reflected pulse amplitudes, under-predict transmitted pulse amplitudes, and over-predict the pulse travel time. These discrepancies are quantified in Chapter 4. The results of the model were used to obtain a general representation of the transient fluctuations in pressure, velocity, and air pocket volume.

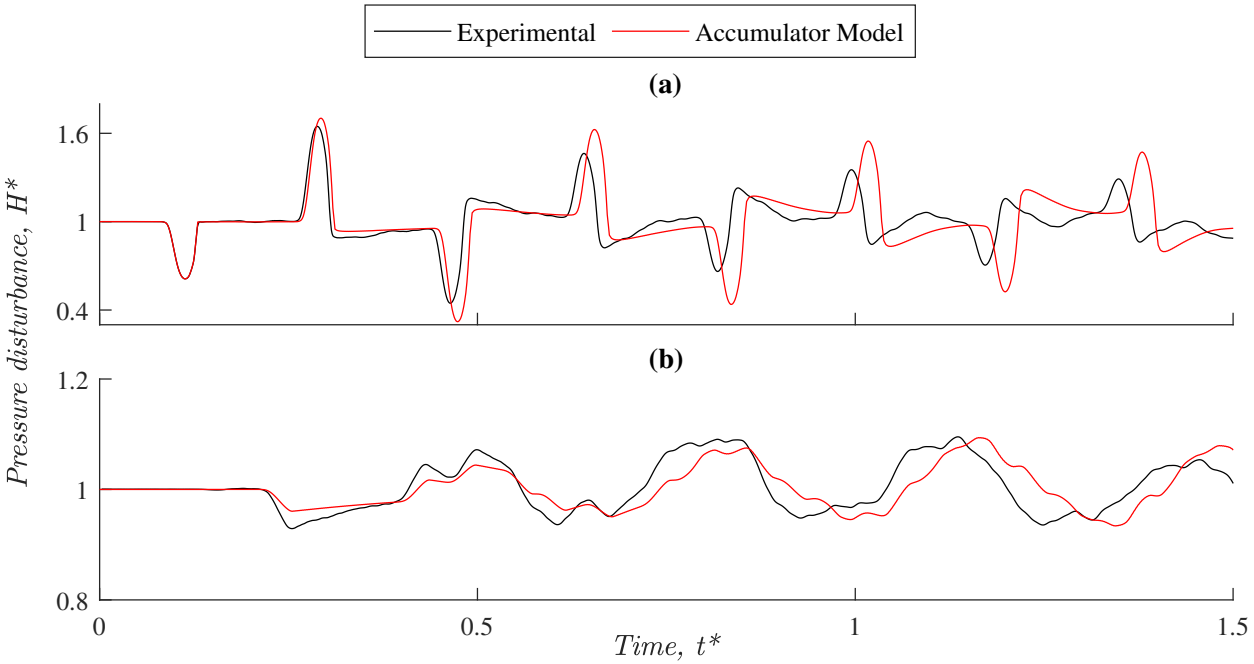

FIGURE 3.1: Modelled and experimental pressure traces for a 16.0 ml air pocket at 3.0 bar initial hydrostatic pressure (pressurised volume = 5.1 ml) (a) 6.21 m upstream of the pocket at PT2 and (b) 6.30 m downstream of the pocket at PT3. The transient generation point is 8.29 m upstream of PT2. The pressure disturbance H is scaled by the initial hydrostatic pressure and the time t is scaled by the pipeline period.

3.4 Results

3.4.1 Time domain observations

The experimental investigation involved the collection of pressure measurements at the transient generation point, upstream of the air pocket, and downstream of the air pocket. Thus, it was possible to assess the properties of both the reflected and transmitted waves. Example traces are provided in this section for a set of three representative air pocket volumes. The approximate obstruction created by the three air volumes at 3.0 bar is shown in Fig. 3.2. The experimental air pocket volumes measured at atmospheric pressure were converted to steady-state volumes within the pipe once pressurised (V_p) using the reversible polytropic equation (Chapter 2, Eqn. 2.7). The steady-state in-pipe volumes were then converted to a length scale, as this can be used to understand the compression behavior of the pocket. The pocket length scale, L_P, was approximated as $L_P \sim V_p^{\frac{1}{3}}$. The value of L_P was expressed as a percentage of the total pipe length L such that $L_P^* = L_P/L \times 10^2$.

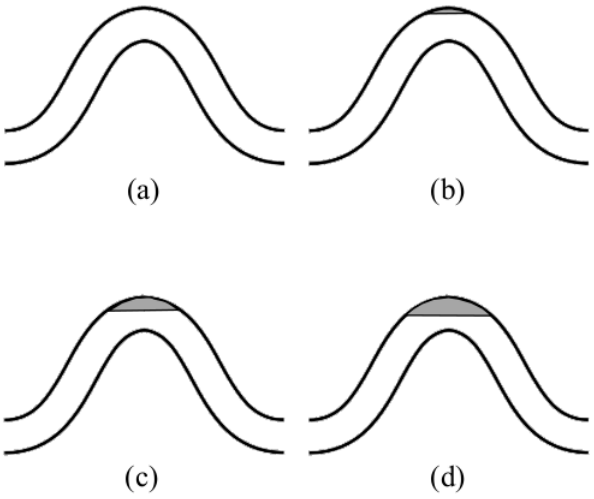

FIGURE 3.2: Approximate obstruction caused by air pocket (shaded) pressurised to 3.0 bar for (a) No air, (b) L_P^* = 0.025% (1.1 ml), (c) L_P^* = 0.041% (5.1 ml), and (d) L_P^* = 0.053% (10.8 ml).

Figures 3.3 and 3.4 show the traces measured at PT1, (the transient generation point), PT2 (6.21 m upstream of the pocket), PT4 (at the air pocket section), and PT3 (6.30 m downstream of the pocket) for the selected air volumes at 3.0 bar and 1.5 bar respectively. The pressure traces presented have

been normalised by the initial hydrostatic pressure such that $H^* = H/H_0$, where H = measured gauge pressure at any time; and H_0 = steady-state initial hydrostatic pressure. The elapsed time since the start of the transient event t was normalised by the pipeline period $T = a/4L$, such that $t^* = t/T$, where a = pipe wave speed and L = pipe length. The incident, reflected, and transmitted pulses are marked on Figs. 3.3 and 3.4.

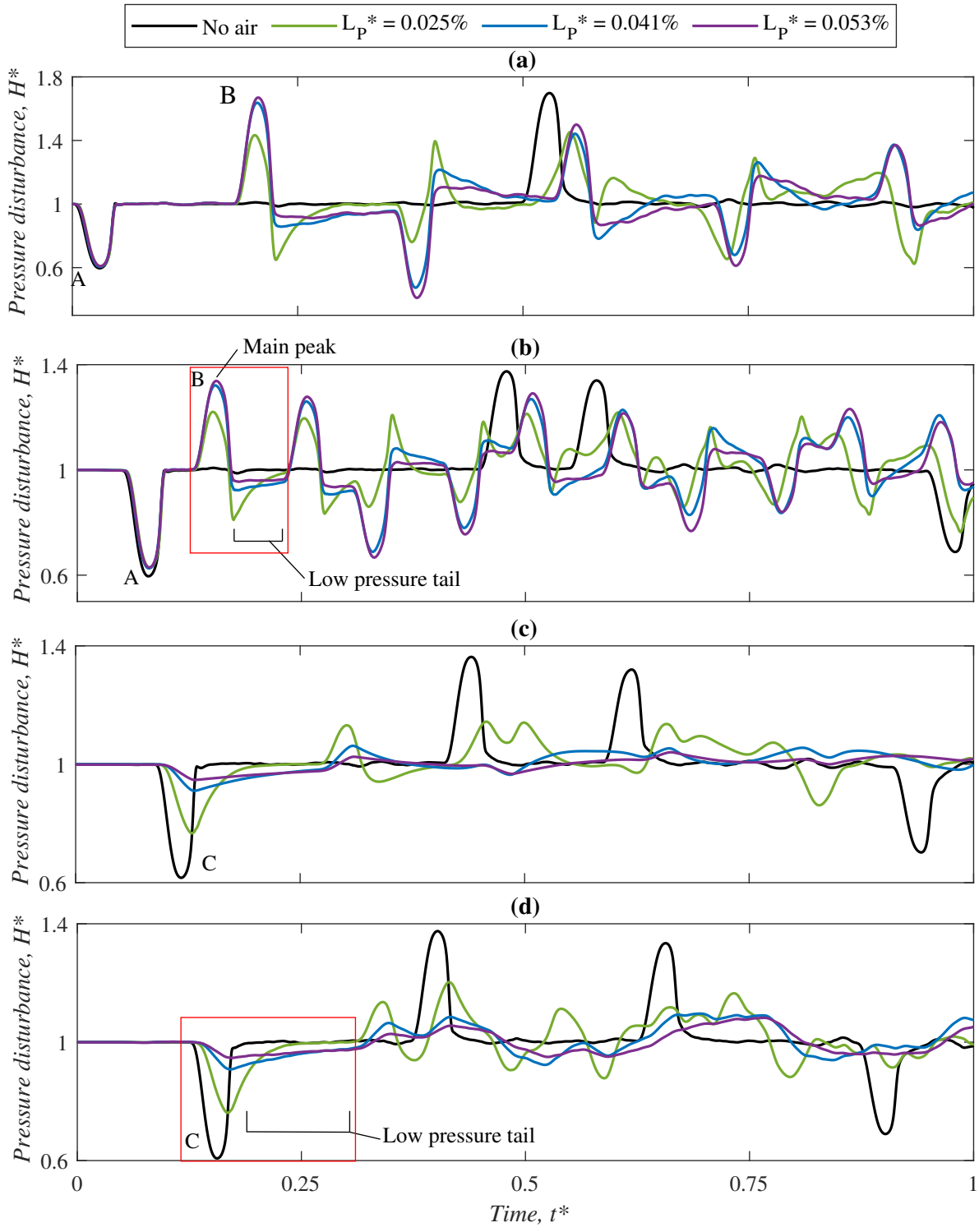

FIGURE 3.3: Experimental pressure traces for a range of representative pocket lengths and the no-air case at an initial hydrostatic pressure of 3.0 bar (a) Pressure trace measured at PT1, at the transient generation point, (b) Pressure trace measured at PT2, 6.21 m upstream of the pocket and 8.29 m downstream of PT1, (c) Pressure trace measured at PT4, at the air pocket section, and (d) Pressure trace measured at PT3, 6.30 m downstream of the pocket. The incident pulse is labelled A, the first pulse reflected from the pocket is labelled B, and the first pulse transmitted past the air pocket is labelled C. The first reflected and transmitted pulses are boxed in (b) and (d). The pocket lengths L_P are scaled by the total pipe length, the pressure disturbance relative to steady state H is scaled by the initial hydrostatic pressure, and the elapsed time t is scaled by the pipeline period.

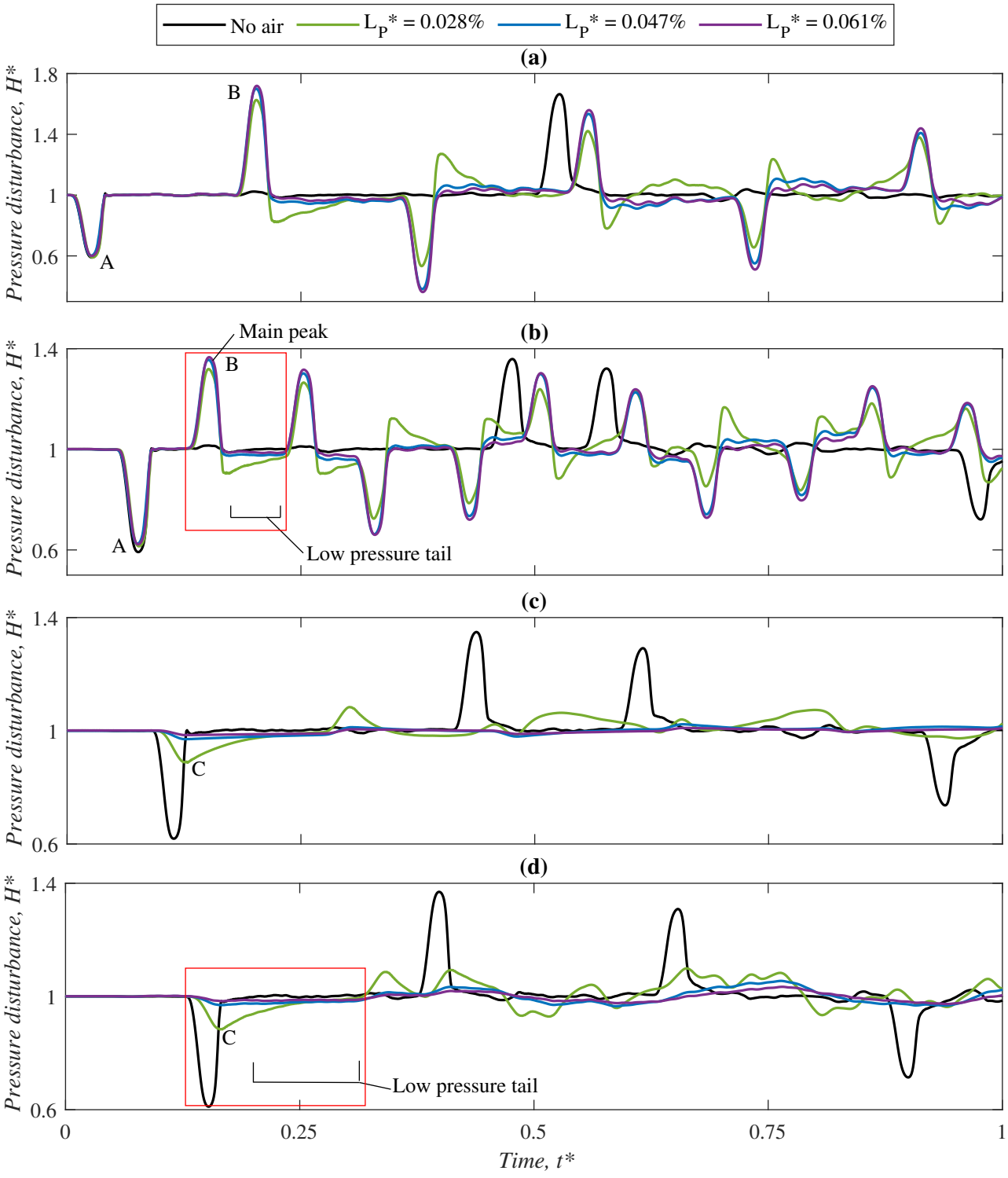

FIGURE 3.4: Experimental pressure traces for a range of representative pocket lengths and the no-air case at an initial hydrostatic pressure of 1.5 bar (a) Pressure trace measured at PT1, at the transient generation point, (b) Pressure trace measured at PT2, 6.21 m upstream of the pocket and 8.29 m downstream of PT1, (c) Pressure trace measured at PT4, at the air pocket section, and (d) Pressure trace measured at PT3, 6.30 m downstream of the pocket. The incident pulse is labelled A, the first pulse reflected from the pocket is labelled B, and the first pulse transmitted past the air pocket is labelled C. The first reflected and transmitted pulses are boxed in (b) and (d). The pocket lengths L_P are scaled by the total pipe length, the pressure disturbance relative to steady state H is scaled by the initial hydrostatic pressure, and the elapsed time t is scaled by the pipeline period.

Figures 3.3 and 3.4 show that the partial reflections occurring at the pocket resulted in significantly more pressure peaks in the transient trace than observed in the no-air case. For instance, by $t^* \approx 0.5$, the arrival time of the first reflected pulse at the upstream sensor (PT2) for the no-air case, four pulses arrived at PT2 for the air pocket scenarios. While the first reflected and transmitted pulses were fairly clear, as boxed in Figs. 3.3 and 3.4, interference patterns developed beyond $t^* \approx 0.3$ as reflections from the air pocket and the ends of the system began to interfere with each other. As boxed in Figs. 3.3 and 3.4, the reflected pulse was followed by a low-pressure peak and extended tail. From a diagnostic standpoint, Meniconi et al. (2016) has shown that this effect is not unique to the in-line air pocket, and a pressure drop following the reflected pulse may also be observed for solid blockage situations where the path of the pressure wave around the blockage is almost straight.

It is also worth noting that the pressure trace for the smallest pocket length varied significantly from the other three traces, which followed each other reasonably closely. For example, the pulse reflection coefficient, which is defined in Section 3.4.3 spans a range of approximately 0.7 to 1 for air pocket sizes of $L_P^* = 0.028\%$ to $L_P^* = 0.07\%$. However, for the smallest air pocket sizes of $L_P^* \lesssim 0.028\%$, the reflection coefficient drops sharply to approximately 0.6. The converse is observed in the transmission coefficient, which increases sharply to approximately 0.55 for the smallest pocket sizes compared to the range of 0-0.4 over the larger pocket sizes tested. The difference in the reflected and transmitted pulses for a small pocket volume can also be observed in Figures 3.3 and 3.4 for $L_P^* = 0.028\%$. This suggests that below a certain pocket volume threshold, small changes in pocket volume begin to have a more significant effect on the transient behavior, or the dominant physical processes of the transient-air interaction begin to change. This may be explained by the underlying physical theory of the interaction. Continuity and momentum theory state that

$$\frac{d\forall_p}{dt} = Q_a \tag{3.1}$$

$$\frac{dH_a}{dx} = 0 \tag{3.2}$$

where Q_a = flow rate at the air-fluid interface due to the volume change of the air pocket under the transient pressure condition; x = distance; and t = time. Equations 3.1 and 3.2 state that any change in the air pocket volume ($\forall_p$) results in a corresponding change to the system flow rate, and that the pressure of the air pocket (H_a) is homogeneous. Differentiating Eqn. 2.7 and applying Eqn. 3.2 gives

$$\frac{dH_a}{dt} = -\frac{nH_a}{\forall_p} Q_a \tag{3.3}$$

where n = polytropic exponent. Consequently, the transient variation of the hydraulic properties of pressure and flow rate depend on the volume of the pocket as well as the instantaneous pressure state. If the preceding equation is considered in terms of the transient fluctuations in pressure and volume, it becomes

$$\frac{dh_a}{dt} = -\frac{n}{\forall_0 + \forall_t} Q_a \tag{3.4}$$

where h_a = transient fluctuation in pressure; $\forall_0$ = steady-state pocket volume; and $\forall_t$ = transient fluctuation in pocket volume. Therefore it can be concluded that for large pockets, where transient volume changes are small relative to the steady-state air volume, the transient behavior is largely dependent on the initial state of the air pocket ($\forall_0$). Meanwhile, for relatively small pockets, where volume fluctuations are significant compared to the steady-state volume, the transient behavior is instead dependent on the instantaneous change in air pocket volume ($\forall_t$). The results of the MOC model were used to check the expected volume fluctuations for each experimental case. The smallest pocket sizes tested experienced greater maximum relative volume changes than the mid-range to upper-range of volumes. The maximum relative air pocket volume changes predicted by the MOC for the range of pocket volumes tested are shown in Fig. 3.5. For the 3.0 bar case, the smallest volumes ($L_P^* \approx 0.024\%$) experienced relative volume changes of approximately 10% of the starting volume compared to other pocket volumes ($L_P^* = [0.027 - 0.074]\%$) in which the relative volume change was generally less than 5%. This observation may, therefore, be attributable to the changing air-transient dynamics as pocket volume is reduced.

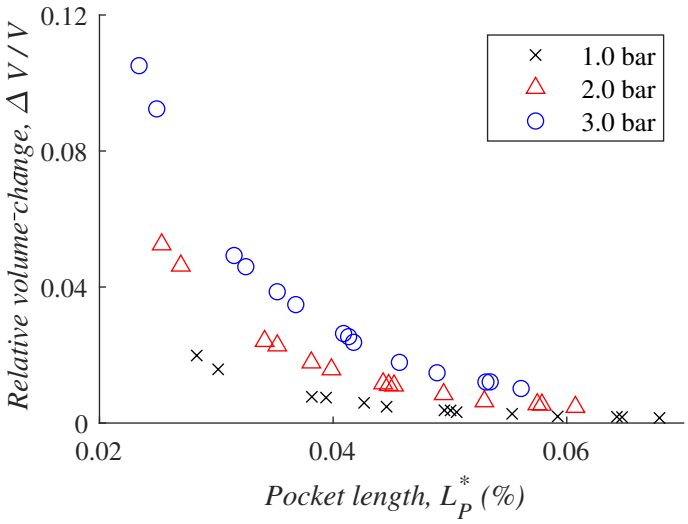

FIGURE 3.5: Maximum relative volume change compared to the steady-state air pocket volume predicted by the MOC with accumulator equation for experimental air pockets at three initial hydrostatic pressures (1.0, 2.0, and 3.0 bar). The pocket length L_P is scaled by the pipe length.

3.4.2 Frequency dependent behaviour

The shapes of the incident, reflected, and transmitted pulses were quantified using their frequency content, calculated using a discrete Fourier transform (DFT). This method enables both the main peaks and the extended tails of the reflected and transmitted pulses to be included in the analysis. However, the experimental trace was subject to interference from ongoing reflections and, in the majority of cases, the low-pressure tail was interrupted by the arrival of further reflections, as shown in Figs. 3.3 and 3.4. When the pulse extents were set to approximately that boxed in Figs. 3.3 and 3.4 some irregularities or oscillation were observed in the DFTs for the pulses, as the full pulse frequency content was not described. It was necessary to artificially generate data points to complete the pulses, with the placement of these additional points based on the shape of the preceding data and modelled pulses generated using non-reflecting boundary conditions. Although the additional points required to complete the pressure tail were required to achieve a smooth DFT, small variations in their placement did not have a significant effect on the shape of the DFT obtained. The average error between the DFT amplitudes for the shortened pulse extent and the DFT with additional points was approximately 2%.

Figure 3.6 shows the DFT amplitude for the frequencies contained in the incident and resultant pulses for a set of representative air lengths. The DFT amplitude was normalised by the initial hydrostatic pressure ($h^* = h/H_0$), while the frequency was normalised by the pipe fundamental frequency ($\omega^* = T\omega$).

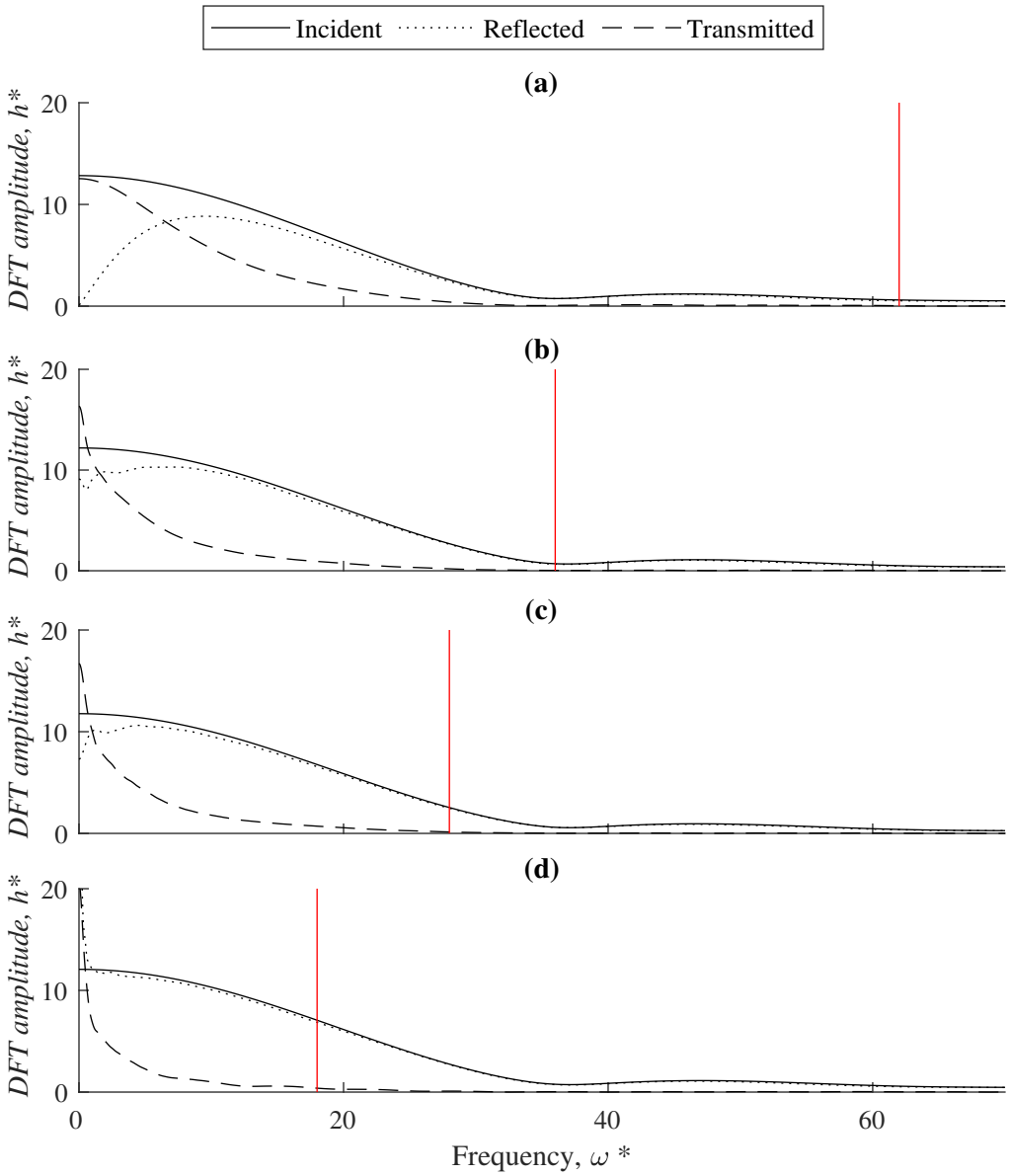

FIGURE 3.6: DFT amplitude of the incident pulse and the first pulses reflected and transmitted pulses from the in-line air pocket at an initial hydrostatic pressure of 3.0 bar for air pocket lengths (a) L_P^* = 0.023%, (b) L_P^* = 0.037%, (c) L_P^* = 0.042% (d) L_P^* = 0.053%. Cut-off frequencies for the transmitted pulse DFT are marked by a red vertical line. The incident and reflected pulses are measured at PT2, 8.29 m downstream from the transient generation point and 6.20 m upstream of the air pocket section. The transmitted pulse is measured at PT3, 6.30 m downstream of the air pocket section. The air pocket length L_P is scaled by the pipe length, the DFT amplitude h is scaled by the initial hydrostatic pressure, and the frequency ω is scaled by the inverse of the pipeline period.

A clear frequency-dependent response was observed in the DFTs of the experimental data. A similar response was observed in the DFT of the MOC outputs. The upper range of frequencies

($\omega^* \approx 20 - 70$) contained in the incident pulse was present in the reflected pulse at approximately the same amplitude (within 4%). In the transmitted pulse, the amplitude of this frequency range was approximately 3% of the incident amplitude, meaning the upper range of frequencies contained in the incident pulse was primarily reflected back by the air pocket. This frequency-dependent transmissivity is due to the compressibility of the air and has previously been observed in the field of acoustics (Domenico, 1982; Leighton et al., 1998). Significant reductions in transmissivity are observed for signal frequencies above the air pocket's resonant frequency, and this frequency content is reflected back by the air. Calculating the resonant frequency for an in-line air pocket is difficult due to the unknown geometry of the pocket (Jang et al., 2009). However, for the off-line pocket case, where the geometry is known, the DFT agreed with theoretical predictions of the resonant frequency as discussed in Chapter 5. For the in-line pocket, the frequency-dependent behavior has been quantified using a cut-off frequency for transmission by the air pocket, defined in this study as the frequency at which the amplitude of the transmitted pulse DFT was first less than 5% of the amplitude of the incident pulse DFT. The cut-off frequencies are marked with vertical lines in Fig. 3.6. The cut-off frequencies for the experimental scenarios are plotted in Fig. 3.7. The cut-off frequency decreased with increasing air volume, consistent with theoretical expectations for the resonant frequency (Jang et al., 2009). The observed trend is approximately linear, with the cut-off frequency decreasing by approximately $\omega^* = 36$ over the range in pocket lengths plotted ($L_P^* = 0.025 - 0.065$).

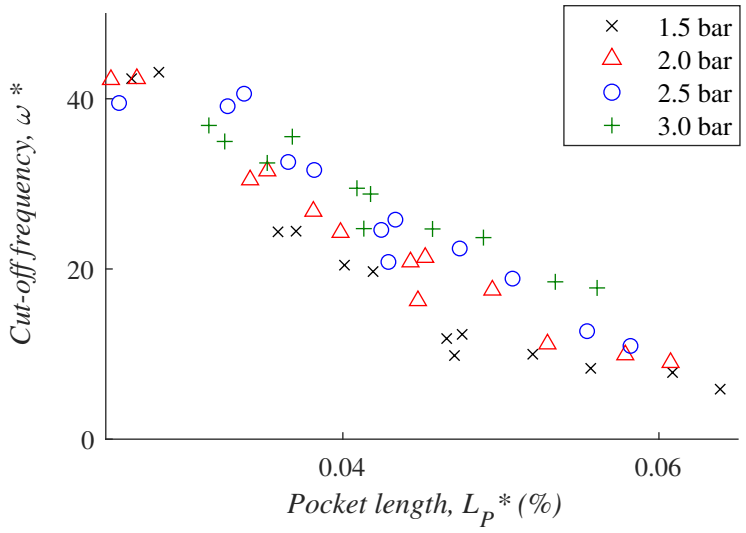

FIGURE 3.7: Experimental cut-off frequencies estimated for pocket volumes at a range of initial hydrostatic pressure (1.5, 2.0, 2.5, and 3.0 bar). The cut-off frequency is the frequency at which the transmitted pulse DFT amplitude measured at PT3 (6.31 m downstream of the air pocket section) is first less than 5% of the incident pulse DFT measured at PT2 (6.20 m upstream of the air pocket section).

This frequency-dependent response is not observed for other pipeline anomalies, such as solid blockages and leaks, which do not impose a significant change in shape on the incident pulse during reflection and transmission (Brunone, 1999; Meniconi et al., 2011). This finding may therefore be incorporated into transient fault detection techniques to identify the presence of air and differentiate solid flow-blocking elements from air blockages.

3.4.3 Reflection and transmission coefficients

Reflection and transmission coefficients provide a quantitative measure of the air pocket's effect on the incident transient pulse. In the time domain, these coefficients are generally obtained by comparing the amplitude of the reflected and transmitted transient signals to the incident amplitude. The time-domain reflection and transmission coefficients were calculated as

$$RC_{exp} = \frac{H_R}{H_I} - \frac{H_{R,0}}{H_{I,0}}, \tag{3.5}$$

$$TC_{exp} = \frac{H_T}{H_I} \,, \tag{3.6}$$

where RC_{exp} = experimental reflection coefficient; TC_{exp} = experimental transmission coefficient; H_I = peak amplitude of the incident pulse measured upstream of the pocket at PT2; H_R = peak amplitude of the first reflected pulse measured upstream of the pocket at PT2; and H_T = peak amplitude of the first transmitted pulse measured downstream of the pocket at PT3. As discussed in Chapter 2, small reflections were observed from the crest section for the no-air case. To clearly identify the effect of the injected air on the response, the authors calculated a reflection coefficient for the crest based on the data for the no-air case at each initial hydrostatic pressure ($H_{R,0}/H_{I,0}$) and subtracted it from the reflection coefficients calculated for the air pocket cases (H_R/H_I) at that initial hydrostatic pressure. The values used in the calculation are marked on example pressure traces in Fig. 3.8.

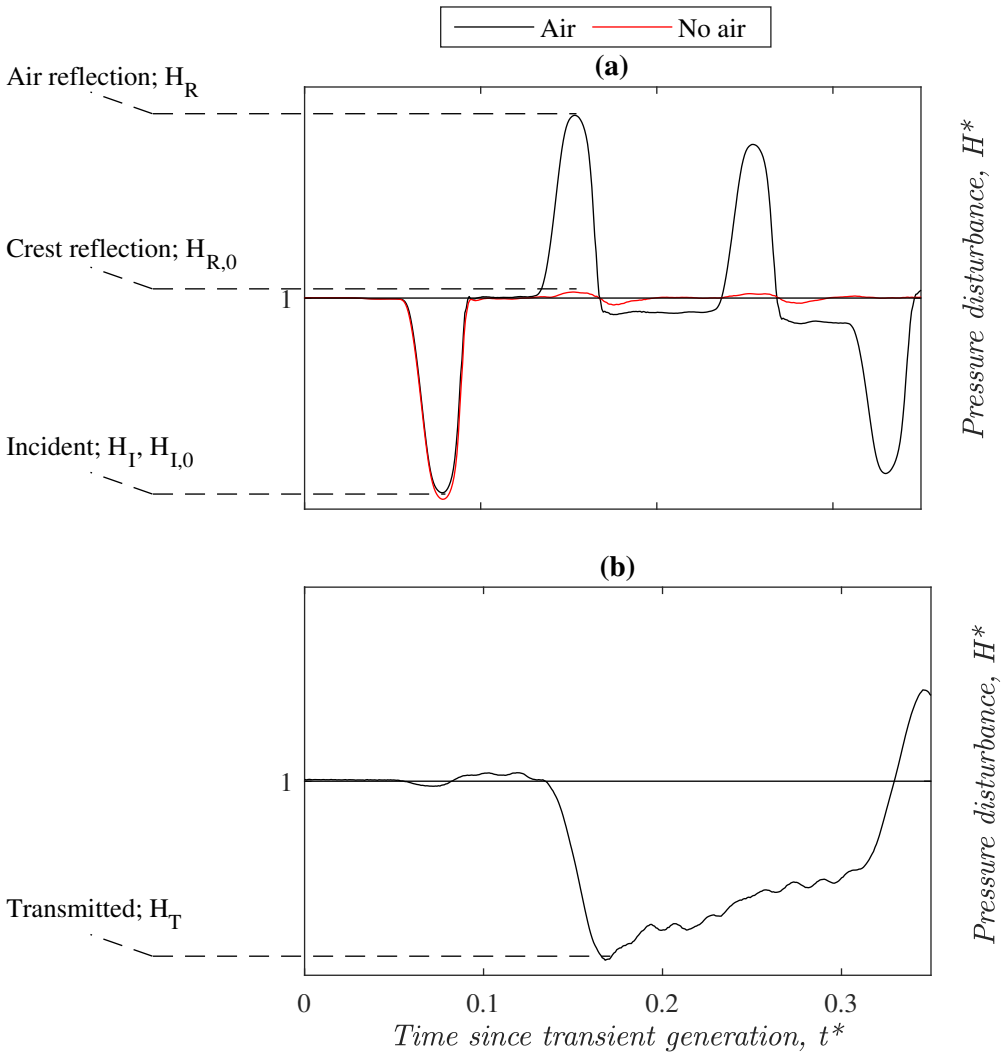

FIGURE 3.8: Illustration of the values used in the calculation of experimental reflection and transmission coefficients (RC_{exp}, TC_{exp}, Eqs. 3.5 and 3.6 respectively), (a) Incident and reflected pulses measured at PT2, 6.21 m upstream of the pocket section, (b) Transmitted pulse measured at PT3, 6.30 m downstream of the pocket section.

The time domain reflection and transmission coefficients for each steady-state pressurised pocket length are shown in Figs. 3.9 and 3.10 for a range of initial hydrostatic pressures. Sensitivity testing showed that the general trends observed were independent of the polytropic constant used to obtain L_P^*, and the standard error in RC_{exp} and TC_{exp} due to experimental variation was approximately 2%. For the no-air case, TC_{exp} was slightly less than 1, indicating that there was a small quantity of energy loss across the 12.85 m pipe section between PT2 and PT3 when air was not present.

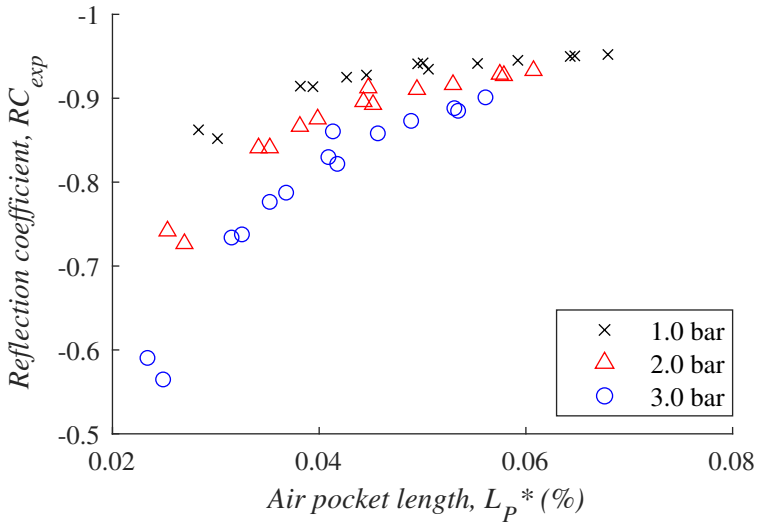

FIGURE 3.9: Experimental reflection coefficient for reflected pulses measured at PT2 for a range of air pocket volumes at different initial hydrostatic pressures (1.0, 2.0, and 3.0 bar), calculated from Eq. 3.5. The pocket length L_P is scaled by the pipe length.

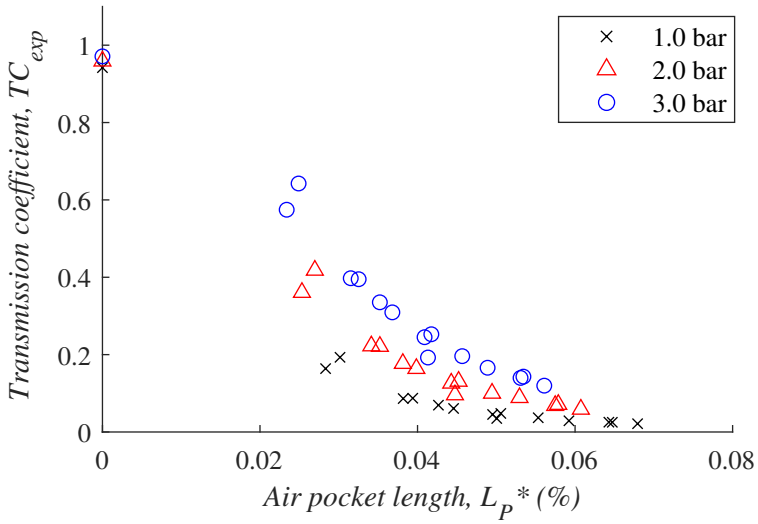

FIGURE 3.10: Experimental transmission coefficient for transmitted pulses measured at PT3 for a range of air pocket volumes at different initial hydrostatic pressures (1.0, 2.0, and 3.0 bar), calculated from Eq. 3.6. The pocket length L_P is scaled by the pipe length.

Figures 3.9 and 3.10 show that increasing the air pocket size increased the absolute value of RC_{exp} and decreased TC_{exp}, with an approximately polynomial trend observed in both cases. The presence of the air pocket created an out of phase reflection ($RC_{exp} < 0$). These observations can be explained by impedance theory. The impedance, Z, of a pipe is given by $Z = \rho a/A$, where

ρ = fluid density and A = cross-sectional area of the pipe (Gong et al., 2013a). It can be used to determine the theoretical reflection coefficient, RC_{th}, which is the amplitude of the reflected pulse relative to the amplitude of the incident pulse. It is defined as

$$RC_{th} = \frac{Z_A - Z_0}{Z_A + Z_0}, \tag{3.7}$$

where Z_A = impedance of the pipe section containing the air pocket; and Z_0 = impedance of the pipe without the air pocket. The value of Z_A is smaller than Z_0 due to the low density of the air and the local reduction in wave speed caused by the air's compressibility. As the size of the air pocket increases, Z_A decreases, therefore increasing the absolute value of RC_{th} in agreement with experimental observations. In addition, RC_{th} is negative, accounting for the out of phase reflection observed. This phase change is the opposite of what would be observed for a solid flow obstruction, which has a greater impedance than the clear pipe. This is a useful point of difference that may be utilised in diagnostic testing when a loss of flow or increase in pumping costs is observed in the system.

Theoretical values for RC_{exp} were calculated using a weighted average density for the crest section and a wave speed at the crest section estimated using the void ratio of the crest section and the wave speed equation presented by Lee (1991). Figure 3.11 shows that RC_{exp} was in agreement with RC_{th}, particularly for the upper range of pocket sizes. The average error was less than 4% across the range of experimental pocket volumes.

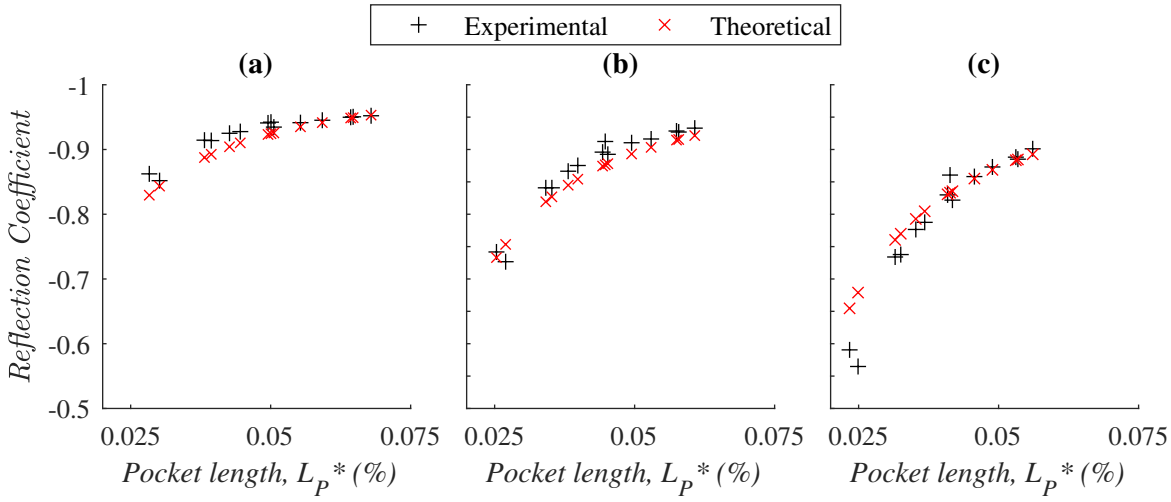

FIGURE 3.11: Comparison of the reflection coefficients calculated from experimental measurements (Eq. 3.5) and predicted by the theoretical impedance equation (Eq. 3.7) for a range of air pocket sizes at initial hydrostatic pressures of (a) 1.0 bar, (b) 2.0 bar, and (c) 3.0 bar. The air pocket length L_P is scaled by the total pipe length.

The range of RC_{exp} and TC_{exp} observed were compared to the values expected for solid blockages under similar conditions. Solid flow blockages generate reflections with an amplitude dependent on the base flow of the system, with severe flow constrictions required to generate reflections under zero base flow of a comparable amplitude to the observed air pocket reflections. The smallest air pocket volumes blocked approximately 6% of the total pipe cross-section but generated reflections under zero base flow comparable to solid blockages which almost entirely block the pipe cross-section (Meniconi et al., 2011). The required local loss coefficients, estimated using MOC modelling for a solid blockage, are shown in Fig. 3.12, with values ranging between $k = 10^6$ and $k = 10^{12}$. This is another useful diagnostic property of the air pocket. If blockage effects are observed in an operational pipeline, it can be tested under zero base flow conditions and the amplitude of the transient reflection compared to the degree of flow loss observed when operational. The outcome may be used to differentiate between air pockets and solid blockages.

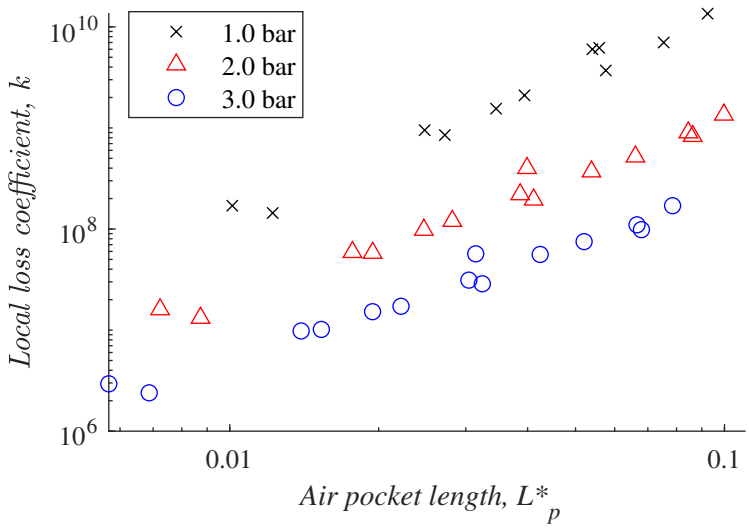

FIGURE 3.12: Local loss coefficients required to match the reflected pulse amplitude measured at PT2 (6.21 m upstream of the air pocket section) for a range of in-line air pocket volumes at initial hydrostatic pressures of 1.0, 2.0, and, 3.0 bar. The air pocket length L_P is scaled by the pipe length.

As discussed previously, past field and experimental studies for the dead-end pocket case have observed reflected peak amplitudes that exceed the initial hydrostatic pressure by a factor of 4-5 due to pocket collapse (Jönsson, 1985; Lee and Martin, 1999). The key dimensions may be used to assess the likelihood of pocket collapse. The work done on the pocket by the transient wave scales as $PA_PU_PT_P$, where P = pressure on the pocket; A_P = pocket surface area; U_P = radial velocity of the air-water interface; and T_P = duration of the compression phase. When the compression length scale (U_PT_P) is longer than the pocket length (L_P), the pocket collapses, resulting in large pressure spikes such as those observed by Jönsson (1985) and Lee and Martin (1999). This work used a short duration transient pulse (6 ms), and the system experienced low velocities due to the lack of base flow. The maximum velocities predicted by the MOC for this experimental case were in the order of 0.1 m/s. This meant the compression scale was too small to result in pocket collapse and, unlike previous studies, large pressure spikes were not observed. The long transient duration ($T_P \sim 0.5 - 3s$) and base flows or high driving pressures applied by Jönsson (1985) and Lee and Martin (1999) meant that the larger pocket volumes used ($L_P \sim 0.02m$) were outweighed by the relative increase in the compression length scale.

The reflection and transmission behaviour was further explored in the frequency domain in order to include the entirety of the reflected and transmitted pulses in the analysis. Transmission and reflection coefficients were calculated in the frequency domain by comparing the DFT amplitudes for the transmitted and reflected pulses to the DFT amplitude of the incident pulse at each frequency:

$$RC_\omega = \frac{h_{R,\omega}}{h_{I,\omega}} \tag{3.8}$$

$$TC_\omega = \frac{h_{T,\omega}}{h_{I,\omega}} \tag{3.9}$$

where RC_ω and TC_ω = reflection and transmission coefficients for a given frequency; and $h_{I,\omega}$, $h_{R,\omega}$, and $h_{T,\omega}$ = DFT amplitudes of the incident, reflected, and transmitted pulses at that frequency. Summing the squares of RC_ω and TC_ω at each frequency gives a measure of the energy contained in the reflected and transmitted pulses relative to the incident pulse and, therefore, of the energy amplification or dissipation that occurs during the reflection and transmission process. Figure 3.13 shows the total energy contained in the reflected and transmitted pulses at each frequency relative to the incident pulse for four representative air lengths. The relative energy ranged between 0.85 and 1 for $\omega^* \gtrsim 5$. For $\omega^* \lesssim 5$, the relative energy increased above 1. This is likely due to minor errors associated with extracting the pulses in the time domain before performing the DFT.

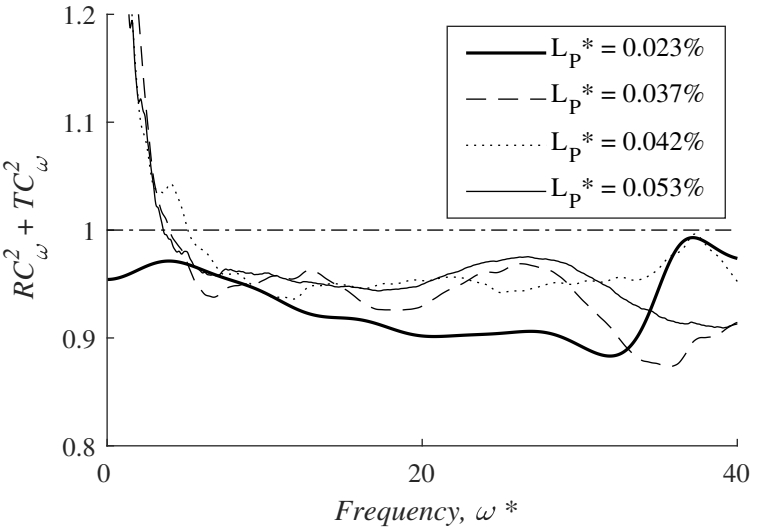

FIGURE 3.13: Summed squares of experimental reflection and transmission coefficients for the range of frequencies contained within the incident pulse for selected air pocket lengths at a initial hydrostatic pressure of 3.0 bar. A reference line is included at $RC_\omega^2 + TC_\omega^2 = 1$. The air pocket length L_P is scaled by the total pipe length and the frequency is scaled by the inverse of the pipeline period.

The average relative energy across the range of frequencies in the reflected and transmitted pulses was less than 1 for the cases tested, despite the amplification observed at low frequencies. This indicates that energy losses occurred between the incident pulse and the reflected and transmitted pulses generated by the pocket. This may be explained by energy balance theory, which is explored in Section 3.4.4.

3.4.4 Energy losses

The results of the MOC were used to carry out an energy balance for the system. The 1D MOC equations, including the accumulator equations for the in-line air pocket boundary (Chapter 2) were used to obtain estimations of the fluid pressure and velocity along the pipe at a range of time steps. The energy equation (Karney and McInnis, 1990; Karney et al., 2015; Duan et al., 2017) was then used to assess the energy balance in the system. The energy equation is

$$\frac{dU_e}{dt} + \frac{dU_a}{dt} + \frac{dT_e}{dt} + D' + W' = 0 \,, \tag{3.10}$$

where U_e = internal energy; U_a = elastic energy stored by the air pocket; T_e = kinetic energy; D' = rate of viscous energy dissipation; and W' = rate at which work is done on the fluid at each boundary. The extended versions of these terms can be found in Karney and McInnis (1990) and Karney et al. (2015). The fluid pressure and velocity, evaluated numerically for each spatial node at each time step, were used to evaluate the energy balance for the pipe at each time step and to calculate the total energy in each form at each time step.

Figure 3.10 shows the variation in the kinetic, internal, and air storage energy of the system for $t^* = 0 - 1.5$. The energies were scaled by the initial energy stored by the air pocket ($E^* = E/U_{a,0}$). Viscous dissipation accounted for less than 2% of the system's kinetic energy and was therefore not shown. The compressibility of the air and the lack of base flow in the system meant that the majority of the system energy was stored in the air pocket, with less than 0.01% of the energy stored in internal and kinetic forms. Because viscous dissipation was negligible within the time-frame of the first air-transient interaction, it is likely that the energy loss observed in the frequency domain is, therefore, attributable to conversion to air pocket storage during the compression and expansion phases.

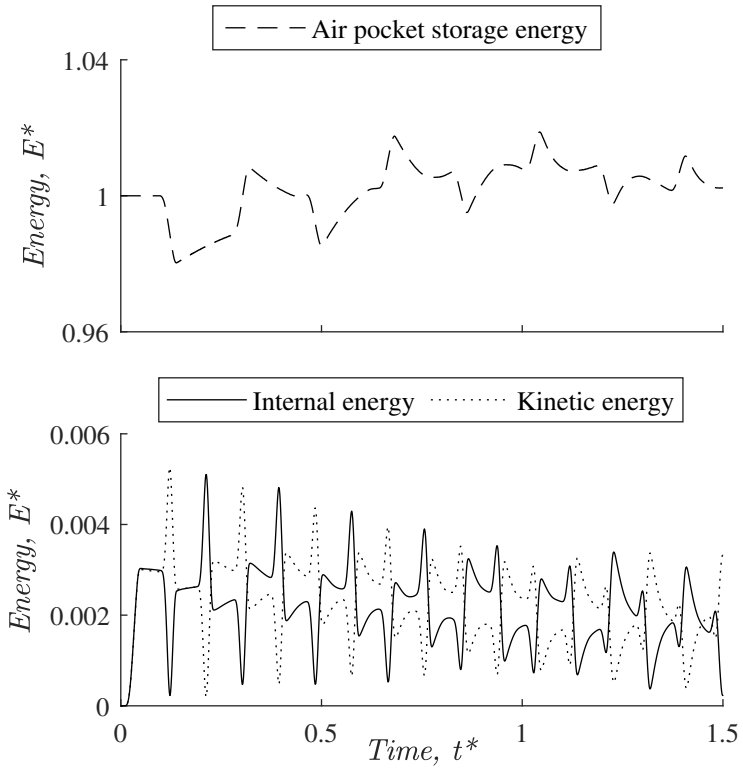

FIGURE 3.14: Air storage, internal, and kinetic energy estimated from the outputs of the MOC with the accumulator equation for pocket length $L_P^* = 0.042\%$ at 3.0 bar initial hydrostatic pressure. The energies are scaled by the initial energy stored in the air pocket and the time is scaled by the pipeline period.

3.4.5 Effects of initial hydrostatic pressure

Initial hydrostatic pressure has been shown to have an effect on the transient trace for the dead-end pocket scenario (Zhou et al., 2002) and the brass block case (Kim, 2008b). The time-domain RC_{exp} and TC_{exp} calculated in Section 3.4.3 provide a quantitative assessment of the effects of initial hydrostatic pressure on the in-line pocket interaction with the transient. Figure 3.10 shows that, for the no-air case, the relative amplitude of the pulse measured at PT3 increased with initial hydrostatic pressure; however, the total range of TC_{exp} for the no-air case was less than 0.02. For larger air lengths (($L_P^* \gtrsim 0.06\%$)), Figs. 3.9 and 3.10 show that the variation in RC_{exp} and TC_{exp} with initial hydrostatic pressure was comparable to the no air case. However, the effect of initial hydrostatic pressure on the reflected and transmitted pulse amplitude became increasingly significant as the air length was reduced below this threshold, with the total range of TC_{exp}

increasing to approximately 0.5 for the smallest pocket volumes ($L_P^* \approx 0.025\%$). This suggests that when assessing the size of the entrapped air pocket from transient reflections and transmissions, the initial hydrostatic pressure should be taken into account.

Inspection of the DFTs for air pockets which occupy a similar length when compressed to different initial hydrostatic pressures (Fig. 3.15) suggested there is only a minor variation in the DFT amplitude for air pockets of the same pressurised volume at different initial hydrostatic pressures, with average variation of less than 0.05 observed in the reflection and transmission coefficient at each frequency in the DFTs plotted. Fig. 3.7 shows that the trend in cut-off frequency with pressure is also relatively minor, with a range of $\omega^* \approx 10$ across the range of pressures tested for air pockets of a similar pressurised volume. This means that it may be possible to determine air pocket volumes relatively accurately from the cut-off frequency alone.

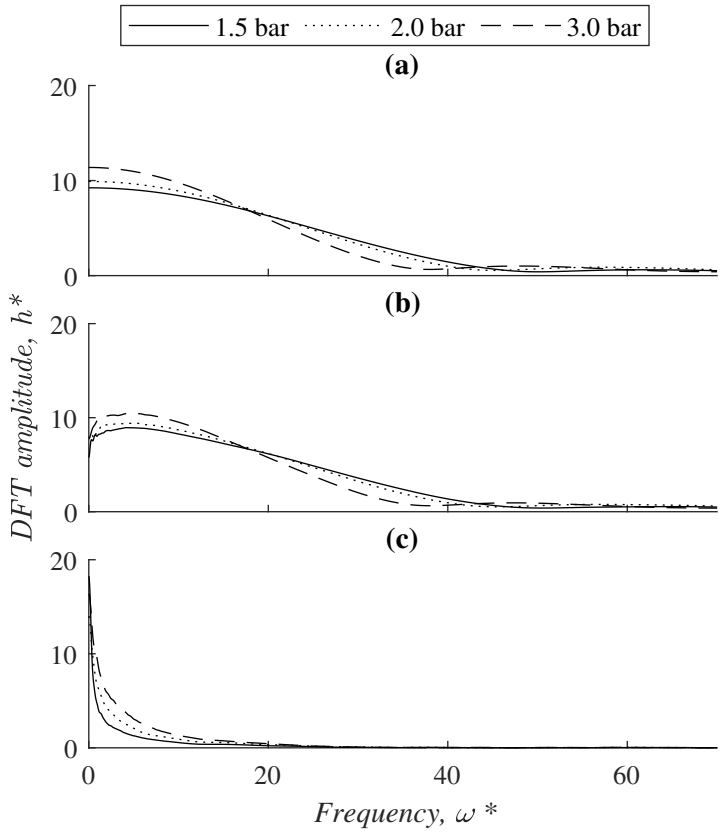

FIGURE 3.15: DFT amplitude of the (a) incident pulse measured at PT2 (8.29 m downstream of the transient generation and 6.21 m upstream of the air pocket section), (b) reflected pulse measured at PT2, and (c) transmitted pulse measured at PT3 (6.30 m downstream of the air pocket section) for comparable pressurised air pocket lengths $L_P^* \approx 0.043\%$ at a range of initial hydrostatic pressures (1.5 bar, 2.0 bar, and 3.0 bar). The DFT amplitude h is scaled by the initial hydrostatic pressure and the frequency ω is scaled by the inverse of the pipeline period.

3.5 Conclusions and recommendations

Controlled experimental investigations are needed to distinguish the effects of entrapped in-line air pockets on fluid transients. The purpose of this chapter is to present experimental data for the in-line air pocket case under realistic system conditions and to characterise the effects of air on the transient in terms of reflection and transmission. To assist in developing a diagnostic framework, it is useful to note how the effects of air compare to other faults that cause a flow constriction at steady-state. Air pockets can often be cheaper to remove than solid blockages, meaning it is advantageous to be able to differentiate between the two cases when flow loss is observed.

The reflective power of the air pocket increases with its length in a polynomial trend, in agreement with impedance theory. Although the low-pressure tail following the transient reflection may also be observed for a solid blockage, the out-of-phase reflection from the flow constriction is unique to the air pocket. Unlike a solid blockage, air pockets also result in a visible reflection under zero base flow conditions regardless of the degree of cross-section blockage. Linking the amplitude and phase of the transient reflection under zero base flow to the observed flow loss during operation can, therefore, be used to differentiate between air and solid blockages.

Analysis in the frequency domain showed that the air pocket transmits only the lower range of frequencies contained in the incident pulse, with the upper range of frequencies being primarily reflected. This frequency-dependent transmissivity is also unique to air among flow-blocking elements. The transmission cut-off frequency decreased as pocket length increased, similar to the resonant frequency of trapped air.

The reflection and transmission coefficients calculated in the frequency domain also indicate that, on average, the incident pulse loses energy over the range of frequencies contained within it during reflection and transmission. An investigation of energy distribution within the system indicated that this energy loss is likely to be due to conversion to air pocket storage.

Six different initial hydrostatic pressures were used in the experimental tests to assess the effects of steady-state pressure on transient behavior. As the air length was reduced, the effect of initial hydrostatic pressure on the amplitude of the transmitted and reflected pulses became increasingly significant.

4 Comparison of numerical models for the interaction of fluid transients with in-line air pockets

4.1 Introduction

As discussed in Chapter 1, common faults such as leaks, discrete blockages, extended blockages, and air pockets may be identified provided there is a numerical model that can recreate the system response to a transient disturbance via inverse analysis. As a result, it is important to understand and be able to accurately model how different anomalies may distort transient signals. As discussed in Chapter 3, even small collections of air can create significant transient reflections and frequency dependent effects which distort the expected response, meaning it is critical to ensure that they are accurately incorporated into network models. This chapter aims to evaluate our current capability for modelling and predicting the dynamics of in-line air pockets through comparison with the new experimental data collected as part of the in-line air pocket study (Chapter 3).

Variable wave speed theory was used in early works for predicting transient behavior with entrained air bubbles. Pearsall (1965) and Falconer et al. (1983) observed experimentally and in the field that the presence of air bubbles results in a significant reduction in transient wave speed even for very small quantities of air due to the added compressibility. Variable wave speed models generally assume that air is distributed homogeneously through the pipeline, and the wave speed is calculated individually for each reach of the pipeline based on the local void ratio and pressure at steady-state

(Fox, 1972; Wylie, 1980). Compressibility theory may also be used to account for changes in the wave speed as a result of variations in void ratio along the pipe with time due to compression and expansion of the air in response to pressure disturbances (Lee, 1991). For cases where the system contains high points, vapor cavities are confined to fixed sections of the computational grid and wave speed reductions are limited to the sections containing the cavities (Provoost, 1976). The variable wave speed model was tested using data from a laboratory pipeline for the case of a long, thin vapour cavity formed at the top of the pipe and was found to provide a reasonable prediction of the shape of the pressure disturbance, but, for the given system, was found to be numerically stable only for very small quantities of air ($V_p/V_{pipe} \lesssim 2x10^{-6}$, where V_p is the air pocket volume and V_{pipe} is the total pipe volume).

The effect of entrapped air on a fluid transient is generally modelled differently when the air exists as a lumped pocket rather than as distributed bubbles. For lumped pockets, the interaction between the transient and entrapped air is most commonly modelled using the accumulator equation to capture the effects of the air's compressibility on transient pressures (Wylie et al., 1993), resulting in reflection and transmission at the pocket as well as wave speed changes as a result of the air. This method has been extensively investigated and developed to predict peak pressures for the case of an air pocket trapped at the end of dead-end pipe (Lee and Martin, 1999; Lee, 2005; Zhou et al., 2011). The case of in-line air partially blocking flow some distance from a boundary is not as well understood, with a particular lack of experimental investigations validating the accumulator model for this scenario. Kim (2008a) carried out numerical investigations using the accumulator model for the case of an off-line pocket, which does not intrude into the flow area, using a reduced wave speed for the entire pipeline based on the volume of air relative to the pipeline volume. This approach achieved good agreement with experimental results in terms of wave timing. Bergant et al. (2018) investigated the accumulator model for the same pocket configuration, and found that it resulted in an amplitude error due to an underestimation of damping, which was reduced through the use of an unsteady friction model. No significant phase lag was observed in the model outputs compared to the experimental transient peaks for this off-line pocket scenario.

Although a range of research has been carried out to numerically predict the behavior of homogeneously distributed bubbles and dead-end pockets, the case of in-line pockets has not been so thoroughly investigated. In particular, little research has been completed in the laboratory to verify the proposed numerical models for an in-line pocket. The purpose of this component of the study is to compare the results of experimental investigations into the reflection and transmission of a rapid transient through an in-line air pocket with the results obtained from the modelling methods presented in the literature. The range of pocket volumes and initial hydrostatic pressures tested, and the use of a sharp input pulse, enables a comprehensive test of the models' predictive accuracy. The experimental results will be used to assess the suitability of the variable wave speed and accumulator models presented in the literature for the in-line pocket scenario. A better understanding of the applicability of existing modelling methods, validated by experimental results, will assist network operators in selecting models for the efficient diagnosis of entrapped air in pipelines through the use of transient detection techniques.

4.2 Numerical modelling

4.2.1 Accumulator model

Experimental data was used to assess the validity of the mathematical models proposed in the literature for representing the in-line pocket case in the MOC. The experimental methods are described in Chapter 2. The accumulator model, described in Chapter 2, was tested first.

Figures 4.1 and 4.2 show the modelled and experimental pressure traces measured at PT2 (6.21 m upstream of the pocket) and PT3 (6.30 m downstream of the pocket) for a set of representative air volumes at 3.0 bar. The pressure disturbances have been normalised by the initial hydrostatic pressure such that $H^* = H/H_0$, where H = measured pressure disturbance at any time and H_0 = initial hydrostatic pressure. The elapsed time t was normalised by the pipeline period T such that $t^* = \frac{a}{4L}t$, where a = transient wave speed and L = pipe length. The air volumes measured at atmospheric pressure were converted to steady-state in-pipe air volumes (V_p) using the reversible

polytropic equation (Chapter 2, Eqn. 2.7). The pocket length scale, L_P, was approximated as $L_P \sim V_p^{\frac{1}{3}}$. The value of L_P was expressed as a percentage of the total pipe length L such that $L_P^* = L_P/L \times 10^2$. The traces are partitioned into half periods, with the pipeline period defined as $T = 4L/a$.

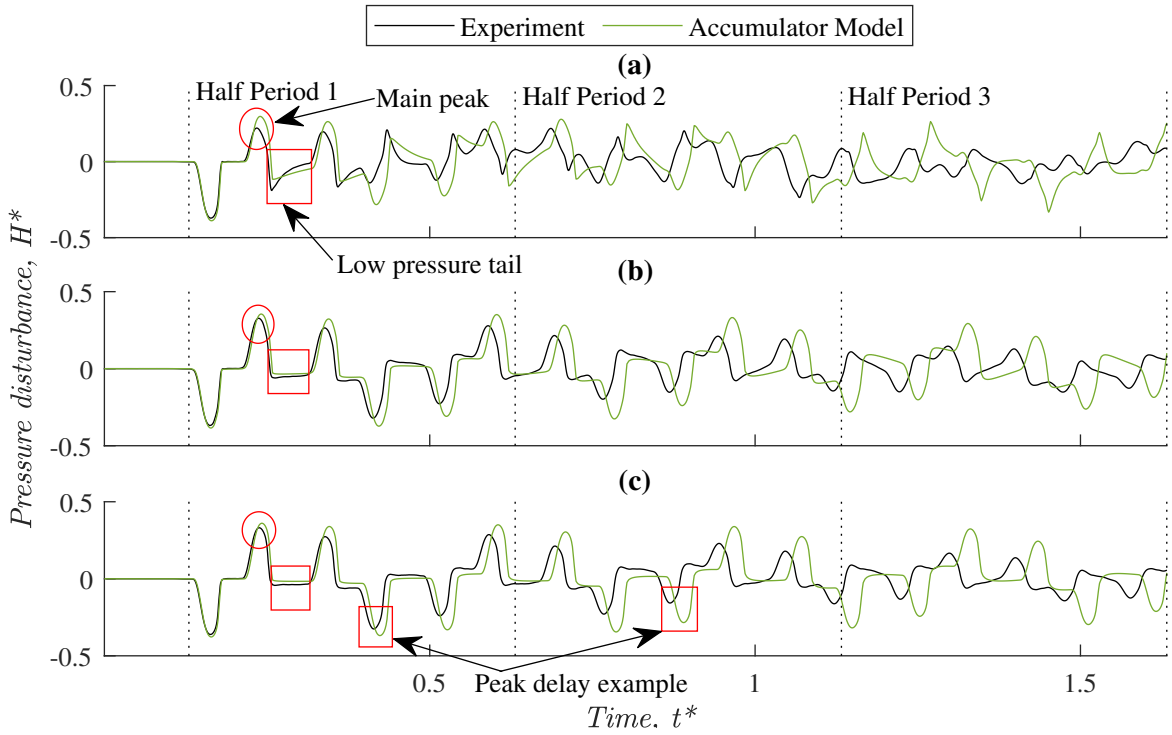

FIGURE 4.1: Experimental and modelled (MOC with accumulator model) transient pressure traces measured 8.29 m downstream of the transient generation point and 6.21 m upstream of the air pocket section at PT2 at an initial hydrostatic pressure of 3.0 bar for pocket sizes (a) L_P^* = 0.025%, (b) L_P^* = 0.041%, and (c) L_P^* = 0.053%. Half periods of the trace are marked with dotted lines. The pressure disturbance H is scaled by the initial hydrostatic pressure, the time t is scaled by the pipeline period, and L_P is scaled by the total pipe length. Examples of the main reflected peak, the following low pressure tail, and peak delay are marked.

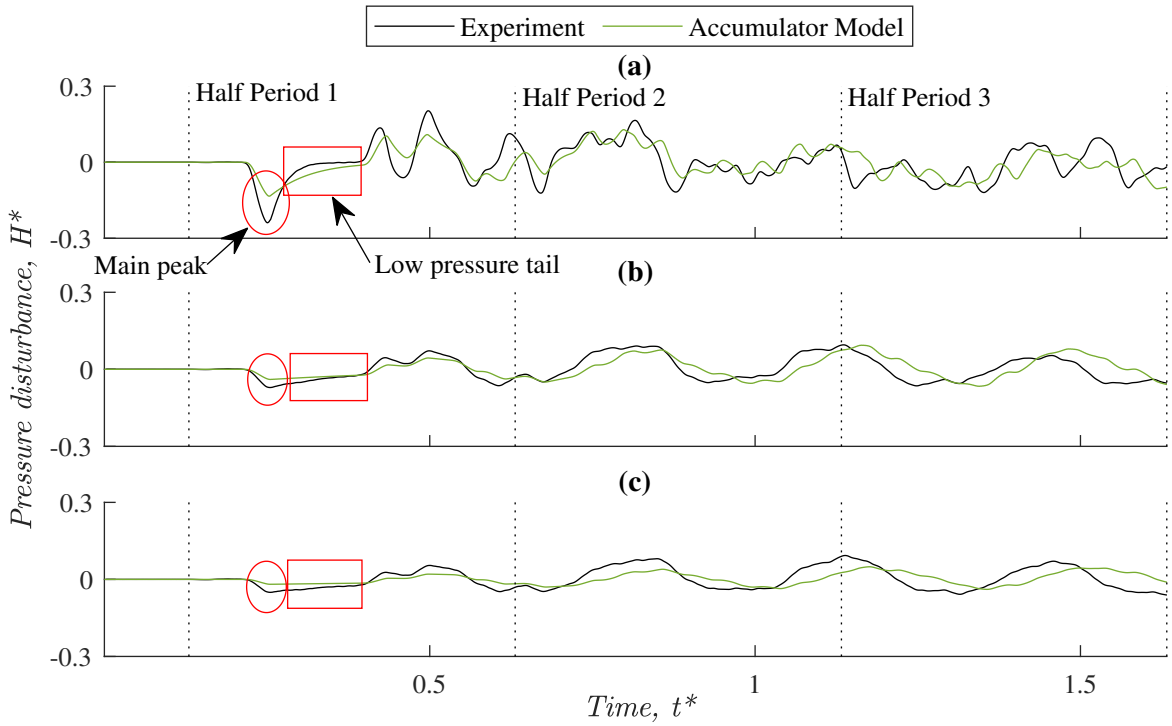

FIGURE 4.2: Experimental and modelled (MOC with accumulator model) transient pressure traces measured 6.30 m downstream of the air pocket section at PT3 at an initial hydrostatic pressure of 3.0 bar for pocket sizes (a) L_P^* = 0.025%, (b) L_P^* = 0.041%, and (c) L_P^* = 0.053%. Half periods of the trace are marked with dotted lines. The pressure disturbance H is scaled by the initial hydrostatic pressure, the time t is scaled by the pipeline period, and L_P is scaled by the total pipe length. Examples of the main reflected peak and the following low pressure tail.

The accumulator model was numerically stable and provided a reasonable estimate of the general shape of the transient pulses. In particular, the accumulator model was able to capture the low-pressure tails following each pulse reflected and transmitted by the air pocket, as identified by Alexander et al. (2020a) (Chapter 3). Examples of low-pressure tails are boxed and labelled on Figs. 4.1 and 4.2. Several key limitations were identified in the modelled results which reduced the accumulator model's accuracy. The pressure pulses predicted by the accumulator model were delayed compared to the experimental results, with the delay becoming more severe over time. The pulses boxed and labelled in Fig. 4.1 demonstrate the difference in peak arrival time predicted by the model and observed in the experiment. For the marked peaks, the phase delay between the model and experiment increased by 83% between the first and second half periods. This phase-delay error

was also observed in predictions of the accumulator model for the dead-end case (Lee, 2005; Zhou et al., 2011; Bergant et al., 2018).

When the transient encounters an air pocket, the incident pulse is split into reflected and transmitted pulses. The accumulator model overestimated the amplitude of the reflected pulse, and underestimated the amplitude of the transmitted pulse. The peaks of the first reflected and transmitted pulses are circled and labelled in Figs. 4.1 and 4.2 to demonstrate the amplitude difference between the model predictions and the experimental measurements. For the marked cases, the model overestimated the reflected pulse amplitude by approximately 30%, and underestimated the transmitted pulse amplitude by approximately 50%. For the dead-end case, experimental investigations by Lee and Martin (1999), Lee (2005), and Zhou et al. (2011) also found that the accumulator model overestimated the peak pressures resulting from reflection by the air pocket. This indicates that there were processes within the experimental system that were not explained by the accumulator model.

4.2.2 Variable wave speed model

The variable wave speed model is implemented in cases where air in free-bubble form is concentrated at a set of nodes. The wave speed at each node is calculated using an effective bulk modulus at that nodal point based on the void ratio and other pipeline characteristics. It is assumed that the air bubbles within the pipe follow a reversible polytropic relationship as per Eqn. 2.7, and the pressure within the air bubbles is in equilibrium with the local fluid pressure (Lee, 1991). When the system is above vapor pressure, the void ratio at a particular node is given by

$$\varepsilon_{i,j} = \left(\frac{H_{i,j-1}}{H_{i,j}} \right)^{1/n} \varepsilon_{i,j-1} \ , \tag{4.1}$$

where ε = void ratio at each node in the MOC grid. The void ratio is calculated based on the volume of air relative to the volume of pipe reach associated with that node ($A\Delta x$). As a result, a key limitation of the variable wave speed model is the grid dependence. When air is not evenly

distributed throughout the pipe, the void ratio and subsequent wave speed estimated at the nodes where air is located are dependent on the pipe discretisation and the length of fluid which is assumed to be associated with the air. In the experimental testing, extraction of the air from the system using the syringe showed that the air remained as a collected pocket located at the top of the crest, as the same volume of air was extracted at the end of each test as was inserted at the beginning. The number of spatial nodes occupied by the air pocket was calculated using its length (Fig. 2.4), and the volumes and spatial discretisation used meant that in all the numerical cases assessed the air pocket could be assumed to be concentrated at the node located at the crest section. The void ratio was assumed to be zero at all other spatial nodes. From this, an effective bulk modulus is calculated (Lee, 1991)

$$\frac{1}{K_T} = \frac{1}{K} + \frac{\varepsilon}{nP} + \frac{cD}{eE} \,, \tag{4.2}$$

where K_T = effective bulk modulus of the gas–liquid mixture; K = bulk modulus of the liquid; c = a constant defining the pipe constraint condition; e = pipe wall thickness; and E = modulus of elasticity of the pipe. The wave speed at a given node for a particular time-step was calculated as

$$a_{i,j} = \left[\rho(1-\varepsilon_{i,j})\frac{1}{K_T}\right]^{\frac{-1}{2}} \,, \tag{4.3}$$

where ρ = density of the liquid. The local wave speed calculated at each node was then included in the MOC characteristic equations in the following time-step. The variation in the wave speed with time is dependent on the pressure and the void ratio at the node, as all other terms will be constant for a given set of system conditions.

The variable wave speed model was found to be numerically unstable for all the experimental scenarios investigated, with numerical oscillation and the outputs eventually becoming complex. The reduced wave speed at the air pocket section meant that the Courant condition ($a\Delta t/\Delta x \leq 1$) was met everywhere in the numerical grid. Reducing the value of the Courant number below unity

had little effect on the stability of the results. The amplitudes of the numerical oscillations observed in the model outputs were of similar severity to those observed for a Courant number of 1, and began to affect the modelled pressure trace after a similar period of time. The overall stability of the model was affected by the air volume, the initial hydrostatic pressure, and the width of the input pulse. The stability improved for smaller air volumes, larger initial hydrostatic pressures, and wider input pulses. This is consistent with the investigations of Provoost (1976), which only achieved stability for $L_P^* \lesssim 0.008\%$. However, the smallest range of pocket volumes used ($L_P^* \approx 0.023\%$) represent a tiny obstruction, with smaller pocket volumes not expected to significantly impact pipeline operation. Furthermore, the range of pressures are consistent with what would be expected in a real pipeline. As a result, the model system conditions required to achieve stability correspond to situations which are unlikely to be relevant for transient-based condition assessment. These considerations mean that the variable wave speed model alone is not a valid modelling tool for the intended application.

4.2.3 Combined model

The approximation of the air pocket as a compressible volume or as a local change in wave speed did not result in a satisfactory match with experimental data when applied in isolation. In an effort to improve the accuracy of the predicted pressure trace, a combined model was developed. For each time-step of the accumulator model, the variable wave speed equations were used to calculate a local wave speed adjacent to the air pocket node based on the current void ratio, which was used in the MOC scheme upstream and downstream of the pocket. This extended the wave speed change imposed by the pocket across the characteristic steps on either side of the pocket. Although this is not strictly physical, as the air pocket represents a boundary condition in the model, it was anticipated that the inclusion may improve the accuracy of the pulse arrival time predicted by the model through the additional consideration of the air's compressibility.

Although the variable wave speed model was unstable by itself, the combination with the accumulator model (which will be referred to as the combined model) yielded stable results. Figures 4.1

and 4.2 show the pressure traces at PT2 and PT3 obtained from the combined model alongside the accumulator model and experimental data. Combining the accumulator model and variable wave speed model improved the pulse arrival times. For the two example pulses boxed, the combined model reduced the phase-delay error by approximately 31% and 43% respectively compared to the accumulator model alone. Similar to the accumulator model, the phase-delay error of the combined model, represented by an increased lag from the experimental data in later oscillation periods, increased with time, indicating that the use of a reduced wave speed at the air pocket location did not account for all the factors affecting the speed of the transient in the experimental system. Sensitivity testing showed that reducing or increasing the calculated wave speeds at the air pocket by up to 90% did not affect the phase-delay error by more than 1-2 numerical time steps. This is likely due to the fact that in the vicinity of the air pocket the calculated wave speed was less than 100 m/s, compared to the wave speed of 1348.5 m/s assumed for the rest of the pipe. As such, the relative size of adjustments to the wave speed at the air pocket is fairly negligible compared to the wave speed in other sections. Similar to the variable wave speed model, there is a degree of grid dependence associated with the combined approach, as the effects on pulse timing will be linked to the length of the reaches over which the reduced wave speed is applied. However, the MOC grid spacing is generally set such that each reach represents a very short distance relative to the total pipe length. As a result, minor adjustments to the grid spacing do not significantly affect the observed phase delay.

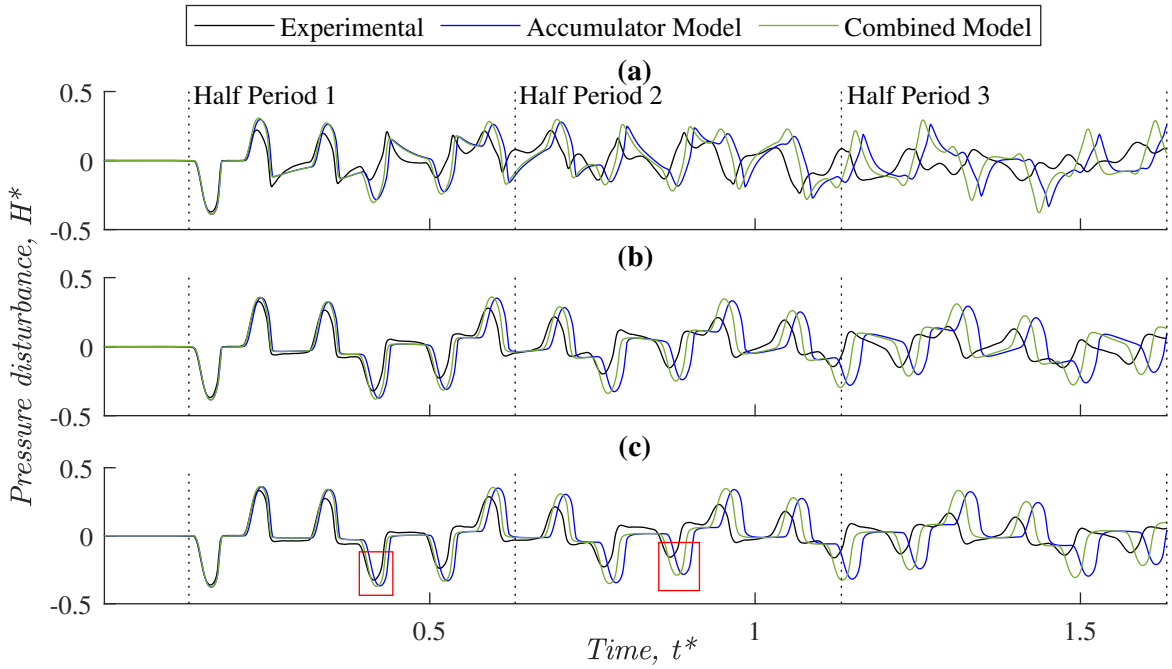

FIGURE 4.3: Experimental and modelled (MOC and the accumulator equation or combined model) transient pressure traces measured 8.29 m downstream of the transient generation point and 6.21 m upstream of the air pocket section at PT2 at an initial hydrostatic pressure of 3.0 bar for pocket sizes (a) L_P^* = 0.025%, (b) L_P^* = 0.041%, and (c) L_P^* = 0.053%. Half periods of the trace are marked with dotted lines. The pressure disturbance H is scaled by the initial hydrostatic pressure, the time t is scaled by the pipeline period, and L_P is scaled by the total pipe length. Examples of the peak time delay are marked.

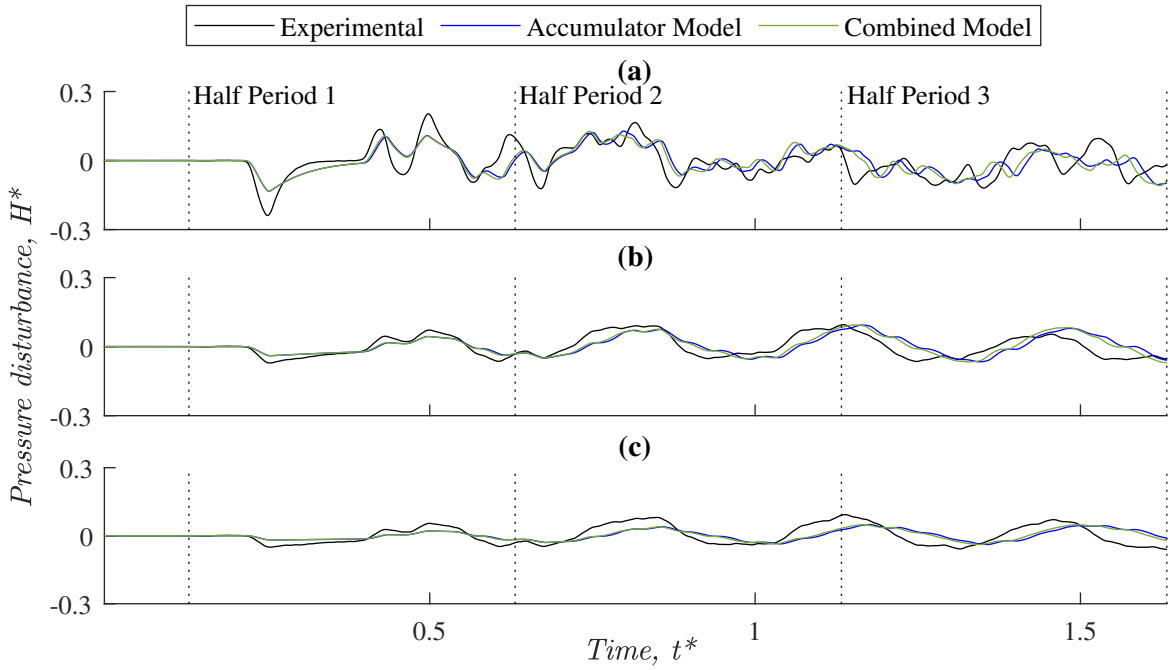

FIGURE 4.4: Experimental and modelled (MOC and the accumulator equation or combined model) transient pressure traces measured 6.30 m downstream of the air pocket section at PT3 at an initial hydrostatic pressure of 3.0 bar for pocket sizes (a) L_P^* = 0.025%, (b) L_P^* = 0.041%, and (c) L_P^* = 0.053%. Half periods of the trace are marked with dotted lines. The pressure disturbance H is scaled by the initial hydrostatic pressure, the time t is scaled by the pipeline period, and L_P is scaled by the total pipe length.

4.3 Model assessment

4.3.1 Residual errors

A comparison of the modelled and experimental pressure traces for the accumulator model and combined model showed that both are affected by phase-delay and amplitude errors. A quantification of these errors will provide an improved understanding of the models' current limitations. The modelled pressure disturbances can be plotted against the experimental pressure disturbances for the same time-step (referred to here as a comparison curve) to better visualise the types of errors which may occur so that they may be quantified. The errors were considered for each half-period of the transient event, to give an understanding of how errors accumulated over time.

Figure 4.5 shows the pressure trace measured and modelled at the transient generation source (PT1) and the corresponding comparison curve for an example of a relatively good model fit, where the model accurately predicts the amplitude and phase of the transient pressure disturbances. The plot of the modelled vs. experimental data forms a line with a 1:1 slope and little residual error around the 1:1 line.

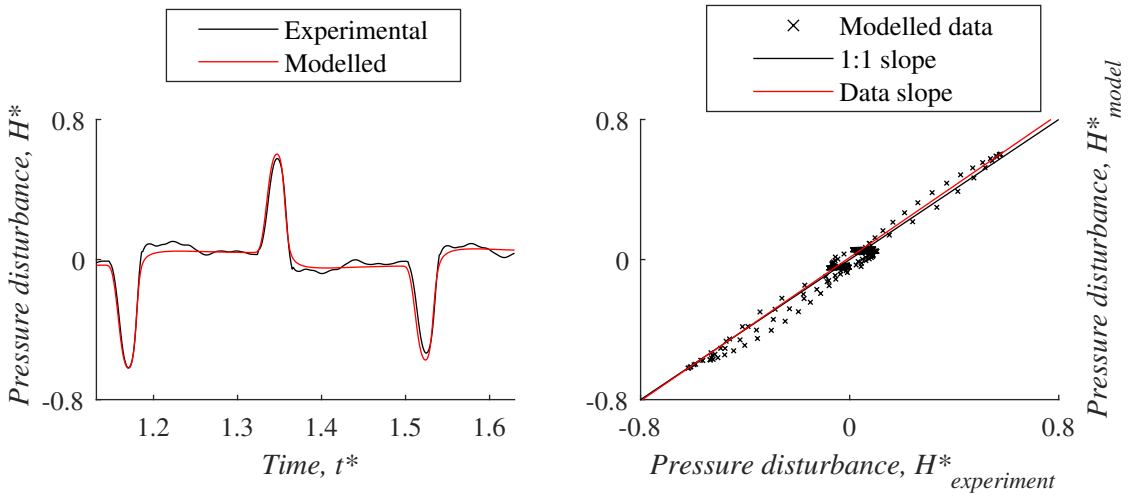

FIGURE 4.5: A demonstration of a relatively good model fit. The first plot shows experimental and modelled pressure traces over time measured at the transient generation point PT1 over one half period. The second plot plots the modelled and experimental data points for each time increment against each other. A line with 1:1 slope corresponding to a perfect model fit and the actual slope of the data are plotted. The pressure disturbances H are scaled by the initial hydrostatic pressure and the time t is scaled by the pipeline period.

Figure 4.6 shows the pressure traces measured at the transient generation source (PT1) and corresponding comparison curves for three commonly observed cases. In Fig. 4.6(a), there is little phase-delay but the model over-predicts the amplitude of the transient peaks. In Fig. 4.6(b) the model predicts the peak amplitudes more accurately, but there is a minor phase-delay which means there is only partial overlap of the pulses. The final case, shown in Fig. 4.6(c), again contains amplitude overestimation by the model, and the phase-delay is large enough that the modelled and experimental pulses do not overlap at all.

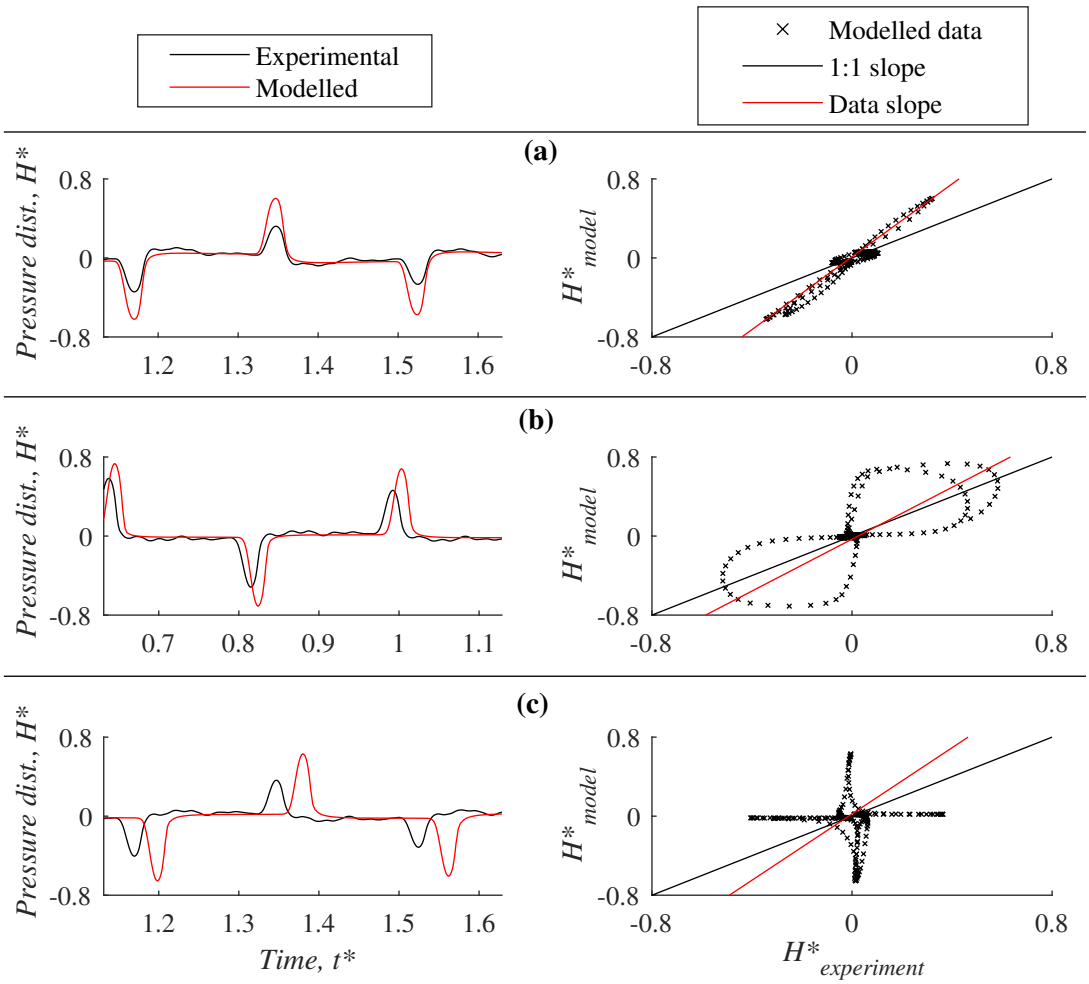

FIGURE 4.6: Example experimental and modelled pressure traces measured at the transient generation point PT1 plotted with time and against each other to demonstrate model fit for three common half period cases: (a) Model overestimates amplitude and pulses coincide, (b) Model overestimates amplitude and pulses partially overlap, (c) Model overestimates amplitude and pulses do not overlap

The primary sources of error in the modelled data are phase-delay and amplitude. As shown in Fig. 4.6, the two major variations observed in the comparison curves were the deviation in slope from the expected 1:1 relationship, and the spread of the data points around the expected straight line. For the case shown in Fig. 4.6(a), where error is primarily related to the amplitude, the slope of the comparison curve (referred to as the data slope) is steeper than the expected 1:1 slope. The spread of the data points around the marked data slope is relatively low. For the cases shown in Fig. 4.6(b) and Fig. 4.6(c), where there is a phase-delay error, the spread of the data points around the marked data slope increases, forming lobe patterns. These lobes are comparable to Lissajous

curves, which are used to describe complex harmonic motion. Lissajous curves are generated by plotting sinusoidal curves against each other, and the shape and angle of the resultant lobes are used to quantify differences in phase and amplitude. Though Lissajous curves are not directly translatable to the comparison curves produced by plotting the experimental and modelled transient traces against each other, the basic theory provides a useful starting point for characterising the suitability of the models for different scenarios. For instance, if the Lissajous curve is a straight line with a slope of 1, the signals are perfectly in phase, whereas if the Lissajous curve is a straight line with a slope of -1, the signals are perfectly out of phase. When the signals are misaligned, the response forms a circle. The properties of the comparison curves will be referred to here as Lissajous properties, obtained through the generalisation of the above concepts to non-sinusoidal signals.

The deviation in the data slope from the expected 1:1 relationship represents the loss in pulse amplitude that was not captured by the model. The data slope is marked in Fig. 4.6 as a red line linking the minimum modelled and experimental pressures to the maximum modelled and experimental pressures. The expected 1:1 relationship is marked as a black line. The amplitude error was calculated as

$$\epsilon_{amplitude} = \frac{H_{mod,max} - H_{mod,min}}{H_{exp,max} - H_{exp,min}} - 1 \ , \tag{4.4}$$

where H_{mod} = modelled pressure disturbance and H_{exp} = experimental pressure disturbance for the given half period. An amplitude error of 0 means the model accurately predicts the experimental pulse amplitudes, while an amplitude error greater than 0 means the model overestimates the pulse amplitudes for the given experimental scenario. For the three cases shown in Fig. 4.6, the amplitude errors were $\epsilon_{amplitude} = [1.84, 1.31, 1.68]$ respectively.

The residual error from a linear distribution represents the phase-delay error, and was quantified using the average absolute residual error between the data points and the data slope, marked on

Fig. 4.6 as a red line. The phase-delay error was scaled by the maximum absolute modelled pressure for each half period

$$\epsilon_{phase} = \frac{1}{|H|_{max,mod}} \frac{\sum_{i=1}^{n} |f(H_{i,mod}) - H_{i,mod}|}{n} , \tag{4.5}$$

where $|H|_{max,mod}$ = maximum absolute modelled pressure for each half period; f = straight line function for the data slope (marked in Fig. 4.6 as a red line); n = number of data points for the given half period; and $H_{i,mod}$ = pressure predicted by the model at each time-step i of the half period. The further the points are from the straight line linking the minimum and maximum pressure disturbances, the more out of phase the modelled data is with the experimental data. In the event that there is no phase delay, the error will be close to zero. For the three cases shown in Fig. 4.6, the phase-delay errors were $\epsilon_{phase} = [0.09, 0.14, 0.28]$ respectively.

4.3.2 Amplitude error

Figures 4.7 and 4.8 show the amplitude errors calculated for the first three half periods of each experimental case following the end of the valve movement for air pockets at initial hydrostatic pressures of 1.0 bar and 2.0 bar, respectively. The amplitude errors were calculated for the pressure trace measured at the transient generation point (PT1). A comparable trend was observed at the other sensors.

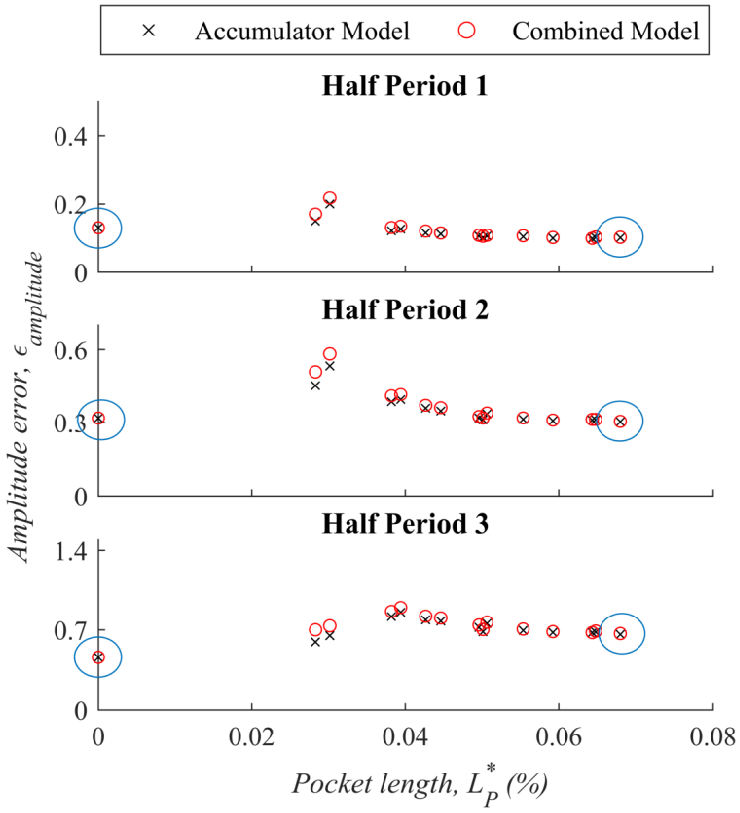

FIGURE 4.7: Calculated amplitude errors (Eq. 4.4) for the accumulator model and combined model compared to the experimental data for the first three half periods of each modelling approach at 1.0 bar initial hydrostatic pressure. The no-air case and levelling-off pocket size are circled. The air pocket length L_P is scaled by the total pipe length.

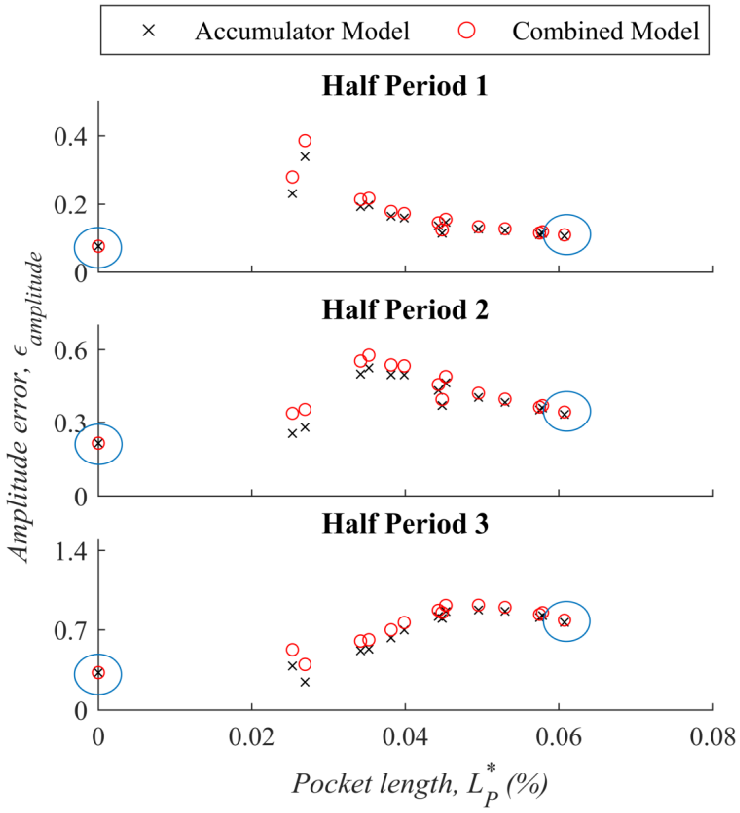

FIGURE 4.8: Calculated amplitude errors (Eq. 4.4) for the accumulator model and combined model compared to the experimental data for the first three half periods of each modelling approach at 2.0 bar initial hydrostatic pressure. The no-air case and levelling-off pocket size are circled. The air pocket length L_P is scaled by the total pipe length.

The two models performed similarly with regard to amplitude prediction. On average, $\epsilon_{amplitude}$ for the combined model is 1% higher than for the accumulator model in half phase 1, 2% higher in half phase 2, and 4% higher in half phase 3. The models were most accurate in predicting amplitude for the upper range of air volumes ($L_P^* \gtrsim 0.05\%$). The amplitude error decreased with increasing pocket volume, and then levelled off at a roughly constant value for $L_P^* \gtrsim 0.06\%$. The amplitude error at which the results levelled off consistently increased with each half period, by approximately 200% from half period 1 to half period 2, and 130% from half period 2 to half period 3. This indicates that the amplitude error is an ongoing effect. In general, the amplitude error increased with decreasing pocket volume, reaching a peak at around $L_P^* = 0.03\%$. This observation may be related to the theory that the smaller air pockets are dominated by accelerations introduced by

rapid mass oscillations, rather than the cushioning behavior described by the accumulator model, resulting in physical interactions which were not captured by the governing accumulator equation in its current form.

4.3.3 Phase-delay error

Figure 4.9 shows the phase-delay errors calculated for the first three half periods of each experimental case following the end of the valve movement for air pockets at a initial hydrostatic pressure of 2.0 bar. The phase-delay errors were calculated for the pressure trace measured at the transient generation point (PT1), and the errors for the no-air case are included for comparison purposes. A comparable trend was observed at the other sensors.

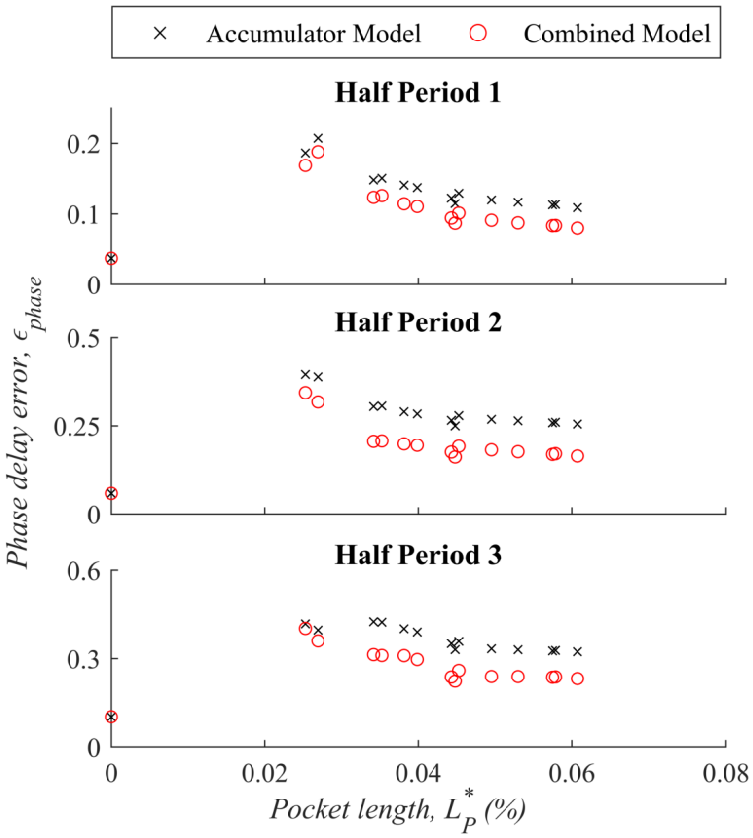

FIGURE 4.9: Calculated phase-delay errors (Eq. 4.5) for the accumulator model and combined model compared to the experimental data for the first three half periods of each modelling approach at 2.0 bar initial hydrostatic pressure. The no-air case and levelling-off pocket size are circled. The air pocket length L_P is scaled by the total pipe length.

The relatively small error ($\epsilon_{phase} < 0.15$) observed for the no-air case across the first three half phases was primarily attributable to minor differences in the pulse shape and experimental noise not predicted by the model, rather than a phase delay. The introduction of air resulted in an increase in the phase-delay error compared to the no-air case by a factor of up to 12 across the range of pocket volumes tested. On average, the phase-delay error for the accumulator model was 35% larger than for the combined model over the range of pocket volumes tested. This is in keeping with observations from the pressure traces (Figs. 4.3 and 4.4), where the accuracy of pulse arrival times was consistently improved through the inclusion of the variable wave speed component. Similar to the amplitude error, the pulse timing predictions for both models became more accurate with increasing pocket volume, and the phase-delay error levelled off at a roughly constant value for $L_P^* \gtrsim 0.05\%$ (approximately double the ϵ_{phase} observed for the no-air case). The implication is that both amplitude and phase error are a minimum once the air pocket size exceeds a certain threshold. The phase-delay error for a given volume increased with each consecutive half period, with the value at which the phase-delay error levelled off for the combined model increasing by approximately 75% between half period 1 and half period 2, and approximately 40% between half period 2 and half period 3. This is consistent with an error in the wave speed, at the location of the air or in the other reaches of the pipe.

The general trend in phase-delay error with pocket volume was consistent across the range of initial hydrostatic pressures used. Figure 4.10 shows the phase-delay error for the accumulator and combined models for a range of initial hydrostatic pressures. Regardless of the initial hydrostatic pressure, the phase-delay error levelled off at the same constant value observed in Fig. 4.9. Above a certain volume threshold, the accuracy of the modelling approaches was therefore independent of both the pocket volume and initial hydrostatic pressure.

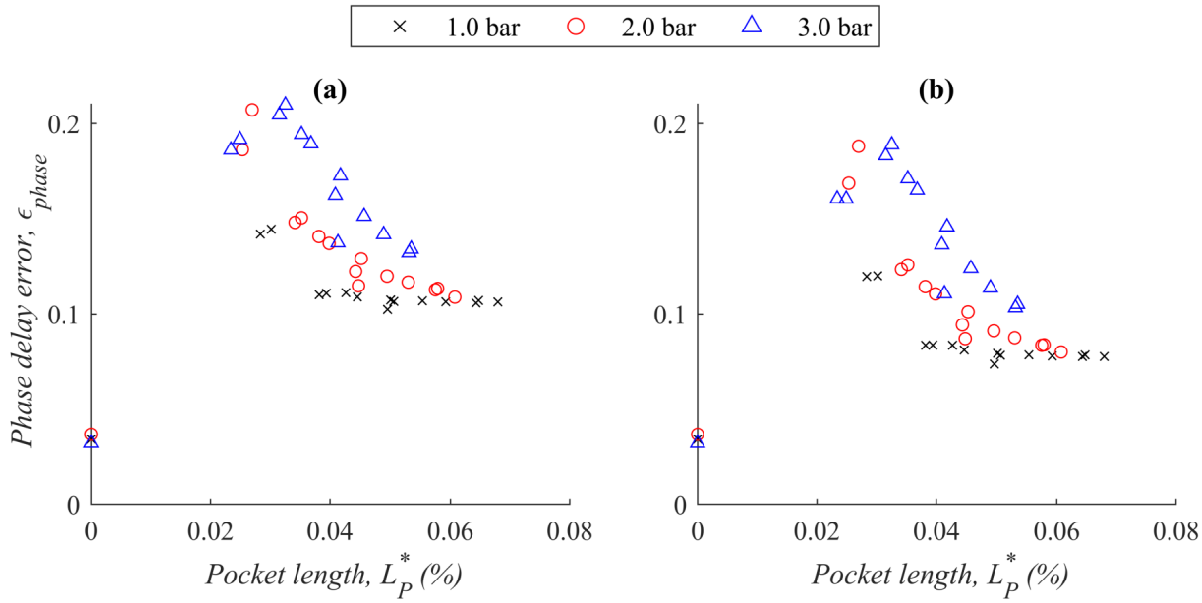

FIGURE 4.10: Calculated phase-delay errors (Eq. 4.5) for the first half period for a range of air pocket sizes at a range of initial hydrostatic pressures (1.0 bar, 2.0 bar, and 3.0 bar) for (a) the accumulator model and (b) the combined model. The air pocket length L_P is scaled by the total pipe length.

4.4 Conclusions and recommendations

This chapter presents a detailed investigation of our current capability for modelling and predicting the dynamics of an in-line air pocket, following Chapter 3 which presents the observations of the in-line air pocket behavior based on new experimental data (Alexander et al., 2020a).

The results obtained in the laboratory were compared to those from existing modelling approaches to assess the models' applicability to a real system. Modelling the pocket as a local accumulator was found to provide a reasonable match to the experimental data, with key shortcomings being the estimation of pulse amplitude and arrival time. A model incorporating the pocket as a local reduction in wave speed was found to be unstable for an in-line air pocket located at a single node.

Combining the accumulator model with the variable wave speed model (the combined model) provided an improved prediction of pulse arrival time. The amplitude and phase-delay errors identified for the accumulator model and combined model were quantified using Lissajous properties. The models were most accurate, in terms of predicting the pulse amplitude and timing, at dimensionless

air volumes in excess of $L_P^* \approx 0.05\%$. Amplitude and phase-delay errors generally reached a peak for the smallest range of pocket volumes tested ($L_P^* \lesssim 0.03\%$). The phase-delay error for the combined model was approximately 35% lower than the phase-delay error for the accumulator model, while the amplitude error was fairly similar between the two models. Both the phase-delay and amplitude error for a given in-pipe air volume increased as the transient progressed.

The investigation was limited by the breadth of the experimental work, with the potential for a greater set of experimental conditions to be investigated in the future. This could include the effects of additional increases or decreases in the air volume or initial hydrostatic pressure on the accuracy of the models. The tests were carried out without any base flow, and the introduction of flow may affect the air-transient interactions. The balance of buoyancy and drag can cause significant shearing and fragmentation over time, particularly in downward-sloping pipes, which requires consideration of the spatial and temporal variation in system elasticity and therefore the pipeline wave speed. The air may also be transported along the pipe with the flow. This would require an understanding of the rate of air movement relative to the system flow rate, and adjustment of the location of the air in the MOC grid accordingly. Theory used in existing two-phase flow models may also be considered.

Future investigations should include a detailed characterisation on how the amplitude and phase-delay errors observed may be overcome. The existing experimental data may be used to determine empirical adjustment factors to overcome the current errors, and determine whether these should be consistent over the duration of the transient or time-varying. Alternatively, different modelling approaches, such as an assessment in the frequency domain, may be investigated to determine whether this would offer greater accuracy.

5 Experimental investigation of the interaction of fluid transients with an off-line air pocket

5.1 Introduction

In this chapter, experimental data was used to investigate the transient transmission and reflection effects of off-line air pockets. The findings were compared to the in-line air pocket case discussed in Chapters 3 and 4. These two pocket configurations have different implications and removal strategies for network operators. This means it is advantageous to differentiate between the two cases as part of transient-based condition assessment. This chapter aims to identify and explain distinguishing features which define the off-line pocket response.

Due to the buoyancy of air, it often collects at high points in the system, either obstructing the main flow path (referred to as an "in-line" pocket), or in cavities beneath valves and hydrants ("off-line"). Similar to a solid blockage, in-line air pockets reduce the pipe cross-section at steady state, resulting in increased energy consumption and pumping cost. However, off-line air pockets do not pose the same risk. Being outside the main flow path, off-line pockets do not create a blockage and are therefore less likely to compromise the hydraulic operation of the system. To optimise the efficiency of network maintenance programs, techniques are needed to differentiate between the two cases in transient-based condition assessment.

Currently, little is known about the interaction of transients with off-line pockets or how this

compares to an in-line pocket. Experimental studies into the transient interaction with an air pocket in the main flow path have investigated the effects of base flow, pocket volume, and pocket profile for a range of scenarios. These include the effect of air trapped at the end of a dead-end pipe subject to a compression wave (Zhou et al., 2011; Vasconcelos and Leite, 2012; Hou et al., 2014; Zhou et al., 2018), the effect of air during the pipe emptying process (Coronado-Hernández et al., 2017; Fuertes-Miquel et al., 2019), and the effect of large air pockets entirely blocking the flow path (Zhou et al., 2013a). The degree of variability observed in the response for these scenarios indicate that the transient reflections created by air are in part dependent on its confining boundaries. These studies have primarily focused on predicting the influence of air on peak surge pressures caused by events such as pump shutdown, meaning transients were generated using long valve movement times relative to the pipe lengths used (in the order of 7-90 L/a). The resultant interference from system boundaries meant that specific features of the air pocket reflection and transmission could not be characterised. For the purposes of developing transient-based condition assessment methods, it is advantageous to isolate individual waves reflected and transmitted from the air to characterise the effects on the wave amplitude, timing and shape. This enables identification of effects unique to air and detailed evaluation of numerical models for the air-transient interaction. Wide-band signals are also required to identify the frequency-dependent behaviour specific to air pockets.

As noted above, previous transient-based studies regarding off-line collections of air have been most commonly focused on predicting air chamber dynamics. Air chambers utilise the cushioning properties of air for surge protection. Given this application, the focus has been on predicting peak surge pressures, and few experimental studies have focused on the case of smaller air pocket volumes in the order of 1-10 ml. The scope of this study is small air pocket volumes which may feasibly form in unwanted locations and disrupt system operations. Previous field and laboratory tests using small air pocket volumes have generated transients using pump shutdown or manual valve closure, and studied the influence of air volume and base flow on the maximum and minimum system pressure, cavity pressure, and cavity water level (Di Santo et al., 2002; Besharat et al.,

2016; Kim et al., 2014b). Bhattarai et al. (2019) noted that optimisation of the air chamber design process has largely focused on numerical analyses, meaning few experimental investigations have involved high-frequency transient testing of small off-line pockets. In one of the most applicable experimental studies, Kim (2008b) and Bergant et al. (2018) carried out high-frequency transient testing for the case where an off-line cavity is entirely filled with air and there is no separating water column between the main pipe and the air-water interface. The off-line pocket was found to reduce the local wave speed and create out-of-phase reflections. For this scenario, where the air pocket entirely fills the cavity and does not block the flow, a simple accumulator model (Wylie et al., 1993), with unsteady friction included, was able to accurately predict the response. For pockets which do not fill their cavity, the properties of the connecting fluid section may also be important (Kim, 2010). Subsequent high-frequency tests by Ferreira et al. (2018) using a small acrylic off-line cavity found that the off-line air introduces additional damping and can amplify transient pressures compared to the no-air case.

For the in-line pocket configuration, the area of comparison for this work is air pockets located in the middle of the pipe which do not obstruct the flow entirely. One of the most comparable experimental studies is that of Pozos-Estrada (2017), which investigated the transient interaction with large in-line air pockets followed by a hydraulic jump using a rapid solenoid movement, with the air found to reduce the transient amplitude and increase the transient period. In addition, Wan et al. (2017) described an experimental study to better understand the effect of in-line air pockets on flow dynamics and head losses at steady state. Previous work by Alexander et al. (2020a) (Chapter 3) for the in-line pocket scenario showed that the amplitude of the reflected wave could be accurately predicted using impedance theory, with larger pocket volumes resulting in increased reflectivity. The presence of in-line air also results in frequency dependent attenuation, with frequencies above the resonant frequency of the air being suppressed in the transmitted pulse.

This chapter aims to describe the effects of an off-line air pocket on transient reflection and transmission, with comparison to the in-line pocket case. Previous studies on air pocket dynamics have only focused on either one of the two types of pocket, with no studies directly comparing the

behaviour of in-line and off-line pockets within the same experimental system. Such comparisons will identify clear distinguishing features for air pocket classification and provide pipeline operators confidence in implementing invasive bleeding procedures in the case of an in-line air blockage. The tests for both configurations were carried out on the same experimental system, and the transients were generated using computer-controlled rapid valve movements. This follows experimental and numerical investigations for the in-line pocket configuration (Chapters 3 and 4).

5.2 Experimental procedure

The experimental methods for collecting the data used in this chapter are outlined in Chapter 2. The data collected for the off-line and in-line air pocket scenarios are used in this chapter. Nine off-line air pocket volumes were tested, ranging from 1.3 ml to 29.4 ml at atmospheric pressure (V_p = {1.3; 5.0; 8.9; 12.8; 17.1; 21.0; 23.8; 25.7; 29.4} ml). As noted previously, fourteen in-line air pocket volumes were tested, ranging from 2.9 ml to 40 ml at atmospheric pressure (V_p = {2.9; 3.5; 7.1; 7.8; 9.9; 11.3; 15.5; 16.0; 16.5; 21.6; 26.5; 33.9; 34.6; 40.0} ml). Each air pocket was subjected to transient tests at initial hydrostatic pressures ranging from 0.5 bar to 3.0 bar in increments of 0.5 bar. Note that the nomination of the upstream and downstream boundary referenced in this chapter are in relation to the origin point of the transient.

Only the pressurised air volumes which were fully contained by the off-line cavity were considered in these investigations, as the largest pocket volumes tested have shown that once the off-line pocket volume exceeds the size of the cavity its behaviour tends to that of a similarly sized in-line pocket. In the experiments, the air pocket volumes were measured outside the pipe at atmospheric pressure before and after each test using a measuring syringe. The pressurised volumes were calculated using the reversible polytropic equation (Chapter 2, Eqn. 2.7).

5.3 Time domain observations

5.3.1 Measured pressure traces

The experimental investigations involved the collection of pressure measurements upstream and downstream of the off-line and in-line air pockets, capturing both the reflected and transmitted waves. Figure 5.1 presents measured pressure traces for a range of in-line and off-line air pocket volumes to show the effect of air pocket volume on the response. Figure 5.2 presents measured pressure traces for a set of in-line and off-line pocket volumes with similar in-pipe volumes (within 5% of the average V_p quoted in the Figure caption) at a range of initial hydrostatic pressures, to show the effect of initial pressure on the response. The pressure traces presented have been normalised by the initial hydrostatic pressure such that $H^* = H/H_0$, where H is the measured pressure disturbance at any time and H_0 is the steady state initial hydrostatic pressure. The elapsed time t was normalised by the pipeline period $T = 4L/a$, such that $t^* = \frac{a}{4L}t$. The solenoid movement generating the transient commences at $t^* \approx 0.085$.

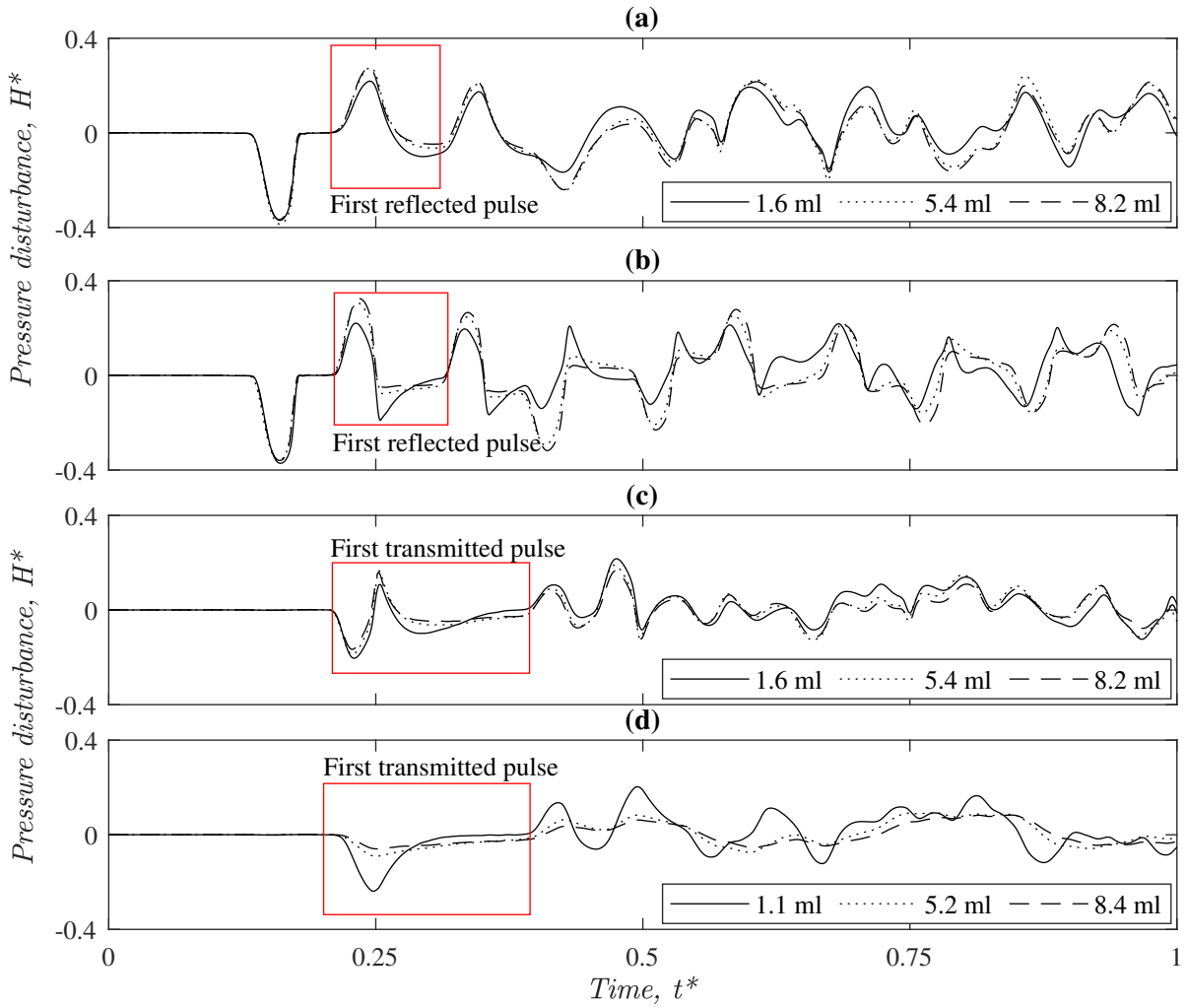

FIGURE 5.1: Experimental pressure disturbances for a range of in-line (1.6 ml, 5.4 ml, 8.2 ml) and off-line (1.1 ml, 5.2 ml, 8.4 ml) air pocket volumes at an initial hydrostatic pressure of 3.0 bar: (a) Off-line configuration trace measured at PT2, 8.29 m downstream of the transient generation point and 6.21 m upstream of the pocket, (b) In-line configuration trace measured at PT2, (c) Off-line configuration trace measured at PT3, 6.30 m downstream of the pocket, and (d) In-line configuration trace measured at PT3. The time t is scaled by the pipeline period and the pressure disturbance H is scaled by the initial hydrostatic pressure. The first pulses reflected and transmitted by the air pocket are boxed.

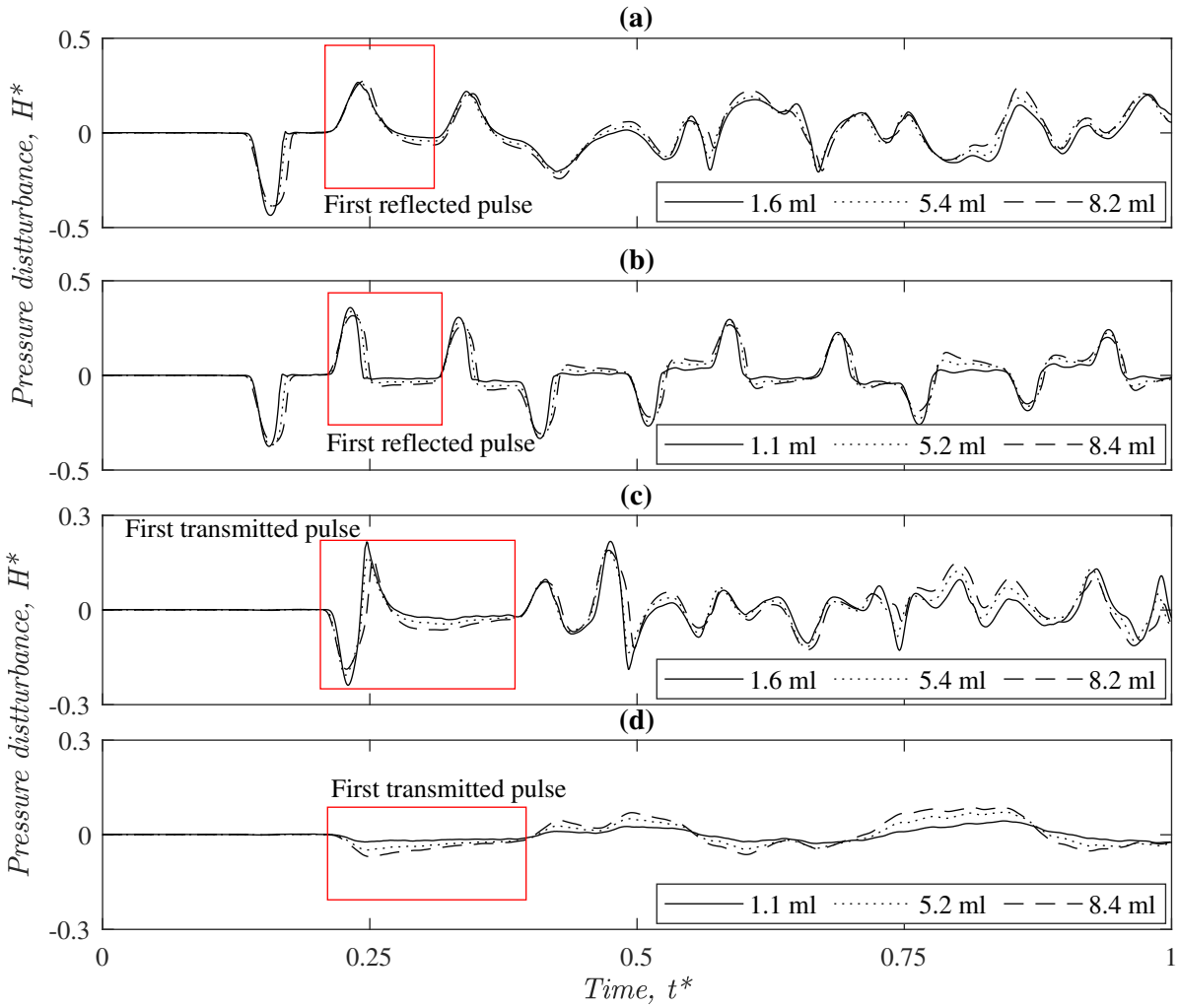

FIGURE 5.2: Experimental pressure disturbances for off-line ($V_p \approx 5.2$ ml) and in-line ($V_p \approx 6.6$ ml) air pockets at a range of initial hydrostatic pressures (1.0, 2.0, and 3.0 bar): (a) Off-line configuration trace measured at PT2, 8.29 m downstream of the transient generation point and 6.21 m upstream of the pocket, (b) In-line configuration trace measured at PT2, (c) Off-line configuration trace measured at PT3, 6.30 m downstream of the pocket, and (d) In-line configuration trace measured at PT3. The time t is scaled by the pipeline period and the pressure disturbance H is scaled by the initial hydrostatic pressure. The first pulses reflected and transmitted by the air pocket are boxed.

The first waves reflected and transmitted by the air pockets have been boxed and labelled in Figs. 5.1 and 5.2. The reflective power of the off-line air pocket increases with its size, and the off-line air pocket response also contains notable frequency-dependent effects, as the shape of the incident pulse is changed during reflection and transmission. Several key differences were observed between the two configurations, particularly with regard to the sharpness of the reflected and transmitted pulses.

This indicates that the in-line and off-line pockets have different frequency dependent effects. The pulses from both pocket types were followed by extended low-pressure tails. The sharpness of the transmitted pulse for the off-line configuration suggests that the majority of the incident pulse's high frequency content was transmitted. The converse was observed for the in-line configuration. These differing effects mean that as the transient progressed the shape of the pressure trace for the off-line pocket case varied significantly from that measured for the in-line pocket case. The frequency-dependent behaviour is explored in further detail in Section 5.4.

5.3.2 Governing processes

Numerical modelling can be used to explain the difference in transient shape observed for the in-line and off-line air pocket case. The simple accumulator model defined in Section 2.2.2 has previously been used to model the in-line pocket scenario, and it is able to capture the general shape of the transient response, albeit with timing and amplitude errors (Alexander et al., 2019) (Chapter 3). It has also been used in previous research to successfully model the off-line case where the air entirely fills the cavity and there is no connecting water column (Kim, 2008b). When the off-line pocket is separated from the main pipe by a short connecting section of fluid, friction and inertia in the connecting section may also be included. This is referred to as the lumped inertia model, which is described in Chapter 2. The lumped inertia model accounts for friction and inertia effects in the connecting section by assuming it is incompressible and inertia in the connector dominates the transient response.

The outputs of the simple accumulator and lumped inertia models are compared to the experimental observations upstream and downstream of the pocket section for the off-line air pocket in Figs. 5.3 and 5.4, which correspond to air pockets occupying 16% and 75% of the cavity respectively. The lumped inertia model predicted the response for the off-line case with much greater accuracy than the simple accumulator model across the range of volumes tested.

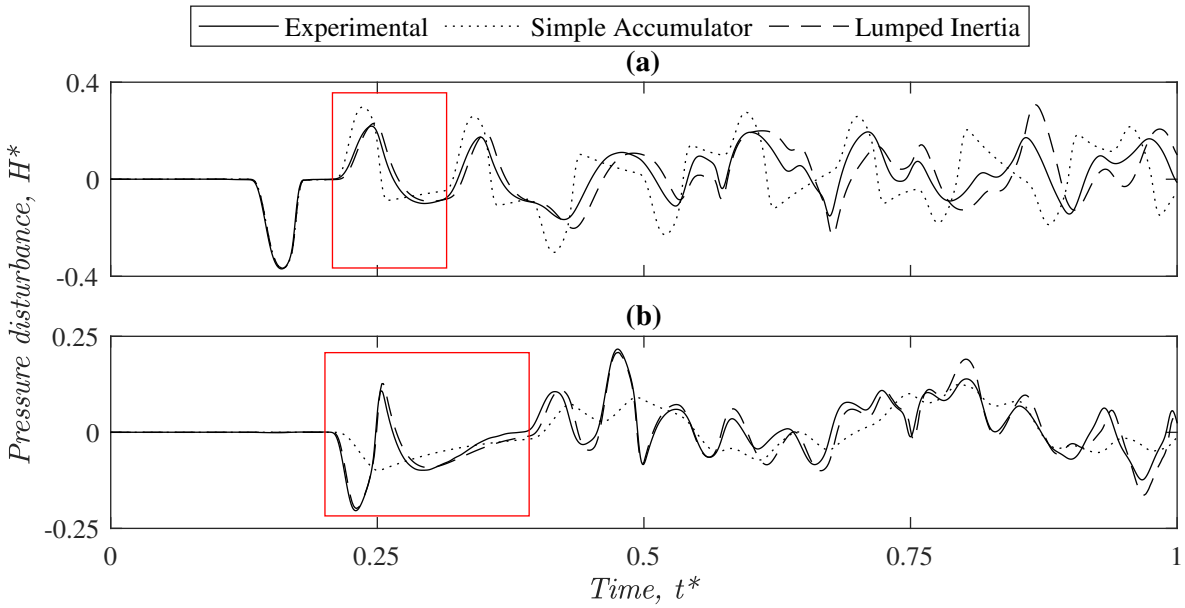

FIGURE 5.3: Experimental and modelled (MOC and air pocket equations, Chapter 2) transient pressure traces for an off-line air pocket (Volume V_p = 1.59 ml) at initial hydrostatic pressure 3.0 bar for (a) Pressure trace measured at PT2, 8.29 m downstream of the transient generation point and 6.21 m upstream of the pocket, and (b) Pressure trace measured at PT3, 6.30 m downstream of the pocket. The time t is scaled by the pipeline period and the pressure disturbance H is scaled by the initial hydrostatic pressure. The first reflected and transmitted pulses are boxed.

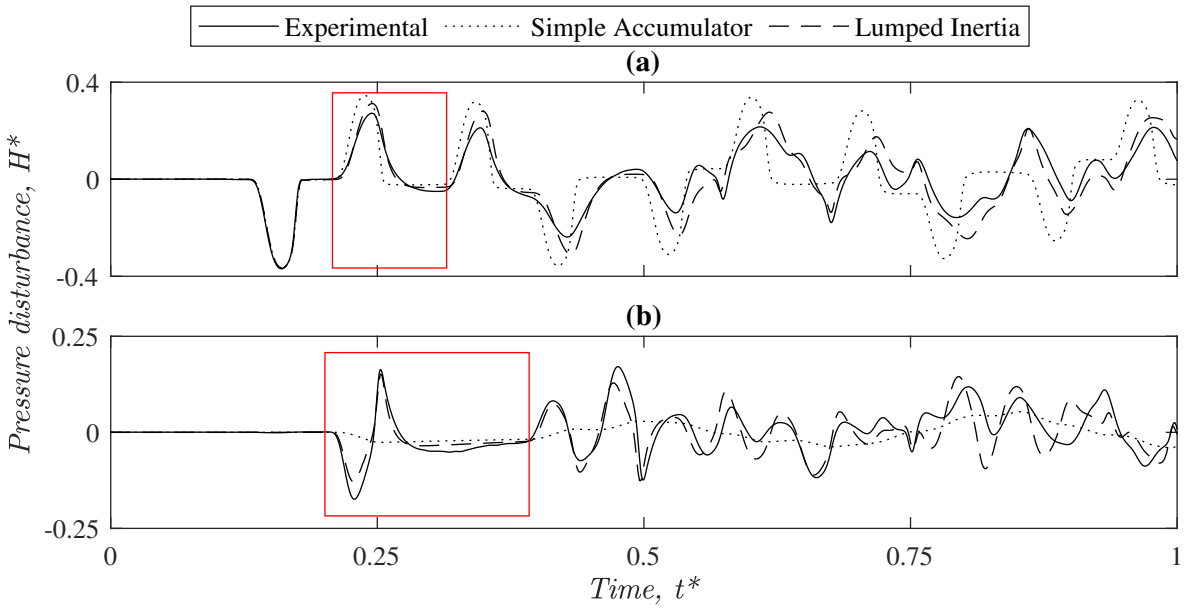

FIGURE 5.4: Experimental and modelled (MOC and air pocket equations, Chapter 2) transient pressure traces for an off-line air pocket (Volume V_p = 7.56 ml) at initial hydrostatic pressure 3.0 bar for (a) Pressure trace measured at PT2, 8.29 m downstream of the transient generation point and 6.21 m upstream of the pocket, and (b) Pressure trace measured at PT3, 6.30 m downstream of the pocket. The time t is scaled by the pipeline period and the pressure disturbance H is scaled by the initial hydrostatic pressure. The first reflected and transmitted pulses are boxed.

The results from modelling indicate that inertia in the cavity and connector was the primary cause of the differences in shape observed in the response due to air pocket configuration. Repetition of the lumped inertia modelling with inertia included, but without friction in the cavity and neck, resulted in a maximum difference of 3.9% in the modelled output for the first reflected and transmitted peaks. In the field off-line pockets may not entirely fill their confining cavity, such as those connecting hydrants to the main pipe, meaning the inertia effects identified represent a distinction between the two configurations in real-world applications. Key features captured by the lumped inertia model include the smoothing of the low-pressure tail following the reflected pulse, and the high frequency pressure fluctuations created during transmission.

5.3.3 Damping

The damping of the transient signal is expected to follow an exponential function (Wang et al., 2002). This can be fitted by obtaining the average transient amplitude in the time domain or the harmonic amplitude in the frequency domain for each period of the transient trace. For the time domain approach, the relationship may be expressed as

$$\frac{H_n}{H_0} = Be^{-kn}, \tag{5.1}$$

where H_n = average amplitude during the n^{th} period of the transient response; H_0 = initial hydrostatic pressure; B = a constant; and k = a constant representing the damping rate. B and k are obtained by fitting an exponential trend to a data series of H_n/H_0 and n.

The average amplitude per period in the time domain for the no-air case and example in-line and off-line pockets is shown in Fig. 5.5, along with the fitted exponential curve and 95% confidence intervals. The 95% confidence intervals included on Fig. 5.5 for the exponential fit show that damping may be subject to greater variability for the air pocket case. This may be attributable to the frequency dependent effects of air.

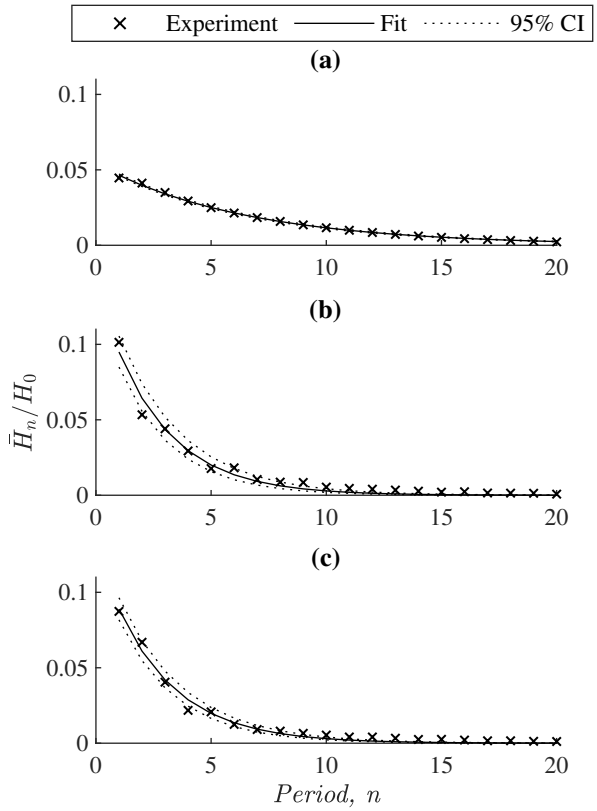

FIGURE 5.5: Average absolute amplitude (H_n) measured at the transient generation point PT1 per period relative to the initial hydrostatic pressure (H_0) for the (a) no-air case, (b) off-line pocket (Volume V_p = 5.43 ml) and (c) in-line pocket (Volume V_p = 5.24 ml), alongside exponential fits and 95% confidence intervals for each scenario.

Figure 5.6 shows the damping rate k obtained for a range of in-line and off-line pocket volumes, as well as the no air case. For the no-air case, the damping rate ranged between 0.13 and 0.19 for the experimental settings tested. Figure 5.6 shows that the presence of air significantly increased the damping rate. The damping rate increased to an average of 0.40 for the in-line air configuration, which was relatively consistent across the range of pocket volumes tested. Greater variation with pocket volume was evident for the off-line case, where the damping rate increased with pocket volume from 0.29 to 0.55 across the range tested.

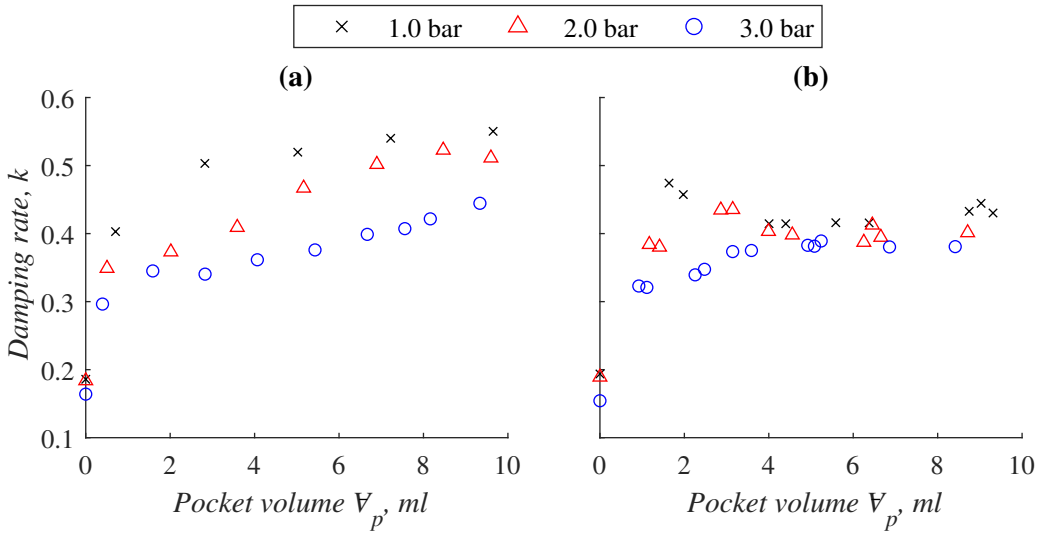

FIGURE 5.6: Damping rates estimated using Eq. 5.1 for (a) off-line pocket case and (b) in-line pocket case for a range of air pocket volumes and initial hydrostatic pressures (1.0, 2.0, and 3.0 bar).

5.4 Frequency domain observations

A discrete Fourier transform (DFT) can be used to quantify the frequency distribution of the incident, reflected, and transmitted pulses. The DFT was carried out on the entire pulse, meaning both the main peak and extended tails of the reflected and transmitted waves were included in the analysis. Figure 5.7 compares the DFT amplitudes of the frequencies contained in the incident and resultant pulses for in-line and off-line air volumes. The DFT amplitude was normalised by the initial hydrostatic pressure ($h^* = h/H_0$), while the frequency was normalised by the pipeline fundamental frequency ($\omega^* = \frac{4L}{a}\omega$).

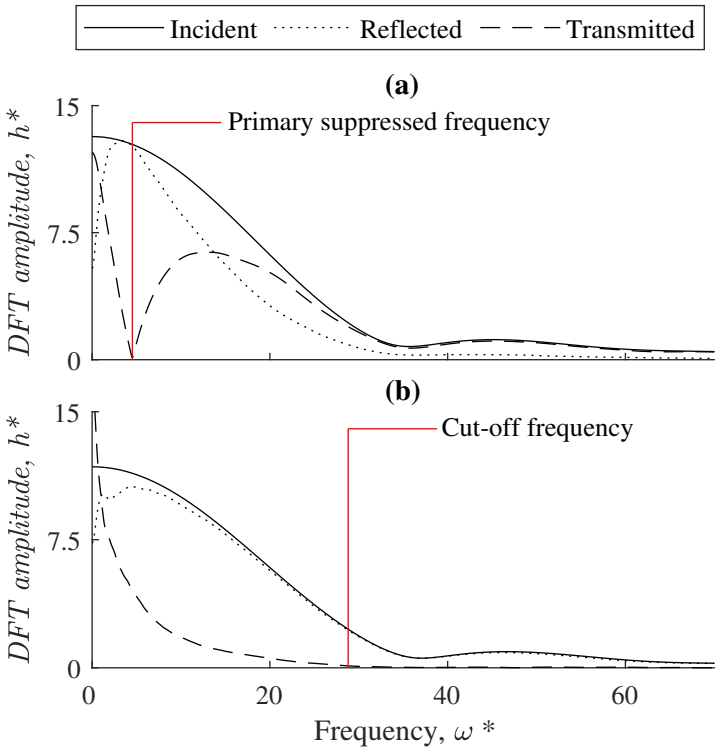

FIGURE 5.7: DFT amplitude of incident, reflected, and transmitted pulses at an initial hydrostatic pressure of 3.0 bar for (a) in-line air pocket (Volume V_p = 5.24 ml), and (b) off-line air pocket (Volume V_p = 5.43 ml). The incident and reflected pulses are measured at PT2 (8.29 m downstream of the transient generation point and 6.21 upstream of the air pocket section), and the transmitted pulse is measured at PT3 (6.30 m downstream of the air pocket section). The frequency ω is scaled by the inverse of the pipeline period and the DFT amplitude h is scaled by the initial hydrostatic pressure.

The general trends observed in Fig. 5.7 were consistent across the range of pocket volumes tested. The incident pulse contained frequencies ranging between $\omega^* = 0$ and $\omega^* = 70$. For the off-line pocket configuration, the DFT showed that the reflection contained a frequency band ranging between $\omega^* = 0$ and $\omega^* \approx 35$. The reflected DFT amplitude reached a peak, corresponding to a local minimum in the transmitted frequency distribution, at $\omega^* \approx 3$, though this value decreased with increasing pocket volume. The reasons for this trend are explored in the following paragraphs. The high frequency content outside this range was primarily transmitted. It has been observed in previous work for the in-line configuration that high frequency content ($\omega^* \gtrsim 20$) is primarily reflected by the pocket (Alexander et al., 2020a) (Chapter 3). For the in-line pocket, the cut-off frequency, marked in Fig. 5.7(a), was identified as a diagnostic tool. The cut-off frequency was

defined as the frequency where the transmitted DFT amplitude is first less than 5% of the incident DFT amplitude, and was found to increase with decreasing pocket volume in an approximately linear fashion.

The frequency dependent effects observed are unique to air pockets due to their compressibility; other common faults such as leaks and solid blockages do not impose such changes on the shape of the incident pulse (Brunone, 1999; Meniconi et al., 2011). A physical understanding of the frequency dependent effects of off-line pockets could be used to inform condition assessment techniques. The reflectivity of a pipeline anomaly such as the off-line air pocket is determined by its impedance relative to that of the main pipe, and previous research by Wylie (1964) states that impedance may be maximised at the resonant frequency of a system. In the medical field, theory has been developed to estimate the resonant frequency of air bubble within a blood vessel (Jang et al., 2009). The same principles may be able to predict the effects of off-line pockets in water supply infrastructure. The resonant frequency, ω, of an air pocket confined to a tube can be obtained from

$$\left(\frac{\omega}{\omega_0}\right)^2 = \frac{r_{cavity}^2}{4r_0}\left(\frac{1}{L_1 - \frac{L_p}{2} + \Delta L} + \frac{1}{L_2 - \frac{L_p}{2} + \Delta L}\right), \tag{5.2}$$

where r_{cavity} = radius of the confining cavity; r_0 = radius of the sphere which would be formed by the same pocket volume in an infinite fluid domain; L_1 and L_2 = length of pipe from the centre of the pocket to the end of the cavity in each direction; L_p = length of the pocket; and ΔL is an end correction factor given as $0.62r_{cavity}$, which accounts for the inertia of liquid outside the cavity (Jang et al., 2009). The end correction factor was determined theoretically by Levine and Schwinger (1948). The resonant frequency of the same pocket in an infinite fluid domain, ω_0, is calculated by

$$\omega_0 = \frac{1}{2\pi R_0}\sqrt{\frac{3nP_0}{\rho}}, \tag{5.3}$$

where n = polytropic exponent; P_0 = ambient pressure; and ρ = fluid density (Minnaert, 1933). The resonant frequency of the off-line air pocket therefore varies with its volume, pressure, and the dimensions of the cavity it is confined to.

Figure 5.8 shows the theoretical resonant frequencies for the range of experimental scenarios compared to the local minimum frequency of the transmitted pulse DFT, which will be referred to as the primary suppressed frequency (marked in Fig. 5.7(b)). In general, the theoretical resonant frequency agreed well with the primary suppressed frequency, supporting the hypothesis that the reflectivity of the pocket was maximised due to resonance. The average error between the theoretical and observed resonant frequencies was approximately 11%. Figure 5.9 shows that the experimental primary suppressed frequency also increased with initial hydrostatic pressure for a given in-pipe volume of air, in agreement with Eqn. 5.3. Similar to the time domain observations, the response of the pocket in the frequency domain was dependent on both the pocket volume and the cavity characteristics.

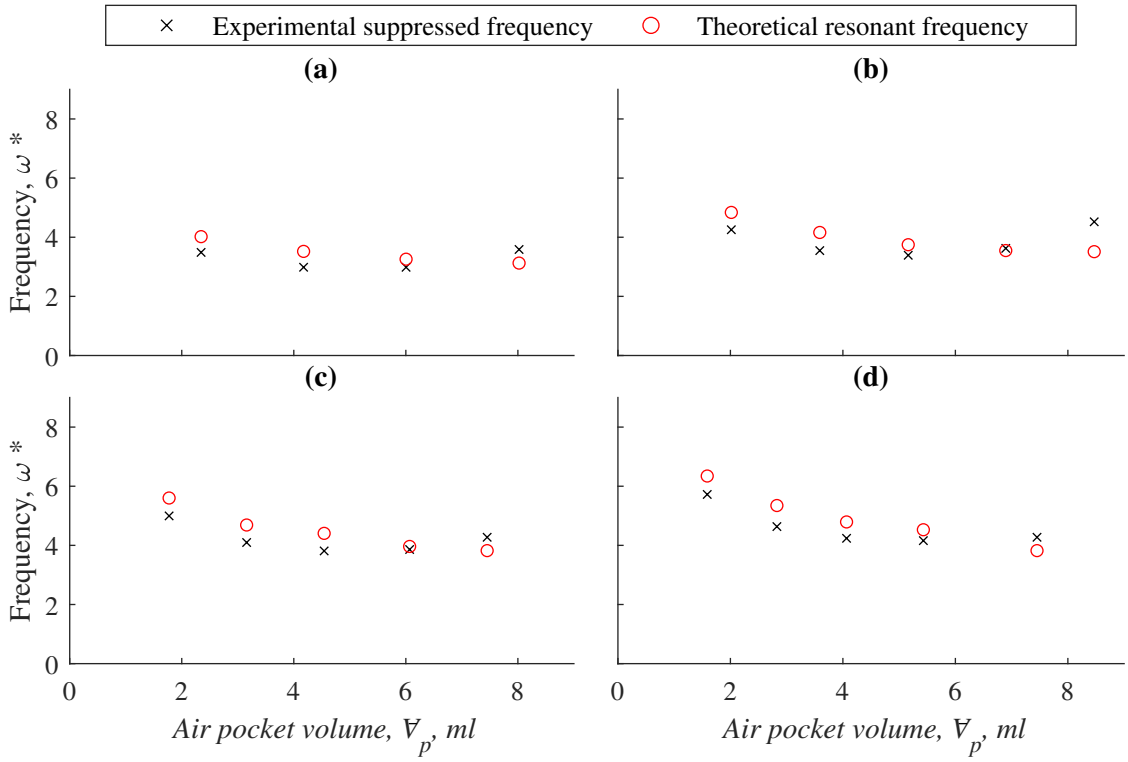

FIGURE 5.8: Comparison of the primary suppressed frequency observed in the experimental transmitted pulse DFTs measured at PT3 (6.30 m downstream of the air pocket section) with the theoretical resonant frequency estimated by Eq. 5.2 for off-line air pocket volumes at initial hydrostatic pressures of (a) 1.5 bar, (b) 2.0 bar, (c) 2.5 bar, and (d) 3.0 bar. The frequency is scaled by the inverse of the pipeline period.

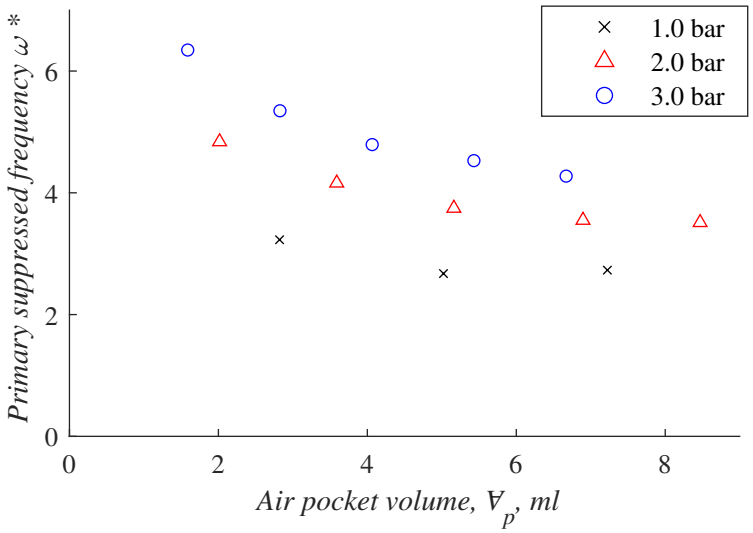

FIGURE 5.9: Primary suppressed frequency for a range of initial hydrostatic pressures.

A limitation of the application of Eqns. 5.2 and 5.3 in this situation is that the transient nature of the problem means that the pressure and volume of the pocket are constantly changing. However, modelling using the lumped inertia approach introduced previously suggested that the maximum variation in the resonant frequency due to transient effects was less than 2%, meaning that for these experiments the resonant frequency at steady state can be considered representative for the transient duration.

The frequency domain findings show that resonance behaviour may be used to differentiate in-line and off-line pockets. For the off-line pocket case, the theoretical equations for the resonant frequency may be used to estimate the pocket volume with a reasonable degree of confidence, if the cavity dimensions and applied pressure are known. The features unique to the in-line and off-line pockets may be used to obtain conclusive diagnoses as part of transient-based condition assessment.

5.5 Conclusions and recommendations

This chapter uses experimental data to characterise the effects of off-line air on the reflection and transmission of a high-frequency transient signal. The observations were compared to findings for

similarly sized in-line air pockets to identify the influence of air pocket configuration on the transient response. The results can be used in transient detection programs to differentiate in-line pockets which are blocking the main flow from off-line pockets which do not obstruct flow, improving the efficiency of network maintenance operations.

Numerical modelling showed that the transient response observed for the off-line pocket case in the time-domain was influenced by inertia in the water column connecting the off-line pocket to the main pipe, meaning that both the pocket volume and the cavity characteristics influenced the transient response. Further analysis in the frequency domain was used to quantify the frequency dependent effects of off-line air pockets. It was found that the reflectivity of the off-line pocket is maximised at the resonant frequency of the air pocket, with good agreement observed between theoretical and experimental results. Meanwhile, in-line air may be characterised using a cut-off frequency, above which signal content is reflected. The observations in the frequency domain have identified a useful approach for differentiating between the two pocket configurations during transient detection. The defining DFT features (the cut-off frequency and the primary suppressed frequency) are simple to distinguish and may also be used to characterise the pocket size. This will enable maintenance resources to focus on potentially more significant in-line air blockages. This further emphasises the need for high frequency wave testing, as the input signal must contain the frequency range needed to identify these features. The transient damping rate may also be used to diagnose air as a preliminary step.

This component of the study was limited by the breadth of experimental conditions considered, with the potential for other scenarios to be investigated in the future. The tests were carried out without any base flow, which may affect the geometry of the in-line pocket due to its location in the main flow path. This study also only considered pockets which were entirely in-line or off-line. However, in the field pockets may form in off-line cavities and become large enough to intrude into the main flow path. Further testing would provide greater understanding of whether it is possible to diagnose this case.

6 Comparison of numerical models for the interaction of a fluid transient with an off-line air pocket

6.1 Introduction

The previous chapter explored the key features of the transient response to an off-line air pocket. It is also important be able to model how off-line pockets may distort transient signals in the time and frequency domains, as it may be necessary to build numerical network models to explain transient responses observed in the field. As observed in Chapter 5, off-line air pockets may not obstruct the flow, but even small collections can create significant transient reflections and frequency dependent effects which distort the expected response. This chapter explores the available modelling approaches for off-line pockets.

A number of methods exist for modelling fluid transients in the time domain, including the Method of Characteristics (MOC), explicit and implicit finite difference methods, finite element techniques, and the Lagrangian wave characteristic model (Wood et al., 2005). Of these, the MOC, a finite difference method, is the most well known and widely researched, as it provides accurate results with relative computational efficiency and ease of programming (Chaudhry, 1979). Pipeline anomalies, like off-line air pockets, can be incorporated as boundary conditions. Off-line air pockets, or air chambers, are most commonly incorporated into the MOC using the simple accumulator equation

(Wylie et al., 1993), which is defined in Chapter 2. The accumulator equation has been previously used successfully as part of large-scale field investigations for the in-line pocket application (Burrows and Qiu, 1995; Stephens et al., 2004b). For off-line pockets which entirely fill their cavity, with no connecting water column, experimental tests using high frequency transients found that the accumulator equation alone was able to provide an accurate prediction of the magnitude, shape and timing of the overall pressure trace (Bergant et al., 2018). However, in many cases off-line pockets do not entirely fill their confining cavity, and are connected to the main flow by a short water column. Experimental and field investigations have noted that the dimensions of the connecting section influence the transient response, especially when it is throttled (Wylie et al., 1993; De Martino and Fontana, 2012). Early studies on air chamber design used a local loss coefficient for the throttled section (Evans and Crawford, 1954; Fok, 1978; Purcell, 1997), which was later deemed to be an unrealistic assumption and no longer justifiable due to the availability of computing power, as in reality hydraulic losses will also occur in the connecting pipeline section separating the water-air interface and the main pipe (Graze and Forrest, 1974). This resulted in the development of the lumped inertia model, which accounts for friction and inertia effects in the connecting section by assuming it is incompressible and inertia in the connector dominates the transient response (Graze and Forrest, 1974; Wylie et al., 1993). Zhou et al. (2013b) and Zhou et al. (2018) have also noted that heat exchange can be important when predicting energy dissipation due to the air-transient interaction. The lumped inertia assumption has not previously been tested against a 1D model without simplifying assumptions. This may be attributable to one of the key drawbacks of the MOC as a solution scheme: that its efficiency is affected by the number of nodes (Duan et al., 2018), and the discretisation required to accurately model short connectors would significantly increase computational costs.

Alternatively, the system response to transient events may be modelled in the frequency domain, using transfer matrices to linearise the frequency domain equivalents of the governing 1D mass and momentum equations. The system frequency response (SFR) approach has become more popular in recent years for pipeline condition assessment via inverse analysis, as short pipe defects can

be efficiently incorporated into the model without increasing the computational effort (Lee et al., 2013; Duan and Lee, 2016). Frequency domain modelling also allows increased flexibility over time domain modelling in that transient generators and receivers can be placed at any location, and are not limited by the MOC discretisation. Although the theory for modelling off-line air pockets in the frequency domain is shown in Wylie et al. (1993), air pockets have not been incorporated into the SFR approach in the condition assessment field to date. Similar to the MOC approach in the time domain, the governing equations are based on the lumped inertia assumption, and the effect of this assumption on the model accuracy has not been evaluated.

The purpose of this chapter is to use experimental results collected for the off-line pocket case to test the lumped inertia assumption for modelling the reflection and transmission of a high frequency transient past an off-line air pocket. The governing equations have not previously been validated for experiments of this nature. Three modelling approaches will be tested: the MOC with lumped inertia (MOC-LI), the SFR approach with lumped inertia (SFR-LI), and an SFR approach employing plane wave theory which does not make a lumped inertia assumption (SFR-PW). An SFR method was selected to model the off-line air pocket without the lumped inertia assumption due to its efficiency compared to the MOC, as discussed previously. The results can be incorporated into transient fault detection techniques to account for the effects of off-line air on the transient response.

6.2 Numerical modelling

6.2.1 Method of characteristics - Lumped inertia model

The MOC approach and associated lumped inertia equations for the off-line pocket boundary are outlined in Chapter 2.

The modelling was implemented with 308 spatial nodes and the time step was set to match the experimental time step. This was compliant with the Courant stability condition. Sensitivity testing carried out for the MOC discretisation showed that further increases in the number of spatial nodes

used did not result in significant differences in the modelled pressure traces over the time period of interest (the first reflected and transmitted pulses). For instance, increasing the spatial discretisation from 308 nodes to 1000 nodes resulted in an average variation of 0.004% in the modelled pressures.

6.2.2 System frequency response: Lumped inertia model

In the frequency domain, concatenated transfer matrices are used to represent adjacent pipeline elements. The transfer matrix is a linearised frequency domain version of the governing mass and momentum equations for 1D flow. For the experimental pipe system consisting of pipe elements connected in series, the general form of the transfer matrix equation is (Chaudhry, 1979)

$$\begin{Bmatrix} q \\ h \\ 1 \end{Bmatrix}^{1} = \boldsymbol{P_0 A_0 P_1 G_0} \begin{Bmatrix} q \\ h \\ 1 \end{Bmatrix}^{0} \tag{6.1}$$

where $\boldsymbol{P_0}$, $\boldsymbol{A_0}$, $\boldsymbol{P_1}$, and $\boldsymbol{G_0}$ are the transfer matrices for the pipe section between the downstream tank and the off-line pocket, the off-line pocket section, the pipe section between the off-line pocket and the solenoid, and the solenoid transient generator, respectively. These link the perturbations in head h and discharge q at the closed upstream valve (superscript 0), to those at the downstream boundary (superscript 1). The extended 3×1 form is used to account for elements with external forcing.

The transfer matrix for the intact pipe section is given by (Wylie et al., 1993)

$$\boldsymbol{P_n} = \begin{bmatrix} \cosh(\mu L) & -\frac{1}{Z_c}\sinh(\mu L) & 0 \\ -Z_c \sinh(\mu L) & \cosh(\mu L) & 0 \\ 0 & 0 & 1 \end{bmatrix} \tag{6.2}$$

where L = pipe section length; $\mu = (\omega/a)\sqrt{1 - igAR/\omega}$; $Z_c = \mu a^2/i\omega gA$; ω = frequency; a = wave speed; A = pipe cross-sectional area; g = gravitational acceleration; and i = imaginary unit. The subscript n used in Eqs. 6.2-6.4 refers to the index of the pipe element for which the transfer matrix is calculated. The friction term R is the summation of steady (R_S) and unsteady (R_U) terms. The steady friction term is $R_S = fQ/gDA^2$, where f = friction factor and D = pipe diameter. The experimental system has zero base flow and therefore exists in the laminar flow region, so the unsteady term was calculated using the integral solutions for Zielke's weighting function in the frequency domain, provided by Vítkovskỳ et al. (2003a).

For the system frequency response with lumped inertia (SFR-LI), the off-line cavity represents a junction with the extended transfer matrix (Wylie et al., 1993)

$$\boldsymbol{A_n} = \begin{bmatrix} 1 & \frac{1}{Z_A} & 0 \\ 0 & 1 & 0 \\ 0 & 0 & 1 \end{bmatrix} \tag{6.3}$$

where Z_A is the impedance of the off-line cavity adjacent to the main pipe. Using the lumped inertia assumption, the impedance of an air pocket is given by $Z_a = in\bar{H}_A/\forall_p\omega$, where $\bar{H}_A$ = absolute head at the pocket; n = polytropic exponent; and $\forall_p$ = air pocket volume. This can be adjusted to the impedance for the overall air chamber, including the connecting sections, using $Z_A = Z_a - (R_c + i\omega/gA_c)l_c - (R_n + i\omega/gA_n)l_n$, where R_c and R_n = resistances associated with the cavity and neck; A_c and A_n = cross-sectional areas of the cavity and neck; and l_c and l_n = lengths of the cavity and neck.The resistance term is defined as $R = 32\nu/gAD^2$, where ν = kinematic viscosity and D = the diameter of the cavity or neck (Wylie et al., 1993).

For a unit perturbation, the transfer matrix for the transient generator is given by

$$\boldsymbol{G_n} = \begin{bmatrix} 1 & 0 & 1 \\ 0 & 1 & 0 \\ 0 & 0 & 1 \end{bmatrix} \tag{6.4}$$

Multiplying the field matrices for each element results in a 3×3 universal matrix U describing the system. Expanding Eq. 6.1 therefore gives

$$q^1 = U_{11}q^0 + U_{12}h^0 + U_{13} \tag{6.5}$$

$$h^1 = U_{21}q^0 + U_{22}h^0 + U_{23} \tag{6.6}$$

where U_{ij} are the system matrix elements. For the experimental system, the boundary conditions are $q^0 = h^1 = 0$, meaning the head response at the closed valve is given by $h^0 = -U_{23}/U_{22}$. Once h^0 is known it can be used to calculate the system response h^1 at any receiver in the system using Eq. 6.6 and the relevant transfer matrix U based on the pipe elements between the closed valve and the receiver. The actual response is obtained by multiplying h^1 by the spectra of the input pressure disturbance of the solenoid. The input spectra is the Fourier transform of the time domain head disturbance.

6.2.3 System frequency response: Plane wave model

The same approach as defined in the previous section for the system frequency response is used in the SFR-PW model. However, the plane wave assumption is used to derive the transfer matrix for the off-line air pocket section ($\mathbf{A_0}$). This derivation assumes that the cavity and neck section of the off-line section are compressible, without the simplification of lumped inertia. The plane wave is a case which applies when physical quantities, in this case pressure and velocity, are constant across the plane perpendicular to the direction of movement (Kinsler et al., 2000). The assumption was

used here as the pressure and velocity variation across the cross-section is small compared to the longitudinal variation along the pipe length.

A schematic of the offline pocket system is shown in Fig. 6.1. The off-line air pocket system is composed of a main pipeline, a neck connecting to the cavity, a cavity filled with water, and an air pocket entrapped at the top of the cavity. These four regions are denoted with superscripts p, c, a, and n to distinguish physical parameters in different regions. The subscripts in, rf, and tr represent incident, reflected, and transmitted waves.

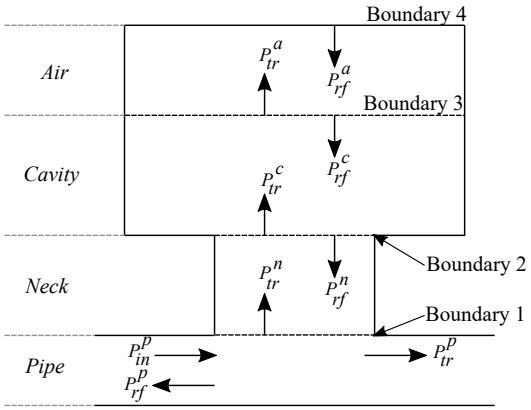

FIGURE 6.1: Schematic for off-line cavity governing transfer matrix equations

At the four boundaries in the system, head (H) and flow (Q) must satisfy continuity boundary conditions. Assuming that the waves considered have a wavelength much larger than the neck diameter, the boundary conditions are given below.

Boundary 1:

$$H_{in}^{p} + H_{rf}^{p} = H_{tr}^{p} = H_{tr}^{n} + H_{rf}^{n} \tag{6.7}$$

$$Q_{in}^{p} - Q_{rf}^{p} = Q_{tr}^{p} + Q_{tr}^{n} - Q_{rf}^{n} \tag{6.8}$$

Boundary 2:

$$H_{tr}^{n} + H_{rf}^{n} = H_{tr}^{c} + H_{rf}^{c} \tag{6.9}$$

$$Q_{tr}^{n} - Q_{rf}^{n} = Q_{tr}^{c} - Q_{rf}^{c} \tag{6.10}$$

Boundary 3:

$$H_{tr}^{c} + H_{rf}^{c} = H_{tr}^{a} + H_{rf}^{a} \tag{6.11}$$

$$Q_{tr}^{c} - Q_{rf}^{c} = Q_{tr}^{a} - Q_{rf}^{a} \tag{6.12}$$

Boundary 4:

$$Q_{tr}^{a} = Q_{rf}^{a} \tag{6.13}$$

If the amplitude of the incident wave (H_{in}^{p}) is normalised to 1, under the plane wave assumption the amplitude of the reflected and transmitted waves correspond to reflection and transmission coefficients (denoted as R and T) in each region. Considering the relationship $Q = HA/\rho a$, where a = wave speed in each region; A = cross-sectional area of each region; ρ = density; and the pipeline impedance $Z = \rho a/A$ in each region, Eqs. 6.7-6.13 can be rewritten as

$$1 + R^p_{rf} = T^p_{tr} = T^n_{tr} + R^n_{rf} e^{ik^n L^n} \tag{6.14}$$

$$\frac{1}{Z^p}(1 - R^p_{rf}) = \frac{1}{Z^p} T^p_{tr} + \frac{1}{Z^n}(T^n_{tr} - R^n_{rf} e^{ik^n L^n}) \tag{6.15}$$

$$T^n_{tr} e^{ik^n L^n} + R^n_{rf} = T^c_{tr} + R^c_{rf} e^{ik^c L^c} \tag{6.16}$$

$$\frac{1}{Z^n}(T^n_{tr} e^{ik^n L^n} - R^n_{rf}) = \frac{1}{Z^c}(T^c_{tr} - R^c_{rf} e^{ik^c L^c}) \tag{6.17}$$

$$T^c_{tr} e^{ik^c L^c} + R^c_{rf} = T^a_{tr} + R^a_{rf} e^{ik^a L^a} \tag{6.18}$$

$$\frac{1}{Z^c}(T^c_{tr} e^{ik^c L^c} - R^c_{rf}) = \frac{1}{Z^a}(T^a_{tr} - R^a_{rf} e^{ik^a L^a}) \tag{6.19}$$

$$\frac{1}{Z^a} T^a_{tr} = \frac{1}{Z^a} R^a_{rf} e^{ik^a L^a} \tag{6.20}$$

where L = region length and $k = \omega/a$. The off-line pocket system behaves as a two-port network, with the reflection and transmission coefficients forming a scattering matrix (Orfanidis, 2002)

$$S = \begin{bmatrix} S_{11} & S_{12} \\ S_{21} & S_{22} \end{bmatrix} = \begin{bmatrix} R^p_{rf} & T^p_{tr} \\ T^p_{tr} & R^p_{rf} \end{bmatrix} \tag{6.21}$$

This can be converted to a transfer matrix T for the off-line pocket system with the following elements (Martin, 2015)

$$T_{11} = \frac{(1 - S_{11})(1 + S_{22}) + S_{12}S_{21}}{2S_{21}} \tag{6.22}$$

$$T_{12} = Z^p \frac{(1 - S_{11})(1 - S_{22}) - S_{12}S_{21}}{2S_{21}} \tag{6.23}$$

$$T_{21} = \frac{1}{Z^p} \frac{(1 + S_{11})(1 + S_{22}) - S_{12}S_{21}}{2S_{21}} \tag{6.24}$$

$$T_{22} = \frac{(1 + S_{11})(1 - S_{22}) + S_{12}S_{21}}{2S_{21}} \tag{6.25}$$

The extended form of the transfer matrix for the off-line air pocket is therefore

$$\boldsymbol{A_n} = \begin{bmatrix} T_{11} & T_{12} & 0 \\ T_{21} & T_{22} & 0 \\ 0 & 0 & 1 \end{bmatrix} \tag{6.26}$$

6.3 Results

6.3.1 Model outputs

The outputs of the three models were compared to experimental data collected for the off-line pocket case, described in Chapter 2. Only the pressurised air volumes which were fully contained by the off-line cavity were considered in these investigations. The pressurised volumes are calculated using the reversible polytropic equation (Chapter 2, Eqn. 2.7).

The outputs of the three models (MOC-LI, SFR-LI, SFR-PW) are plotted in the time domain to show the performance of the models in predicting the first reflected and transmitted pulses from the off-line air pocket. Figures 6.2 and 6.3 compare the modelled and measured pressure traces on either side of the air pocket for three representative pocket volumes. Time t was normalised by the pipeline period ($t^* = \frac{a}{4L}t$), while the pressure disturbance H was normalised by the initial hydrostatic pressure H_0 ($H^* = H/H_0$). The pressurised volume of the off-line air pocket was converted to a length ($L_a = \forall/A_{cavity}$) and normalised by the length of the cavity ($L_a^* = L_a/L_{cavity}$). The first pulses reflected and transmitted by the air pocket are boxed in Figs. 6.2 and 6.3, respectively. All three models were able to predict the general shape of the first reflected and transmitted pulses, capturing the pressure peaks and following low-pressure tails, with some discrepancy in the amplitude, shape, and timing of the pressure disturbances.

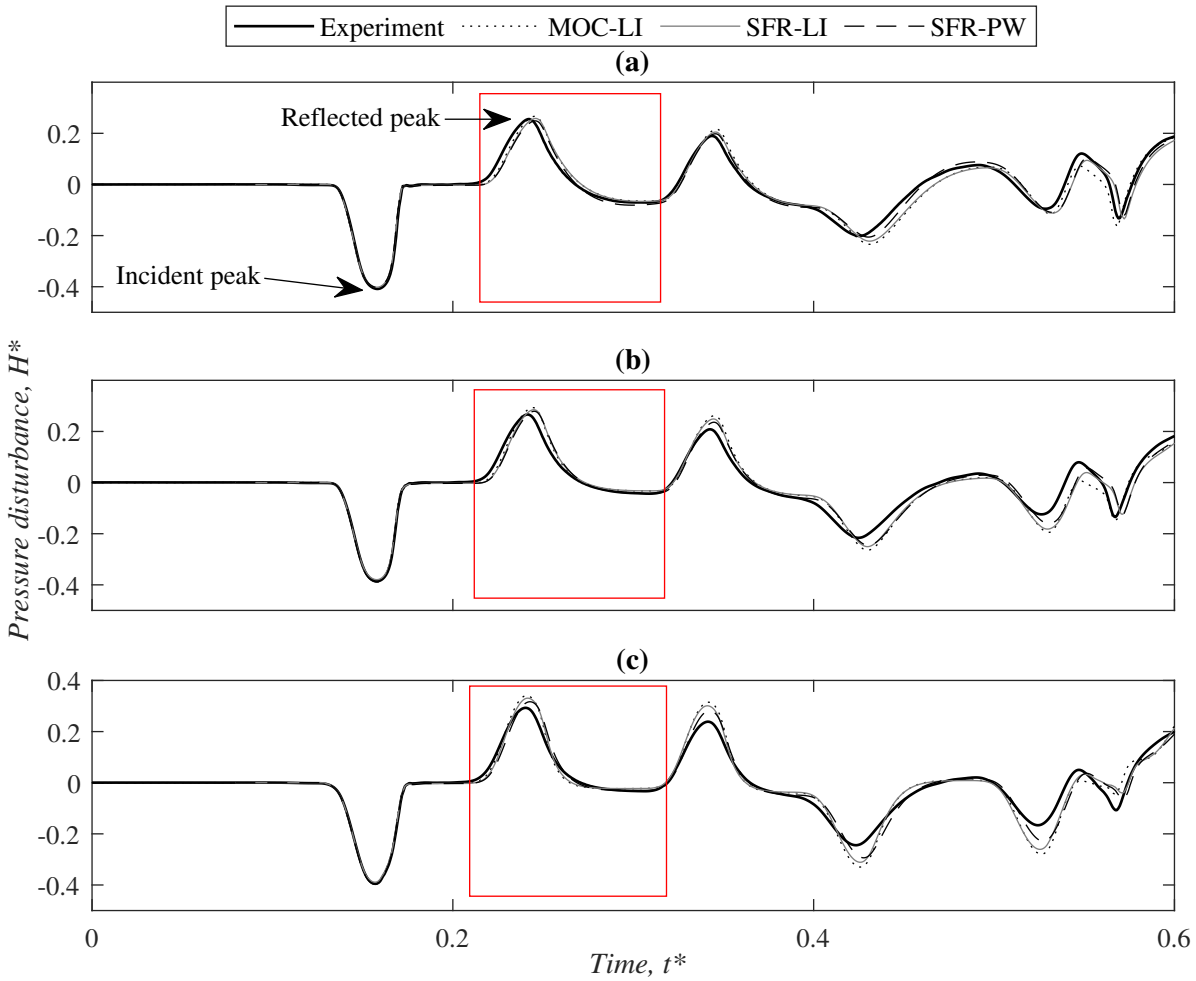

FIGURE 6.2: Experimental and modelled transient pressure traces for the three models (MOC-LI, SFR-LI, SFR-PW) measured at PT2, 8.29 m downstream of the transient generation point and 6.21 m upstream of the air pocket, for an off-line air pocket at an initial hydrostatic pressure of 2.0 bar for (a) L_a^*=0.20, (b) L_a^*=0.51, and (c) L_a^*=0.84. The air pocket length L_a is scaled by the cavity length, the pressure disturbance H is scaled by the initial hydrostatic pressure, and the time t is scaled by the pipeline period. The first pulse reflected from the air pocket is boxed, and the incident and reflected peaks are marked.

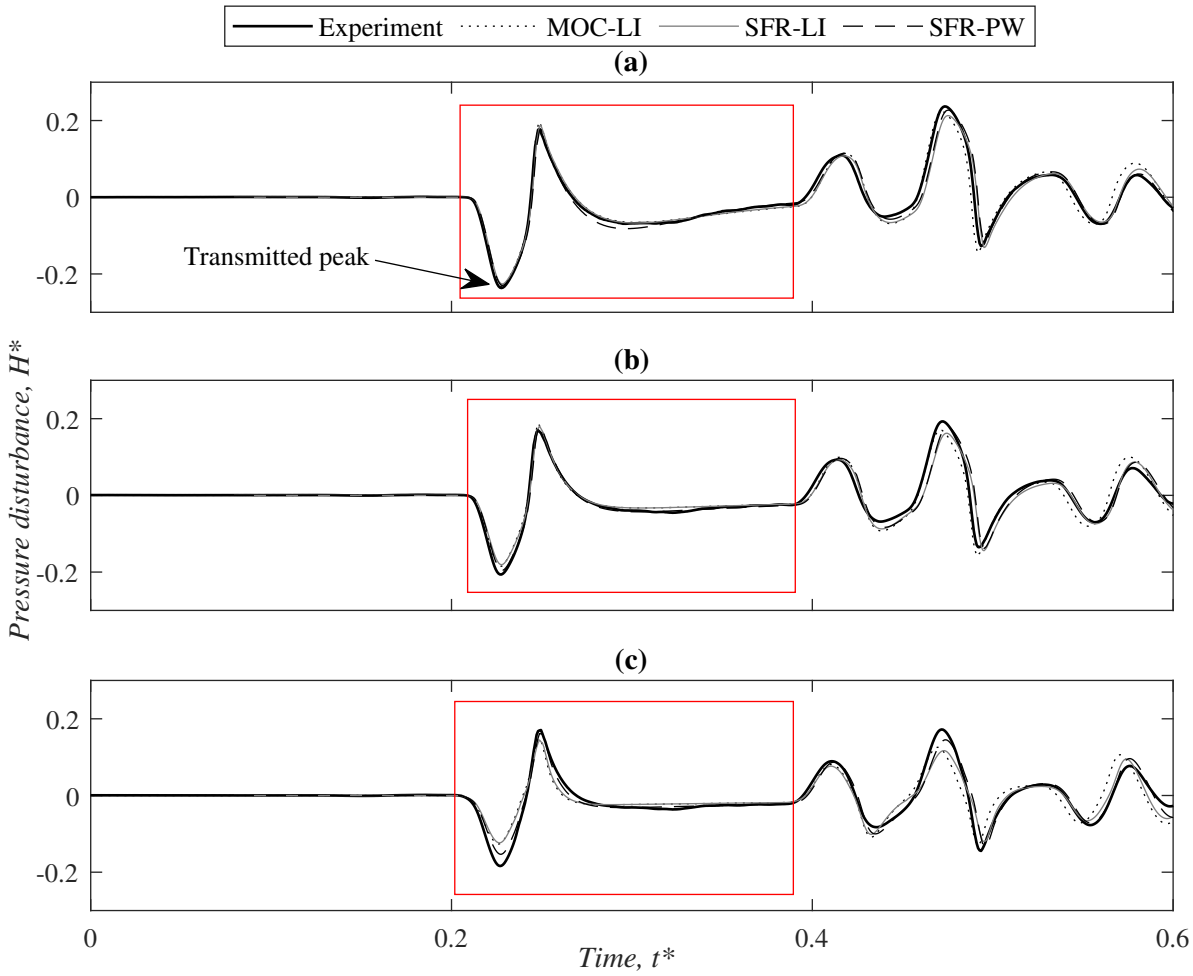

FIGURE 6.3: Experimental and modelled transient pressure traces for the three models (MOC-LI, SFR-LI, SFR-PW) measured at PT3, 6.30 m downstream of the pocket, for an off-line air pocket at an initial hydrostatic pressure of 2.0 bar for (a) L_a^*=0.20, (b) L_a^*=0.51, and (c) L_a^*=0.84. The air pocket length L_a is scaled by the cavity length, the pressure disturbance H is scaled by the initial hydrostatic pressure, and the time t is scaled by the pipeline period. The first pulse transmitted from the air pocket is boxed, and the transmitted peak is marked.

As the transient progressed, the differences between the three models were compounded by further air pocket reflections and transmissions, boundary reflections, and hydraulic and thermal energy losses in the system. A cursory inspection of the pressure traces suggested that the frequency domain models (SFR-LI, SFR-PW) provided the most accurate prediction of the upstream response at PT2 in terms of the wave shape and timing, while the time domain model (MOC-LI) provided a more accurate prediction of the downstream response at PT3. A detailed investigation of the model performance was required to assess the accuracy of the lumped inertia approach for modelling the

off-line air pocket scenario.

6.3.2 Assessment approach

The following sub-sections evaluate the accuracy of the three models (MOC-LI, SFR-LI, SFR-PW) in predicting the transient response. Key measures of the model fit are identified and used to quantify the accuracy for the range of experimental scenarios considered.

The primary purpose of this investigation was to assess methods for predicting the off-line air pocket response, which can be incorporated into larger system models in the future. To this end, the model performance assessment centred on the first pulses reflected and transmitted by the off-line air pocket. Subsequent pressure disturbances are also influenced by system boundary reflections and network losses, which are not the focus of this investigation. The pulses of interest are boxed in Figs. 6.2 and 6.3. It should be noted that the extended low-pressure tails following both pulses were interrupted by subsequent reflections. This means the entire pulse created by the air pocket cannot be considered, and the pulses used for analysis were cut off at approximately the locations boxed on Figs. 6.2 and 6.3. This affects the quantification of the pulse signal frequency distribution as introduced later. However, the outputs of the three modelling approaches were treated in the same manner, and the succeeding parts of the extended tails are of low amplitude relative to the rest of the pulse and are predicted similarly by the three models. This suggests the frequency distribution errors calculated are not significantly biased by this approach.

The primary properties of the transient response which can be used to assess model performance are timing and frequency distribution, which determines the pocket shape. Errors in both these properties were evident in the traces presented in Figs. 6.2 and 6.3, so the model assessment aimed to quantify and compare these errors between the three modelling approaches.

6.3.3 Peak arrival time error

Since the MOC and SFR modelling approaches are based on the same equations, the arrival time of the initial pressure disturbance created by the solenoid was identical between the three models, as can be observed in Fig. 6.2. The timing of the subsequent transient peaks, which are easily identifiable, may be used as a basic property for characterising the air pocket location. The variations in pulse shape between the predictions of the three models meant that the arrival times of the reflected and transmitted peaks (marked on Figs. 6.2 and 6.3) differed between the three cases. Note that the precision level of the numerical models was set to match the experimental precision, and the spatial locations of the air pocket section and sensors were matched between the two models based on the MOC discretisation. The errors in the arrival time of the peaks were quantified using the time difference between the arrival of the incident pulse peak, and the arrival of the first reflected and transmitted peaks. The error was calculated as

$$\epsilon = \frac{\Delta t_{mod} - \Delta t_{exp}}{\Delta t_{exp}} \tag{6.27}$$

where Δt is the time difference between the arrival of the incident peak at PT2 and the arrival of either the reflected peak at PT2 or the transmitted peak at PT3 for the models and experiment. The peak arrival time errors calculated for each experimental scenario are shown in Fig. 6.4.

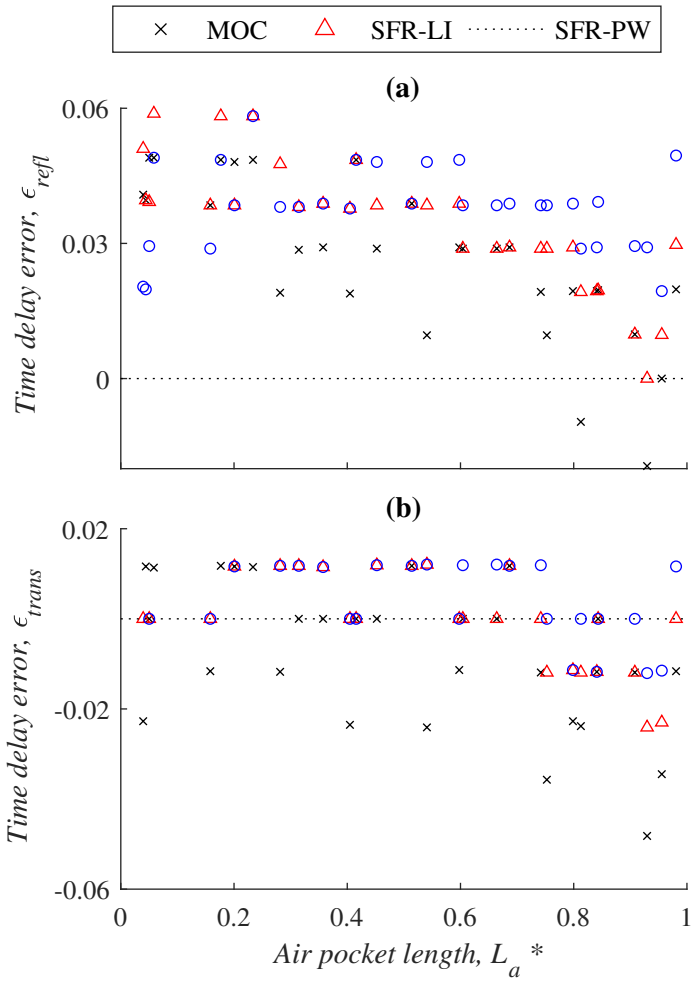

FIGURE 6.4: Time delay error between the experiment and models (MOC-LI, SFR-LI, SFR-PW) estimated by Eq. 6.27 for (a) first reflected peak from the off-line air pocket measured at PT2 (8.29 m downstream of the transient generation point and 6.21 m upstream of the air pocket section) and (b) first transmitted peak from the off-line air pocket measured at PT3 (6.30 m downstream of the air pocket). The air pocket length is scaled by the off-line cavity length. A dotted reference line is drawn at zero.

For the given experimental scenarios, there was no significant trend in the peak arrival time error with initial hydrostatic pressure, and a weak negative correlation with pocket volume across the range of volumes tested. On average, the MOC approach over-predicted the arrival time for the reflected peak by 2.6%, and under-predicted the arrival time for the transmitted peak by 0.8%. The SFR-LI and SFR-PW approaches generally over-predicted the arrival time for both the reflected and transmitted peaks. For both models the errors in the arrival time for the reflected and transmitted peaks were approximately 3.5% and 0.4%, respectively. The timing analysis showed that the MOC

and SFR approaches performed comparatively for the reflected and transmitted peak timing. In particular, the lumped inertia assumption does not significantly affect the peak timing. On average, the errors were approximately 1-2 time steps.

6.3.4 Signal frequency distribution error

The pulses reflected and transmitted by the air pocket were converted to the frequency domain to assess the signal frequency distribution. The advantage of conversion to the frequency domain is that the shape and amplitude of the pulse can be considered simultaneously, whereas they may be difficult to separate in the time domain. A discrete Fourier transform (DFT) was used to obtain the magnitude of each frequency contained in the time domain pulses. Figure 6.5 shows example DFTs for the reflected and transmitted pulses. The frequency ω was normalised by the inverse of the pipeline period ($\omega^* = \frac{4L}{a}\omega$), while the amplitude was normalised by the initial hydrostatic pressure ($h^* = h^*/H_0$).

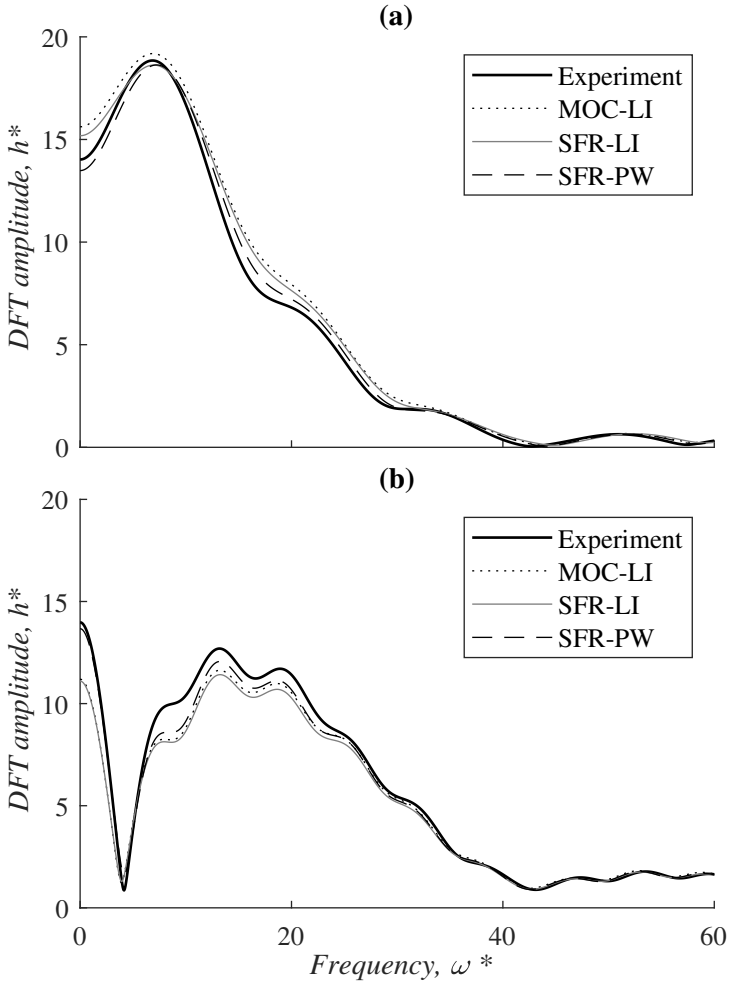

FIGURE 6.5: Experimental and modelled DFT amplitudes for an off-line air pocket at an initial hydrostatic pressure of 2.0 bar, pocket length L_a^*=0.51, for (a) the first reflected pulse from the off-line air pocket measured at PT2 (8.29 m downstream of the transient generation point and 6.21 m upstream of the air pocket section), and (b) the first transmitted pulse from the off-line air pocket measured at PT3 (6.21 m downstream of the air pocket section). The DFT amplitude h is scaled by the initial hydrostatic pressure and the frequency ω is scaled by the inverse of the pipeline period.

The model performance was quantified using relative root mean squared error (RMSE) for the pulse DFTs. The relative RMSE is given by

$$RMSE = \sqrt{\frac{1}{n}\sum_{i=1}^{n}\frac{(y_i - \hat{y}_i)^2}{y_i}} \tag{6.28}$$

where n is the number of observations, y is the observed data series and $\hat{y}$ is the predicted data

series. The RMSE was calculated for frequencies up to the point at which the signal has almost entirely damped ($h^* < 2$). Figure 6.6 shows the RMSEs obtained for the three models for the range of pocket sizes tested. Note that there was no significant trend in the RMSE of the normalised DFTs with initial hydrostatic pressure.

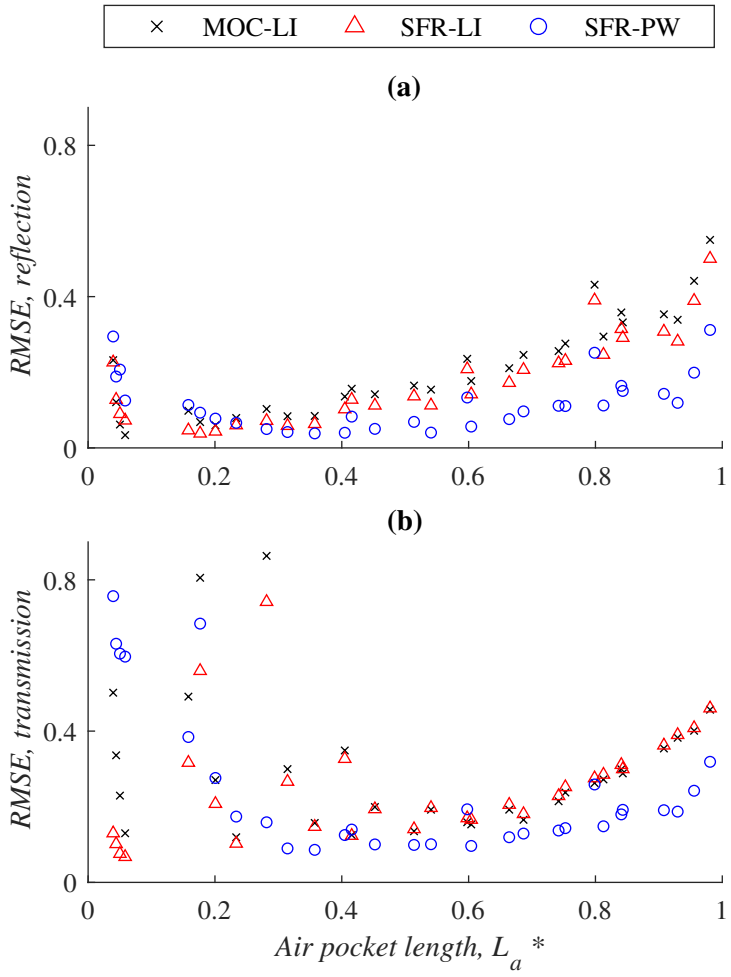

FIGURE 6.6: Root mean squared error for the MOC, SFR-LI, and SFR-PW models compared to experimental observations for a range of pocket sizes for (a) the first reflected pulse DFT from the off-line air pocket measured at PT2 (8.29 m downstream of the transient generation point and 6.21 m upstream of the air pocket section), and (b) the first transmitted pulse DFT from the off-line air pocket measured at PT3 (6.21 m downstream of the air pocket section). The pocket length L_a is scaled by the off-line cavity length.

Figure 6.6 shows that, for the reflected pulse DFT, the RMSE for all models tended to increase with increasing air pocket size, in an approximately quadratic trend. The exception to this observation was the smallest pocket volume tested ($L_a^* \approx 0.05$), which resulted in comparably large errors,

suggesting the models are less accurate for pocket volumes which are small relative to their confining cavity. It has been noted previously for the in-line pocket case that the time domain response for small pocket volumes differs significantly to that observed for larger volumes (Alexander et al., 2020a) (Chapter 3). This was thought to be due to the fact that for small pocket volumes the transient response has a greater dependence on the instantaneous volume change, as opposed to the steady state volume, which may not be well explained by the models. The RMSEs calculated indicate that pockets below $L_a^* \approx 0.3$ are approaching this transition point, as below this threshold the RMSE tended to increase with decreasing pocket volume, particularly for the MOC-LI model. For the range of medium to large pocket volumes tested ($L_a^* > 0.3$), the SFR-PW model generally resulted in the lowest RMSE for the reflected pulse DFT. For the reflected pulse, the RMSE for SFR-PW model was approximately 20-25% of that observed for the MOC-LI and SFR-LI models on average.

Figure 6.6 shows that, for the transmitted pulse DFT, the RMSE for all models tended to increase with increasing air pocket size for $L_a^* \gtrsim 0.4$, from RMSE $\approx$ 0.1 to RMSE $\approx$ 0.5. Below this threshold, a larger degree of variability was evident, with errors of up to RMSE $\approx$ 0.9 observed. Inspection of the data indicated that this is partly related to errors associated with the resonance behaviour of the pocket. As noted in Alexander et al. (2020d) (Chapter 5), the transmitted pulse DFT reaches a sharp local minimum at the resonant frequency of the pocket (at $\omega^* \approx 4$ for the DFT shown in Fig. 6.5b). Due to the sharpness of this section of the transmitted pulse DFT, variations in the location of the local minimum visibly affect the RMSE. Figure 6.7 plots the RMSEs against the relative error in the resonant frequency, defined as $\epsilon_{res} = (\omega_{res,mod} - \omega_{res,exp})/\omega_{res,exp}$, where $\omega_{res,mod}$ = resonant frequency of modelled data and $\omega_{res,exp}$ = resonant frequency of the experimental data. The resonant frequency is defined as the frequency at which the transmitted pulse DFT reaches a local minimum. A moderate correlation was observed between the RMSE and the relative error in the resonant frequency. Greater variation in the resonant frequency error was evident for $L_a^* \lesssim 0.4$, corresponding to the variation observed in the RMSE for this range. For $L_a^* \gtrsim 0.4$, the RMSE for SFR-PW model was approximately 50% of that observed for the MOC-LI

model, and approximately 47% of that observed for the SFR-LI model on average.

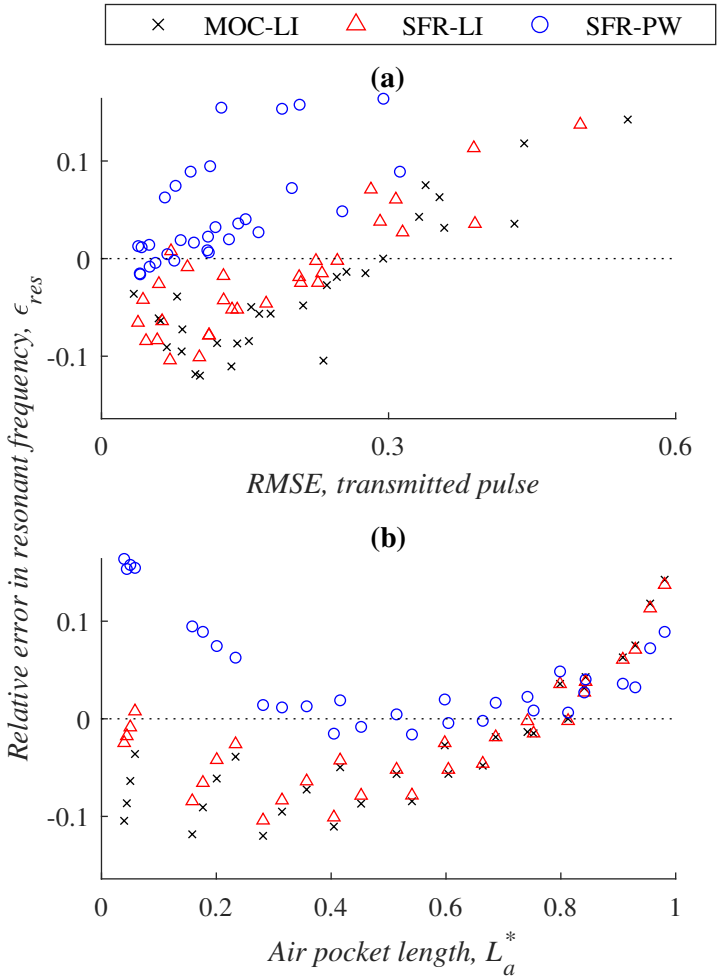

FIGURE 6.7: Comparison of the relative error in the observed resonant frequency between the MOC-LI, SFR-LI, and SFR-PW models with (a) RMSE and (b) air pocket size.

For both the reflected and transmitted pulses, future modelling efforts should primarily aim to improve the prediction accuracy for small pocket sizes. This may include considerations for both the instantaneous volume changes and consistency with regards to capturing the resonant frequency. However, the general findings for the range of data collected show that consideration of the transient as a plane wave which interacts with each interface in the off-line section separately, rather than treating the section as a lumped body of fluid, is generally able to provide greater accuracy in the signal frequency distribution of the transient pulse for this experimental case.

6.4 Conclusions and recommendations

Off-line air pockets may not adversely affect the operation of pipeline systems, but can interfere with transient-based condition assessment techniques. This means it is important to understand how they may be included in network models. The major assumption in past modelling of off-line air pockets has been the lumped inertia assumption, which infers that the connecting water column between the off-line pocket and the main pipe behaves as an incompressible unit. This chapter tested this assumption in the method of characteristics (MOC-LI) and a system frequency response model (SFR-LI) against a system frequency response model which does not assume an incompressible unit at the connector (SFR-PW).

The outputs of the three models for the first pulses reflected and transmitted by the air pocket were compared to experimental data for a range of pocket volumes and initial hydrostatic pressures. Two properties of the first reflected and transmitted pulses were used to assess the models' performance: timing and signal frequency distribution. It was found that error in the pressure peak arrival time was primarily dependent on the modelling approach used, with the MOC model performing better than the SFR models. However, both models had average peak arrival time errors of less than 4%. As discussed previously, an MOC model for off-line air pockets which does not use the lumped inertia assumption is likely to require significant additional computing power, which may outweigh the additional benefit with regards to timing. With regards to the frequency distribution, the RMSE error for the reflected pulse DFT for the SFR-PW model was approximately 20-25% of the RMSE calculated for the lumped inertia models. The RMSE error for the transmitted pulse DFT for the SFR-PW model was approximately 47-50% of the RMSE calculated for the lumped inertia models.

These findings indicate that, for the experimental conditions tested, the lumped inertia assumption results in a reduction in the model performance. The differences in performance are likely to accumulate with ongoing reflections and interference. It is clear from the discrepancies in the response over later periods that, if long-term results are required, more work must be done to improve the accuracy of the off-line pocket model and the overall MOC and SFR equations for the

1D case. It is recommended that 3D CFD modelling as implemented by Zhou et al. (2018) for the dead-end case be considered as part of future work to better understand the significance of thermal dissipation and friction for this application. Although this approach is more computationally demanding, it may provide additional insight into the governing physical processes.

The findings of this investigation are limited by the range of the experimental conditions tested. Both SFR models do not account for changes in the level of the air-water interface with time due to transient disturbances, suggesting the MOC may be better suited to large transients which result in significant volume changes. The SFR-PW may be well suited to large cavity volumes, such as the surge tank scenario, where travel through the connecting section becomes more important. It is recommended that future investigations explore the effect of transient amplitude and pulse duration, as well as cavity dimensions and assumptions regarding friction within the cavity, to further improve understanding of the modelling approaches available for off-line pockets. It is also recommended that future field investigations aim to better understand and quantify the interference of air pockets in transient assessments of real pipelines. The approach could also be investigated for the surge chamber application.

7 Investigation of the effects of base flow on the interaction of off-line air pockets with fluid transients

Chapter 5 investigated the transient response due to off-line air pockets for scenarios where the system has no flow. In the interests of practicality for real-world testing, it is also useful to understand the effects of flow on the transient response.

Other experimental investigations into off-line air have primarily focused on surge protection devices and the prediction of peak pressures following shutdowns. Increasing the flow was found to increase the magnitude of the resultant pressure peaks, which is likely to be related to its relationship with the Joukowsky head rise (Besharat et al., 2016; Di Santo et al., 2002). Varying flow conditions were also observed to change the shape and timing of the response (Kim, 2008b). However, it should be noted that the changes to the initial hydrostatic pressure needed to alter the flow may affect pocket volume, which will also influence features of the transient response. It may be difficult to separate these effects. The theoretical equations governing the off-line air pocket dynamics (Karney and McInnis, 1992; Kim, 2008a) indicate that the system base flow should not be a governing variable. As the investigations by Di Santo et al. (2002) and Besharat et al. (2016) were primarily aimed at investigating shutdowns, the transient was generated by a sudden in-line valve closure which stopped the flow rather than allowing ongoing flow throughout the transient event. Besharat et al. (2016) carried out a second set of tests using ongoing flow, again noting that the magnitude of the pressure disturbances increased with Reynolds number. With the exception of Kim (2008b),

the investigations above generally did not aim to characterise the specific effects of the air on the reflected and transmitted waves, which are of interest for transient-based fault detection. In addition, the responses for no-flow and flow scenarios have not previously been compared for the same experimental system.

The objective of this section is to use experimental results, supplemented by the outputs of numerical modelling, to compare transient responses due to an off-line air pocket for flow and no-flow scenarios. The experimental investigation spans a range of flow velocities and off-line air pocket volumes. The experiments use a side discharge solenoid valve to generate the transient, meaning flow is maintained during the transient event.

7.1 Experiment and modelling methods

The general methodology for the transient experiments is described in Chapter 2. In this set of experiments, the pipe length and transducer locations were modified. The modifications and experimental scenarios are described below. For this case, the upstream and downstream ends were nominated based on the flow direction.

The experimental set-up, shown in Fig. 7.1, consisted of a 52.7 m straight stainless steel pipe of 22.25 mm internal diameter. Tanks at either end were used to pressurise the system. A Baccara solenoid valve was installed adjacent to the downstream tank and programmed to generate a high frequency pulse by opening and closing over a 6 ms period. The resultant pressure disturbances were measured along the system by five PCB Piezotronics Model 102A07 dynamic pressure transducers (A1, B1, C1, D1, and E1). Static transducers were fitted at the same locations to measure gauge pressures in the system. Specifications for the solenoid valve and pressure transducers can be found in Chapter 2.

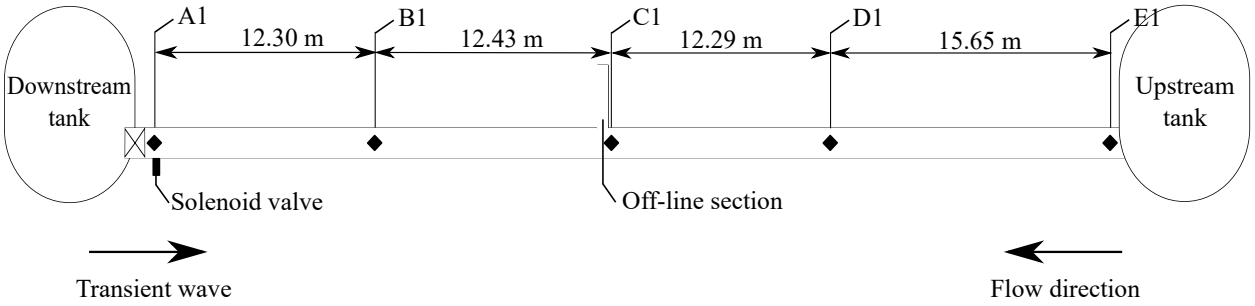

FIGURE 7.1: Diagram of experimental set-up

The steel off-line cavity described in Chapter 2 was screwed to the pipe 24.73 m from the downstream tank (Fig. 7.2). The cavity had a 177 mm length and 8.5 mm diameter, and was separated from the main pipe by a short neck section of 24.9 mm length and 6.3 mm length. Air was inserted into the cavity via a bleed valve at the top. A measuring syringe was used to measure the volume of air inserted, and to extract the air at the end of the test to ensure no air had moved elsewhere in the pipe. The eight air pocket volumes tested ranged from 1 ml to 10 ml at atmospheric pressure (V = {1; 2; 3; 4; 5; 6; 8; 10} ml).

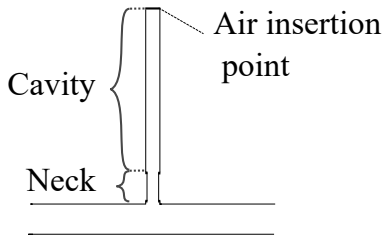

FIGURE 7.2: Diagram of off-line pocket section

For the no-flow scenario, each pocket volume was tested at five initial hydrostatic pressures ({1.0; 1.5; 2.0; 2.5; 3.0} bar). Within the no-flow scenario, two cases were tested. In the first case, the upstream tank was pressurised, and the in-line valve adjacent to the solenoid valve closed. In the second case, the in-line valve was opened, and the downstream tank pressurised to the same pressure as the upstream tank. These cases represent two different boundary conditions adjacent to the solenoid valve: a closed valve, and a pressurised tank.

For the flow scenario, the in-line valve was opened and a pressure differential was set between the two tanks. The downstream tank was held at a constant pressure of 1.0 bar. The upstream tank

pressure was set to six different levels to achieve a range of flow velocities ({1.25; 1.50; 1.75; 2.00; 2.75} bar). The corresponding flow velocities were estimated by measuring level changes in a sight glass mounted on the downstream tank. The conditions for each test are shown in Table 7.1.

TABLE 7.1: Flow scenario test conditions

Upstream head (bar)	Downstream head (bar)	Measured velocity (u, m/s)	Reynolds number ($\frac{uD}{\nu}$)
1.25	1.00	0.82	18,300
1.50	1.00	1.22	27,200
1.75	1.00	1.52	33,800
2.00	1.00	1.79	39,900
2.75	1.00	2.52	56,100

Each set of conditions was repeated 10 times, and the standard errors were less than 1% of the absolute pressure readings.

In the experiments, the air pocket volumes were measured outside the pipe at atmospheric pressure before and after each test using a measuring syringe. The pressurised volumes were calculated using the reversible polytropic equation (Chapter 2, Eqn. 2.7).

Numerical modelling using the MOC was used to explain key observations. The governing equations for the off-line air pocket boundary are included in Chapter 2.

7.2 Results

7.2.1 Time domain

The pressure disturbances were measured on both the upstream and downstream sides of the air pocket section, meaning both the reflected and transmitted waves were captured. Time t was normalised by the pipeline period ($t^* = \frac{a}{4L}t$), while the pressure disturbance H was normalised by the initial hydrostatic pressure at the air pocket H_a ($H^* = H/H_a$). The head at the pocket was obtained from static transducer measurements at C1. The volume of the off-line air pocket once pressurised was converted to a length and normalised by the length of the off-line cavity ($L_a^* = L_a/L_{cavity}$). Figures 7.3 and 7.4 show the pressure traces measured downstream and upstream of the pocket respectively, for comparable L_a^* across the three scenarios: the no-flow case with the in-line valve at the downstream end shut, the no-flow case with the in-line valve open, and the flow case. The incident, reflected, and transmitted pulses are marked on Figs. 7.3 and 7.4.

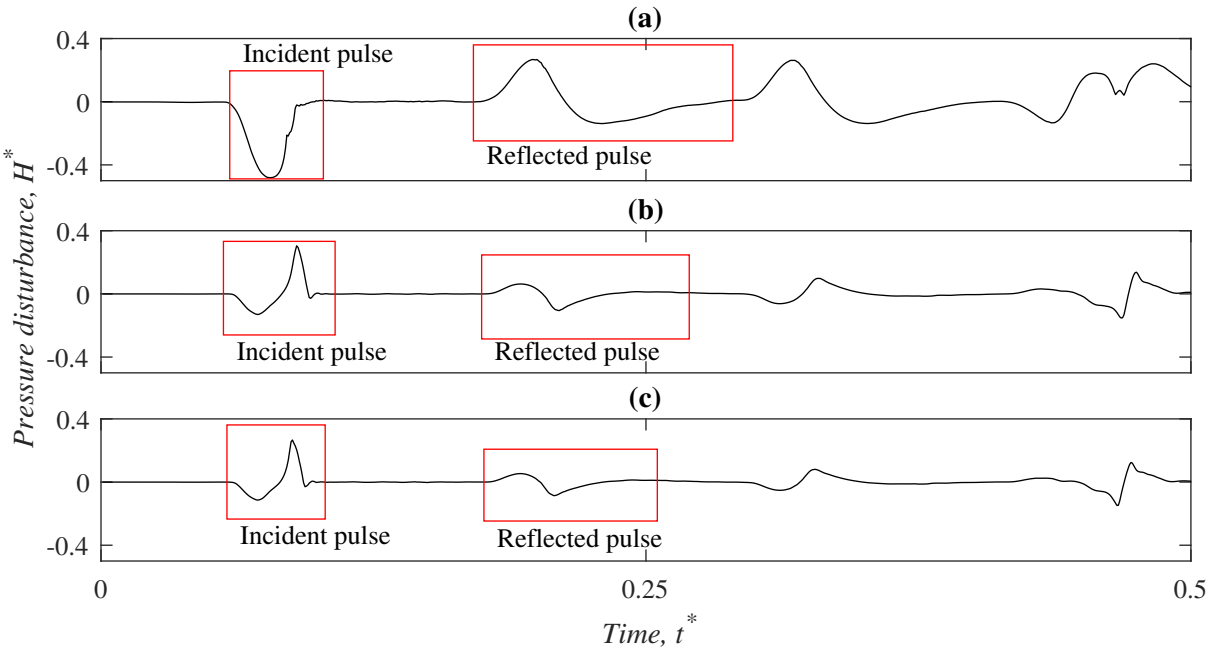

FIGURE 7.3: Pressure traces measured at transducer B1, 12.30 m upstream of the transient generation point and 12.43 m downstream of the off-line pocket section, for off-line air pocket length L_a^* =0.09, for (a) no flow with in-line valve closed, (b) no flow with in-line valve open, and (c) flow (Re = 18,300). The pressure disturbance H is scaled by the initial hydrostatic pressure and the time t is scaled by the pipeline period. The incident pulse and the first pulses reflected by the air pocket are boxed and labelled.

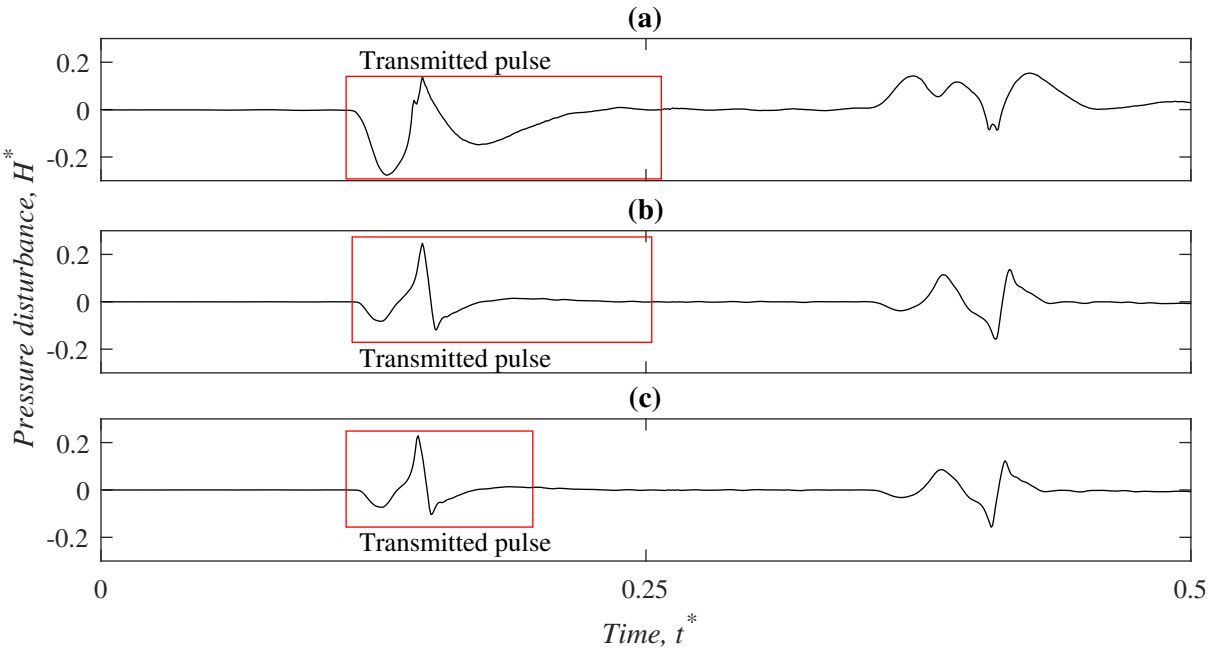

FIGURE 7.4: Pressure traces measured at transducer C1, 12.29 m upstream of the off-line pocket section, for L_a^* =0.09, for (a) no flow with in-line valve closed, (b) no flow with in-line valve open, and (c) flow (Re = 18,300). The pressure disturbance H is scaled by the initial hydrostatic pressure and the time t is scaled by the pipeline period. The incident pulse and the first pulses reflected by the air pocket are boxed and labelled.

The comparisons here focus on the first pulses reflected and transmitted by the off-line air pocket for each set of flow conditions. Figures 7.3 and 7.4 show that the incident pulse shape is dependent on the flow conditions and the boundary condition adjacent to the solenoid (open reservoir or closed valve) due to interference from the boundary reflection. Conversion to the frequency domain enables the comparison of responses regardless of the incident signal shape.

7.2.2 Frequency domain

The incident, reflected, and transmitted pulses for each scenario were converted to the frequency domain using a discrete Fourier transform (DFT). The DFT quantifies the magnitude of each frequency contained in the pulses. For comparison purposes, numerical results for the three scenarios were generated using the MOC, using a simple input disturbance at the boundary similar to the incident pulse shown in Fig. 7.3(a). The frequency content for the modelled pulses obtained

for flow and no-flow conditions are plotted in Fig. 7.5, showing that, theoretically, the air pocket response is unaffected by the system base flow. The DFT amplitude was normalised by the initial hydrostatic pressure at the pocket ($h^* = h/H_a$), while the frequency was normalised by the pipeline fundamental frequency ($\omega^* = \frac{4L}{a}\omega$).

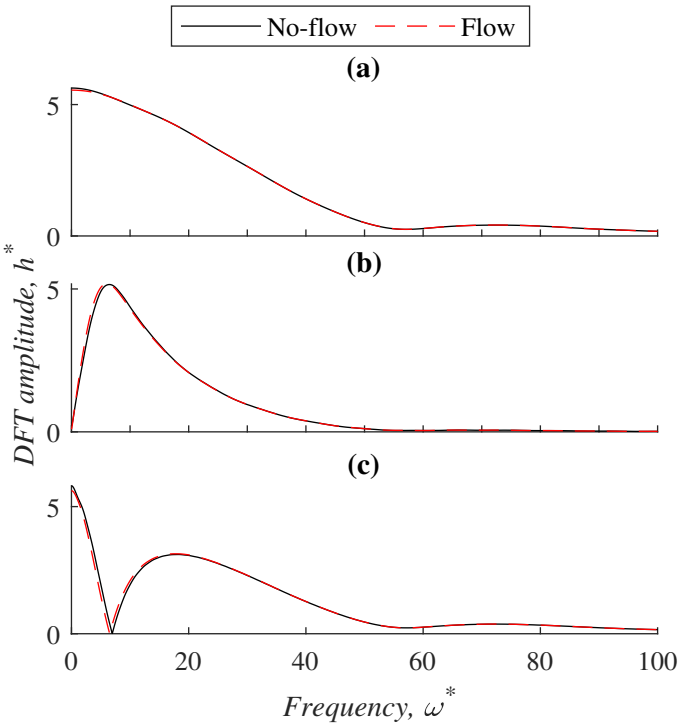

FIGURE 7.5: DFT amplitude of modelled pulses (MOC model with off-line air pocket equations, Chapter 2) for off-line pocket length L_a^* =0.09 for no flow (in-line valve closed) and flow (Re = 18,300) case: (a) incident pulse measured at B1, 12.30 m upstream of the transient generation point and 12.43 m downstream of the off-line pocket section, (b) first reflected pulse measured at B1, and (c) first transmitted pulse measured at C1, 12.29 m upstream of the off-line pocket section. The DFT amplitude h is scaled by the initial hydrostatic pressure and the frequency ω is scaled by the inverse of the pipeline period.

Example experimental DFTs for each set of flow conditions are shown in Fig. 7.6. The DFTs show that the bandwidth of the incident pulse varies across the three scenarios. A -10dB bandwidth is marked on Fig. 7.6 for each case, with the limits defined as approximately 31% of the maximum DFT amplitude. The input pulse for the scenarios shown in Fig. 7.6(a-c) contained frequency bands of $\omega^* \approx \{0, 30.0\}$, $\omega^* \approx \{3.6, 34.4\}$, and $\omega^* \approx \{5.3, 88.8\}$ respectively. The comparisons in this study have been considered only over the common bandwidth between the three scenarios

($\omega^* \approx \{5.3, 30.0\}$), as analyses outside this range may be subject to errors introduced by division by low numbers.

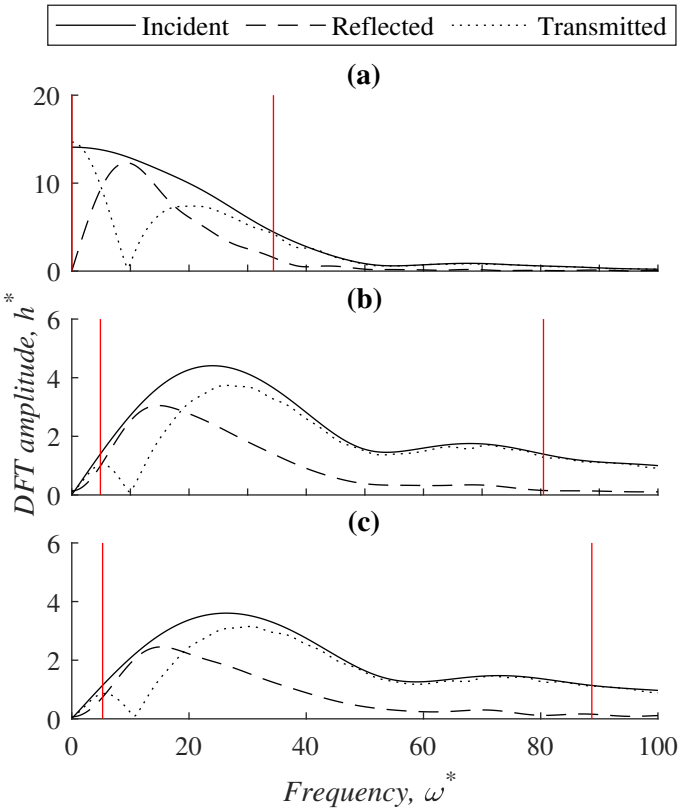

FIGURE 7.6: DFT amplitude of incident pulse measured at B1 (12.30 m upstream of the transient generation point and 12.43 m downstream of the off-line pocket section) first reflected pulse measured at B1, and first transmitted pulse measured at C1 (12.29 m upstream of the off-line pocket section) for off-line air pocket length $L_a^* = 0.09$ for (a) no flow with closed valve boundary, (b) no flow with open valve boundary, and (c) flow (Re = 18,300). The -10dB bandwidth limits of the pulses are marked with vertical red lines. The DFT amplitude h is scaled by the initial hydrostatic pressure and the frequency ω is scaled by the inverse of the pipeline period.

Given the differences in input frequency content, the reflected and transmitted pulse spectra are most easily compared using reflection and transmission coefficients calculated at each frequency. The coefficients were calculated as

$$RC(\omega^*) = \frac{h_R(\omega^*)}{h_I(\omega^*)} \tag{7.1}$$

$$TC(\omega^*) = \frac{h_T(\omega^*)}{h_I(\omega^*)} \tag{7.2}$$

where RC = reflection coefficient and TC = transmission coefficient calculated at each frequency ω^*, using the amplitude of the incident pulse spectrum h_I and the reflected or transmitted spectrum amplitude at that frequency (h_R and h_T respectively). Reflection and transmission coefficients for two representative pocket volumes are plotted in Figs. 7.7 and 7.8 alongside the RC and TC obtained from the MOC for the off-line pocket. In general, the RC and TC are comparable across the three experimental scenarios within the common bandwidth, confirming that flow has little impact on the effect of the off-line pocket. Some minor variation is evident, with the mean range in RC and TC being approximately 0.05 for both pocket volumes plotted. The agreement between the MOC prediction of RC and TC and the experimental observation improves with increasing pocket volume. This has been observed previously by the authors for in-line and off-line pockets (Alexander et al., 2020a,c) (Chapters 4 and 6).

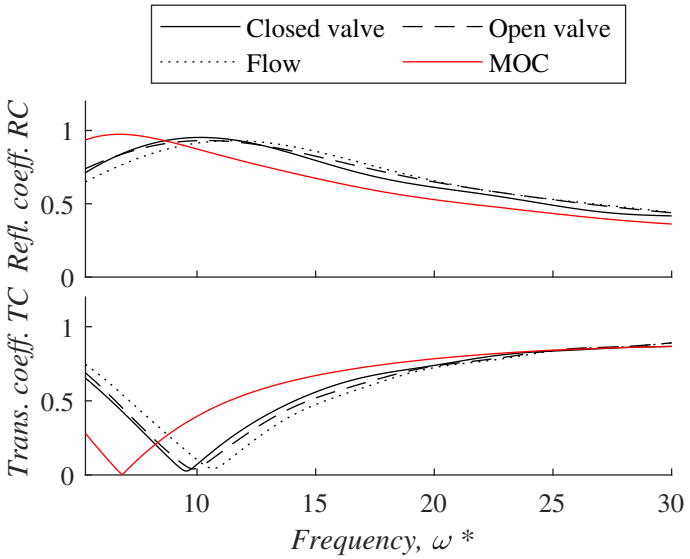

FIGURE 7.7: Reflection and transmission coefficient (RC and TC) for the measured DFTs for the first reflected and transmitted pulses from an off-line air pocket of length $L_a^* = 0.09$ relative to the incident pulse DFT amplitude. The frequency ω is scaled by the inverse of the pipeline period.

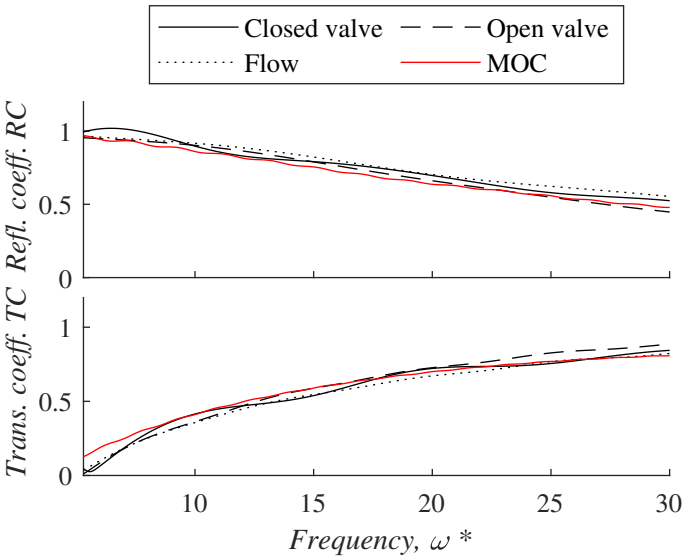

FIGURE 7.8: Reflection and transmission coefficient (RC and TC) for the measured DFTs for the first reflected and transmitted pulses from an off-line air pocket of length $L_a^* = 0.47$ relative to the incident pulse DFT amplitude. The frequency ω is scaled by the inverse of the pipeline period.

It also important to note the resonant behaviour in the off-line pocket response, which is shown in Fig. 7.6 and has been observed previously for the off-line case (Alexander et al., 2020d) (Chapter 5). The transient transmissivity is minimised ($TC \approx 0$) at the resonant frequency of the off-line pocket. For $L_a^* = 0.09$ (Fig. 7.7) this can be observed at $\omega^* \approx 10$. The resonant frequency depends on the pressure condition, cavity dimensions, and pocket size (Jang et al., 2009). As such, the resonant frequency may not always be captured within the input signal bandwidth. For example, in Fig. 7.8, the resonant frequency for L_a^* =0.47 falls at the lower boundary of the common bandwidth ($\omega^* \approx \{5.3, 30.0\}$). The resonant behaviour is an easily identifiable characteristic of off-line air, and Figs. 7.7 and 7.8 highlight the importance of selecting an input signal with a bandwidth which encompasses the range of likely resonant frequencies for unwanted off-line pockets.

7.3 Conclusions and recommendations

A greater understanding of the interaction of fluid transients and off-line air pockets will aid transient-based condition assessment techniques for water supply pipelines. This component of the

study investigated the effects of base flow on the transient response using experiments supplemented with numerical modelling. The findings may be used to inform testing and analysis protocols for operational pipes.

The pulses created by the off-line air pocket were used to calculate reflection and transmission coefficients at each frequency to enable comparison between the flow and no-flow cases, as the different boundary conditions next to the solenoid generator (closed valve and open reservoir) affected the input pulse shape. Numerical modelling showed that the flow and no-flow cases result in the same RC and TC at every frequency contained in the pulse. Comparison between the experimental results for each set of system conditions also showed only minor variation in RC and TC between the flow and no-flow scenarios across the common bandwidth. This finding confirms that transient-based diagnostics can be carried out for off-line air pockets without the need for costly and disruptive system shutdowns. However, it is important to select a input bandwidth that encompasses identifying features such as the resonant frequency.

Further experimental investigations are needed to characterise the effects of flow on in-line air pockets trapped in the main flow path. This may present a challenge due to the possibility for movement or shearing of the air pocket under the influence of flow.

8 Pipe deterioration: Experimental methods and findings

8.1 Introduction

Deterioration of the pipe wall has been observed to affect the transient wave speed in field pipes. In the laboratory, thinner-walled sections are generally used to represent areas of corrosion. This investigation explores the possibility of carrying out controlled corrosion on pipe specimens in the laboratory to further assess the effect of deterioration on the transient response, without the accessibility limitations that may occur in the field. An experimental accelerated corrosion program was implemented to investigate the effects of wall deterioration in mild steel pipes on the transient wave speed. No previous studies have tracked the expected reduction in wave speed with controlled corrosion in the laboratory. Three possible wall deterioration cases were considered: internal-only, external-only, and internal-external. The experimental work was carried out in two stages. The first stage consisted of a preliminary small-scale study to investigate practicalities around the application of the method to pipes and to compare the observed mass loss to Faraday's Law predictions. The second stage consisted of accelerated corrosion of full-scale pipe sections, along with transient testing at regular intervals.

8.2 Experimental methods

8.2.1 Corrosion theory

The experiments were carried out in the University of Canterbury Fluids Laboratory. When simulating corrosion of metals in the laboratory, time constraints mean the corrosion process must be accelerated. One of the most common methods is immersion in a salt (NaCl) bath with application of an impressed current, creating an electrolytic cell. A schematic of the cell and the key reactions is shown in Fig. 8.1. Water is reduced at the stainless steel cathode and iron is oxidised on the surface of the mild steel pipe (the anode) in a non-spontaneous electrochemical reaction. The movement of Fe^{2+} and OH^- ions through the NaCl electrolyte between the anode and cathode completes the electrical circuit. The reaction between Fe^{2+} and OH^- ions in the solution forms an iron hydroxide precipitate which is rapidly oxidised to form a rust deposit.

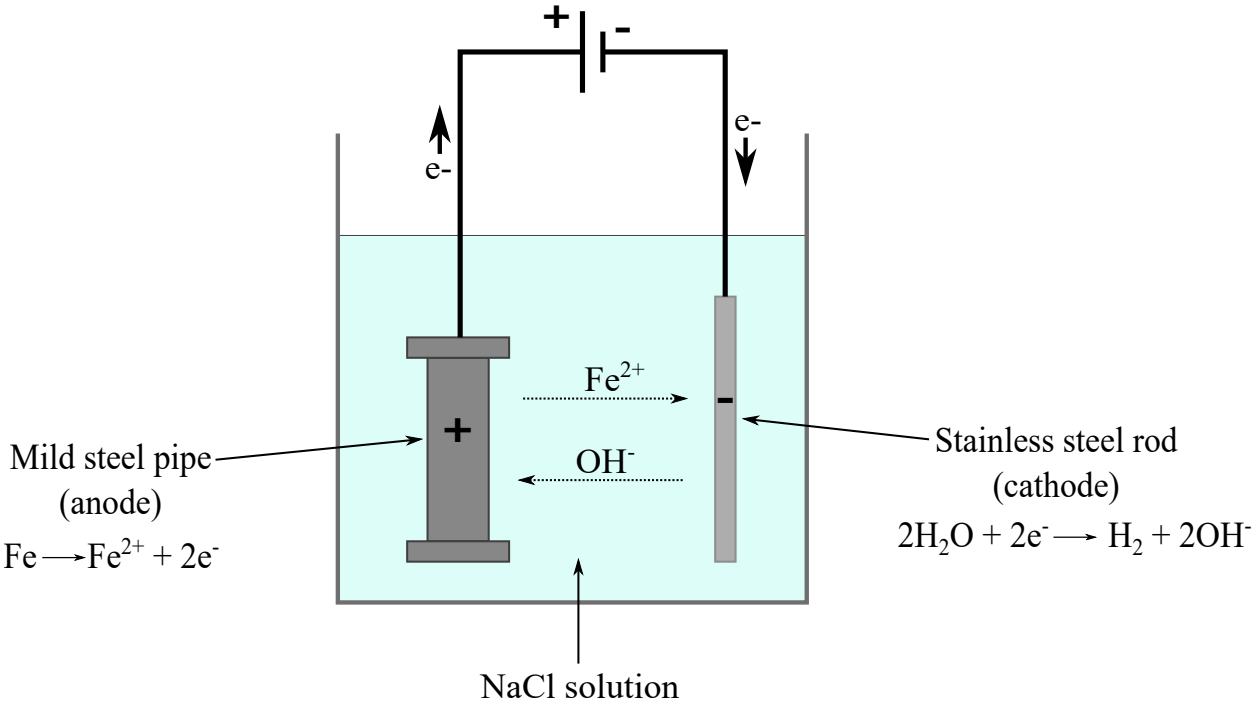

FIGURE 8.1: Schematic of electrolytic cell reaction for the accelerated corrosion process

Methods similar to this have been used extensively in evaluating the effects of corrosion on steel-reinforced concrete (El Maaddawy and Soudki, 2003; Caré and Raharinaivo, 2007; Kivell et al.,

2011), and can achieve levels of corrosion in days or weeks which would usually occur over years. The method also allows easy control of the corrosion degree desired, with the rate of corrosion being proportional to the impressed current according to Faraday's Law

$$m = \frac{tIM}{zF} \tag{8.1}$$

where m = mass loss; t = time; I = impressed current; M = molar mass of the element; z = valency of the element; and F = Faraday's constant. Limited information exists on the effectiveness and practicalities of using the technique for pipes, with the closest example being work by Yang et al. (2020). Yang et al. (2020) corroded sections of 25 mm diameter and 210 mm length to degrees of material loss ranging between 10% and 70%. The samples were used to better understand the tensile fracture behaviour of corroded pipes. A study by Regier (2015) investigated the corrosion of corrugated steel culverts. The results from Regier (2015) showed significant discrepancies with the corrosion rates predicted by Faraday's Law (up to 380% in large-scale specimens). The discrepancies were thought to be due to the proximity of the electrodes to the specimens and rapid increases in the corrosion rate following perforation of the steel surface.

8.2.2 Small-scale specimens

Initially, a set of small-scale specimens were corroded to better understand the possible corrosion rates and identify key factors to consider for the full-scale tests. Four sections of 300 mm length were cut from a 100NB, 5.4 mm wall thickness mild steel pipe. The four corrosion cases were:

- Internal corrosion only, with one central electrode placed inside the pipe, which was filled with 3.5% NaCl. The base of the section was capped. This prevented any corrosion on the external surface.
- External corrosion only, with four electrodes placed at equal spacing around the outside of the pipe section. The electrodes were at a distance of 50 mm from the pipe wall. The base of

the section was capped and the section submerged in a plastic bucket filled with 3.5% NaCl solution. The pipe was not filled, to prevent corrosion on the internal surface.

- External corrosion only, as described above. In this case, the four electrodes were placed at a distance of 100 mm from the pipe wall, to investigate the effect of electrode distance.
- Internal and external corrosion. One central electrode was placed inside the pipe, and four were placed at equal spacing around the pipe, 50 mm from the pipe wall. The section was submerged in a plastic bucket filled with 3.5% NaCl solution.

The electrodes were cut from 8mm stainless steel rods and held in place using acrylic mounting plates. A schematic of the specimens is shown in Fig. 8.2, and photographs of the specimens are shown in Fig. 8.3. The pipe sections and electrodes were connected to dual-channel TENMA 72-10500 5A bench-top power supplies. The applied currents and expected corrosion rates based on Faraday's Law (Eq. 8.1) are shown in Table 8.1.

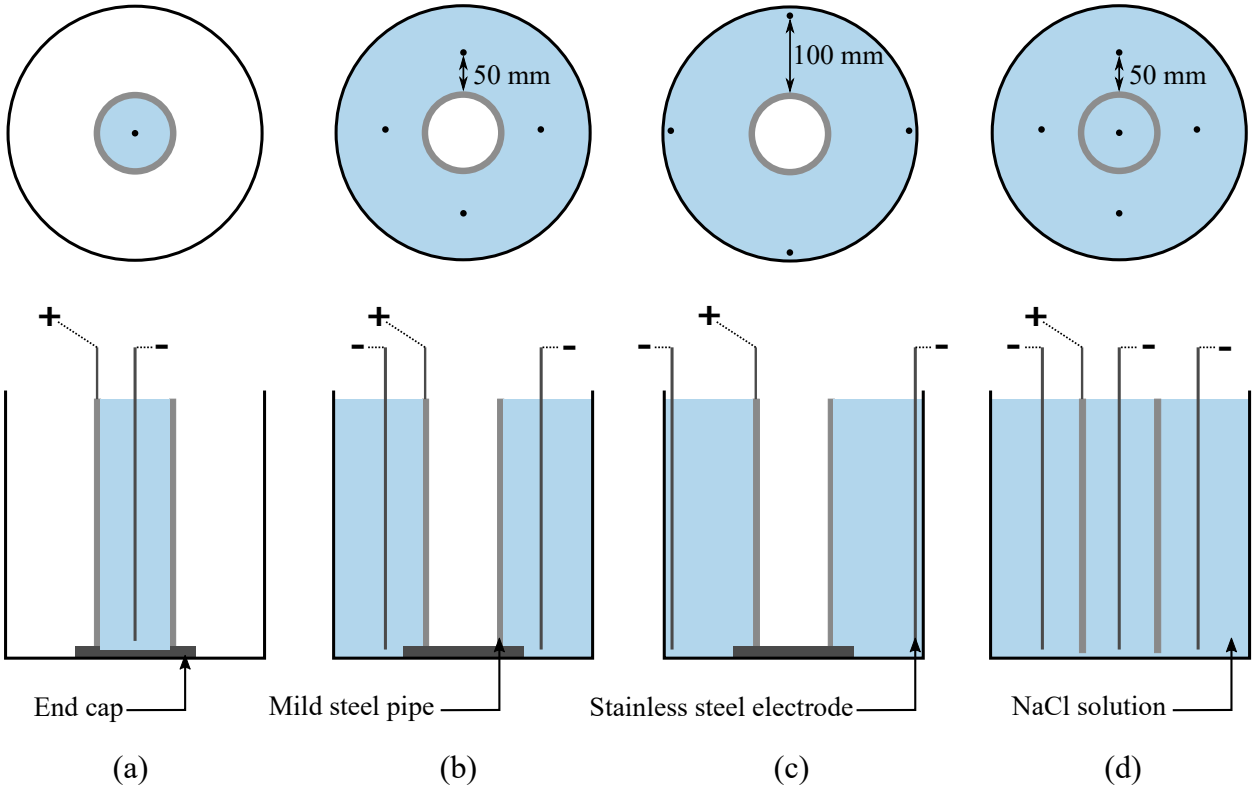

FIGURE 8.2: Diagrams of small-scale corrosion specimens: (a) Internal only, (b) External only, electrodes at 50 mm spacing, (c) External only, electrodes at 100 mm spacing, (d) Internal and external

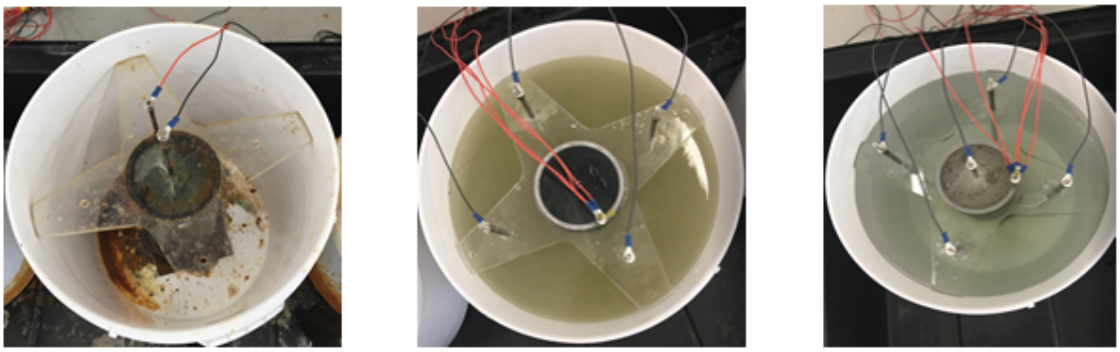

FIGURE 8.3: Photographs of small-scale corrosion specimens: (a) Internal only, (b) External only, electrodes at 50 mm spacing, (c) Internal and external

TABLE 8.1: Small-scale corrosion test conditions

	Internal only	External only	Internal+External	
			Internal	External
Current per electrode (A)	5.1	1.48	2.97	0.74
Number of electrodes	1	4	1	4
Total current (A)	5.1	5.9	2.97	2.97
Expected corrosion rate (mm/hr)	0.0072	0.0084	0.0042	0.0042

Regular cleaning was required to remove the iron rust precipitates formed in the cell. The external-only specimens were cleaned daily to remove the rust build-up, as greater periods without cleaning resulted in significant pitting on the pipe surface which affected the ability to collect wall thickness measurements. The internal-only specimen was also cleaned daily, but was found to be highly susceptible to stubborn precipitate build-up. This was hypothesised to be due to the concave internal surface causing precipitate deposits to crush together. The limited access to the internal pipe wall made these precipitate deposits difficult to scrape away, and corrosion ceased once a substantial layer of precipitate formed. This means current intensity, cleaning interval, and flow agitation should be carefully controlled in large-scale tests to prevent excessive build-up which cannot be easily removed. Subsequent short tests showed that the precipitate deposits could be managed by reducing the cleaning interval or the applied current. Similar observations were made

of the internal-external specimen, which was less susceptible to the precipitate build-up due to the lower current intensity. The specimens were corroded for approximately 300-400 hours, with the exception of the internal-only specimen which was corroded for approximately 200 hours. This reduced period was due to the significant precipitate build-up limiting corrosion in some areas of the specimen.

Wall thickness measurements were taken at regular intervals using a Sauter Thickness Gauge TN 80-0.01 ultrasonic scanner. The specimens were cleaned and lightly sanded to ensure a smooth surface. Spot measurements were taken in an evenly spaced grid, with 10 nodes along the specimen length and 20 nodes around the specimen circumference. Five ultrasound measurements were taken at each location and averaged. Figure 8.4 shows the average wall thickness measured at the pipe midpoint for each specimen for the test duration, compared to the theoretical wall thickness predicted by Faraday's Law. In general, the corrosion rate for the external-only and the internal-external specimens was approximately 80% of the expected rate, with variations of approximately 5% across the 200 nodes. Electrode spacing was observed to have little effect on the thickness loss rate for the external-only cases, with a difference in the deterioration rate of approximately 1.5% and comparable variation observed in thickness loss around the pipe circumference, indicating that a separation of 50 mm is sufficient to manage preferential corrosion. For the internal-only case, the mid-point corrosion rate was similar to the theoretical rate, with an error of less than 4%. This was likely due to the significant precipitate deposits which formed in some regions of the pipe, reducing the amount of available surface area and increasing the current intensity on exposed areas.

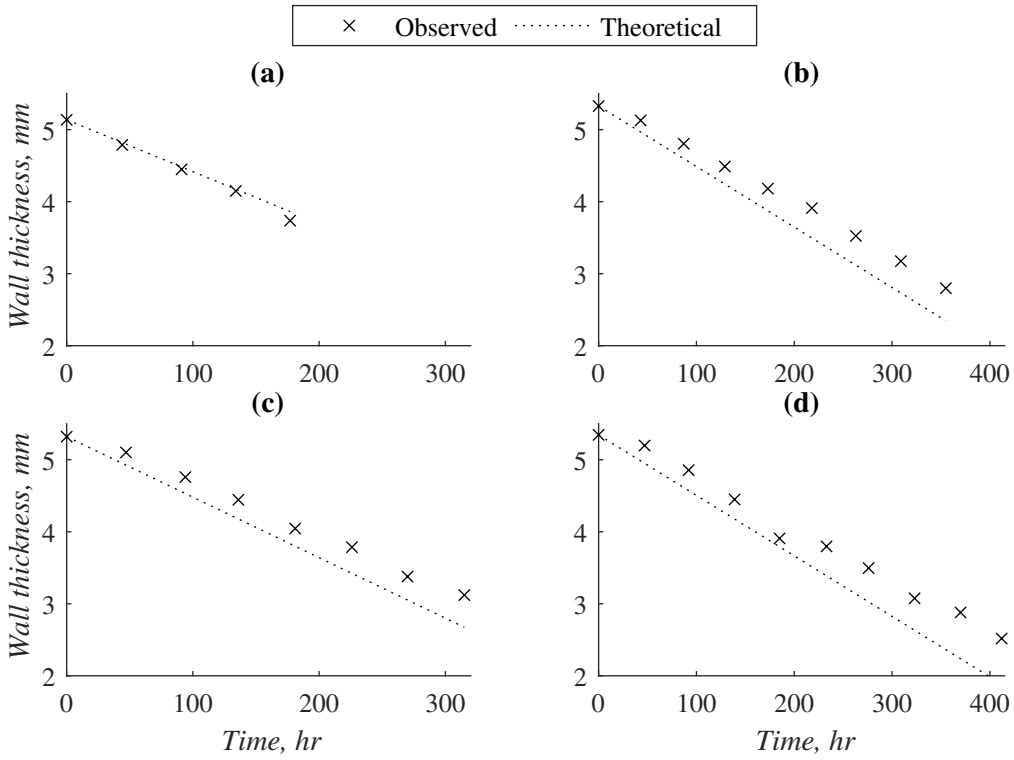

FIGURE 8.4: Observed wall thickness variation with time at the small-scale specimen midpoint compared to the theoretical prediction of Eq. 8.1 for (a) internal-only, (b) external-only (50 mm electrode separation), (c) external-only (100 mm electrode separation), (d) internal and external accelerated corrosion procedures.

A range of coatings were also tested on the external surfaces for use on the large-scale internal-only specimen, as both ends were intended to be left open to facilitate agitation of the electrolyte to reduce precipitate build-up. The four coating cases tested were: Septone Acrylic Lacquer, Wattyl Killrust Etch Primer, Galmet Enamel Spray Paint, and a coating of Wattyl Killrust Etch Primer followed by Septone Acrylic Lacquer. Specimens coated with the primer alone and the enamel spray paint were subject to significant peeling following a period of submersion in the electrolytic cell. Both the acrylic paint and the primer and acrylic paint combination were effective in coating the pipe surface without peeling.

It was also noted that the seam weld on the external surface corroded rapidly for external corrosion cases, and this seam should be protected on full-scale specimens to prevent leakage and ensure safe pressurisation.

8.2.3 Full-scale specimens

The full-scale testing apparatus was constructed in the University of Canterbury Fluids Laboratory following the completion of the small-scale testing. The findings of the small-scale experiments were used to inform the full-scale experimental methods. Three 6.5 m lengths of 100NB, 5.4 mm wall thickness mild steel pipe were tested, for the following corrosion scenarios: internal-only, external-only, and internal-external. The full-scale experimental program consisted of two components: accelerated corrosion and transient testing. Stainless steel flanges were welded to the specimen ends to enable connection to the transient testing apparatus.

Accelerated corrosion

The accelerated corrosion was carried out using a similar process to that employed for the small-scale testing, with additional considerations based on the findings of the small-scale tests. Before commencing corrosion, the welds at the end flanges and along the external seam were protected by a layer of Denso Tape. To prevent internal corrosion on the external-only specimen, the ends of the specimen were capped using stainless steel flange plates. To prevent external corrosion on the internal-only specimen, the outer wall of the specimen was coated with Septone Acrylic Lacquer.

The corrosion apparatus is shown in Fig. 8.5 and Fig. 8.6. The specimens were placed horizontally in PVC troughs (7400L×300W×240D). Acrylic pipe mountings at 2 m spacings were used to hold the specimens in place. The 8 mm stainless steel electrodes were mounted around and within the pipe using acrylic electrode mountings at 1500 mm spacings, as shown in Fig. 8.7. The external electrodes were mounted at a distance of 75 mm from the pipe wall. The troughs were filled to above the electrode level with 3.5% NaCl solution. A Pedrollo TopFloor2 pump was used to circulate flow through the internal-only and internal-external specimens to agitate corrosion precipitates inside the pipe. The dual-channel TENMA 72-10500 5A bench-top power supplies were connected to the electrodes at one end of the cell. The applied current settings are summarised in Table 8.2. Multiple channels were connected in series to achieve the required current for the internal electrodes.

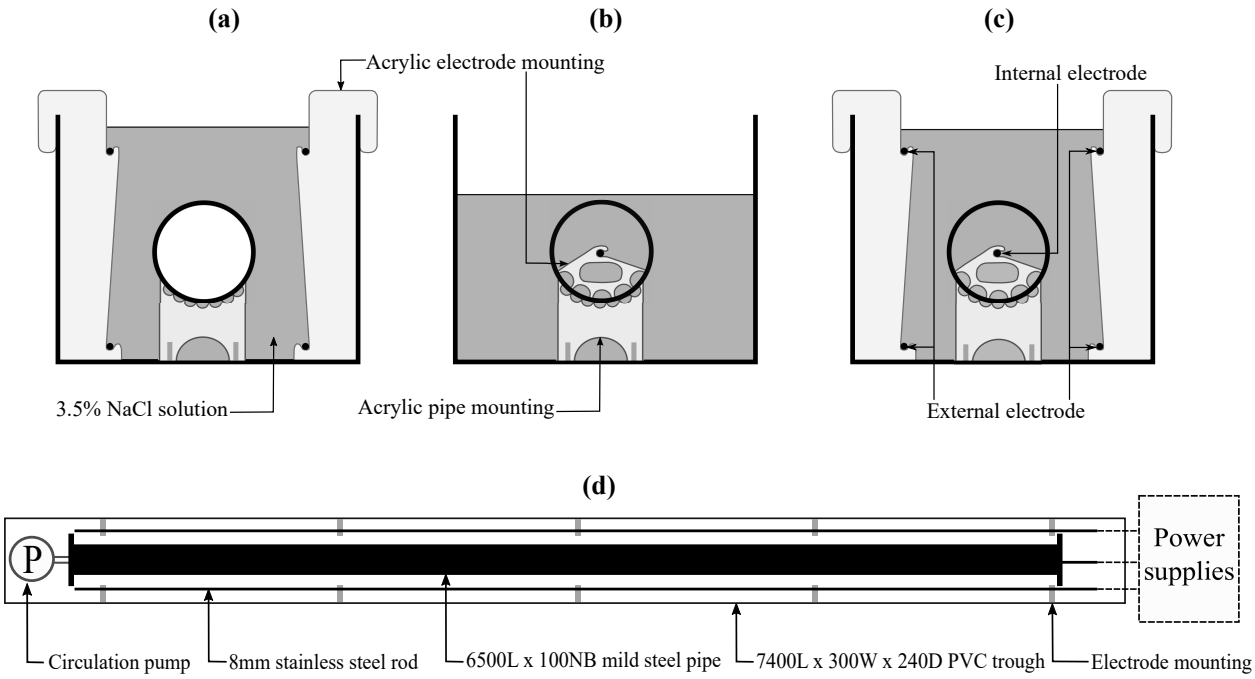

FIGURE 8.5: Diagrams of pipe corrosion set-up: elevation view of (a) external-only specimen, (b) internal-only specimen, (c) internal-external specimen, and (d) plan view of the deterioration cell.

FIGURE 8.6: Photograph of large-scale pipe corrosion set-up

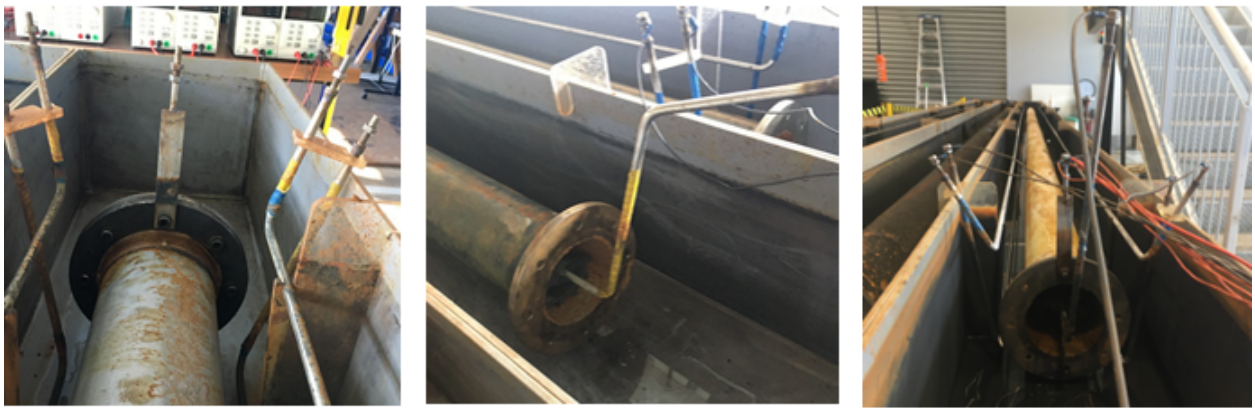

(a) (b) (c)

FIGURE 8.7: Photographs of electrode terminations for (a) external-only, (b) internal-only, and (c) internal-external

TABLE 8.2: Full-scale corrosion test conditions. The expected corrosion rate is 80% of the theoretical corrosion rate, as observed for the small-scale specimens.

	Internal only	External only	Internal+External	
			Internal	External
Current per electrode (A)	9.8	5.0	2.4	9.6
Number of electrodes	1	4	1	4
Total current (A)	9.8	19.9	9.6	9.6
Theoretical corrosion rate (mm/day)	0.015	0.031	0.015	0.015
Expected corrosion rate (mm/day)	0.012	0.025	0.012	0.012
Cleaning interval (days)	4	4	4	4
Transient testing interval (days)	16	8	8	8

The specimens were cleaned at 4-day intervals to manage build-up of precipitates and pitting of the pipe surface. The electrolyte solution and accumulated precipitates were pumped from the troughs, and the troughs and specimens cleaned. For specimens undergoing internal corrosion, the internal surface was cleaned using a 150 mm polypropylene flue brush attached to a 4.5 m rod. Following cleaning, the specimens were re-submerged in fresh NaCl solution.

Wall thickness measurements were taken at 8-day intervals for the external-only and internal-external specimens, and at 16-day intervals for the internal-only specimen. The wall thickness measurements were collected using a Sauter Thickness Gauge TN 80-0.01 ultrasonic scanner. For the internal-external specimen, the external diameter was measured using an 0.01 mm precision micrometer to quantify the distribution of losses from the internal and external surfaces. The specimens were lightly sanded to ensure a smooth surface. Spot measurements were taken in an evenly spaced grid, with 32 nodes along the specimen length (200 mm spacing) and 4 nodes around the specimen circumference. Five ultrasound measurements were taken at each location and averaged.

The surface corroded relatively smoothly without noticeable deep pits forming. Rather, the surface was uniformly covered in shallow pits of approximately 1 mm diameter. This shallow pitting, combined with the sanding performed before each round of wall thickness testing, meant that the surface remained smooth enough to provide a contact surface for the ultrasonic sensor. The pits that formed on the internal surface, which could be observed at the ends of the pipe, became deeper over time compared to those on the external surface, likely because the surface was not sanded at regular intervals. The corrosion was continued until the samples perforated, as from that point they could no longer be pressurised. Figure 8.8 below shows the pitting behaviour and the eventual perforation of the external-only sample.

FIGURE 8.8: Photograph of the pitting behaviour observed for the external-only sample and the eventual perforation of the surface.

Transient testing

The specimens were subjected to transient testing at 8-day intervals for the external-only and internal-external specimens, and at 16-day intervals for the internal-only specimen, following the completion of wall thickness measurements. The transient testing apparatus is shown in Fig. 8.9. The pipe is inclined at an angle of 3.5°. The transient generation system was mounted at the low end. The system was a 150 mm long section of mild steel pipe with the same dimensions as the corrosion specimens. A ring of five computer-controlled solenoid valves were attached around the

circumference of the section. A flange plate with a ball valve was fitted at the high end of the specimen.

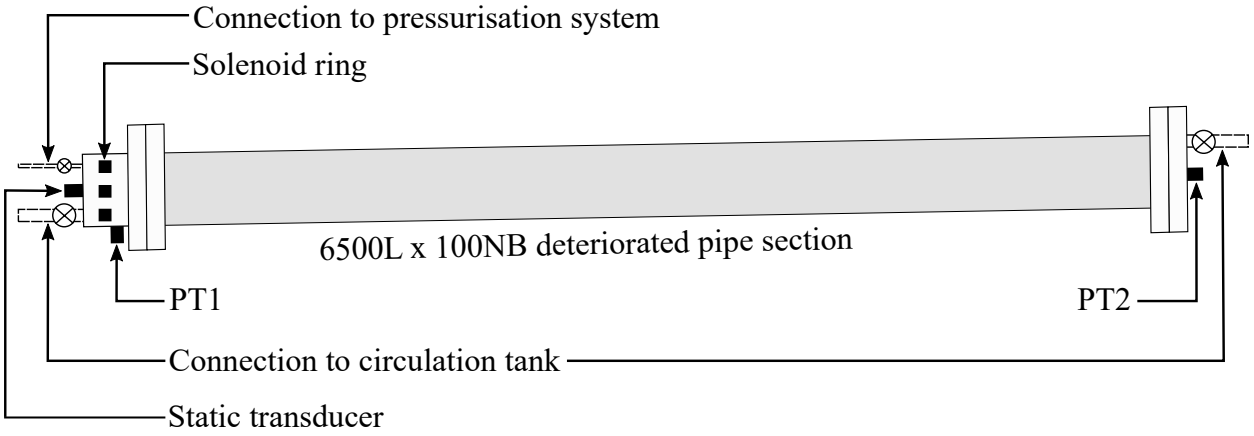

FIGURE 8.9: Transient testing configuration

The specimen was filled from the low end with clean water from a circulation tank through a ball valve and hose connection and a Pedrollo TopFloor2 pump. A similar ball valve and hose connection at the high end was opened which drains back into the circulation tank, and flow was permitted to circulate for approximately 10 minutes to allow trapped air to leave the pipe. At the end of the circulation period, the ball valves connecting the pipe to the circulation tank were closed and the specimen was pressurised. The pressurisation system consisted of a computer-controlled air over water tank, which was set to a gauge pressure of 3.0 bar. The specimen was connected to the tank via a length of 8 mm OD Ledalon N12 tubing, and reached a pressure of approximately 3.3 bar after opening the connecting bleed valves. Following pressurisation, the ball valve at the high end was opened for a short period to allow collected air to escape. The specimen remained connected to the pressurisation system for the duration of the transient tests.

The transient signal was generated using the ring of 5 Baccara GEM-SOL Direct Operated side discharge solenoid valves (2.4 mm orifice, 1/4-inch port). The valves were simultaneously opened and closed over a period of 6 ms to generate the transient pulse. The control system for the valve was designed and made at the University of Canterbury. The pressure disturbances were measured by three transducers for a period of 3 seconds following the transient pulse generation, enough

time for the system to return to steady state. An IPS Series 7975011 static transducer mounted on the end plate of the transient generator section measured the gauge pressure during the transient test. PCB Piezotronics Model 102A07 dynamic pressure transducers were fitted on the transient generator section (PT1) and the end plate (PT2) to measure relative pressure disturbances. The sampling frequency for the transducers was 100,000 Hz.

To assess experimental error, the transient signal was repeated 20 times for each corrosion case. The intervening period between tests was approximately one minute, to ensure the transient disturbances had damped entirely before starting the next test. A standard error was calculated for each time step in each experimental scenario. Over the time period of interest, including the incident pulse and first pulse measured at PT2, the average standard error was less than 0.4% of the pressure reading. As previously discussed, a range of precautions were taken to manage air in the system. Water was left standing overnight in the circulation tank before filling to allow air to leave solution, as the mains supply has been observed to have a relatively high air content. After bleeding the pipe following pressurisation, preliminary transient tests were carried out to ascertain whether any air was present in the system, identified by additional reflections or reductions in the expected system wave speed. Additional circulation and bleeding was carried out until the air was removed.

8.3 Results

8.3.1 Accelerated corrosion

The observed variations in average wall thickness with time for the external-only, internal-only, and internal-external cases are plotted in Figs. 8.10, 8.11, and 8.12 respectively. The theoretical losses predicted by Faraday's Law and the expected losses based on the small-scale tests are plotted for comparison.

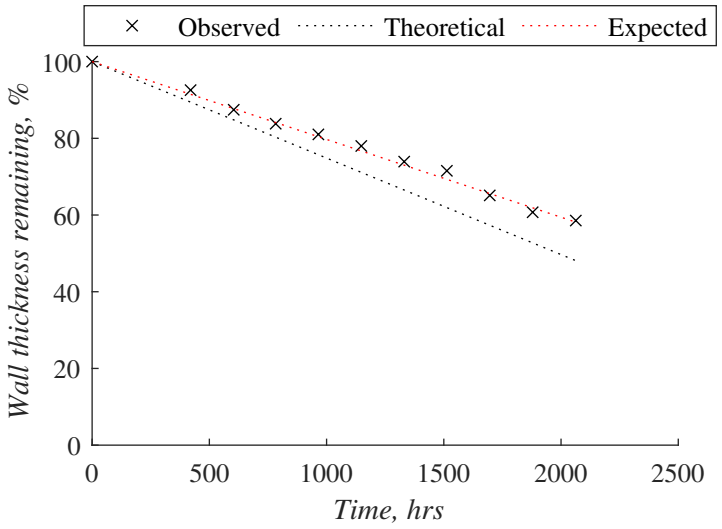

FIGURE 8.10: Variation in average wall thickness with time for the large-scale external-only corrosion case compared to the theoretical prediction by Eq. 8.1

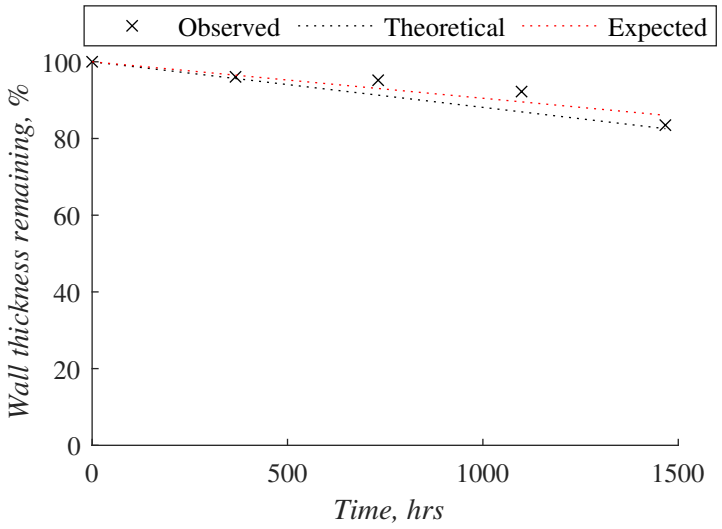

FIGURE 8.11: Variation in average wall thickness with time for the large-scale internal-only corrosion case compared to the theoretical prediction by Eq. 8.1

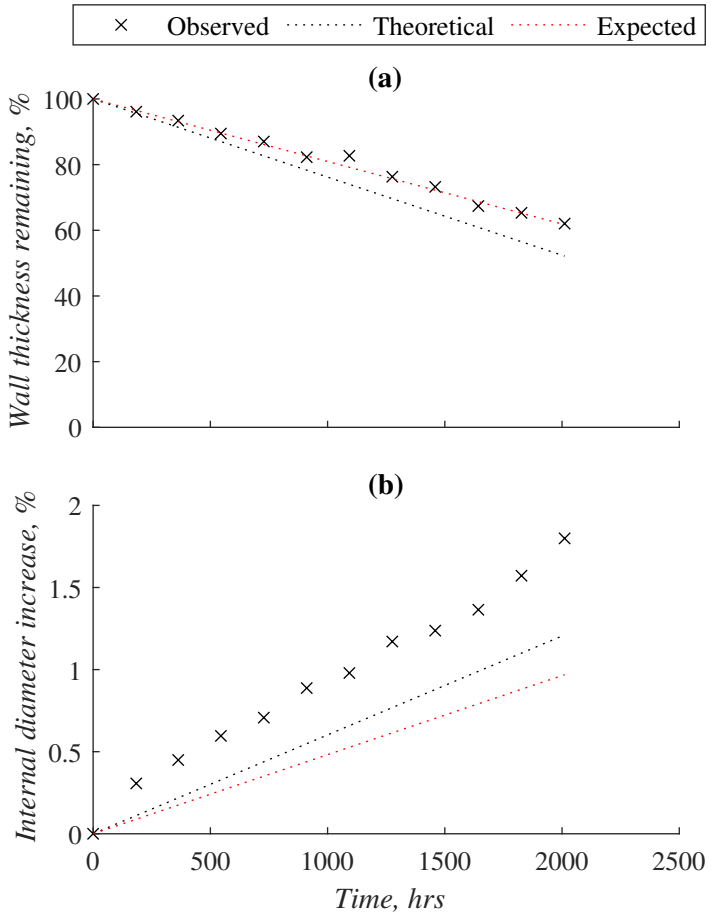

FIGURE 8.12: Variation in pipe cross-section dimensions with time for the large-scale internal-external corrosion case: (a) Average wall thickness (b) Internal diameter compared to the theoretical prediction by Eq. 8.1

In most cases, the corrosion rates observed in the small-scale tests could be used to predict the corrosion rates for the large-scale specimens. The variation in wall thickness from the expected values was approximately 0.75% across the three corrosion cases. For the internal-external case, the observed increase in internal diameter was approximately 1.9 times greater than expected, indicating that greater material loss occurred on the internal surface compared to the external surface. Limitations on the current that could be applied to the internal surface without excessive by-product formation meant that only 17% wall thickness loss was achieved for the internal-only sample over a 1500 hour corrosion period, corresponding to approximately 3 months. The relatively slow corrosion rate limited the amount of data that could be collected from the specimen.

The variability in wall thickness increased as corrosion progressed, as shown in Figs. 8.13, 8.14, and

8.15 for the three corrosion cases. For the first time steps, the average variation in the wall thickness samples relative to the specimen mean was less than 2%. As the corrosion time progressed up to the maximum time period of over 2000 hours, this increased to approximately 10% for the external-only and internal-external specimens. The variation was observed to be relatively consistent along the specimen length and around the specimen circumference for the three corrosion cases, without significant spatial trends in the corrosion. The exception to this was adjacent to the pipe ends, which were subject to a greater degree of corrosion, particularly next to the Denso-Tape seam covering the pipe join and flange welds. It is likely that preferential corrosion occurred in these regions due to the greater concentration of current as less pipe material was exposed. As shown previously in Fig. 8.8, this was where the first perforation occurred on the samples. The variability observed along the pipe length and around the circumference may be attributed to heterogeneities in the pipe material and the formation of corrosion pits, which can act as focal points for increased corrosion (Mohebbi and Li, 2011). However, this is likely representative of the corrosion variability which may occur in a field pipe subjected to natural variations in the surrounding soil conditions (Denison, 1931; Rodhe and Herrera, 1988; Rajani and Kleiner, 2001).

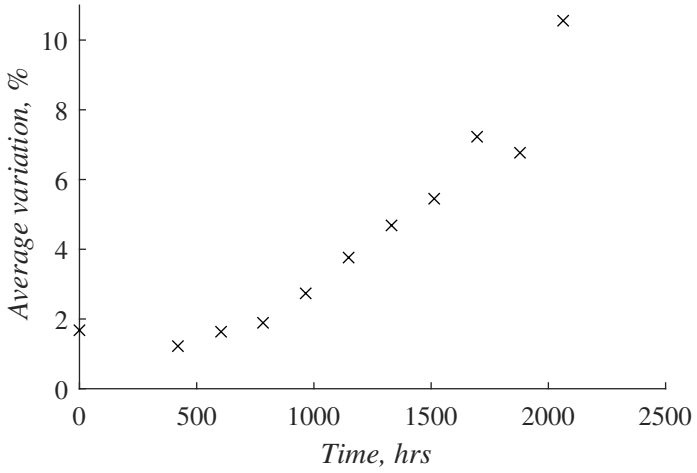

FIGURE 8.13: Average variation in wall thickness relative to the specimen mean for external-only corrosion case

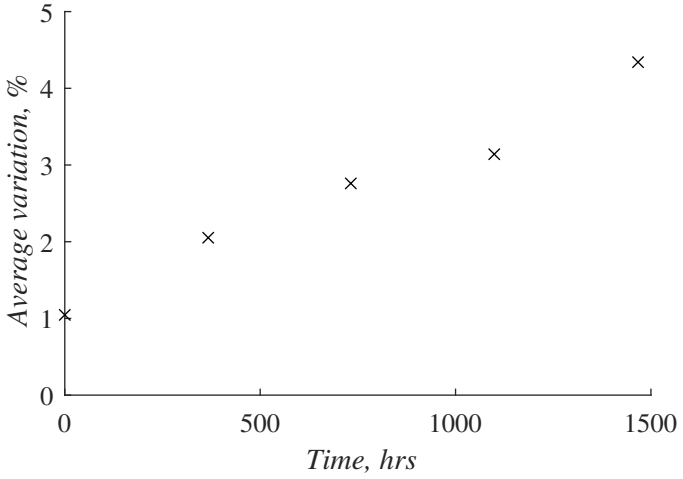

FIGURE 8.14: Average variation in wall thickness relative to the specimen mean for internal-only corrosion case

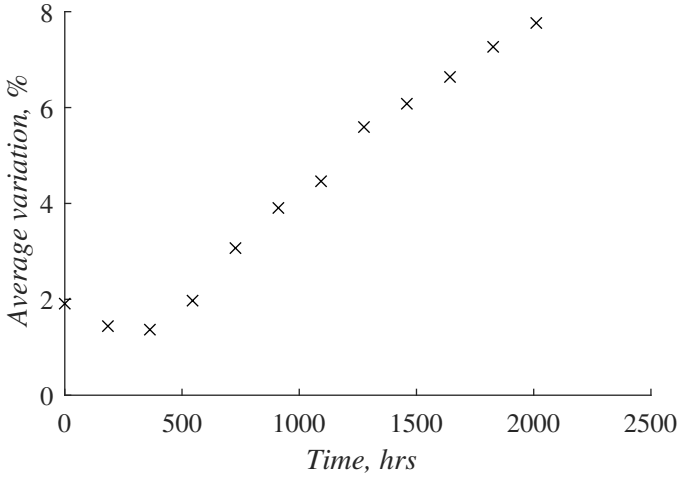

FIGURE 8.15: Average variation in wall thickness relative to the specimen mean for internal-external corrosion case

8.3.2 Transient testing

The experimental transient testing returned sets of pressure traces showing the pressure disturbances at PT1 and PT2 with time following the generation of the solenoid pulse, for each corrosion scenario and wall thickness loss case. These measurements were collected on either end of the corroded section at a separation of 6.59 m. Figure 8.16 shows example traces measured at PT1 (the transient generation point) and PT2 (the other end of the corroded section). The pressure traces presented have been normalised by the initial hydrostatic pressure such that $H^* = H/H_0$, where H = measured

gauge pressure at any time and H_0 = steady-state initial hydrostatic pressure measured by the static transducer.

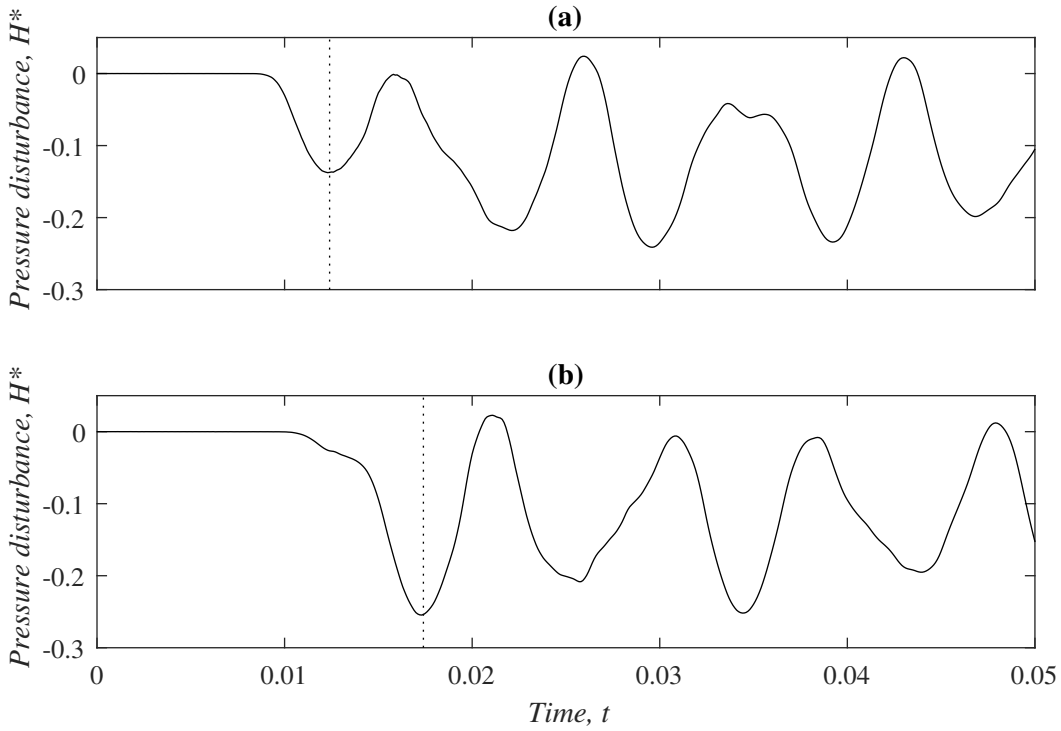

FIGURE 8.16: Example pressure traces measured at (a) PT1, the transient generation point, and (b) PT2, the other end of the corroded section, 6.59 m from the transient generation point. The approximate arrival time of the initial pulse at each sensor is marked with a dotted line. The pressure disturbance H is scaled by the initial hydrostatic pressure.

The experimental wave speed was evaluated based on the lag time between the incident pulse measured at PT1 and the transmitted pulse measured at PT2. The cross-correlation of the two series was used to measure their relative displacement, with the wave travel time corresponding to the lag time at which the cross-correlation is maximised. The distance between the two sensors (6.59 m) was then used to evaluate the wave speed for each scenario.

Alternatively, the wave speed may be determined from the measured wall thickness data and the theoretical wave speed equation (Wylie et al., 1993)

$$a^2 = \frac{K_f}{\rho} \frac{1}{1 + c\frac{K_f D}{eE}} \tag{8.2}$$

where K_f = bulk modulus of elasticity of the fluid; ρ = fluid density; c = constraint condition; D = pipe internal diameter; e = pipe wall thickness; and E = Young's modulus of elasticity for the pipe material. Assuming that the corrosion process does not affect the modulus of elasticity of the remaining steel (Stephens et al., 2008), the measured wall thickness and internal diameter can be used to estimate the wave speed. In the Yang et al. (2020) accelerated corrosion experiments, no substantial change was observed in the modulus of elasticity compared to the uncorroded case up to corrosion degrees of 70% wall thickness loss.

Figures 8.17, 8.18, and 8.19 compare the wave speeds estimated by direct measurement and the theoretical equation for the three corrosion cases. A moderate negative relationship was observed between the degree of wall thickness loss and wave speed for the external-only and internal-external cases. The limited data collected for the internal-only specimen restricted the conclusions that could be drawn for this case. Although a degree of variability was observed in the time series trend, for an individual time interval the average variation in the wave speed across the 20 transient tests was less than 1%. This suggests that the variations observed with time are not created by experimental error due to the sampling rate or pipe length. The variations may be attributable to disparities in the air content of the mains supply or tiny air bubbles, which were not overcome through the settling, circulation, and bleeding procedures. On average, the theoretical equation overestimated the measured wave speed by 0.16%, 1.5%, and 1.1% for the external-only, internal-only, and internal-external cases respectively.

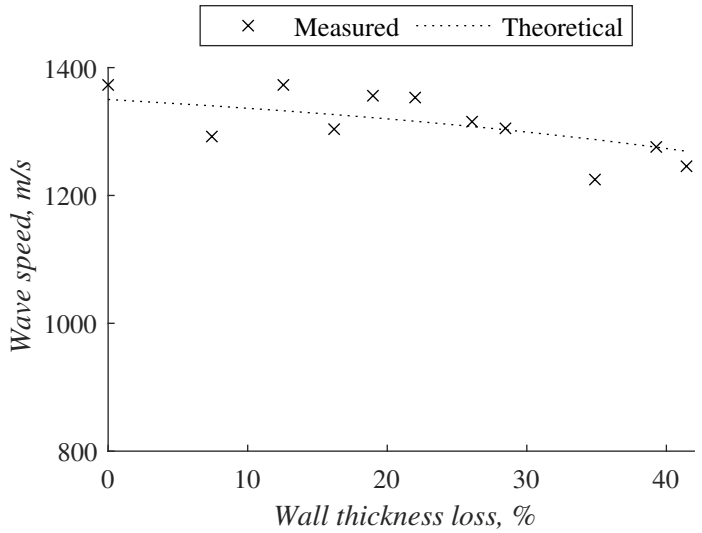

FIGURE 8.17: Wave speeds estimated for the large-scale external corrosion case for degrees of wall thickness loss from direct measurement and the theoretical equation (Eq. 8.2)

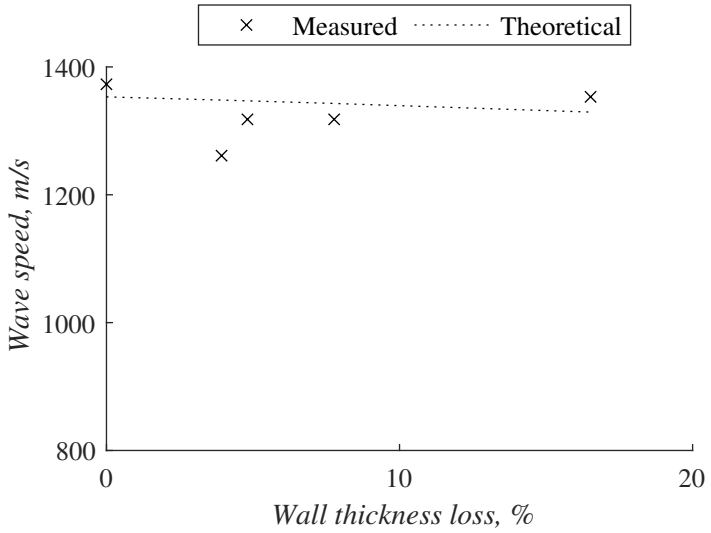

FIGURE 8.18: Wave speeds estimated for the large-scale internal corrosion case for degrees of wall thickness loss from direct measurement and the theoretical equation (Eq. 8.2)

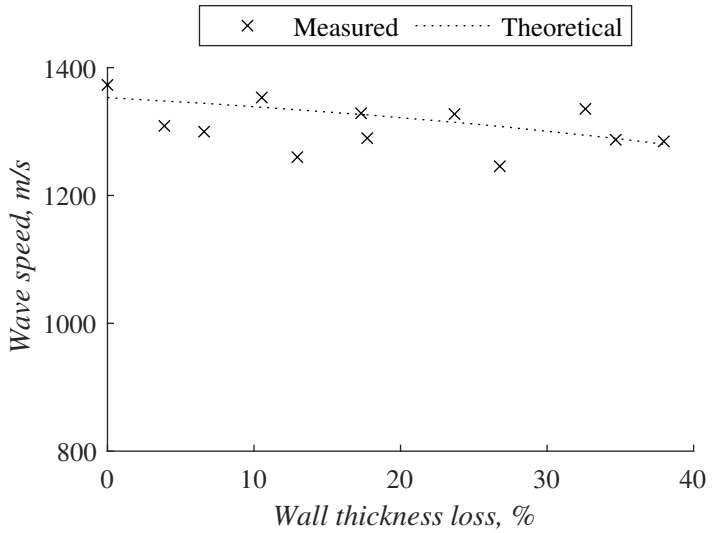

FIGURE 8.19: Wave speeds estimated for the large-scale internal-external corrosion case for degrees of wall thickness loss from direct measurement and the theoretical equation (Eq. 8.2)

Over the maximum wall thickness loss of approximately 40%, a reduction of approximately 6% was observed in the measured wave speed. If the theoretical equation is assumed to apply as the pipe continues to lose material, the wave speed may reduce by a further 40% (to approximately 800 m/s). This corresponds to a 90% wall thickness loss and extreme leakage or bursting risk. Figure. 8.20 shows the theoretical wave speed reductions which may occur with wall thickness loss for the three experimental corrosion cases, assuming that loss occurs equally on the internal and external surfaces for the internal-external case. As the original pipe diameter was approximately 100 mm, the increases in internal diameter were relatively small (<5%), even in the case of severe corrosion. This means that the loss in wave speed for pipes of this size is primarily governed by the wall thickness loss, meaning the effects of internal and external corrosion may be indistinguishable. For smaller pipes, the variation across corrosion cases will increase as changes to the diameter due to internal corrosion become more significant. Figure. 8.20 indicates that if a change in wave speed is conclusively identified through direct measurement of pulse arrival times the pipe is likely to be severely corroded. This is particularly true for areas with relatively heterogeneous soil conditions, where corrosion is limited to short sections. Direct measurement may also be used to identify sections where the pipe material has been incorrectly recorded in the network database.

For instance, similarly sized PVC and other plastic pipes may have wave speeds of approximately 400 m/s, meaning direct measurement of wave speed could be utilised in record verification.

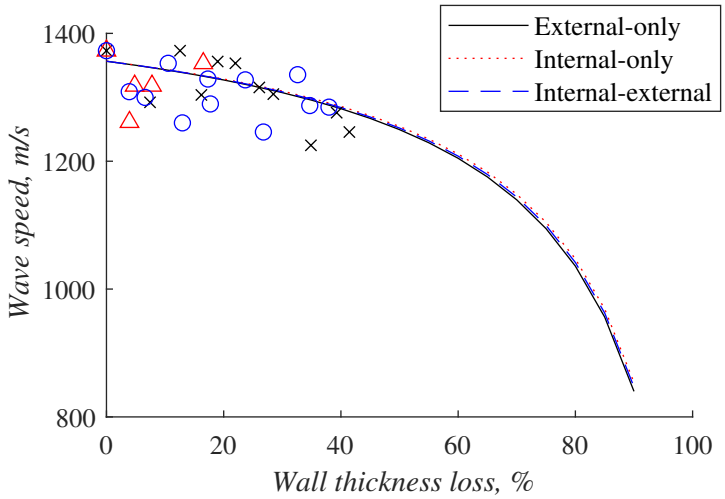

FIGURE 8.20: Theoretical wave speeds for varying degrees of wall thickness loss for a range of corrosion scenarios (external-only, internal-only, internal-external). The experimental data points are plotted as coloured scatter points corresponding to the given corrosion case.

In addition to direct measurement of the wave speed, the reflections created at corroded sections may also be used to identify and characterise wall thickness loss. This method has been explored in previous experimental work (Gong et al., 2013b, 2012; Hachem and Schleiss, 2012). As discussed in Chapter 3 for the in-line air pocket case, the size of the transient reflection from a discontinuity is determined by the impedance change. The impedance is given by $Z = \rho a/A$, where ρ = fluid density and A = cross-sectional area of the pipe (Gong et al., 2013a). It can be used to determine the theoretical reflection coefficient, RC, for the interface between an intact pipe and corroded pipe. The reflection coefficient is defined as

$$RC = \frac{Z_C - Z_0}{Z_C + Z_0}, \tag{8.3}$$

where Z_C = impedance of the corroded pipe section; and Z_0 = impedance of the intact pipe. The theoretical reflection coefficients estimated for the three experimental corrosion cases are plotted in Fig. 8.21. For the case where part of the pipe is corroded but neighbouring sections remain

intact, *RC* can increase to approximately 0.25. Greater variability may also be observed across the possible corrosion scenarios, with internal-only corrosion resulting in the smallest *RC* for a given wall thickness loss, as the reduction in wave speed is balanced by the increase in the cross-sectional area.

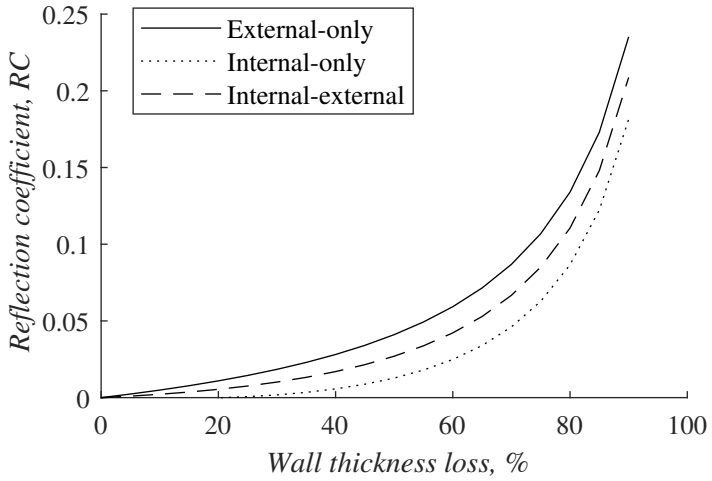

FIGURE 8.21: Theoretical reflection coefficients for varying degrees of wall thickness loss for a range of corrosion scenarios (external-only, internal-only, internal-external)

8.4 Conclusions and recommendations

Previous investigations into the transient interaction with a deterioration pipe section have either represented deterioration in the laboratory as a section with a thinner wall or material with lower wave speeds, or carried out field testing on real deteriorated pipe. However, access limitations in the field mean that the true pipe condition cannot always be accurately measured. This section focused on investigating a method for corroding mild steel pipes in the laboratory, enabling a controlled corrosion rate and testing at a range of wall thickness loss intervals which may correspond to years or decades in the field.

An accelerated corrosion process for steel has been used for applications relating to reinforced concrete and corrugated culverts, but the method has not previously been applied to pipes. Small-scale preliminary investigations identified key considerations for the accelerated corrosion of mild steel pipes in an electrolytic cell. In particular, by-product build-up and current application must

be carefully managed to ensure the pipe surface remains exposed and without significant pitting, to allow for continued corrosion and the collection of wall thickness measurements.

Large-scale specimens were corroded over a period of approximately 3 months, achieving wall thickness loss of up to 40%. Three corrosion cases were tested, external-only, internal-only, and internal-external. The corrosion rates observed in the small-scale specimens could be used to predict the degree of wall thickness loss in the large-scale specimens with an error of approximately 0.75%. Wall thickness measurements and transient wave testing were carried out at regular intervals. The direct measurements of the transient wave speed were compared to those estimated using the measured wall thickness and internal diameter and the theoretical wave speed equation. A moderate negative relationship was observed between wall thickness and wave speed, and the outputs of theoretical equation agreed with the direct measurements with an error of less than 5%. The experiments were constrained by time, particularly for the internal-only case, with the considerations identified previously restricting the corrosion rates that could be achieved, and hence the variations in wave speed that were observed. The measured wave speeds were likely subject to temporal variability due to testing conditions which could not be adequately controlled, such as the the small quantities of air in the pipe. These inconsistencies will also occur in the field, with additional limitations on the level of control that can be achieved. As fine precision may not be practicable, direct measurement of the wave speed will likely be most useful in identifying severely corroded sections or sections of differing material, where expected wave speed variations are in the order of 100-1000 m/s.

The accelerated corrosion of pipe sections in the laboratory represents an interesting research area for transient-based fault detection studies. It is recommended that future studies further explore the corrosion process to identify methods of increasing the possible corrosion rates without the need for increased cleaning, as down-time associated with specimen cleaning could outweigh the time savings. This would enable experimentalists to achieve greater wall thickness loss and observable wave speed changes in a manageable time-frame. Future transient testing should also explore the possibility of constructing a series system where the corroded pipe can be connected to an intact

pipe. This would enable measurement of the reflection coefficient of the wave reflected at the interface in addition to direct measurement of the wave speed.

9 Practical implications

The findings presented in Chapters 3-8 will be used to inform transient-based condition assessment methodologies. This chapter considers the practical considerations around diagnosing air pockets and deteriorated pipe sections in the field.

9.1 Detection of air pockets in the field

9.1.1 Identifying features

In Chapters 3-7, a series of unique features were identified for diagnosing air pockets:

- **Reflection phase:** Both in-line and off-line air pockets create an out-of-phase reflection due to the reduction in impedance at the air pocket location, unlike a discrete or extended solid blockage, which increases the impedance of the pipe section. A deteriorated pipe section will also create an out-of-phase reflection if the wave is transmitted from a region of low deterioration to a region of high deterioration.
- **Reflection amplitude:** The amplitude of the transient reflection due to an in-line or off-line air pocket is independent of the system base flow, unlike solid blockages and leaks which will produce a smaller transient reflection under no-flow or low-flow conditions.
- **Frequency signature:** Due to its compressibility, an air pocket will produce a frequency dependent reflection. This enables differentiation between in-line and off-line air pockets, as an in-line air pocket acts as a low-pass filter, while the reflectivity of an off-line pocket is maximised at its resonant frequency. This effect is unique to air pockets among other

common pipeline anomalies, such as leaks and blockages, which reflect and transmit all frequencies in the incident signal equally.

- **Wave speed signature:** An air pocket will cause a local reduction in the wave speed due to the increased void ratio. A reduction in the wave speed can also be observed in deteriorated pipe sections due to the reduction in the wall thickness. Both can affect the arrival times of subsequent signals at receivers. An air pocket results in a relatively significant reduction in wave speed (often by an order of magnitude) in a localised region, whereas a deteriorated section will generally result in a smaller reduction in wave speed (up to approximately 50%) over an extended length of pipe. Furthermore, the reduction in wave speed due to an air pocket may be temporary as air has the potential to dissolve or move elsewhere in the pipe. This highlights the important of repeating testing at intervals before commencing excavations to repair or replace sections of pipe where reduced wave speed is observed, as entrapped air easily be mistaken for corrosion.

9.1.2 Identification methodology

Steady-state monitoring represents a good starting point for diagnosing air pockets in pipeline systems, as a problematic in-line air pocket is often identifiable due to the resultant restriction of flow and increased energy costs. This may also be the case for off-line pockets which have grown to exceed the volume of their cavity. However, an air pocket cannot be easily differentiated from a solid blockage at steady-state without either excavation or disruptive changes to the flow regime to attempt to sweep the potential pocket from the system. The transient-based techniques identified in this paper represent a method for characterising the blockage type non-invasively, so that the appropriate remediation techniques can be applied with confidence. Air pockets may also be identified indirectly as part of diagnoses of other known faults. For instance, the pipe may be tested for the transient response of a known leak, and previously unidentified in-line or off-line air pocket may be found due to its interference pattern in the response.

Once a steady-state blockage's rough location has been determined based on steady-state observations, transient testing can be carried out with receivers in a range of locations measuring the transient response. As the features summarised above are based on the underlying physics governing the transient-fault interaction, they provide consistent indicators of fault type. The reflection phase, frequency signature, and wave speed signature can be used as indicators of an air blockage versus a solid blockage. Both the reflection amplitude and the frequency signature may be used to estimate the air pocket volume. The methodology offers flexibility in that multiple features are available to assess the characteristics of the air pocket, for instance, in the case that a full pulse cannot be extracted for frequency analysis, the air pocket may be characterised based on the reflected or transmitted peak phase and amplitude.

Once an air pocket is identified based on the response characteristics, determining its location generally becomes a function of other parameters related to the system rather than the fault itself. While it is important to differentiate between fault types and severity so that remediation work may be appropriately prioritised, it is also critical that faults are accurately located, to minimise the cost and disruption associated with remediation. In time domain reflectometry, the fault location can be obtained using the estimated wave speed and the elapsed time between measured reflected signals.

Transient testing in the field is likely to be an iterative procedure, and the techniques used will vary on a case-by-case basis. The initial aim is to identify the transient transmission, which can generally be done using signal processing techniques. A deviation in wave speed or frequency content can be used to obtain an initial indication that an air pocket is present. However, a transient reflection is required to narrow down the location of the fault. If the transient reflection and transmission are not immediately identifiable, options include generating the transient from the other end of the system or moving the generator or receivers to another access point. It was also found that numerical models in the time or frequency domain can be used to predict the response due to an air pocket with relative accuracy during the first few periods, though the match is likely to deteriorate with ongoing reflections. These models may be utilised as a part of an inverse analysis, though it is important to account for errors in the model around wave amplitude and timing, which may lead

to inaccuracies in predictions of pocket volume and location.

9.1.3 Limitations and uncertainty

The methodology outlined above primarily relies on the ability to extract individual reflections and transmissions arising from the pipeline anomaly. This means that, particularly in the case of air pockets, it is important to select a relatively high-frequency input transient signal. This ensure that it contains a frequency band sufficient to capture the frequency-dependent behaviour, and that the signal wavelength is short enough that reflections and transmissions may be isolated.

The primary limitation of the detection approach is the complexity associated with field systems. Transient disturbances and reflections are created not just by anomalies, but also by system components such as pipe bends, inlets and outlets, and junctions, valve movements, and ongoing noise associated with road loading and water usage. There is also a significant amount of attenuation in real systems compared to designed laboratory systems. Both of these considerations limit the amount of useful information that can be obtained in a real system. In many cases, the reduction in wave speed associated with an air pocket may be the most reliable indicator if the details of reflections and transmission are obscured. This highlights the importance of regular testing, as a sudden drop in wave speed can be used to diagnose air as opposed to the gradual reduction which may be observed as pipes deteriorate.

Uncertainty will also arise in locating air pockets due to considerations such as the accuracy of the wave speed estimation and the distance of the fault from the sensor. In particular, aging pipes in heterogeneous soils may yield highly uncertain results due to the potential for variable wave speed along the pipe length as a result of corrosion. The air pocket is also unique in that it creates a lag in the signal, which adds a further element of uncertainty when estimating the fault location. The optimum approach is to carry out testing with multiple sensors distributed along the pipe length, as this increases the probability of capturing reflections close to the fault, minimising the effects of wave speed uncertainty.

9.2 Detection of deterioration in the field

9.2.1 Identifying features

Deterioration of the pipe wall has been observed to affect the transient wave speed. Transient waves travel more slowly through weak- or thin-walled sections. A reduction in wave speed over an extended length of pipe is most likely to be attributable to corrosion on the internal surface, the external surface, or both. As discussed above, air pockets will also cause a reduction in wave speed. However, this is generally a relatively localised reduction which may vary with time as the air pocket grows, fragments, or moves elsewhere in the pipe. Except in extremely heterogeneous soils, pipe deterioration occurs along an extended reach of pipe, and the associated wave speed reduction is permanent and generally occurs gradually over a time-scale of years.

9.2.2 Identification methodology

Pipe corrosion is often more difficult to detect at steady-state than an air pocket. In the case of internal corrosion, deposits may form which compromise water quality and aesthetics, and eventually corrosion may lead to water losses through minor leaks. Areas of likely corrosion may also be identified through a desktop assessment of asset age and the soil environment properties. Once an area of interest has been identified, transient testing can be carried out. The wave speed is best assessed by determining the travel time between two points in the time domain or the frequency domain. As discussed in Chapter 8, if a conclusive change in the wave speed is identified it is likely that the pipe is severely corroded, as the wave speed begins to drop rapidly beyond a wall thickness loss of approximately 40%. The theoretical equation for the wave speed can be used with the pipe material and diameter to estimate the remaining wall thickness.

Similar to the air pocket, reductions in wave speed associated with deterioration can also be incorporated into inverse system models used as part of diagnostics. This work did not evaluate the accuracy of the numerical models for corroded sections.

9.2.3 Limitations and uncertainty

The deterioration work discussed in Chapter 8 was primarily meant as an exploration of the accelerated corrosion method and how it may be utilised to test real corroded pipes in the laboratory. As an initial feasibility study, it covered the simplest case study of uniform corrosion, with an effort made to maintain smooth surfaces to enable operation of the ultrasound scanner. There is potential to extend the approach to explore scenarios that may occur in the field such as deep pitting and non-uniform corrosion. This could provide an interesting complement to work that has been done previously in the field to better understand transient responses in aging pipes and expand on the methodology outlined above.

As discussed, both corrosion and air pockets can cause wave speed reductions. If a wave speed reduction is observed, it is recommended that testing be carried out at the same location on several additional occasions to increase certainty that the wave speed reduction is due to corrosion rather than an entrapped air pocket. However, in some cases air can become firmly trapped, and may not move during the testing period. As discussed above, a number of techniques exist for identifying air pockets which may form a complement to the wave testing approach.

In transient wave speed testing the spacing between sensors must be carefully considered. Sensors should not be too far apart, as the signal may be lost due to attenuation and other system reflections. As discussed for the air pocket case, system interference is likely to be a significant source of uncertainty and may limit the amount of useful information that can be gained from this approach in a real system. However, transient waves travel at speeds of over 1,000 m/s, meaning that if sensors are too close together it may not be possible to discern wave speed changes within their sampling resolution.

9.3 Repair strategy

The matter of fault detection is separate to the matter of remedial action. Once a fault such as an air pocket has been successfully detected and characterised, network authorities face the question of the

next action to take. Unfortunately, it is not practical to simply define an "action level" where repair or remediation should be carried out. Pipe networks are beset with ongoing operational issues including the gradual formation of blockages and air pockets, the sudden development of leaks, and the risk of contamination or perforation due to corrosion. As a result, network management is highly dependent on the client and their budget. Limited resources mean that anomalies will be treated with consideration to how their effects rank in comparison to other network issues. For example, an air pocket on a smaller pipe branch will be prioritised below an air pocket blocking flow on a main trunk. Similarly, a solid blockage may be treated before an air blockage as the air blockage has greater potential to dissolve or break apart. The aim of transient-based fault detection is to provide the network manager with the information they require, such as the size and location of an air pocket, which can be converted to an approximate cost with regard to loss of flow and energy usage. This information can then be fed into a decision-making framework, which falls in the field of infrastructural management. The aim of transient testing is to maximise the available information about the network to help inform decision-making, while minimising the cost and disruption associated with obtaining that information.

9.4 Future research

The practical implications of this work's findings should direct future research. The primary source of uncertainty at this stage is the applicability of the findings in real field systems which contain many sources of noise and reflections. While useful features could be identified in a heavily controlled laboratory environment, the method is yet to be validated in more complex laboratory systems or in the field. As an initial step, it may be useful to recreate more complex scenarios containing junctions and other anomalies in the laboratory so that the properties and location of the air pocket or deterioration can still controlled. However, the ultimate feasibility assessment is in the form of field studies where the anomaly characteristics are unknown. The complexities associated with field testing will likely require additional developments to the method outlined above.

10 Conclusions and recommendations

10.1 Summary and conclusions

10.1.1 Overall objectives

Fluid transients may be used as a non-invasive pipeline diagnostic technique, allowing long stretches of pipe to be assessed with a short period of time. Transient-based testing involves the analysis of measured pressure fluctuations to identify and characterise pipeline anomalies based on their effects on transient amplitude and timing. The aim of this thesis was to improve understanding of how transient pulses interact with selected pipeline anomalies, particularly those which have received little experimental attention. The findings may be used to supplement transient-based condition assessment technologies for water supply networks.

The work of this thesis focused on the transient interaction with two main fault types: entrapped air pockets and deteriorated sections. While numerous experimental and numerical investigations have characterised the effects of leaks and solid blockages on the transient response in depth, air pockets and deterioration have received less attention, perhaps because they are more difficult to recreate in a laboratory setting. However, to carry out effective transient diagnoses it is important to understand the effects of the range of anomalies that may occur. Specific conclusions regarding each fault type are summarised below.

10.1.2 Entrapped air pockets

The effects of air on transient signals are important to understand for a variety of reasons. As well as having the potential to damage pipelines and increase operating costs, air pockets are also known to create significant transient responses even when only present in small quantities. This means that when using transients as a condition assessment tool it is critical to understand the impact of air and to be able to model it accurately. Previous studies on air pockets have primarily focused on the contribution of air in damping or amplifying damaging transient events, rather than identifying specific characteristics of the reflection and transmission of controlled transient signals. Controlled experiments using rapid transients were required to gain further insight into this application.

In this thesis, experiments were carried out in the laboratory to collect data for a range of in-line and off-line pocket volumes under realistic system conditions. A rapid transient pulse was used to maximise the information that could be obtained from the waves reflected and transmitted by the air.

The experimental data for the in-line and off-line pocket configurations was used to characterise the effects of pocket volume, configuration, and initial hydrostatic pressure on the transient response via analyses in the time and frequency domain. Impedance theory was used to explain the relationship between air pocket volume and reflective power in the time domain. In addition, MOC modelling in the time domain showed that air configuration (in-line versus off-line) affects the shape of the pulses reflected and transmitted from the air pocket due to the contribution of friction and inertia in the connecting water column between the off-line pocket and the main pipe. The experiments and modelling carried out demonstrated that the air pocket response is independent of the system base flow. This means air pockets will still create sizeable transient reflections under low-flow conditions, unlike solid blockages. It is particularly valuable to identify features differentiating air pockets from solid blockages, which may be more costly to remove. The presence of air was also found to increase the transient damping rate relative to the no-air case.

Analysis of the experimental data in the frequency domain yielded useful findings regarding the

effects of air pocket volume and configuration on the transient response. The first pulses reflected and transmitted by the air pockets were extracted and converted to the frequency domain using Fourier transforms. The reflectivity of the air pocket was shown to be frequency dependent, with this characteristic being unique to air among common pipeline faults. The frequency-dependent behaviour was hypothesised to be due to the resonant properties of air, which are influenced by the system properties and the air geometry. For the off-line configuration, the reflectivity of the air was maximised at its resonant frequency, which can be easily calculated due to its constrained state within an off-line cavity. The in-line air pocket was observed to suppress transmission above a certain frequency, though the unknown geometry of in-line pockets meant the resonant frequency could not be easily calculated. This frequency-dependent phenomenon may be used to diagnose the presence of air as well as its volume and configuration. The input pulse and boundary conditions should be carefully considered to ensure that the transient frequency range enables identification of these features.

The controlled experimental investigations presented here provided the basis for evaluating existing numerical models of the in-line pocket scenario. The in-line air pocket was modelled using the MOC, a widely used fluid transient modelling approach. The standard accumulator equation for incorporating in-line air into the MOC scheme was demonstrated to result in compounding errors in the estimation of pulse amplitude and timing. A combination of the accumulator approach with a wave speed reduction at the air pocket based on the local reduction in density was used to reduce the time delay error. The amplitude error relative to the no-air case was observed to increase with decreasing pocket volume, indicating that the rapid mass oscillations that occur for small air pockets dominated by acceleration are not be captured by the accumulator equation in its current form.

Potential modelling approaches were also evaluated for the off-line pocket configuration. The major assumption in previous studies modelling air outside the main flow path has been the lumped inertia assumption, which states that the connecting water column between the main pipe and the air interface responds as an incompressible unit. The performance of lumped inertia models

formulated based on the MOC and SFR approaches was compared to an SFR model derived using plane wave theory which allowed for compressibility in the connecting sections. The pulse timing and frequency distribution were used to assess the models' performance against the experimental data. The timing error for all approaches was less than 5%, with the MOC returning the lowest error. However, the SFR-PW model reduced the error of the predicted pulse frequency distribution compared to the lumped inertia approaches by 50-75%, with these differences likely to accumulate as the transient progresses.

10.1.3 Pipeline deterioration

Aging pipe networks are prone to wall thickness loss due to corrosion, which may occur on either the internal or external surface when the pipe material is exposed to an aggressive environment. This increases the risk of leaks and bursting. Monitoring of pipe wall thickness could result in significant cost savings through improved scheduling and prioritisation of pipe replacement based on the severity of material loss. In previous laboratory work, deterioration has been represented using thinner walled pipe sections, and while field testing has been carried out on real corroded pipes, it is often difficult to fully characterise the pipe condition in the field.

In this thesis, an accelerated corrosion program was implemented in the laboratory for a series of mild steel pipe specimens. Wall thickness measurements and transient wave speed tests were carried out at regular intervals on full-scale specimens which were corroded on the external surface, internal surface, or both. This meant a series of corrosion intervals could be tested over a period of months which is representative of years or decades of corrosion in the field.

Though accelerated corrosion via electrolysis had previously been employed for reinforced concrete and corrugated culverts, this was the first time the method had been implemented for a full-scale pipe. For the experimental procedures used, the corrosion rate was approximately 80% of that predicted by Faraday's Law for both small-scale and large-scale specimens. The primary issue encountered was by-product build-up, which had the potential to halt corrosion or pit the external surface such that ultrasound measurements could not be collected. Key considerations for controlling build-up

included restricting the applied current, cleaning at regular intervals, and circulating the electrolyte during corrosion.

Direct measurement of the transient wave speed was carried out for a range of corrosion intervals. The measured wave speed was found to agree reasonably well with the theoretical predictions based on the measured wall thickness and internal diameter. The findings were limited by the speed of the corrosion, and the observed variation was likely caused by external factors such as the air content in the mains supply. However, the observations showed that if a conclusive difference in the wave speed is observed, it is likely that the pipe is severely corroded or that the pipe material has been incorrectly recorded in the network database.

10.2 Recommendations for future work

A number of avenues exist for further study into air-transient interactions. Given the significant reflection created by small quantities of air, further investigations in this area would represent a valuable addition to current knowledge. In the experimental space, this includes testing a greater range of conditions. In the case of in-line air, base flow could be introduced to investigate the effect of air movement and ongoing shearing and fragmentation of the air. The geometry of in-line air could be studied in order to better define the resonance effects observed in the frequency domain. In the modelling field, further experiments could be carried out to test the capabilities of the approaches discussed and explore possible improvements, particularly in describing the transient response for small pocket volumes governed by rapid volume changes. Three-dimensional CFD modelling may also be employed to better understand thermal dissipation and friction and inform 1D modelling approaches. In particular, the three modelling approaches discussed for the off-line pocket configuration merit further study, to investigate the applicability of each model based on the system conditions and cavity and air dimensions.

The work on deterioration was meant to be exploratory, and this thesis aimed to investigate the electrolysis methodology for accelerated pipeline corrosion in the laboratory. The accelerated corrosion

of pipes is an interesting area of study that may be useful for other fields outside transient-based condition assessment, including materials science, water quality, and other condition assessment applications. Future studies should aim to carry out more extensive preliminary investigations, particularly focusing on how the process may be expedited to achieve greater levels of corrosion within shorter time-frames. In the transient field, it is recommended that future studies also explore the relationship between the degree of corrosion and the reflection coefficient from the interface with an intact pipe, in addition to the direct measurement of the wave travel time. This would provide an interesting comparison to previous studies where the corroded section has been represented using a thin-walled pipe.

In this thesis, heavily controlled laboratory experiments were used to improve theoretical understanding of the transient interaction with air pockets and deteriorated sections. In reality, these techniques must be shown to be effective in complex systems containing a range of transient-reflecting elements. Extensive field testing on operational systems will be required to validate the effectiveness of transient techniques as a part of a condition assessment strategy. This will require a synthesis of knowledge regarding transient interactions with common anomalies, such as leaks, blockages, air pockets, and corroded sections, as well as inherent system features such as bends, valves, and junctions.

References

Abbott, M. B. (1966). *An introduction to the method of characteristics*. American Elsevier.

Alexander, J., Lee, P. J., Davidson, M., Duan, H.-F., Li, Z., Murch, R., Meniconi, S., and Brunone, B. (2019). Experimental validation of existing numerical models for the interaction of fluid transients with in-line air pockets. *Journal of Fluids Engineering*, 141(12).

Alexander, J., Lee, P. J., Davidson, M., Li, Z., Murch, R., Duan, H.-F., Meniconi, S., and Brunone, B. (2020a). Experimental investigation of the interaction of fluid transients with an in-line air pocket. *Journal of Hydraulic Engineering*, 146(3):04019067.

Alexander, J., Lee, P. J., and Li, Z. (2020b). Investigation of the effects of base flow on the interaction of off-line air pockets with fluid transients. In *22nd Australasian Fluid Mechanics Conference*. Australasian Fluid Mechanics Society.

Alexander, J., Li, Z., Lee, P. J., Davidson, M., and Duan, H.-F. (2020c). Comparison of numerical models for the interaction of a fluid transient with an off-line air pocket. *Journal of Hydraulic Engineering (accepted for publication)*.

Alexander, J., Li, Z., Lee, P. J., Davidson, M., and Duan, H.-F. (2020d). Experimental investigation of the effects of air pocket configuration on fluid transients in a pipeline. *Journal of Hydraulic Engineering*, 146(12):04020081.

Auditor-General (2014). Water and roads: Funding and management challenges. Technical report, The Office of the Controller and Auditor-General, New Zealand.

AWWSC (2002). *Deteriorating buried infrastructure management challenges and strategies*. Office of Ground Water and Drinking Water, US Environmental Protection Agency Washington.

Barnea, D. (1987). A unified model for predicting flow-pattern transitions for the whole range of pipe inclinations. *International Journal of Multiphase Flow*, 13(1):1–12.

Beck, S., Curren, M., Sims, N., and Stanway, R. (2005). Pipeline network features and leak detection by cross-correlation analysis of reflected waves. *Journal of Hydraulic Engineering*, 131(8):715–723.

Bergant, A., Tijsseling, A., Kim, Y.-i., Karadžić, U., Zhou, L., Lambert, M. F., and Simpson, A. R. (2018). Unsteady pressures influenced by trapped air pockets in water-filled pipelines. *Strojniski Vestnik/Journal of Mechanical Engineering*, 64(9):501–512.

Bergant, A., Tijsseling, A. S., Vítkovskỳ, J. P., Covas, D. I., Simpson, A. R., and Lambert, M. F. (2008). Parameters affecting water-hammer wave attenuation, shape and timing — Part 1: Mathematical tools. *Journal of Hydraulic Research*, 46(3):373–381.

Besharat, M., Tarinejad, R., and Ramos, H. M. (2016). The effect of water hammer on a confined air pocket towards flow energy storage system. *Journal of Water Supply: Research and Technology - AQUA*, 65(2):116–126.

Bhattarai, K. P., Zhou, J., Palikhe, S., Pandey, K. P., and Suwal, N. (2019). Numerical modeling and hydraulic optimization of a surge tank using particle swarm optimization. *Water*, 11:715.

Bracken, M., Johnston, D., and Coleman, M. (2010). Acoustic based condition assessment of asbestos cement water transmission laterals. *Pipelines 2010: Climbing New Peaks to Infrastructure Reliability: Renew, Rehab, and Reinvest*, pages 815–825.

Brunone, B. (1999). Transient test-based technique for leak detection in outfall pipes. *Journal of Water Resources Planning and Management*, 125(5):302–306.

Burrows, R. and Qiu, D. (1995). Effect of air pockets on pipeline surge pressure. *Proceedings of the Institution of Civil Engineers - Water, Maritime and Energy*, 112:349–361.

Cabrera, E., Abreu, J., Pérez, R., and Vela, A. (1992). Influence of liquid length variation in hydraulic transients. *Journal of Hydraulic Engineering*, 118(12):1639–1650.

Cannizzaro, D. and Pezzinga, G. (2005). Energy dissipation in transient gaseous cavitation. *Journal of Hydraulic Engineering*, 131(8):724–732.

Caré, S. and Raharinaivo, A. (2007). Influence of impressed current on the initiation of damage in reinforced mortar due to corrosion of embedded steel. *Cement and Concrete Research*, 37:1598–1612.

Carlos, M., Arregui, F., Cabrera, E., and Palau, C. (2011). Understanding air release through air valves. *Journal of Hydraulic Engineering*, 137(4):461–469.

Chaiko, M. and Brinckman, K. (2002). Models for analysis of water hammer in piping with entrapped air. *Journal of Fluids Engineering*, 124(1):194–204.

Chaudhry, M. H. (1979). *Applied hydraulic transients*. Springer.

Chaudhry, M. H. (1987). *Applied hydraulic transients*. Van Nostrand Reinhold, New York.

Cole, I. S. and Marney, D. (2012). The science of pipe corrosion: A review of the literature on the corrosion of ferrous metals in soils. *Corrosion Science*, 56:5–16.

Colombo, A. F. and Karney, B. W. (2002). Energy and costs of leaky pipes: Toward comprehensive picture. *Journal of Water Resources Planning and Management*, 128(6):441–450.

Colombo, A. F., Lee, P., and Karney, B. W. (2009). A selective literature review of transient-based leak detection methods. *Journal of Hydro-environment Research*, 2:212–227.

Coronado-Hernández, O. E., Fuertes-Miquel, V. S., Besharat, M., and Ramos, H. M. (2017). Experimental and numerical analysis of a water emptying pipeline using different air valves. *Water*, 9(2):98.

Costello, S., Chapman, D., Rogers, C., and Metje, N. (2007). Underground asset location and condition assessment technologies. *Tunnelling and Underground Space Technology*, 22(5-6):524–542.

Covas, D. and Ramos, H. (2010). Case studies of leak detection and location in water pipe systems by inverse transient analysis. *Journal of Water Resources Planning and Management*, 136(2):248–257.

Covas, D., Stoianov, I., Butler, D., Maksimovic, C., Graham, N., and Ramos, H. (2001). Leakage detection in pipeline systems by inverse transient analysis - from theory to practice. In *International Conference on Computing and Control in the Water Industry*.

Cubrinovski, M., Hughes, M., Bradley, B. A., Noonan, J., Hopkins, R., McNeill, S., and English,

G. (2014). Performance of horizontal infrastructure in Christchurch City through the 2010-2011 Canterbury Earthquake sequence, research report 2014–02.

De Martino, G. and Fontana, N. (2012). Simplified approach for the optimal sizing of throttled air chambers. *Journal of Hydraulic Engineering*, 138(12):1101–1109.

Denison, I. (1931). Correlation of certain soil characteristics with pipe-line corrosion. *Bureau of Standards Journal of Research*, 7:631–642.

Di Santo, A. R., Fratino, U., Iacobellis, V., and Piccinni, A. F. (2002). Effects of free outflow in rising mains with air chamber. *Journal of Hydraulic Engineering*, 128(11):992–1001.

Domenico, S. (1982). Acoustic wave propagation in air-bubble curtains in water—Part I: History and theory. *Geophysics*, 47(3):345–353.

Duan, H. and Lee, P. (2016). Transient-based frequency domain method for dead-end side branch detection in reservoir pipeline-valve systems. *Journal of Hydraulic Engineering*, 142(2):04015042.

Duan, H., Meniconi, S., Lee, P., Brunone, B., and Ghidaoui, M. (2017). Local and integral energy-based evaluation for the unsteady friction relevance in transient pipe flows. *Journal of Hydraulic Engineering*, 143(7):04017015.

Duan, H.-F., Che, T.-C., Lee, P. J., and Ghidaoui, M. S. (2018). Influence of nonlinear turbulent friction on the system frequency response in transient pipe flow modelling and analysis. *Journal of Hydraulic Research*, 56(4):451–463.

Duan, H.-F., Lee, P. J., Ghidaoui, M. S., and Tung, Y.-K. (2012). Extended blockage detection in pipelines by using the system frequency response analysis. *Journal of Water Resources Planning and Management*, 138(1):55–62.

Ebacher, G., Besner, M.-C., Lavoie, J., Jung, B., Karney, B., and Prévost, M. (2011). Transient modeling of a full-scale distribution system: Comparison with field data. *Journal of Water Resources Planning and Management*, 137(2):173–182.

El Maaddawy, T. A. and Soudki, K. A. (2003). Effectiveness of impressed current technique to simulate corrosion of steel reinforcement in concrete. *Journal of Materials in Civil Engineering*, 15(1):41–47.

Evans, W. and Crawford, C. (1954). Design charts for air chambers on pump lines. *Transactions of the American Society of Civil Engineers*, 119:1025–1036.

Falconer, R., Banks, W., and Ellis, J. (1983). Surge pressures at Riding Mill Pumping Station: Actual values and theoretical predictions. In *4th International Conference on Pressure Surges*, pages 21–23.

Ferrante, M. and Brunone, B. (2003). Pipe system diagnosis and leak detection by unsteady-state tests. 2. wavelet analysis. *Advances in Water Resources*, 26(1):107–116.

Ferreira, J., Ghezzi, E., Ferrante, M., and Covas, D. (2018). Pressure wave behaviour due to entrapped air in hydraulic transient events. In *13th International Conference on Pressure Surges*.

Fok, A. T. (1978). Design charts for air chamber on pump pipe lines. *Journal of the Hydraulics Division*, 104(9):1289–1303.

Fox, J. (1972). Pressure transients in pipe networks - A computer solution. In *1st International Conference on Pressure Surges*, pages 1–9.

Fuertes, V., Cabrera, E., Izquierdo, J., and Iglesias, P. (1999). Peak pressure evaluation in pipelines with entrapped air pockets. In *3rd ASME/JSME Joint Fluids Engineering Conference*.

Fuertes-Miquel, V. S., Coronado-Hernández, O. E., Iglesias-Rey, P. L., and Mora-Meliá, D. (2019). Transient phenomena during the emptying process of a single pipe with water–air interaction. *Journal of Hydraulic Research*, 57(3):318–326.

Gao, H., Tang, X., Li, X., and Shi, X. (2018). Analyses of 2d transient models for vaporous cavitating flows in reservoir-pipeline-valve systems. *Journal of Hydroinformatics*, 20(4):934–945.

Gong, J., Lambert, M., Zecchin, A., Simpson, A., Arbon, N., and Kim, Y.-i. (2016). Field study on non-invasive and non-destructive condition assessment for asbestos cement pipelines by time-domain fluid transient analysis. *Structural Health Monitoring*, 15(1):113–124.

Gong, J., Lambert, M. F., Simpson, A. R., and Zecchin, A. C. (2014). Detection of localized deterioration distributed along single pipelines by reconstructive MOC analysis. *Journal of Hydraulic Engineering*, 140(2):190–198.

Gong, J., Lambert, M. F., Simpson, A. R., Zecchin, A. C., et al. (2012). Distributed deterioration detection in single pipes using the impulse response function. In *14th Water Distribution Systems Analysis Conference*.

Gong, J., Simpson, A. R., Lambert, M. F., Zecchin, A. C., Kim, Y.-i., and Tijsseling, A. S. (2013a). Detection of distributed deterioration in single pipes using transient reflections. *Journal of Pipeline Systems Engineering and Practice*, 4(1):32–40.

Gong, J., Simpson, A. R., Lambert, M. F., Zecchin, A. C., Kim, Y.-i., and Tijsseling, A. S. (2013b). Detection of distributed deterioration in single pipes using transient reflections. *Journal of Pipeline Systems Engineering and Practice*, 4(1):32–40.

Gong, J., Stephens, M. L., Arbon, N. S., Zecchin, A. C., Lambert, M. F., and Simpson, A. R. (2015). On-site non-invasive condition assessment for cement mortar-lined metallic pipelines by time-domain fluid transient analysis. *Structural Health Monitoring*, 14(5):426–438.

Govier, G. W. and Aziz, K. (1972). *The flow of complex mixtures in pipes*. Van Nostrand Reinhold New York.

Graze, H. and Forrest, J. (1974). New design charts for air chambers. In *5th Australasian Conference on Hydraulics and Fluid Mechanics*, pages 34–41.

Hachem, F. and Schleiss, A. (2012). Detection of local wall stiffness drop in steel-lined pressure tunnels and shafts of hydroelectric power plants using steep pressure wave excitation and wavelet decomposition. *Journal of Hydraulic Engineering*, 138(1):35–45.

Hou, Q., Tijsseling, A. S., Laanearu, J., Annus, I., Koppel, T., Bergant, A., Vučković, S., Anderson, A., and van't Westende, J. M. (2014). Experimental investigation on rapid filling of a large-scale pipeline. *Journal of Hydraulic Engineering*, 140(11):04014053.

Hu, Y., Wang, D., and Chowdhury, R. (2010). Condition assessment methods for AC pipe and current practices. *Pipelines 2010: Climbing New Peaks to Infrastructure Reliability: Renew, Rehab, and Reinvest*, pages 867–877.

Izquierdo, J., Fuertes, V., Cabrera, E., Iglesias, P., and Garcia-Serra, J. (1999). Pipeline start-up with entrapped air. *Journal of Hydraulic Research*, 37(5):579–590.

Jang, N. W., Gracewski, S. M., Abrahamsen, B., Buttaccio, T., Halm, R., and Dalecki, D. (2009). Natural frequency of a gas bubble in a tube: Experimental and simulation results. *The Journal of the Acoustical Society of America*, 126:EL34–EL40.

Jang, T. U., Wu, Y.-b., Xu, Y., and Qiang, S. (2017). A scheme for improving computational efficiency of quasi-two-dimensional model. *Journal of Hydrodynamics*, 29(2):243–250.

Jönsson, L. (1985). Maximum transient pressures in a conduit with check valve and air entrainment. In *International Conference on the Hydraulics of Pumping Stations*, pages 55–76.

Jönsson, L. (1994). Leak detection in pipelines using hydraulic transients. *Transactions on Ecology and the Environment*, 7.

Jönsson, L. and Larson, M. (1992). Leak detection through hydraulic transient analysis. In *Pipeline Systems*, pages 273–286. Springer.

Kapelan, Z., Savic, D., and Walters, G. (2002). Hybrid GA for calibration of water distribution models. *Proc. EWRI*.

Kapelan, Z., Savic, D., and Walters, G. (2003a). Optimal sampling design for calibration of transient network models using multi-objective gas. In *International Conference on Pumps, Electromechanical Devices and Systems Applied to Urban Water Management*.

Kapelan, Z. S., Savic, D. A., and Walters, G. A. (2003b). A hybrid inverse transient model for leakage detection and roughness calibration in pipe networks. *Journal of Hydraulic Research*, 41(5):481–492.

Karney, B., Malekpour, A., and Nault, J. (2015). Metrics for the rapid assessment of transient severity in pipelines. *Pipelines 2015*, pages 815–824.

Karney, B. W. and McInnis, D. (1990). Transient analysis of water distribution systems. *Journal - American Water Works Association*, 82(7):62–70.

Karney, B. W. and McInnis, D. (1992). Efficient calculation of transient flow in simple pipe networks. *Journal of Hydraulic Engineering*, 118(7):1014–1030.

Kim, S.-G., Lee, K.-B., and Kim, K.-Y. (2014a). Water hammer in the pump-rising pipeline system with an air chamber. *Journal of Hydrodynamics*, 26(6):960–964.

Kim, S.-G., Lee, K.-B., and Kim, K.-Y. (2014b). Water hammer in the pump-rising pipeline system with an air chamber. *Journal of Hydrodynamics*, 26(6):960–964.

Kim, S. H. (2008a). Impulse response method for pipeline systems equipped with water hammer protection devices. *Journal of Hydraulic Engineering*, 134(7):961–969.

Kim, S.-H. (2010). Design of surge tank for water supply systems using the impulse response method with the ga algorithm. *Journal of Mechanical Science and Technology*, 24(2):629–636.

Kim, Y. I. (2008b). *Advanced numerical and experimental transient modelling of water and gas pipeline flows incorporating distributed and local effects*. PhD thesis, University of Adelaide.

Kinsler, L. E., Frey, A. R., Coppens, A. B., and Sanders, J. V. (2000). *Fundamentals of Acoustics*. John Wiley & Sons Inc, New York.

Kivell, A., Palermo, A., and Scott, A. (2011). Effects of bond deterioration due to corrosion in reinforced concrete. In *9th Pacific Conference on Earthquake Engineering*, pages 81–88.

Korteweg, D. (1878). Ueber die fortpflanzungsgeschwindigkeit des schalles in elastischen röhren. *Annalen der Physik*, 241(12):525–542.

Lai, A., Hau, K., Noghrehkar, R., and Swartz, R. (2000). Investigation of waterhammer in piping networks with voids containing non-condensable gas. *Nuclear Engineering and Design*, 197:61–74.

Lai, C. (1991). Unaccounted for water and the economics of leak detection. *Water Supply*, 9(3).

Lauchlan, C., Escarameia, M., May, R., Burrows, R., and Gahan, C. (2005). Air in pipelines: A literature review. *HR Wallingford. Report SR*.

Lee, N. and Martin, C. (1999). Experimental and analytical investigation of entrapped air in a horizontal pipe. In *3rd ASME/JSME Joint Fluids Engineering Conference*, pages 189–196.

Lee, N. H. (2005). *Effect of pressurization and expulsion of entrapped air in pipelines*. PhD thesis, Georgia Institute of Technology.

Lee, P. J., Duan, H.-F., Ghidaoui, M., and Karney, B. (2013). Frequency domain analysis of pipe fluid transient behaviour. *Journal of hydraulic research*, 51(6):609–622.

Lee, P. J., Lambert, M. F., Simpson, A. R., Vítkovskỳ, J. P., and Liggett, J. (2006). Experimental verification of the frequency response method for pipeline leak detection. *Journal of Hydraulic Research*, 44(5):693–707.

Lee, P. J., Vítkovskỳ, J. P., Lambert, M. F., Simpson, A. R., and Liggett, J. A. (2005). Frequency domain analysis for detecting pipeline leaks. *Journal of Hydraulic Engineering*, 131(7):596–604.

Lee, T. (1991). Numerical computation of fluid pressure transients in pumping installations with air entrainment. *International Journal for Numerical Methods in Fluids*, 12:747–763.

Leighton, T., Ramble, D., Phelps, A., Morfey, C., and Harris, P. (1998). Acoustic detection of gas bubbles in a pipe. *Acta Acustica united with Acustica*, 84:801–814.

Levine, H. and Schwinger, J. (1948). On the radiation of sound from an unflanged circular pipe. *Physical Review*, 73(4):383–406.

Liggett, J. A. and Chen, L.-C. (1994). Inverse transient analysis in pipe networks. *Journal of Hydraulic Engineering*, 120(8):934–955.

Liu, Z. and Kleiner, Y. (2012). State of the art review of inspection technologies for condition assessment of water pipes. *Measurement*, 46:1–15.

Liu, Z., Kleiner, Y., Rajani, B., Wang, L., and Condit, W. (2012). Condition assessment technologies for water transmission and distribution systems. *United States Environmental Protection Agency*.

Mandhane, J., Gregory, G., and Aziz, K. (1974). A flow pattern map for gas—liquid flow in horizontal pipes. *International Journal of Multiphase Flow*, 1:537–553.

Martin, C. (1976). Entrapped air in pipelines. In *2nd International Conference on Pressure Surges*, volume 2, pages 15–27. British Hydromechanics Research Association, Bedford, UK.

Martin, C. and Wiggert, D. (1986). Hydraulic transients in circulating cooling water systems. Technical report, Electric Power Research Institute, Georgia Inst. of Technology and Michigan State University.

Martin, F. (2015). *Artificial transmission lines for RF and microwave applications*. John Wiley & Sons.

Meniconi, S., Brunone, B., and Ferrante, M. (2011). In-line pipe device checking by short-period analysis of transient tests. *Journal of Hydraulic Engineering*, 137(7):713–722.

Meniconi, S., Brunone, B., Ferrante, M., and Capponi, C. (2016). Mechanism of interaction of pressure waves at a discrete partial blockage. *Journal of Fluids and Structures*, 62:33–45.

Meniconi, S., Duan, H. F., Lee, P. J., Brunone, B., Ghidaoui, M. S., and Ferrante, M. (2013). Experimental investigation of coupled frequency and time-domain transient test–based techniques for partial blockage detection in pipelines. *Journal of Hydraulic Engineering*, 139(10):1033–1040.

Millette, J. R., Hammonds, A. F., Pansing, M. F., Hansen, E. C., and Clark, P. J. (1980). Aggressive water: Assessing the extent of the problem. *Journal - American Water Works Association*, 72(5):262–266.

Minnaert, M. (1933). On musical air-bubbles and the sounds of running water. *The London, Edinburgh, and Dublin Philosophical Magazine and Journal of Science*, 16(104):235–248.

Mohapatra, P. K., Chaudhry, M. H., Kassem, A., and Moloo, J. (2006). Detection of partial blockages in a branched piping system by the frequency response method. *Journal of Fluids Engineering*, 128(5):1106–1114.

Mohebbi, H. and Li, C. (2011). Experimental investigation on corrosion of cast iron pipes. *International Journal of Corrosion*, 2011.

Naser, G., Karney, B. W., Nixon, W., Ghidaoui, M. S., and Brunone, B. (2004). A quasi two-dimensional approach in transient flow modeling. In *12th Annual Conference of Computational Fluid Dynamics*.

Nash, G. A. and Karney, B. W. (1999). Efficient inverse transient analysis in series pipe systems. *Journal of Hydraulic Engineering*, 125(7):761–764.

Nixon, W. and Ghidaoui, M. S. (2007). Numerical sensitivity study of unsteady friction in simple systems with external flows. *Journal of Hydraulic Engineering*, 133(7):736–749.

Ocasio, J. (1976). Pressure surging associated with pressurization of pipelines containing entrapped air. *Special MS Research Report*.

Orfanidis, S. J. (2002). *Electromagnetic waves and antennas*. Rutgers University New Brunswick, NJ.

Pearsall, I. (1965). The velocity of water hammer waves. In *Proceedings of the Institution of Mechanical Engineers*, volume 180, pages 12–20. SAGE Publications Sage UK: London, England.

Pezzinga, G. (1999). Quasi-2D model for unsteady flow in pipe networks. *Journal of Hydraulic Engineering*, 125(7):676–685.

Pozos, O. (2007). *Investigation on the effects of entrained air in pipelines*. PhD thesis, University of Stuttgart.

Pozos, O., Gonzalez, C. A., Giesecke, J., Marx, W., and Rodal, E. A. (2010). Air entrapped in gravity pipeline systems. *Journal of Hydraulic Research*, 48(3):338–347.

Pozos-Estrada, O. (2017). Investigation of the combined effect of air pockets and air bubbles on fluid transients. *Journal of Hydroinformatics*, 20(2):376–392.

Provoost, G. (1976). Investigation into cavitation in a prototype pipeline caused by water hammer. In *2nd International Conference on Pressure Surges*.

Pudar, R. S. and Liggett, J. A. (1992). Leaks in pipe networks. *Journal of Hydraulic Engineering*, 118(7):1031–1046.

Purcell, P. J. (1997). Case study of check-valve slam in rising main protected by air vessel. *Journal of Hydraulic Engineering*, 123(12):1166–1168.

Rajani, B. and Kleiner, Y. (2001). Comprehensive review of structural deterioration of water mains: Physically based models. *Urban Water*, 3(3):151–164.

Regier, C. (2015). *Investigation of the failure mechanisms of intact and deteriorated culverts*. PhD thesis, Queen's University.

Rodhe, H. and Herrera, R. (1988). *Acidification in tropical countries*. John Wiley and Sons Inc.

Rubio Scola, I., Besançon, G., and Georges, D. (2017). Blockage and leak detection and location in pipelines using frequency response optimization. *Journal of Hydraulic Engineering*, 143(1):04016074.

Sander, R. (2015). Compilation of Henry's law constants (version 4.0) for water as solvent. *Atmospheric Chemistry & Physics*, 15(8).

Schaschl, E. and Marsh, G. (1963). Some new views on soil corrosion. *Materials Protection*, 2(11):8–17.

Smolders, S., Verhoest, L., De Gueldre, G., and Van De Steene, B. (2009). Inspection of deteriorating asbestos cement force mains with georadar technique. *Water Science and Technology*, 60(4):995–1001.

Soares, A. K., Covas, D. I., and Reis, L. F. R. (2011). Leak detection by inverse transient analysis in an experimental pvc pipe system. *Journal of Hydroinformatics*, 13(2):153–166.

Spellman, F. R. (2003). *Handbook of water and wastewater treatment plant operations*. CRC Press.

Stephens, M., Lambert, M., Simpson, A., Vítkovskỳ, J., and Nixon, J. (2004a). Field tests for leakage, air pocket, and discrete blockage detection using inverse transient analysis in water distribution pipes. In *Critical Transitions in Water and Environmental Resources Management (Proceedings of the World Water and Environmental Resources Congress)*, pages 1–10.

Stephens, M., Simpson, A., and Lambert, M. (2008). Internal wall condition assessment for water pipelines using inverse transient analysis. In *10th Annual Symposium on Water Distribution Systems Analysis*.

Stephens, M., Vitkovsky, J., Lambert, M., Simpson, A., Karney, B., and Nixon, J. (2004b). Transient analysis to assess valve status and topology in pipe networks. In *9th International Conference on Pressure Surges*.

Stephens, M. L. (2008). *Transient response analysis for fault detection and pipeline wall condition assessment in field water transmission and distribution pipelines and networks*. PhD thesis, University of Adelaide.

Stephens, M. L., Lambert, M. F., and Simpson, A. R. (2013). Determining the internal wall condition of a water pipeline in the field using an inverse transient. *Journal of Hydraulic Engineering*, 139(3):310–324.

Streeter, V. L. and Lai, C. (1962). Water-hammer analysis including fluid friction. *Journal of the Hydraulics Division*, 88(3):79–112.

Tang, K., Karney, B., and Brunone, B. (2001). Leak detection using inverse transient calibration and GA - Some early successes and future challenges. In *6th International Conference on Computing and Control in the Water Industry*.

Titchall, A. (2016). Call for national water asset policy. *Water New Zealand Water Journal*, 197.

Tran, D., Perera, B., and Ng, A. (2010). Hydraulic deterioration models for storm-water drainage pipes: Ordered probit versus probabilistic neural network. *Journal of Computing in Civil Engineering*, 24(2):140–150.

Tuck, J. and Lee, P. (2013). Inverse transient analysis for classification of wall thickness variations in pipelines. *Sensors*, 13(12):17057–17066.

USA National Research Council, N. (1982). *Drinking Water and Health: Volume 4*. The National Academies Press, Washington, DC.

Vardy, A. E. and Hwang, K.-L. (1991). A characteristics model of transient friction in pipes. *Journal of Hydraulic Research*, 29(5):669–684.

Vasconcelos, J. G. and Leite, G. M. (2012). Pressure surges following sudden air pocket entrapment in storm-water tunnels. *Journal of Hydraulic Engineering*, 138(12):1081–1089.

Vítkovskỳ, J., Lambert, M., Simpson, A., and Bergant, A. (2003a). Frequency-domain transient pipe flow solution including unsteady friction. In *Proceedings of the International Conference on Pumps, Electromechanical Devices and Systems Applied to Urban Water Management*, pages 773–780.

Vítkovskỳ, J., Lee, P. J., Stephens, M. L., Lambert, M. F., Simpson, A. R., and Liggett, J. A. (2003b). Leak and blockage detection in pipelines via an impulse response method. In *Pumps, Electromechanical Devices and Systems Applied to Urban Water Management*. Taylor & Francis.

Vítkovskỳ, J. and Simpson, A. (1997). Calibration and leak detection in pipe networks using inverse transient analysis and genetic algorithms. Technical report, Department of Civil and Environmental Engineering, University of Adelaide.

Vitkovsky, J. P., Lambert, M. F., Simpson, A. R., Wang, X.-J., et al. (2001). An experimental verification of the inverse transient technique for leak detection. In *Conference on Hydraulics in Civil Engineering: The State of Hydraulics*.

Vítkovskỳ, J. P., Simpson, A. R., and Lambert, M. F. (2002). Minimization algorithms and experimental inverse transient leak detection. In *EWRI*.

Volk, C., Dundore, E., Schiermann, J., and Lechevallier, M. (2000). Practical evaluation of iron corrosion control in a drinking water distribution system. *Water Research*, 34(6):1967–1974.

Vreeburg, I. J. and Boxall, J. B. (2007). Discolouration in potable water distribution systems: A review. *Water Research*, 41:519–529.

Wan, W.-y., Li, C.-y., and Yu, Y.-q. (2017). Investigation on critical equilibrium of trapped air pocket in water supply pipeline system. *Journal of Zhejiang University-SCIENCE A*, 18(3):167–178.

Wang, X.-J., Lambert, M. F., Simpson, A. R., Liggett, J. A., and V ı´ tkovskỳ, J. P. (2002). Leak detection in pipelines using the damping of fluid transients. *Journal of Hydraulic Engineering*, 128(7):697–711.

Water New Zealand (2006). Pipe inspection manual. Technical report, The New Zealand Water and Wastes Association.

Water New Zealand (2019). National performance review 2018-2019. Technical report, The New Zealand Water and Wastes Association.

Watercare (2014). *Water reticulation design guidelines*. Watercare.

Watters, G. Z. (1971). *The behavior of PVC pipe under the action of water hammer pressure waves*. PhD thesis, Utah State University.

Whiteman, K. and Pearsall, I. (1962). Reflux valve and surge tests at a station. *Fluid Handling*, 13:248–250.

Whiteman, K. and Pearsall, I. S. (1959). *Reflux valve and surge tests at Kingston Pumping Station*. British Hydromechanics Research Association.

Wisner, P. E., Kouwen, N., and Mohsen, F. N. (1975). Removal of air from water lines by hydraulic means. *Journal of the Hydraulics Division*, 101(2):243–257.

Wood, D. J. (1970). Pressure surge attenuation utilizing an air chamber. *Journal of the Hydraulics Division*, 96(5):1143–1156.

Wood, D. J., Lingireddy, S., Boulos, P. F., Karney, B. W., and McPherson, D. L. (2005). Numerical methods for modeling transient flow in distribution systems. *Journal - American Water Works Association*, 97(7):104–115.

Wylie, E. (1964). *Resonance in pressurized piping systems*. PhD thesis, University of Michigan.

Wylie, E. (1980). Free air in liquid transient flow. In *3rd International Conference on Pressure Surges*, pages 27–42.

Wylie, E. B., Streeter, V. L., and Suo, L. (1993). *Fluid transients in systems*, volume 1. Prentice Hall Englewood Cliffs, NJ.

Yang, Y., Liu, F., and Xi, F. (2020). Tensile fracture behavior of corroded pipeline: Part 1—Experimental characterization. *Advances in Materials Science and Engineering*, 2020.

Zhao, M. and Ghidaoui, M. S. (2006). Investigation of turbulence behavior in pipe transient using a $k - -\epsilon$ model. *Journal of Hydraulic Research*, 44(5):682–692.

Zhou, F. (2000). *Effects of trapped air on flow transients in rapidly filling sewers*. PhD thesis, University of Alberta.

Zhou, F., Hicks, F., and Steffler, P. (2002). Transient flow in a rapidly filling horizontal pipe containing trapped air. *Journal of Hydraulic Engineering*, 128(6):625–634.

Zhou, L., Liu, D., and Karney, B. (2013a). Investigation of hydraulic transients of two entrapped air pockets in a water pipeline. *Journal of Hydraulic Engineering*, 139(9):949–959.

Zhou, L., Liu, D., Karney, B., and Wang, P. (2013b). Phenomenon of white mist in pipelines rapidly filling with water with entrapped air pockets. *Journal of Hydraulic Engineering*, 139(10):1041–1051.

Zhou, L., Liu, D., Karney, B., and Zhang, Q. (2011). Influence of entrapped air pockets on hydraulic transients in water pipelines. *Journal of Hydraulic Engineering*, 137(12):1686–1692.

Zhou, L., Wang, H., Karney, B., Liu, D., Wang, P., and Guo, S. (2018). Dynamic behavior of entrapped air pocket in a water filling pipeline. *Journal of Hydraulic Engineering*,

144(8):04018045.

Zielke, W. (1968). Frequency-dependent friction in transient pipe flow. *Journal of Basic Engineering*, 90(1):109–115.

A Copyright Permissions

This appendix contains copyright permissions for the re-use of the publications presented in this thesis.

Chapter 3: Alexander, J., Lee, P.J., Davidson, M., Li, Z, Murch, R., Duan, H.F., Meniconi, S., Brunone, B. (2020). Experimental investigation of the interaction of fluid transients with an in-line air pocket. Journal of Hydraulic Engineering, 146(3).

From: PERMISSIONS
Sent: Thursday, 16 April 2020 2:01 AM
To: ASCE Library; Jane Alexander
Subject: RE: Copyright permissions

Dear Jane,
Thank you for your inquiry. As an original author of an ASCE journal article or proceedings paper, you are permitted to reuse your own content (including figures and tables) for another ASCE or non-ASCE publication (including thesis), provided it does not account for more than 25% of the new work. This email serves as permission to reuse your work, Experimental Investigation of the Interaction of Fluid Transients with an In-Line Air Pocket. *Journal of Hydraulic Engineering*, 146(3), 04019067.

A full credit line must be added to the material being reprinted. For reuse in non-ASCE publications, add the words "With permission from ASCE" to your source citation. For Intranet posting, add the following additional notice: "This material may be downloaded for personal use only. Any other use requires prior permission of the American Society of Civil Engineers. This material may be found at https://doi.org/10.1061/(ASCE)HY.1943-7900.0001691."

Each license is unique, covering only the terms and conditions specified in it. Even if you have obtained a license for certain ASCE copyrighted content, you will need to obtain another license if you plan to reuse that content outside the terms of the existing license. For example: If you already have a license to reuse a figure in a journal, you still need a new license to use the same figure in a magazine. You need a separate license for each edition.

For more information on how an author may reuse their own material, please view:
http://ascelibrary.org/page/informationforasceauthorsreusingyourownmaterial

Sincerely,

Leslie Connelly
Manager, Publications Marketing
American Society of Civil Engineers
1801 Alexander Bell Drive
Reston, VA 20191

Chapter 4: Alexander, J., Lee, P.J., Davidson, M., Duan, H.F., Li, Z., Murch, R., Meniconi, S. and Brunone, B. (2019). Experimental validation of existing numerical models for the interaction of fluid transients with in-line air pockets. Journal of Fluids Engineering, 141(12).

From: Beth Darchi
Sent: Friday, 1 May 2020 2:33 AM
To: Jane Alexander
Subject: RE: Permission for thesis with publication

Dear Ms. Alexander,

It is our pleasure to grant you permission **to use all or any part of** the ASME paper "Experimental Validation of Existing Numerical Models for the Interaction of Fluid Transients With In-Line Air Pockets," by Jane Alexander, Pedro J. Lee, Mark Davidson, Huan-Feng Duan, Zhao Li, Ross Murch, Silvia Meniconi, Bruno Brunone, J. Fluids Eng. December 2019, 141(12), cited in your letter for inclusion in a thesis entitled The Interaction of Fluid Transients with Pipe Anomalies to be published by University of Canterbury.

Permission is granted for the specific use as stated herein and does not permit further use of the materials without proper authorization. Proper attribution must be made to the author(s) of the materials. Please note: if any or all of the figures and/or Tables are of another source, permission should be granted from that outside source or include the reference of the original source. ASME does not grant permission for outside source material that may be referenced in the ASME works.

As is customary, we request that you ensure full acknowledgment of this material, the author(s), source and ASME as original publisher. Acknowledgment must be retained on all pages where figure is printed and distributed.

Many thanks for your interest in ASME publications.

Sincerely,

Beth Darchi
Publishing Administrator
ASME
2 Park Avenue
New York, NY 10016-5990
Tel 1.212.591.7700
darchib@asme.org

Chapter 5: Alexander, J., Li, Z., Lee, P.J., Davidson, M., Duan, H.F. (2020). Experimental investigation of the effects of air pocket configuration on fluid transients in a pipeline. Journal of Hydraulic Engineering, 146(12).

From: PERMISSIONS [permissions@asce.org]
Sent: 10 October 2020 03:56
To: Jane Alexander
Subject: RE: Copyright permission

Dear Jane,

Thank you for your inquiry. As an original author of an ASCE journal article or proceedings paper, you are permitted to reuse your own content (including figures and tables) for another ASCE or non-ASCE publication (including your theis), provided it does not account for more than 25% of the new work. This email serves as permission to reuse your work, Experimental Investigation of the Effects of Air Pocket Configuration on Fluid Transients in a Pipeline. Journal of Hydraulic Engineering, 146(12), 04020081,https://doi.org/10.1061/(ASCE)HY.1943-7900.0001823.

A full credit line must be added to the material being reprinted. For reuse in non-ASCE publications, add the words "With permission from ASCE" to your source citation. For Intranet posting, add the following additional notice: "This material may be downloaded for personal use only. Any other use requires prior permission of the American Society of Civil Engineers. This material may be found at [URL/link of abstract in the ASCE Library or Civil Engineering Database]."

Each license is unique, covering only the terms and conditions specified in it. Even if you have obtained a license for certain ASCE copyrighted content, you will need to obtain another license if you plan to reuse that content outside the terms of the existing license. For example: If you already have a license to reuse a figure in a journal, you still need a new license to use the same figure in a magazine. You need a separate license for each edition.

Sincerely,

Leslie Connelly
Manager, Publications Marketing
American Society of Civil Engineers
1801 Alexander Bell Drive
Reston, VA 20191

Chapter 6: Alexander, J., Li, Z., Lee, P.J., Davidson, M., Duan, H.F.. Comparison of numerical models for the interaction of a fluid transient with an off-line air pocket. Accepted for publication by Journal of Hydraulic Engineering, 2020 (DOI 10.1061/(ASCE)HY.1943-7900.0001878).

From: PERMISSIONS [permissions@asce.org]
Sent: 20 November 2020 08:57
To: Jane Alexander
Subject: RE: Copyright permission

Dear Jane,

Thank you for your inquiry. As an original author of an ASCE journal article or proceedings paper, you are permitted to reuse your own content (including figures and tables) for another ASCE or non-ASCE publication (including your theis), provided it does not account for more than 25% of the new work. This email serves as permission to reuse your work, Comparison of numerical models for the interaction of a fluid transient with an off-line air pocket, Journal of Hydraulic Engineering, https://doi.org/10.1061/(ASCE)HY.1943-7900.0001878.

A full credit line must be added to the material being reprinted. For reuse in non-ASCE publications, add the words "With permission from ASCE" to your source citation. For Intranet posting, add the following additional notice: "This material may be downloaded for personal use only. Any other use requires prior permission of the American Society of Civil Engineers. This material may be found at [URL/link of abstract in the ASCE Library or Civil Engineering Database]."

Each license is unique, covering only the terms and conditions specified in it. Even if you have obtained a license for certain ASCE copyrighted content, you will need to obtain another license if you plan to reuse that content outside the terms of the existing license. For example: If you already have a license to reuse a figure in a journal, you still need a new license to use the same figure in a magazine. You need a separate license for each edition.

Sincerely,

Leslie Connelly
Manager, Publications Marketing
American Society of Civil Engineers
1801 Alexander Bell Drive
Reston, VA 20191